PONTIFICIA UNIVERSIDAD CATÓLICA DEL PERÚ

Escuela de Posgrado

Preparación y Optimización de Películas Delgadas de Sistemas de Carbono-Sílice Dopados con Tierras Raras para Aplicaciones Luminiscentes

Tesis para obtener el grado académico de Doctora en Física que presenta:

Loreleyn Flor Flores Escalante

Asesores:

Dr. Rolf Grieseler
Dr. Albrecht Winnacker

Lima, 2021

RESUMEN

El uso de elementos de tierras raras (RE) en materiales de luminiscencia ha permitido introducir mejoras en diversas aplicaciones. En iluminación, por ejemplo, los fósforos amarillos YAG ($Y_3Al_5O_{12}:Ce^{3+}$) son ampliamente utilizado en LED blancos. En los sistemas de telecomunicaciones e Internet, se utilizan amplificadores de fibra dopada con erbio (Er^{3+}) para aplicaciones en la región de longitud de onda de las telecomunicaciones (1530-1550 nm). En láseres, YAG:Nd^{3+} encuentran su aplicación en láseres de estado sólido con una línea de emisión de 1,06 μm. Los YAG también pueden estar dopados con Tm^{3+} (1,93-2,04 μm) o Er^{3+} (2,94 μm) y se utilizan principalmente en aplicaciones médicas. En las células solares, las capas de convertidor espectral están diseñadas para aumentar la eficiencia de las células solares. El espectro solar AM1.5G se puede modificar mediante procesos llamados Up-conversion, quantum cutting, and down-shifting. Por tanto, se mejoraría el EQE de las células solares.

El estudio central de este trabajo fue la preparación y optimización de la luminiscencia de los iones Tb^{3+} e Yb^{3+} en la relativamente nueva matriz de *a*-SiOC: H para aplicaciones luminiscentes como convertidores espectrales descendentes. El método utilizado para la optimización de la luminiscencia se basa en tratamientos de recocido, composición de la matriz y co-dopaje con elementos Tb e Yb. Los detalles experimentales se presentan en el **Capítulo 3**. El primer objetivo de este trabajo se centró en la preparación de capas de *a*-SiOC: H que pueden cultivarse en la superficie de una célula solar de prueba (célula de Si + capa antirreflejante). La literatura reporta trabajos previos sobre SiOC. Sin embargo, la mayoría de ellos se basan principalmente en la preparación a temperaturas cercanas a los 1000 °C, lo que provocaría daños en la celda solar debido a la alta temperatura. Por esta razón, se utilizó un sistema de pulverización catódica de RF con enfriamiento del sustrato. Las propiedades ópticas de la matriz dependen de la composición de Si, C y O. por lo que, el **Capítulo 4** se enfoca en el estudio de (1) el análisis de composición y la estructura, (2) el cálculo de la banda prohibida y la energía de Urbach, (3) el efecto del tratamiento de recocido en la estructura de la red atómica y (4) los procesos que impulsan la luminiscencia de matriz.

El segundo objetivo de este trabajo fue la optimización de la fotoluminiscencia de los iones Tb^{3+} e Yb^{3+} en muestras de *a*-SiOC:H dopadas con uno de los dos iones. Una luminiscencia creciente de los iones de RE^{3+} requiere (1) aumentar el número de iones RE^{3+} activos, (2) reducir las fuentes de pérdida de energía y (3) aumentar el número de sensibilizadores. El **Capítulo 5** examina estos procesos en detalle. En la literatura, la emisión

de iones RE^{3+} está bien reportada. Sin embargo, los mecanismos de transferencia no radiativa de energía de los estados de defecto (en materiales amorfos basados en silicio) a los dopantes de RE son poco discutidos. Además, el ion RE^{3+} en tales materiales no reemplazará a ninguno de los iones en la matriz como si lo hace en el caso de los materiales cristalinos dopados con elementos de RE. En materiales amorfos (que contienen oxígeno), el ion RE^{3+} se ubicará en un sitio rodeado localmente por átomos de oxígeno. Por lo tanto, este trabajo estudia y propone mecanismos de excitación para los iones Tb^{3+} e Yb^{3+}. Estos mecanismos pueden aplicarse en la matriz *a*-SiOC: H y extenderse a materiales basados en Si y SiO_x. Finalmente, estudios previos del efecto del carbono mostraron una mejora de la luminiscencia de los iones RE^{3+}. Por tanto, se llevó a cabo un estudio sistemático de luminiscencia basado en el cambio de composición del carbono. Este trabajo estudia las ventajas y desventajas del dopaje con carbono en la activación de la luminiscencia de los iones RE^{3+}. Los resultados también se presentan en el **Capítulo 5**.

El tercer objetivo de este trabajo fue la optimización de la luminiscencia del Yb en muestras de *a*-SiOC:H co-dopadas. Entre los diferentes sistemas de iones RE^{3+} para aplicaciones de corte cuántico (QC) en el infrarrojo cercano, los que incluyen iones Yb^{3+} parecen ser los más apropiados porque el ión Yb^{3+} tiene una transición a aproximadamente 980 nm (~ 1,22 eV) justo por encima de la banda prohibida del silicio cristalino de 1,1 eV. Los iones Tb^{3+} se utilizaron para mejorar la emisión de los iones Yb^{3+}. Por lo tanto, los convertidores descendentes de infrarrojo cercano encuentran una posible aplicación en las células solares de silicio. La capa de convertidor espectral se colocará en la parte superior de la superficie de la célula solar, por lo que la capa de QC tiene la ventaja de que se puede optimizar independientemente de la celda. En este trabajo se identifican y estudian los mecanismos asociados a la transferencia de energía del huésped a los iones RE^{3+}. Se estimó el rendimiento cuántico de fotoluminiscencia de la capa convertidora espectral. Además, se prepararon las capas en la superficie frontal de las células de mc-silicio, y se estudió su efecto en la eficiencia cuántica externa. Por último, se estudió el mecanismo de transferencia cooperativa entre los iones Tb^{3+} e Yb^{3+}; los cuales son utilizados para explicar el proceso de QC. Este mecanismo cooperativo se ha atribuido a los procesos de QC en muchas matrices cristalinas y amorfas. Sin embargo, a pesar de numerosos documentos que adscriben sus resultados al mecanismo de transferencia cooperativa, pocos realmente lo prueban. Por lo tanto, también se analiza el papel de los iones Tb^{3+} en la luminiscencia del Yb. Los resultados se presentan en el **Capítulo 6**.

Als Dissertation genehmigt in der Doktorats Programm in Werkstoffwissenschaften von der Technischen Fakultät der Friedrich-Alexander Universität Erlangen-Nürnberg, Deutschland.
Ort and tag der mündlichen Prüfung:

Approved as a dissertation in the Doctoral Program in Physics of the Pontifical Catholic University of Peru.
Place and day of the oral examination:

Vorsitzender des Promotionsorgans:
Prof. Dr.-Ing. Knut Graichen

Chairman of the doctoral examination board: Dr.-Ing. Knut Graichen

Gutachter:
Prof. Dr. Albrecht Winnacker
Prof. Dr. Rolf Grieseler
Priv.-Doz. Dr. Miroslaw Batentschuk
Prof. Dr. Andrés Guerra
Prof. Dr. María Elena López

Reviewer:
Prof. Dr. Albrecht Winnacker
Prof. Dr. Rolf Grieseler
Priv.-Doz. Dr. Miroslaw Batentschuk
Prof. Dr. Andrés Guerra
Prof. Dr. María Elena López

To my parents Mirtha and Antonio, and my little siblings Yoselyn and Antonio

"...I'm starting with the man in the mirror

I'm asking him to change his ways

And no message could've been any clearer

If you wanna make the world a better place

Take a look at yourself and then make a change..."

(Man in the mirror, Michael Jackson)

Acknowledgments

I would like to thank the National Council of Science and Technology of Peru – CONCYTEC for the Peruvian Doctoral Scholarship in the frame of the Pontificia Universidad Católica del Perú (PUCP) doctorate Program. I would also like to thank the German Academic Exchange Service - DAAD and CONCYTEC for funding bilateral research.

I would like to thank Prof. Roland Weingärtner and Prof. Rolf Grieseler, my advisors in Peru, for their support during my thesis work. I also would like to thank Prof. Albrecht Winnacker, my advisor in Germany, for the wonderful opportunity to perform part of my Ph.D. at the i-MEET institute.

My special thanks I would like to address to Priv.-Doz. Dr. Miroslaw Batentschuk who supports me during my research stage in Germany. He was always ready to assist with administrative tasks as well as in the discussion of the results during our group meetings.

My infinite thanks to Dr. Andres Osvet for all his help with optical characterization, the input of ideas, discussion of results, correction and improvement of my manuscripts, as well as his invaluable teachings on science. His work with the Ph. D. students is invaluable.

I would like to thank Prof. Alberto Gago and Prof. Francisco De Zela from Physics Section in Peru for their valuable time in the administrative procedures and doubts. Thank you for your trust.

This thesis would not be complete without successful collaboration. I would like to express my gratitude to Prof. Andres Guerra for the constructive feedback during the development of my thesis. I also would like to thank Dr. Anastasiia Barabash and Eggi Völkel for SEM measurements. Without her work, my studies would be almost impossible. Finally, I want to thank Prof. Dr. Dominique de Ligny and Hagar Elkhouly for their help in PLE measurements.

I would love to acknowledge i-MEET people José, Osbel, Violeta, Jhonas, Liudmyla, Jack for the friendly atmosphere in more than one year of warm companionship. You guys got more than one good laugh out of me. Also, my warmest thanks to my colleagues and friends Karem, José, Jorge, Carlos, Alvaro, Mary, Amaru from the Materials Science group,

Physics Section in Peru. Thanks also to all the people who in some way contributed to the realization of this thesis.

Most fundamentally, I would like to thank my parents Mirtha and Antonio, who are always aware of all my adventures despite not understanding what I do. Thanks also to my little brothers Yoselyn and Antonio for always being present in my life.

Last but not least, I would like to thank the review committee members for their effort and time in reading my work.

Abstract

The uses of rare-earth (RE) elements in luminescence materials led to important improvements in a variety of applications. In lighting, for example, YAG yellow phosphors ($Y_3Al_5O_{12}:Ce^{3+}$) are widely used for white LED devices. In telecommunication and internet systems, erbium (Er^{3+})-doped fiber amplifiers are used in the telecom wavelength region (1530-1550 nm). In laser, YAG:Nd^{3+} are used in solid-state lasers with an emission line at 1.06 μm. YAG can also be doped with Tm^{3+} (1.93-2.04 μm) or Er^{3+} (2.94 μm) and are mainly used in medical applications. In solar cells, spectral converter layers are designed to increase the efficiency of solar cells. The AM1.5G solar spectrum can be modified by processes called up-conversion, quantum cutting, and down-shifting. Thus, it would improve the EQE of solar cells.

The central study of this work was the preparation and optimization of the luminescence of Tb^{3+} and Yb^{3+} ions in the relatively new *a*-SiOC:H matrix for luminescent applications as spectral downconverters. The method used for luminescence optimization is based on annealing treatments, matrix composition and co-doping with Tb and Yb elements. Experimental details are presented in **Chapter 3**. The first goal of this work focused on the preparation of *a*-SiOC:H layers that can be grown on the surface of a test solar cell (Si cell + antireflective layer). The literature reports previous works on SiOC. However, most of them are mainly based on preparation at temperatures close to 1000 °C, which would lead to damage in solar cell due to the high temperature. For this reason, an RF-sputtering system with substrate cooling was used. The matrix optical properties depend on the Si, C, and O composition. So, **Chapter 4** focus on the study of (1) composition and structure analysis, (2) the bandgap and Urbach energy calculation, (3) the effect of the annealing treatment on the atomic network structure, and (4) the processes driving the matrix luminescence.

The second goal of this work was the optimization of the annealing temperature and RE(Tb, Yb) concentration to improve the photoluminescence of the Tb^{3+} and Yb^{3+} ions in single doped *a*-SiOC:H samples. An increasing RE luminescence requires (1) to increase the number of active RE^{3+} ions, (2) to reduce the sources of energy loss, and (3) to increase the number of sensitizers. **Chapter 5** examines those processes in detail. In the literature, the RE^{3+} ion emission is well reported. However, there is limited discussion of the mechanisms of non-radiative energy transfer from defect states to RE dopants in silicon-based amorphous

materials. Furthermore, the RE^{3+} ion in such materials will not replace any of the ions in the matrix as it does in the case of RE doped crystalline materials. In amorphous materials (containing oxygen), the RE^{3+} ion will be located at a site locally surrounded by oxygen atoms. Hence, this work studies and proposes excitation mechanisms for Tb^{3+} and Yb^{3+} ions. These mechanisms can be applied to the *a*-SiOC:H matrix and be extended to Si and SiO_x-based materials. Finally, previous studies of the effect of carbon showed an enhancement of the luminescence of RE^{3+} ions. Therefore, a systematic study of luminescence was carried out based on changing the carbon composition. This work seeks to study the advantages and disadvantages of carbon doping in activating RE luminescence. The results are also presented in **Chapter 5**.

The third goal of this work was the optimization of the annealing temperature and RE(Tb, Yb) concentration to improve the Yb luminescence in co-doped *a*-SiOC:H samples. Among different RE^{3+} ions systems for near-infrared quantum cutting (QC) applications, those including Yb^{3+} ions seem to be the most appropriate because the Yb^{3+} ion has a transition at about 980 nm (~1.22 eV) just above the crystalline silicon bandgap of 1.1 eV. The Tb^{3+} ions (ion donor) are used to enhance the Yb emission. Thus, near-infrared downconverter (DC) layers have found a possible application in silicon solar cells. The spectral converter layer will be put on the top of the solar cell surface, incorporating the DC layer leads to the advantage of a layer that can be optimized independently of the cell. This work identifies and studies the mechanisms associated with the energy transfer from the host to the RE^{3+} ions. Photoluminescence quantum yield of the spectral converter layer was estimated. Also, the layers were prepared on the front surface of mc-silicon cells, and their effect on the external quantum efficiency was studied. In addition, the cooperative transfer mechanism between Tb^{3+} and Yb^{3+} ions were studied, which are used to explain the QC process. This cooperative mechanism has been attributed to QC processes in many crystalline and amorphous matrices. However, despite numerous documents that ascribe their results to the cooperative transfer mechanism, few actually prove it. Therefore, the role of the Tb^{3+} ions in the Yb luminescence is also discussed. The results are presented in **Chapter 6**.

Zusammenfassung

Die Verwendung von Elementen der Seltenen Erden (RE) in Lumineszenzmaterialienführte zu wichtigen Verbesserungen in einer Vielzahl von Anwendungen. In Beleuchtungssystemen werden zum Beispiel gelbe YAG-Leuchtstoffe ($Y_3Al_5O_{12}:Ce^{3+}$) für weiße LED-Geräte eingesetzt. In Telekommunikations- und Internetsystemen werden Erbium (Er^{3+})-dotierte Faserverstärker im Telekom-Wellenlängenbereich (1530-1550 nm) verwendet. In Lasern werden YAG:Nd^{3+} in Festkörperlasern mit einer Emissionslinie bei 1,06µm verwendet. YAG kann auch mit Tm^{3+} (1,93-2,04 µm) oder Er^{3+} (2,94 µm) dotiert werden und wird vor allem in medizinischen Anwendungen eingesetzt. In Solarzellen sollen Spektralwandlerschichten den Wirkungsgrad von Solarzellen erhöhen. Das AM1.5G-Sonnenspektrum kann durch Prozesse wie Up-conversion, quantum cutting und down-shifting. Dadurch würde sich der EQE von Solarzellen verbessern.

Der zentrale Fokus dieser Arbeit war die Präparation und Optimierung der Lumineszenz von Tb^{3+}-und Yb^{3+}-Ionen in der relativ neuen *a*-SiOC:H-Matrix für lumineszierende Anwendungen als spektrale Downconverter. Die zur Optimierung der Lumineszenz verwendete Methode basiert auf Tempern, der Matrixzusammensetzung und der Co-Dotierung mit den Elementen Tb und Yb. Experimentelle Details werden in **Kapitel 3** vorgestellt. Das erste Ziel dieser Arbeit konzentrierte sich auf die Präparation von *a*-SiOC:H-Schichten, die auf der Oberfläche einer Testsolarzelle (Si-Zelle + Antireflexionsschicht) gezüchtet werden können. In der Literatur wird über frühere Arbeiten zu SiOC berichtet, die meisten von ihnen basieren jedoch auf der Herstellung bei Temperaturen nahe 1000 °C, was aufgrund der hohen Temperatur zu Schäden in der Solarzelle führen würde. Aus diesem Grund wurde ein RF-Sputtersystem mit Substratkühlung verwendet. Die optischen Eigenschaften der Matrix hängen von der Si-, C- und O-Zusammensetzung ab. Daher konzentriert sich **Kapitel 4** auf die Untersuchung (1) der Zusammensetzung und Strukturanalyse, (2) der Berechnung der Bandlücke und der Urbach-Energie, (3) der Auswirkung des Temperns auf die atomare Netzwerkstruktur und (4) der Prozesse, die die Matrix-Lumineszenz antreiben.

Das zweite Ziel dieser Arbeit war die Optimierung der Photolumineszenz von Tb^{3+}- und Yb^{3+}-Ionen in einfach dotierten *a*-SiOC:H-Proben. Eine Verstärkung der RE-Lumineszenz erfordert (1) die Erhöhung der Anzahl der aktiven RE^{3+} -Ionen, (2) die Reduzierung von Energieverlustquellen und (3) die Erhöhung der Anzahl der Sensibilisatoren. In **Kapitel 5** werden diese Prozesse im Detail untersucht. In der Literatur wird viel über die Emission von RE^{3+}-Ionen berichtet. Die Mechanismen der nicht strahlenden Energieübertragung von Defektzuständen auf RE-Dotierstoffe in amorphen Materialien auf Siliziumbasis werden jedoch nur begrenzt diskutiert. Außerdem ersetzt das RE^{3+}-Ion in solchen Materialien keines der Ionen in der Matrix, anders als es bei RE-dotierten kristallinen Materialien der Fall ist. In amorphen Materialien (die Sauerstoff enthalten) wird sich das RE^{3+}-Ion an einem Ort befinden, der lokal von Sauerstoffatomen umgeben ist. Daher werden in dieser Arbeit Anregungsmechanismen für Tb^{3+}- und Yb^{3+}-Ionen untersucht und vorgeschlagen. Diese Mechanismen können auf die *a*-SiOC:H-Matrix angewandt und auf Si- und SiO_x-basierte Materialien erweitert werden. Schließlich zeigten frühere Studien über den Einfluss von Kohlenstoff eine Verstärkung der Lumineszenz von RE^{3+}-Ionen. Daher wurde eine systematische Untersuchung der Lumineszenz basierend auf der Veränderung der Kohlenstoffzusammensetzung durchgeführt. Ziel dieser Arbeit ist es, die Vor- und Nachteile der Kohlenstoffdotierung bei der Aktivierung der RE-Lumineszenz zu untersuchen. Die Ergebnisse werden ebenfalls in **Kapitel 5** vorgestellt.

Das dritte Ziel dieser Arbeit war die Optimierung der Yb-Lumineszenz in co-dotierten *a*-SiOC:H-Proben. Unter den verschiedenen RE^{3+}-Ionensystemen für Nahinfrarot-quantum cutting (QC) scheinen diejenigen, die Yb^{3+}-Ionen enthalten, am besten geeignet zu sein, da das Yb^{3+}-Ion einen Übergang bei etwa 980 nm (~1,22 eV) direkt über der Bandlücke von kristallinem Silizium 1,1 eV hat. Die Tb^{3+}-Ionen (Ionendonator) werden zur Verstärkung der Yb-Emission verwendet. So haben Nahinfrarot downconverter (DC) eine mögliche Anwendung in Silizium-Solarzellen gefunden. Die Spektralkonverterschicht wird auf die Oberfläche der Solarzelle aufgebracht. Durch die Einbeziehung der DC-Schicht ergibt sich der Vorteil einer Schicht, die unabhängig von der Zelle optimiert werden kann. In dieser Arbeit werden die mit der Energieübertragung vom Wirt auf die RE^{3+}-Ionen verbundenen Mechanismen identifiziert und untersucht. Die Photolumineszenz-Quantenausbeute der Spektralwandlerschicht wurde geschätzt. Außerdem wurden die Schichten auf der Vorderseite von mc-Siliziumzellen hergestellt und ihre Auswirkungen auf die externe Quanteneffizienz untersucht. Darüber hinaus wurde der Mechanismus des

kooperativen Transfers zwischen Tb^{3+}- und Yb^{3+}-Ionen untersucht, der zur Erklärung des QC-Prozesses herangezogen wird. Dieser kooperative Mechanismus wurde den QC-Prozessen in vielen kristallinen und amorphen Matrizen zugeschrieben. Doch trotz zahlreicher Veröffentlichungen, die ihre Ergebnisse dem kooperativen Transfermechanismus zuschreiben, gibt es nur wenige, die ihn tatsächlich beweisen. Daher wird auch die Rolle der Tb^{3+} -Ionen in der Yb-Lumineszenz diskutiert. Die Ergebnisse wurden in **Kapitel 6** vorgestellt.

Table of Contents

Acknowledgments vi

Abstract viii

Zusammenfassung x

List of Figures xvi

List of Tables xxi

CHAPTER 1. Theoretical Background 1

1.1 Introduction 1

1.2 Electronic Configuration of Rare-Earth Ions in Solid 3

1.3 Luminescence Mechanism in RE^{3+} Active Centers 7

1.3.1 Radiative 4f-4f recombination 7

1.3.2 Non-radiative recombination 8

1.4 Energy transfer 10

1.4.1 Förster and Dexter energy transfer 11

1.4.2 Phonon-assisted energy transfer 13

1.4.3 Cross-relaxation energy transfer 13

1.5 Quantum Cutting 15

1.5.1 Working principles of quantum cutting 15

1.5.2 Efficiency and limitations of the QC process 17

1.5.3 Quantum cutting for photovoltaic applications 18

CHAPTER 2. General Considerations in Silicon Oxycarbide 25

2.1 Overview of silicon oxycarbide structure 25

2.2 Effects on the SiOC atomic network by growth technique 27

2.3 Bond redistribution under thermal process in SiOC 28

2.4 Optical properties of Silicon Oxycarbide Glasses 30

2.4.1 Refractive index and bandgap 30

2.4.2 Identification and origin of host emission 30

CHAPTER 3. Experimental 34

3.1 Production of Thin Films 34

3.1.1 Sample preparation 34

3.1.2 Post-deposition annealing treatments 36

3.2 Characterization 37

3.3 Sample composition 38

3.3.1 Penetration depth simulation 38

3.3.2 Calibration experiment 39

CHAPTER 4. Results and Discussion: Amorphous Hydrogenated Silicon Oxycarbide 43

4.1 Composition and Structure Analysis 43

4.1.1 Elemental composition 43

4.1.2 Bonding Formation 45

4.2 Bandgap and Urbach Energy 49

4.2.1 Determination of the absorption coefficient of *α*-SiOC:H samples 50

4.2.2 Determination of the bandgap and Urbach energy 53

4.3 Annealing effect on the structural properties 56

4.4 Host Luminescence 59

4.5 Conclusion 63

CHAPTER 5. Results and Discussion: Tb and Yb-doped amorphous SiOC:H thin films 65

5.1 Introduction 65

5.2 Sample composition 67

5.3 Post-deposition annealing effect on the RE^{3+} luminescence 68

5.3.1 Tb^{3+} luminescence in *α*-SiOC:H 68

5.3.2 RE^{3+} luminescence based on a two-level model 75

5.3.3 Yb^{3+} luminescence in *α*-SiOC:H 79

5.4 Matrix composition effect on the RE^{3+} luminescence 84

5.4.1 Tb^{3+} luminescence in *α*-SiOC:H 85

5.4.2 Yb^{3+} luminescence in *α*-SiOC:H 91

5.5 Conclusions 96

CHAPTER 6. Results and Discussion: Yb-Tb doped *α*-SiOC:H thin films 98

6.1 Sample composition 99

6.2 Post-deposition annealing effect on the Tb^{3+} and Yb^{3+} luminescence 100

6.3 Yb concentration in Yb-doped *α*-SiOC:H 104

6.4 Tb concentration effect on the Yb^{3+} luminescence 106

6.5 Photoluminescence quantum yield of Yb-Tb doped *α*-SiOC:H thin films 115

6.6 Performance of Yb-Tb co-doped *α*-SiOC:H layers on Si solar cells 119

6.6.1 Modification of the incident solar spectrum by a Down-shifting layer 119

6.6.2 Modeling of the reflectance 121

6.6.3 External quantum efficiency of *α*-SiOC:H on Si cells 122

6.7 Conclusions 125

CHAPTER 7. General Conclusions and Outlook 127

7.1 Goals **127**

7.2 Conclusions **129**

7.3 Outlook **133**

APPENDIX **135**

REFERENCES **140**

Papers and conferences **155**

List of Figures

***Figure 1.1**. Rare earth global market applications, adapted from [2]. 2*

***Figure 1.2**. Schematic of the configurational coordinate diagram: (a) $4f^N$-$4f^N$ configuration; (b) charge transfer CT and $4f^N$-$4f^{N-1}5d$ configuration. 8*

***Figure 1.3**. Schematic energy transfer processes between two ions. D is the donor and A is the acceptor. (a) Radiative resonant transfer; (b) resonant nonradiative transfer; (c) phonon-assisted nonradiative transfer; (d) cross-relaxation. 11*

***Figure 1.4**. Cross-relaxation between two Tb^{3+} ions, resulting in the emission from the $^5D_4$ state. 14*

***Figure 1.5**. PL integrated intensity of Tb^{3+} ions of various Tb doped matrices versus the atomic Tb concentration, adapted from [44]. 14*

***Figure 1.6**. Summary of quantum cutting mechanisms. 16*

***Figure 1.7**. AM1.5G spectrum showing the fraction (highlighted in green) absorbed by a typical silicon-based PV cell and the spectral regions that can be utilized through quantum-cutting and up-conversion processes, adapted from [64]. 20*

***Figure 1.8**. Schematic diagram of a QC system. The converter layer is located on the front surface of a solar cell. 21*

***Figure 1.9**. External quantum efficiency (EQE) for various PV cells. 21*

***Figure 1.10**.Comparison of surface reflection from a silicon solar cell, with and without a typical anti-reflection coating, adapted from [71]. 23*

***Figure 1.11**. **(a)** Schematic representation of components in an encapsulated Si solar cell. **(b)** Schematic representation with a DC layer on the front surface of the solar cell. 24*

***Figure 2.1**. Schematic of two SiO_4 tetrahedrons sharing one corner oxygen. All bond angles around each silicon atom are ~110° (tetrahedron angle). 25*

***Figure 2.2**. Si, C, and O ternary diagram. 26*

***Figure 2.3**. Schematic representation of the a-silicon oxycarbide glass structure at 800 – 1000 °C growth temperature [78]. 28*

***Figure 2.4**. Schematic representation of exchange bonds. Me: methyl ($–CH_3$). 29*

***Figure 2.5**. Overview of the bond evolution under annealing treatment. 29*

***Figure 3.1**.Schematic representation of the RF-magnetron sputtering system. 35*

***Figure 3.2**. Schematic representation of Tb and Yb concentration as well as thickness gradient at the sample holder. 35*

***Figure 3.3**. Schematic representation of the tube furnace used for annealing treatments. 36*

***Figure 3.4**. Heating ramp rate from 500 to 900 °C annealing temperature. 36*

***Figure 3.5 (a)** Penetration depth simulation for a system of a-SiOC:H layer on Si substrate. **(b)** Penetration depth simulation for a system of a-SiOC:H layer and an aluminum layer (200 nm thickness) on Si substrate. The trajectories of the backscattered electrons are in red; those of the absorbed electrons are in blue. 39*

***Figure 3.6**. Two types of substrates are used for sample deposition. The first one is Si substrates and the second one is Al substrates on Si. 40*

***Figure 3.7**.Correction fraction for Si, C, and O as a function of thickness. 42*

***Figure 4.1**. Si-C-O ternary diagram. The red line shows the composition of stoichiometric silicon oxycarbide. The blue line shows silicon composition at 33 at.%. 45*

***Figure 4.2**. IR absorption spectra of a-SiOC:H thin films grown on c-Si(100), (a) from 400 to 1300 cm^{-1}, and (b) from 1900 to 4000 cm^{-1}. 47*

***Figure 4.3**. Recorded Raman scattering spectra for as-grown samples, an excitation wavelength of 532 nm was used for excitation. 47*

***Figure 4.4**. Center band associated with the Si—O and Si—C vibration modes in the IR spectrum for a-SiOC:H thin film grown on c-Si (100). 48*

***Figure 4.5**. Schematic representations of the absorption coefficient for an amorphous semiconductor..... 50*

***Figure 4.6**. Transmittance spectra of an a-SiOC:H thin film grown on a silica substrate, from as-grown to 800 °C annealing, in argon atmosphere. The layer thickness is around 440 nm. 51*

***Figure 4.7**. Refractive index of a-SiOC:H thin film, from as-grown to 800 °C post-deposition annealing, in argon atmosphere. The refractive index of α-SiC* [131] and the refractive index of a-SiO2** [132] are also considered. 51*

***Figure 4.8**. **(a)** Absorption coefficient in a logarithmic scale of a-SiOC:H thin film grown on a silica substrate, from as-grown to 800 °C post-deposition annealing in argon atmosphere. **(b)** Absorption coefficient in a logarithmic scale of a-Si:H [134], a-SiO_x:H (O =52 at.%) [134], and a-SiOC:H (O = 40.1 at.%) samples. The spectral regions of ban-to-band (I), band-tail (II), and defect absorption (III) are indicated for the a-Si:H case. 52*

***Figure 4.9**.Tauc-plot for bandgap calculation. The dashed lines represent the extrapolation linear region... 53*

***Figure 4.10**. log (α) vs $\hbar\omega$ to obtain the Urbach energy. The dashed lines represent the linear fit region..... 54*

***Figure 4.11**. **(a)** Representative E_{gap} values, using the Tauc-plot model (E_{Tauc}), band fluctuation model (E_{BF}), and iso-absorption energy (E_{04}), from as-grown to 800 °C post-deposition annealing in argon atmosphere. **(b)** The Urbach energy values, using the Urbach model (E_{Urbach}) and the band fluctuation model ($1/\beta$)..... 55*

***Figure 4.12**. The IR absorption spectra of a-SiOC:H thin films grown on c-Si(100), (a) from 400 to 1300 cm^{-1}, and (b) from 1900 to 4000 cm^{-1}. The carbon compositions correspond to samples in as-grown conditions... 57*

***Figure 4.13**. Raman scattering spectra recorded from a-SiOC:H thin film, from as-grown to 800 °C post-deposition annealing in argon atmosphere, an excitation wavelength of 532 nm..... 58*

***Figure 4.14**. (a) PL emission of a-SiOC:H thin film grown on c-Si (100), from as-grown to 800 °C post-deposition annealing in an argon atmosphere. (b) The Gaussian deconvolution shows the different components in the red (~1.9 eV), green (~2.4 eV), and blue (~2.8 eV) range. All measurements were taken at room temperature. 59*

***Figure 4.15**. (a) and (b) PL emission of a-SiOC:H thin film grown on c-Si (100), from as-grown to 700 °C post-deposition annealing, in forming gas and argon atmosphere. (c) Ratio of the PL intensities for the centered bands at ~2.4 eV and ~1.9 eV..... 61*

***Figure 4.16**. PL emission of a-SiOC:H thin film at 500 °C post-deposition annealing, (a) for different compositions and (b)for different annealing times. (c) The ratio of the absorption bands intensities corresponding to the Si—O and Si—C bonds as a function of the annealing temperature. 62*

***Figure 5.1**. Schematic illustration for an RE^{3+} ion optical excitation. 66*

***Figure 5.2**.(a)-(c) PL emission spectra of Tb-doped samples at 375 nm excitation wavelength. (d)-(f) PLE excitation spectra of Tb-doped samples (1.1 at.%) at 545 nm detection wavelength. The annealing temperature was ranged up to 1000 °C. 69*

***Figure 5.3**.(a) PL emission of Tb-doped samples at 375 nm excitation wavelength. (b) PLE excitation spectra of Tb-doped samples at 517 nm detection wavelength. 70*

***Figure 5.4**. PLE excitation spectra of Tb-doped (1.1 at.%) samples at 545 nm detection wavelength for as-grown and 900 °C. Absorption coefficient spectra in blue (as-grown) and red (900 °C) dotted lines. 71*

***Figure 5.5**. Normalized decay curves for Tb-doped (1.1 at.%) samples. (a) At as-grown, (b) - (d) at 800 °C and 25 min., 2 hours, and 4 hours, respectively. (e) At 900 °C and 4 hours. (f) At 1000 °C and 4 hours. All measurements were taken at room temperature. 72*

***Figure 5.6**. **(a)** PL emission spectra of Tb-doped (1.1 at.%) samples at 375 nm excitation wavelength. **(b)** Integrated Tb and host related PL. The annealing temperature was ranged up to1000 °C. 74*

***Figure 5.7**. (a) PL emission spectra of Tb-doped (1.4 at.%) a-SiOC:H samples at 325 nm excitation wavelength. (b) Excitation power dependence of Tb-doped samples from as-grown up to 750 °C annealing temperature. The dashed line is a guide for the eye. 77*

***Figure 5.8**. (a) excitation power dependence of Tb doped a-SiOC:H samples at as-grown, and (b) excitation power dependence at 750 °C annealing temperature. The dashed line is a guide for the eye. 78*

***Figure 5.9**.(a) Matrix PL emission at 375 nm excitation wavelength, (b) PL emission spectra of Yb^{3+} ion, (c) PLE excitation spectrum of Yb-doped (2.9 at.%) sample, and (d) Integrated PL intensity as a function of the annealing temperature. The annealing temperature was ranged up to 600 °C. 79*

***Figure 5.10**.Normalized decay curves for Yb-doped (2.9 at.%) samples at 402 nm excitation wavelength, (a) at as-grown, (b) at 400 °C, (c) at 500 °C, and (d) at 600 °C annealing temperature. All measurements were taken at room temperature. 81*

***Figure 5.11**. Schematic representation of (a) resonant energy transfer, (b) Si nanoclusters mediated excitation, (c) defect-related Auger excitation (DRAE) mechanism, and (d) nonradiative resonant energy transfer by dipole coupling (Förster mechanism). Adapted from [184–186]. 84*

***Figure 5.12**. PL spectra of Tb-doped samples at 375 nm excitation wavelength, (a) at as-grown, (b) at 800 °C, and (c) at 900 °C annealing temperature. PLE spectra of Tb-doped samples at 545 nm detection wavelength, (d) as-grown, (e) at 800 °C, and (f) at 900 °C annealing temperature. 87*

***Figure 5.13**. Normalized decay curves for Tb doped samples at 375 nm excitation wavelength, (a) as-grown, (b) at 800 °C, and (c) at 900 °C annealing temperature. All measurements were taken at room temperature. 88*

***Figure 5.14**. Schematic representation of the mechanism for Tb ion excitation in Tb-doped a-SiOC:H. Energy levels are not scaled, adapted from [134]. 90*

***Figure 5.15**. Host PL spectra of Yb-doped samples at 375 nm excitation wavelength, (a) carbon 8.6 at.% and Yb 2.1 at.%. (b) carbon 40.1 at.% and Yb 2.9 at.%. (c) Yb PL spectra of Yb-doped samples at 375 nm excitation wavelength. (d) Yb PLE spectra at ~980 nm detection wavelength at 500 °C annealing temperature. 91*

***Figure 5.16**. Normalized decay curves for Yb-doped samples at 402 nm excitation wavelength, (a) at as-grown, (b) at 500 °C, and (c) at 600 °C annealing temperature. All measurements were taken at room temperature. 92*

***Figure 5.17**. (a) Normalized Yb PL of Yb-doped a-SiOC:H samples. (b) Normalized matrix PL of Yb-doped a-SiOC:H samples. The carbon composition was set up between ~9 and 40 at.%, annealing treatments were performed up to 600 °C. 93*

***Figure 5.18**. Schematic representation of the mechanism for Yb^{3+} ion excitation in Yb-doped a-SiOC:H. Energy levels are not scaled. 95*

***Figure 6.1**. (a) PL emission spectra of Yb-Tb co-doped a-SiOC:H sample (blue line). The red dashed line shows the matrix emission. The three arrows indicate the ~545 nm ($^5D_4 \rightarrow {}^7F_5$), 588 nm ($^5D_4 \rightarrow {}^7F_4$), and 621 nm ($^5D_4 \rightarrow {}^7F_3$) emission. (b) Yb and Tb PL spectra after background (host emission) correction. (c) Yb and Tb integrated luminescence signal for different annealing temperatures. (d) Tb PLE spectra at 545 nm detection wavelength at 500 °C annealing temperature. (e) Yb PLE spectra at 980 nm detection wavelength at 500 °C annealing temperature. The Yb and Tb concentration were 6.0 and 0.8 at.%, respectively. 102*

***Figure 6.2**. Normalized decay curves for Yb-Tb co-doped a-SiOC:H samples at 375 nm excitation wavelength, (a) Yb decay curves, detection at 980 nm, (b) Tb decay curves, detection at 545 nm. 103*

***Figure 6.3**. Integrated PL intensity in Yb-doped a-SiOC:H samples. 105*

***Figure 6.4**. Normalized PL spectra of two representative Yb doping concentrations in Yb-doped a-SiOC:H samples **(a)** 4.0at% and **(b)** 5.4 at.%. 106*

***Figure 6.5**. PL spectra in the visible and IR region for two representative Tb (0.8 at.%) and Yb (1.8 and 6.0 at.%) doping concentrations. (a) and (c) PL spectra in the visible range. (b) and (d) PL spectra in the IR region at 375 nm excitation wavelength. 107*

***Figure 6.6.** Relative Yb PL of Yb-Tb co-doped a-SiOC:H samples. The Tb doping was set up at 0.8 at.%, annealing temperature up to 700 °C. 108*

***Figure 6.7**. Normalized Tb decay curves for Yb-Tb co-doped samples at 375 nm excitation wavelength, detection at 545 nm for samples at 500 °C annealing temperature. 108*

***Figure 6.8**. PL spectra in the visible and IR region for two representative Tb (2.6 at.%)-Yb (1.1 at.%) and Tb (1.9 at.%)-Yb (3.5 at.%) doping concentrations. (a) and (c) PL spectra in the visible range. (b) and (d) PL spectra in the IR region at 375 nm excitation wavelength. 109*

***Figure 6.9**. Relative Yb PL of Yb-Tb co-doped a-SiOC:H samples. The Tb doping was set up from 0.8 to 2.6 at.%, annealing temperature up to 700 °C. 110*

***Figure 6.10**. Average lifetime values for Tb (main emission at ~545 nm) and Yb (~ 980 nm) for Yb-Tb co-doped and Yb-doped a-SiOC:H as a function of RE total concentration. 111*

***Figure 6.11**. Schematic representation of QC by cooperative process in Yb-Tb co-doped a-SiOC:H. Energy levels are not scaled. 112*

***Figure 6.12**. Average lifetime as a function of annealing temperature. (a) Tb excited state lifetime in milliseconds range detection. (b) Yb excited state lifetime in microseconds range detection. (c) Tb excited state lifetime in microseconds range detection, in Tb-doped and Yb-Tb co-doped samples. (d) matrix excited state lifetime in microseconds range detection..... 113*

***Figure 6.13**. Schematic representation of the mechanism for Yb and Tb ion excitation in Yb-Tb co-doped a-SiOC:H. Energy levels are not scaled..... 114*

***Figure 6.14**. Light emitted and scattered by a luminescent sample of Yb -Tb co-doped a-SiOC:H, collected by an integrating sphere. Excitation wavelength 370 nm. 116*

***Figure 6.15**. Light emitted and scattered by a reference sample, collected by an integrating sphere. Excitation wavelength 370 nm. 117*

***Figure 6.16**. **(a)** Transmittance spectra for fused silica substrate, reference sample on fused silica substrate, and Yb (3.5 at.%)-Tb (1.9 at.%) co-doped a-SiOC:H as-grown. (b) PL spectra at 375 nm excitation wavelength. 117*

***Figure 6.17**. **(a)** Layering arrangement on mc-Si cell. **(b)** Luminescence spectrum (red line), absorption coefficient (blue line), incident spectrum AM1.5G, and the region of the spectrum absorbed by the silicon (green). **(c)** Film absorption in function of thickness and wavelength. 120*

***Figure 6.18**. **(a)** Simulation of the reflectance with increasing DSL layer thickness "d" nm. **(b)** and **(d)** Total number of photons lost in the range of the solar spectrum (300-1100 nm) as a function of thickness and its variation (%) with respect to the bare cell. **(c)** Film reflectance in function of thickness and wavelength.... 121*

***Figure 6.19**. **(a)** Yb-Tb co-doped a-SiOC:H layer on the front surface of an mc-Si cell. **(b)** EQE spectra for bare mc-Si cells. **(c)** EQE spectra for mc-Si cells with Tb-doped a-SiOC:H layers. 122*

***Figure 6.20**. **(a)** and **(c)** EQE spectra of mc-Si cells with a-SiOC:H and Tb doped a-SiO:H films. **(b)** and **(d)** EQE spectra for mc-Si cells with Tb-doped and Yb-Tb doped a-SiOC:H layers. 124*

List of Tables

Table 1.1. *Electronic configuration of the isolated RE atoms and their corresponding ions listed according to the energy of each orbit, RE^{3+} radius, and main emission wavelength; adapted from [6,7].* *2*

Table 1.2. *The selection rules for the allowed intra-configurational f-f transitions.* *6*

Table 1.3. *Number of phonons-assisted by silicate host and OH^- vibration.* *10*

Table 1.4. *NIR quantum-cutting materials co-doped with RE^{3+}-Yb^{3+} for PV applications, adapted from [34].* *22*

Table 1.5. *List of QC-PV devices from different type of solar cells [63].* *22*

Table 2.1. *Bond length, tetrahedron angle, and bridge bond angle for a-SiO_2 and a-SiOC.* *26*

Table 2.2. *Refractive index values for three host classifications.* *30*

Table 2.3. *Representative values for E_{gap} and $\alpha(\lambda)$.* *30*

Table 2.4. *Luminescence attributed to the presence of carbon in the samples.* *33*

Table 2.5. *Luminescence bands and their association with radiative defects.* *33*

Table 3.1. *Values of Ar and H_2 gas flow rate, base pressure, working pressure, and RF powers.* *35*

Table 3.2*. Thickness and normalized atomic composition (in at.%) without considering aluminum.* *40*

Table 3.3. *m and b values obtained from the linear fit in* ***Figure 3.7****.* *41*

Table 4.1. *Elemental composition of a-SiOC:H samples (at as-grown).* *44*

Table 4.2. *IR band centers corresponding to the vibration modes of Si—C and Si—O bonds in SiO_x and a-SiC:H.* *46*

Table 5.1. *Elemental composition of a-SiOC:H samples (as-grown).* *67*

Table 5.2. *Tb excited state luminescence lifetime for a Tb doped sample.* *73*

Table 5.3. *Yb excited state luminescence lifetime for an Yb-doped sample.* *81*

Table 5.4. *Experimental branching ratios ($\beta_{j\to i}$) for the four $^5D_4 \to {}^7F_J$ (J=3, 4, 5 and 6) Tb transitions of Tb doped a-SiOC:H samples.* *86*

Table 5.5. *Tb average luminescence lifetime for Tb doped samples with different carbon concentrations.* .. *88*

Table 5.6. *Average luminescence lifetime for Yb-doped samples with different carbon concentration.* *93*

Table 6.1. *Elemental composition of a-SiOC:H samples (as-grown).* *99*

Table 6.2. *Tb and Yb average luminescence lifetime for a Yb-Tb co-doped sample.* *101*

Table 6.3. *Average lifetime of Yb-doped samples with 2.1 and 4.0 at.% Yb doping.* *104*

Table 6.4. *Tb and Yb average lifetime for Yb-doped, Tb-doped, and Yb-Tb co-doped samples at 500 °C annealing temperature.* *108*

Table 6.5. *Quantum yield values for silica-based matrices.* *116*

CHAPTER 1. Theoretical Background

1.1 Introduction

Luminescent materials, also called phosphors, convert certain types of energy into electromagnetic radiation. The incandescence or black-body emission, as a consequence of heating a solid, is not luminescence [1]. Luminescence can be excited in different ways. And the list includes electromagnetic radiation (photoluminescence), electric discharge or electric field (electroluminescence), electron flux (cathodoluminescence), among others.

The uses of rare-earth (RE) elements in luminescence materials led to many improvements in a variety of applications. For example:

- In lighting, since the 1980s, the use of RE elements has led to high-efficiency lamps and adjustable color emission. Today, $Y_2O_3:Eu^{3+}$ (red), $(Ce,Tb)MgAl_{11}O_{19}$ or $(La,Ce)PO_4:Tb^{3+}$ (green), and $BaMgAl_{10}O_{17}:Eu^{2+}$ (blue) are used in all triband fluorescent lamps, which represent about half the fluorescent lamps worldwide [2]. Later, in the 1990s, with the invention of blue chips, RE elements have been used in LED devices, for instance, YAG yellow phosphor ($Y_3Al_5O_{12}:Ce^{3+}$) widely used for white LED devices.
- In telecommunication and internet systems, the fiber is based on silica. In those systems an amplification system is required due to the signal attenuation after 50 or 100 km. Commonly, erbium (Er^{3+})-doped fiber amplifiers (EDFA), proposed in 1987 [3], are used in the telecom wavelength region (1530-1550 nm).
- In laser, Nd is used in solid-state lasers $YAG:Nd^{3+}$ with an emission line at 1.06 μm or doubled at 532 nm. YAG can also be doped with Yb^{3+} (1.03 μm), Tm^{3+} (1.93-2.04 μm), Er^{3+} (2.94 μm), among others, where long wavelengths are mainly used to medical applications [3].

As mentioned above, RE metals have been applied in various sectors of the global market. **Figure 1.1** shows their main applications in industry. Among their many uses, approximately 9% of the total production is used in phosphors, with lighting and display being the main applications (~97%) [2,4].

Figure 1.1. Rare earth global market applications, adapted from [2].

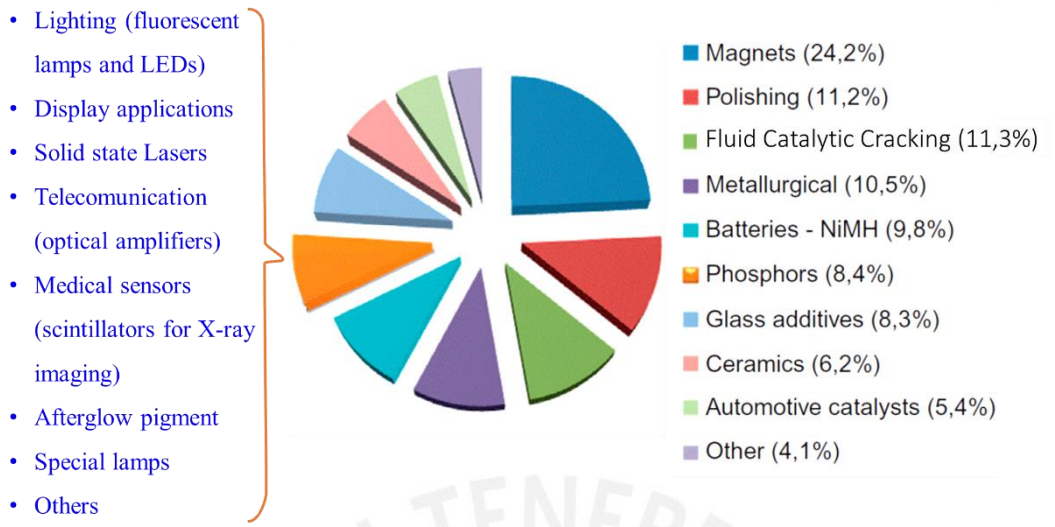

RE elements are composed by a group of 15 lanthanoid elements from lanthanum La (Z=57) to lutetium Lu (Z=71) [5,6]. The RE elements (from Pr to Yb except for Gd) have the electronic configuration like $[Xe]6s^2 4f^n 5d^0$ [6], and for RE ions (RE^{3+}) have the electronic configuration like $[Xe]6s^0 4f^{n-1} = [Xe]4f^N$ (**Table 1.1**). Where N represents the number of electrons from 0 to 14. The RE^{3+} ionics radius are consigned in **Table 1.1**. The large radius result in very low polarizability, which reflects the rather ionic nature of the metal-ligand bonds [7].

Table 1.1. Electronic configuration of the isolated RE atoms and their corresponding ions listed according to the energy of each orbit, RE^{3+} radius, and main emission wavelength; adapted from [6,7].

Element		Z	Electronic configuration		RE^{3+}	$\lambda_{main\ emission}$
			RE atom	RE^{3+}	radius (Å)	(nm)
Lanthanum	La	57	$[Xe]6s^2 5d^1 4f^0$	$[Xe]4f^0$	1.06	-
Cerium	Ce	58	$[Xe]6s^2 4f^1 5d^1$	$[Xe]4f^1$	1.03	-
Praseodymium	Pr	59	$[Xe]6s^2 4f^3 5d^0$	$[Xe]4f^2$	1.01	610, 1060, 1300
Neodymium	Nd	60	$Xe]6s^2 4f^4 5d^0$	$[Xe]4f^3$	0.99	1060
Promethium	Pm	61	$[Xe]6s^2 4f^5 5d^0$	$[Xe]4f^4$	0.98	
Samarium	Sm	62	$[Xe]6s^2 4f^6 5d^0$	$[Xe]4f^5$	0.96	590
Europium	Eu	63	$[Xe]6s^2 4f^7 5d^0$	$[Xe]4f^6$	0.95	615
Gadolinium	Gd	64	$[Xe]6s^2 4f^7 5d^1$	$[Xe]4f^7$	0.94	311
Terbium	Tb	65	$[Xe]6s^2 4f^9 5d^0$	$[Xe]4f^8$	0.92	550
Dysprosium	Dy	66	$[Xe]6s^2 4f^{10} 5d^0$	$[Xe]4f^9$	0.91	570
Holmium	Ho	67	$[Xe]6s^2 4f^{11} 5d^0$	$[Xe]4f^{10}$	0.89	550, 970, 1450
Erbium	Er	68	$[Xe]6s^2 4f^{12} 5d^0$	$[Xe]4f^{11}$	0.88	545, 1500
Thulium	Tm	69	$Xe]6s^2 4f^{13} 5d^0$	$[Xe]4f^{12}$	0.87	480
Ytterbium	Yb	70	$[Xe]6s^2 4f^{14} 5d^0$	$[Xe]4f^{13}$	0.86	980
Lutetium	Lu	71	$[Xe]6s^2 4f^{14} 5d^1$	$[Xe]4f^{14}$	0.85	-

1.2 Electronic Configuration of Rare-Earth Ions in Solid

When a RE ion is in a solid, which means a distribution of ligands surround it, the energy levels distribution of the localized center will be different from the free ion case. In general, various properties such as the site symmetry, coordination, and covalence [6] characterize the host matrix. Those characteristics may modify the energy levels of the ionic center as well as the intensity of transitions between those levels.

In the free ion case, when the degenerated 4f orbitals of the RE ion become partially populated with electrons, the coulombic and magnetic spin interactions of electrons lift the degeneracy of the 4f levels [6]. The electron experiences multiple interactions such as:

a) the attractive Coulomb interaction between the electrons and the nuclei (central field approximation).
b) the repulsive Coulomb interaction (among electrons), in this case, the different shapes and orientations of the 4f orbitals lift the degeneracy of the 4f electronic levels and leads to the spectroscopic term $^{2S+1}$L, where 2S +1 is the spin multiplicity and L is the total orbital angular momentum.
c) the spin-orbit coupling (LS coupling), due to the interaction between the magnetic field generated by the orbiting electron and the intrinsic magnetic moment of the electron, lifts the degeneracy of the 4f electronic levels leading to the spectroscopic levels $^{2S+1}L_J$ [5], where J is the total angular momentum of the f electrons.

The energy difference between the lower and the higher energy level undergoes the interactions considered above will be as follows: central field (10^5 cm^{-1}) > interelectronic repulsion (10^4 cm^{-1}) > spin-orbit coupling (10^3 cm^{-1}) > ligand field (10^2 cm^{-1}) [7].

For a RE ion in a solid and considering a weak crystal field, an appropriate localized model is usually used to study the RE optical properties in a solid. The crystal field (CF) model considers a central atom (such as a RE ion) to be surrounded by a distribution of charges (neighboring ligands). The CF model considers an electrostatic field at the position of the ionic center. Also, in the CF approximation, it is assumed that there is no sharing of electronic charges between the central atom and the ligands [8]. It is a general agreement that RE^{3+}-ligand coordination occurs predominantly via ionic bonding interactions, leading to a strong preference for negatively charged groups [9]. The large ionic radius (**Table 1.1**) leads to RE^{3+} complexes with coordination numbers higher than six [7]. Lanthanide complexes exhibit coordination numbers ranging from six to twelve (in solid-state and in solutions), with eight and nine being the most common [9].

The interaction between the ligand's potential and the 4f electrons (RE ion electronic cloud) is represented by a crystal field Hamiltonian H_{CF} [10]. The crystal field potential is considered as a perturbation and can be expressed as:

$$H_{CF} = \sum_i eV(\bar{r}_i) \qquad \textbf{(1.1)}$$

The sum is over all 4f electrons, and $V(\bar{r}_i)$ is the potential acting on the electrons and reflects the symmetry at the site of the ionic center.

A general form to represent H_{CF} is $H_{CF} = H_{CF(even)} + H_{CF(odd)}$ [11]. The role of the $H_{CF(odd)}$ is to mix states of opposite parity like 4f and 5d orbitals [12]. It follows that transitions between the new 4f levels become partially electric dipole allowed. The role of the $H_{CF(even)}$ is responsible for the J-mixing effect, so J is no longer a good quantum number. Thus, the new eigenstate labels will now take into account the symmetry point groups [11]. Another consequence of the $H_{CF(even)}$ is the Stark splitting. Where the multiple splits depend on the symmetry of the crystal field, there are fewer levels for higher ion site symmetries [5]. The $^{2S+1}L_J$ level can be split into several sublevels by the Stark effect. The number of split sublevels is, at most, (2J+1) or (J + ½) for J being integer or half-integer value, respectively [5]. The splitting is in a range from ten to a few hundred cm^{-1} [10].

The RE ion energy levels can be divided into three categories: those corresponding to $4f^N$ configuration, $4f^{N-1}5d$ configuration, and those corresponding to charge transfer (CT) state, some characteristics are detailed below:

a) The $4f^N$ energy levels are slightly influenced by the host because the highly localized 4f shell is shielded by the 5s and 5p shells. So, the same energy levels can be used in a variety of matrices [13]. These have been extensively investigated in lanthanum fluoride LaF_3 by Dieke et al. [14].
b) The $4f^{N-1}5d$ energy levels are at higher energy than the $4f^N$ levels, which correspond with the promotion of a 4f electron to the 5d sub-shell. Also, it will depend on the host because the external 5d orbitals interact directly with the ligand orbitals.
c) CT state energy levels, as for the $4f^{N-1}5d$ energy levels, their levels are at higher energies than $4f^N$ configuration. Their transitions are often observed in the UV spectral range. Often, the charge transfer transition is described as the promotion of an electron from one of the surrounding ions to the 4f orbital of the central ion [15].

If the electron-dynamic lattice interaction is considered, the CF (in **equation 1.1**) can be expressed as a Taylor expansion of the equilibrium position of the ion [10]:

$$H_{CF} = H_{CF-static} + \sum_i \frac{\partial V}{\partial Q_i} Q_i + higher\ order\ terms \qquad (1.2)$$

Where, Q_i represents the normal modes of the lattice vibration. The zeroth-order term ($H_{CF\text{-}static}$) leads to a radiative electric dipole transition. The first and higher-order terms ($H_{CF\text{-}dynamic}$) will describe the modulations of the crystal field due to the effect of the vibrations of the ligands. It is also called the ion-lattice or electron-phonon interaction. The effect of the lattice vibrations leads mainly to a change of the absorption line shape (or band), and it may affect the energy transfer between optical ion centers [16].

Transition Selection Rules

It is known that the RE luminescence intensity depends on the electronic matrix element of optical transitions between the RE electronic levels. The optical transitions are predominantly dipole electric, dipole magnetic, or quadrupole electric transitions [17]. When the electric dipole transition is not allowed, the optical transition may take place as a magnetic dipole, for instance, the 4f-4f transitions. However, the electronic transitions probability for the latter is weaker compared with the electric dipole transition.

The 4f-4f transitions are electric dipole parity-forbidden by Laporte's rule for free RE^{3+} ions. However, many intense spectrums have been shown in several f-f transitions. The explanation for that arises from the Judd-Ofelt theory. In 1962, Judd [18] and Ofelt [19] independently proposed that f-f transitions occur through a forced (or induced) electric dipole mechanism. More in detail, the Judd and Ofelt approach considers the $H_{CF(odd)}$ (odd part of the crystal field) as a perturbation that mixes the opposite parity states (4f and 5d orbitals) using perturbation theory up to first order in the wavefunctions [11]. Thus, the 4f-4f transitions become partially electric dipole allowed (Laporte's rule is relaxed) [11]. **Table 1.4** summarizes the selection rules for the allowed f-f transitions according to the Judd-Ofelt theory [16]. In 4f-4f spectra, the induced electric dipole and magnetic dipole transition frequently have both the same order of intensity magnitude [3].

Table 1.2. The selection rules for the allowed intra-configurational f-f transitions.

	Spin S	**Total angular momentum J**
Electric dipole	$\Delta S = 0$ (electrons promotion without a change in their spin)	a) $\Delta J \leq 6$ b) For rare earth ion with an even number of electrons - $J=0 \rightarrow J'=0$ is forbidden - $J=0 \rightarrow J'=1, 3, 5$ are weak - $J=0 \rightarrow J'=2, 4, 6$ should be strong
Magnetic dipole	$\Delta S = 0, \pm 1$	$\Delta J = 0, \pm 1$ (with $J=0 \rightarrow 0$ forbidden)

Even when Judd-Ofelt theory is in a satisfactory agreement with the experimental results, there are some additional phenomena to take into consideration when a RE ion undergoes a crystal field influence [20]. For example:

a) The even term of the crystal field is responsible for the J-mixing effect of the $J = 0$ and $J \neq 0$ states. Thus, there is an increase in the probability of the $J=0 \leftrightarrow J'=0$ transition [12], even when this transition is forbidden. Thus, the selection rules in **Table 1.4** can be relaxed to some extent.

b) The site symmetry in a host crystal will affect the intensity of some electronic transitions. The intensity of electric dipole f-f transitions depends strongly on the symmetry of the occupied sites [5] because they are forbidden in a centrosymmetric site (i.e., in the presence of an inversion center) [21]. Whereas the magnetic dipole f-f transitions are slightly affected by the site symmetry because they are parity-allowed [5]. For example, the main Eu^{3+} emission lines are 4f-4f transitions (located between 550 and 750 nm) corresponding to the $^5D_0 \rightarrow {}^7F_{J=0,1,2,4,6}$ transitions. The emission line $^5D_0 \rightarrow {}^7F_2$ is weak in YBO_3, while it has a strong intensity in Y_2O_2S [13]. That occurs because the hypersensitivity emission line $^5D_0 \rightarrow {}^7F_2$ (610 nm, exceptional red color purity) is dipole electric allowed and strongly affected by the symmetry of the host matrix.

1.3 Luminescence Mechanism in RE^{3+} Active Centers

To explain the RE ion-optical transitions an appropriate localized model called the configurational coordinate model will be used. The configurational coordinate model considers the effect of the dynamic lattice modes on the activator. It will be assumed only one representative lattice mode, which is taken to be the "breathing mode" in which the surrounding lattice pulsates (harmonic oscillator model) in and out about the optically active ion [16]. Thus, it will consider the interaction RE ion - lattice vibration. The effect of the lattice vibrations will be mainly:

a) To change the feature shape of the absorption line (or band), but not the strength of the transition (which is given by the electronic matrix element) [22].
b) To give rise to the non-radiative process of the ions [16].
c) When the concentration of electronic centers is high so that adjacent centers may interact with each other, the lattice vibration may affect the transfer of optical excitation energy between adjacent centers [16].

A schematic illustration of a coordinate diagram is shown in **Figure 1.2 (a)** and **(b)**. In the configurational coordinate diagram, the energy E is plotted versus the configurational coordinate R. The latter is the metal-ligand distance, which is an structural parameter that varies during the vibration [1]. More details about the configurational coordinate diagram can be found in many textbooks [1,10,16].

1.3.1 Radiative 4f-4f recombination

Radiative 4f-4f transitions are called the weak-coupling scheme ($\Delta R = 0$) [1]. It leads to a sharp peak because the coupling between electrons and vibrational modes is low. The 4f-4f recombination is represented (by the pink arrow) in **Figure 1.2 (a)**. The wavelength of a particular 4f levels transition is well defined and mostly independent of the nature of the host [23]. Also, their intensities are weak and can be reduced because of the crystal field effects (e.g., as was discussed earlier for Eu^{3+} case). The oscillator strength f is of the order of $\sim 10^{-5}$ to 10^{-8} for the 4f → 4f partially electric dipole allowed transitions and 10^{-8} for the magnetic dipole transitions [5]. The decay times of the luminescence due to the 4f-4f transitions are mostly in the range of μs-ms [23] as the electric dipole transitions are weak compared with an allowed electric dipole transition ($f = 1$, radiative lifetime $\sim 10^{-9}$ s, for n = 1, λ = 500 nm) [16].

Figure 1.2. Schematic of the configurational coordinate diagram: (a) $4f^N$-$4f^N$ configuration; (b) charge transfer CT and $4f^N$-$4f^{N-1}5d$ configuration.

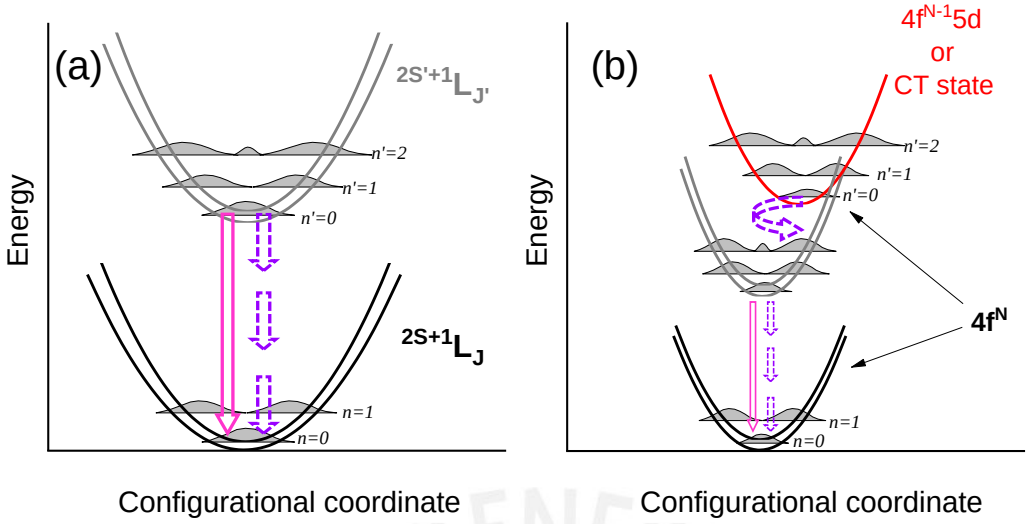

1.3.2 Non-radiative recombination

Non-radiative 4f-4f recombination

In the 4f-4f configurational coordinate diagram, there is no cross-point between the 4f excited state ($^{2s'+1}L_{J'}$) and the 4f ground state ($^{2s+1}L_J$). There is no relaxation process by thermal activation. However, the phonon energy plays an important role in non-radiative transitions, quenching of luminescence may explain by a case called multiphonon-emission relaxation [24]. The multiphonon relaxation is often the dominating relaxation mechanism between the 4f excited levels of a RE ion [24]. Non-radiative 4f-4f mechanisms recombination are represented by the purple dotted arrow in **Figure 1.2 (a)**. For transitions between 4f levels, the temperature dependence of the non-radiative rate can be estimated with the exponential energy gap law developed by van Dijk and Schuurmans (**equation 1.3**) [25,26].

$$W_{non-rad}(T) = W(0)(n+1)^{\frac{\Delta E}{h\nu}} \qquad (1.3)$$

Where $W(0) = \beta \exp\left(-\alpha(\Delta E - 2h\nu_{max})\right)$, $h\nu_{max}$ is the largest phonon energy in the host, α and β are constants for a given host lattice, and ΔE is the energy gap between two energy levels between the populated state and the next lower-lying energy level of the lanthanide ion.

According to **equation 1.3**, the multiphonon relaxation rate ($W_{multiph}$) will decrease exponentially with an increase of ΔE and will depend on the particular host phonon

energy [27]. $W_{multiph}$ will increase if ΔE is equal to or less than 4-5 times the highest vibrational frequency (ν_{max}) provided by the surroundings [22]. In that case this amount of energy may excite simultaneously a few high energy vibrations, and it becomes the dominant depopulation mechanism [28]. Therefore, large values of $h\nu_{max}$ can quench the RE ion light emission. In the Tb^{3+} ion case, which can be emitted from $^5D_3 \rightarrow {}^7F_{j=0-6}$ (blue emission) and from $^5D_4 \rightarrow {}^7F_{j=0-6}$ (green emission), The energy gap between the $^5D_3$ and $^5D_4$ levels is about 5000 cm^{-1}. Thus, in a diluted Tb^{3+} system case in a small energy phonon matrix, and just considering that the ion interacts with their intermediate surroundings, the Tb^{3+} luminescence would show some blue Tb^{3+} emission [1].

Non-radiative $4f^N$-$4f^{N-1}5d$ and Charge transfer

The $4f^N$-$4f^{N-1}5d$ transitions are represented in **Figure 1.2 (b)**. It shows three-parabolas, the parallel parabolas (in black and grey) belong to the same 4f configuration. The third parabola (in red) originates from a different configuration ($4f^{N-1}5d$) and is probably connected to the ground state by an allowed transition. This leads to, broad and intense bands (allowed by the electric dipole transitions) in the excitation or absorption spectrum. When the system relaxes to the ground state, it will be first relaxed to the excited state of the second parabola (in grey). The emission may occur now from the second parabola. This situation is usually found for the Tb^{3+} ion case, and it will occur in the following sequence $^7F \rightarrow 4f^75d$ excitation, $4f^75d \rightarrow {}^5D$ relaxation, and $^5D \rightarrow {}^7F$ emission [22].

The CT state also can be represented by the red curve in **Figure 1.2 (b)**, for instance, the Eu^{3+}-O^{2-} state or Yb^{3+}-O^{-2}. Comparing both cases, the luminescence from the Eu^{3+} charge transfer state cannot be observed, because the intersection of CT state and ^5D_J levels lead to a fast relaxation to the ^5D_J levels [22]. The UV radiation is efficiently absorbed by a transition to the CT state of the Eu^{3+} ion. Afterward, non-radiative decay to the lower 4f levels is expected. Luminescence occurs from the ^5D_J states of Eu^{3+} [29]. Whereas, for the Yb^{3+} ion case, the charge transfer luminescence can be expected at lower temperatures (T < 300 K) [29] as far as the only excited state $^2F_{5/2}$ is located just ~10000 cm^{-1} above the ground state $^2F_{7/2}$. The Yb^{3+}-CT state absorption band is reported to the range from 200 to 250 nm in oxides [29]. For T > 300 K, the thermal quenching strongly reduces the emission from the CT state of Yb^{3+} ions as it was reported in Y_2O_2S:Yb^{3+} [30]. However, the 4f emission under CT state excitation increases at high temperatures because of the increased amount of excitation transfer from the CT state [30].

Non-radiative recombination through OH^- vibrations

Finally, a strong non-radiative path may occur caused by the high energy of stretching vibration of the hydroxyl groups (OH^- vibrations), which is particularly efficient in the quenching of the emitting levels of RE^{3+} ions. The coupling between RE ions and the stretching vibrations of the OH^- groups (~3200 cm^{-1} [31]) will strongly quench the Tb^{3+} blue luminescence as well as the Yb^{3+} IR emission, because two and three phonons, respectively, are just needed (**Table 1.3**). According to this, in silicates (phonon energy 1000 - 1100 cm^{-1} [31]), the host phonons can quench the Tb^{3+} blue luminescence but do not quench the Yb^{3+} IR emission. Then, the control of the residual OH content is as much important as the host used.

Table 1.3. Number of phonons-assisted by silicate host and OH^- vibration.

	transition	silicate	OH^- groups
Tb^{3+}	$^5D_3 \rightarrow {}^5D_4$	~ five	~ two
	$^5D_4 \rightarrow {}^7F_0$	~ fifteen	~ five
Er^{3+}	$^4I_{13/2} \rightarrow {}^4I_{15/2}$	~ seven	~ two
Yb^{3+}	$^2F_{5/2} \rightarrow {}^2F_{7/2}$	~ ten	~ three
Eu^{3+}	$^5D_0 \rightarrow {}^7F_6$	~ twelve	~ four

1.4 Energy transfer

When the luminescence centers are in close proximity, they can interact with each other. The excited state of one center can transfer its energy to the other one. The energy transfer ET refers to a process in which an excited atom or molecule (donor) transfers its excitation energy to an acceptor atom or molecule during the lifetime of the donor excited state [32]. Literature also refers to the donor as sensitizer and acceptor as the activator. Sensitizer ions are used when the optical absorption of the activator ions is weak in a given region of the (visible or UV) spectrum and the energy transfer mechanism is used to enhance the luminescence of the activator, such luminescence is called sensitized luminescence [33]. The host lattice itself (optical band absorption) can transfer the energy to the activator ions, in this case, it will be called the host lattice sensitization [15].

Four underlying ET mechanisms have been proposed and observed between two ions (without considering the upconversion mechanism): (a) resonant radiative transfer through the emission of a donor and re-absorption by an acceptor ion; (b) Förster and Dexter energy transfer associated with non-radiative resonance energy transfer between an absorber (donor) ion and an emitter (acceptor) ion; (c) multiphonon-assisted ET; and (d) cross-relaxation between two identical ions (**Figure 1.3**) [34].

Figure 1.3. Schematic energy transfer processes between two ions. D is the donor and A is the acceptor. (a) Radiative resonant transfer; (b) resonant nonradiative transfer; (c) phonon-assisted nonradiative transfer; (d) cross-relaxation.

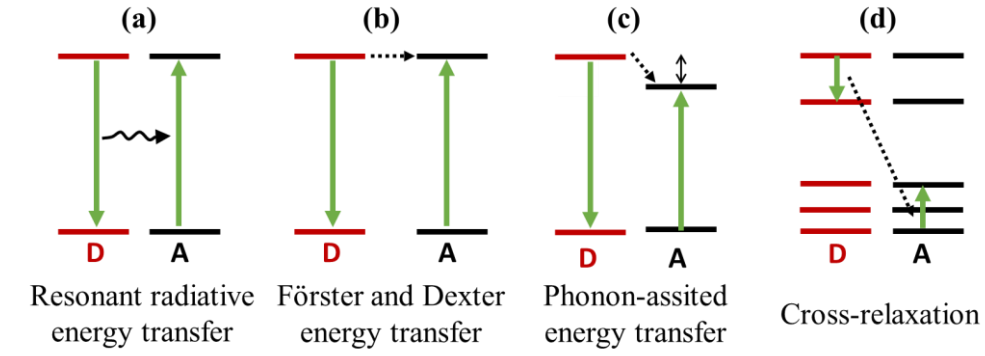

1.4.1 Förster and Dexter energy transfer

Förster and Dexter [33] studied the non-radiative resonant ET (**Figure 1.3 (b)**). For this, the energy differences between the ground and excited states of the donor (sensitizer) and the acceptor (activator) must be equal [35]. The energy transfer probability per unit time W_{DA} between both donor and acceptor centers is generally approximated as in **equation 1.4** [22]. The integral represents the spectral overlap between the normalized donor emission and the normalized acceptor absorption. The square of the matrix is expressed in terms of the distance between the donor and acceptor (R_{DA}). Thus, W_{DA} will be distance dependent (R_{DA}) ruled by the interaction type (exchange or multipolar interaction [32]). E is the energy involved in the transfer.

$$W_{DA} = \frac{2\pi}{\hbar}|\langle D, A^*|H_{DA}|D^*, A\rangle|^2 \int g_D(E) g_A(E) dE \qquad (1.4)$$

Following **equation 1.4**, for exchange interaction, the distance dependence is exponential decreasing [36]:

$$W_{DA}^{exc} = \frac{1}{\tau_0}\exp\left[\Upsilon\left(1 - \frac{R_{DA}}{R_C}\right)\right] \qquad (1.5)$$

Where $\Upsilon = 2R_C/L$. L is a constant called the effective average Bohr radius. R_C is the acceptor-donor critical distance for which the W_{DA} transfer rate constant equals the W_{Donor} [22].

For coulomb multipolar interaction, the distance dependence is given by R_{DA}^{-s} [36].

$$W_{DA}^{multi} = \frac{1}{\tau_0}\left(\frac{R_C}{R_{DA}}\right)^s \qquad (1.6)$$

With s = 6, 8, 10 for dipole-dipole, dipole-quadrupole, and quadrupole-quadrupole interaction, respectively [34].

When the donor internal rate constant (W_{Donor}) satisfies that $W_{Donor} < W_{DA}$, then the donor-acceptor energy transfer will occur [22]. For the case of exchange-mediated transfer, the critical distance R_C is not much larger than $7 - 8$ Å [22]. Whereas for the multipolar interaction, R_C can be much larger than 50-100 Å, i.e., 35 Å (dipole-dipole), 8 Å (dipole-quadrupole), 2 Å (quadrupole-quadrupole) [37].

In the case of RE^{3+} ions in solids, dominant multipolar ion-ion interaction governs the energy transfer, and exchange interaction is of minor importance. It happens because the 4f wavefunction is well localized, and the overlap of wavefunctions of ions is very small even between the nearest neighbor sites [38]. When the dipole transition is not completely allowed for donor and (or) acceptor, as in the f-f transition case, it is possible that the higher-order interactions such as dipole-quadrupole or quadrupole-quadrupole might have a higher transfer probability for small distances [35].

The increasing of W_{DA} will significantly decrease the donor decay time (τ_D) [1,34], i.e., the donor emission decay curve will deviate from a simple exponential curve [35]. In the beginning, the decay is faster, because the donors close to the acceptors decay first. After a while, other donors, further away from acceptors and still excited, start transferring energy. After a very long time, donors that are very far from acceptors will finally decay with their intrinsic lifetime [39].

In the case of acceptors randomly distributed with various distances to a donor in a crystal, some considerations have to be included in the energy transfer processes [1]:

a) Direct transfer from donor to acceptor with no migration among donors.
b) Energy migration among donors before the transfer to the acceptor, so that the energy of excitation may reach an acceptor after hopping resonantly among donors. The energy migration process transfers the excitation energy far from the site where the absorption took place [40].
c) A fast transfers energy migration among donors or acceptors with no energy transfer between donor and acceptor [40,41]. This condition can be applied for high concentrations of donors and acceptors because of the perfect resonance energy transfer conditions. The donor concentration should remain low to avoid migration among them [39].

1.4.2 Phonon-assisted energy transfer

Phonon-assisted ET (**Figure 1.3 (c)**) will occur when the resonance condition (between the donor and the acceptor) is not well satisfied, resulting in a small spectral overlap [35]. In this case, the energy mismatch (ΔE) between the transition energies of the donor and the acceptor will be compensated by the simultaneous emission or absorption of one or more phonons [38]. $\Delta E = Nh\nu_{max}$, $h\nu_{max}$ is the largest phonon energy in the host, and N is the number of emitted phonons during the relaxation. For example, it was revealed that the phonons of about 400 cm^{-1} in the Y_2O_3 host contribute dominantly to the phonon-assisted process [34]. According to the Miyakawa–Dexter theory [42], the probability of phonon-assisted energy transfer per unit time is given in **equation 1.7**.

$$W_{PA}(\Delta E) = W_{PA}(0)e^{-\beta \Delta E} \qquad (1.7)$$

Where: $W_{PA}(0)$ is equal to the resonant transfer probability given by **equation 1.4**, β is a parameter determined by the strength of electron-lattice coupling as well as by the energy of the phonon involved [38].

1.4.3 Cross-relaxation energy transfer

A cross-relaxation (**Figure 1.3 (d)** process usually refers to a resonant ET between identical ions, acting as both donors and acceptors [40]. The excited ion transfers only part of its energy to another ion [22]. Cross relaxation has been measured as the dominating factor in non-radiative relaxations at high concentrations [15]. In the Tb^{3+} ion case, cross-relaxation quenches the emission from the higher $^5D_3$ level in favor of the emission originating from the lower $^5D_4$ level (**Figure 1.4**) [43]. Cross-relaxation also might occur at low concentrations. For instance, the blue Eu^{3+} emission is quenched even at relatively low Eu^{3+} concentrations in favor of the red emission [37]. This means that cross-relaxation can change the emission color of the phosphor by an increase in the activator concentration.

The dependence of the light emission intensity and the RE concentration can be distinguished in two ranges [44]. At low concentration, where the emission intensity is proportional to the number of active RE ions. At high concentrations, where the light emission has an exponential decay with the concentration. **Figure 1.5** shows the Tb case. When the RE ion concentration is increased, cross-relaxation may give rise to the energy migration between donors [40]. The first transfer step is followed by many others. Afterward, the excitation energy can reach a remote site, where it will be lost by a non-radiative process (quenching site). Thus, the luminescence will be reduced. This

phenomenon is called concentration quenching [22]. Concentration quenching of luminescence also has its origin in the paired or coagulated of the activator ions transforming themselves into a quenching center [35].

Figure 1.4. Cross-relaxation between two Tb^{3+} ions, resulting in the emission from the $^5D_4$ state.

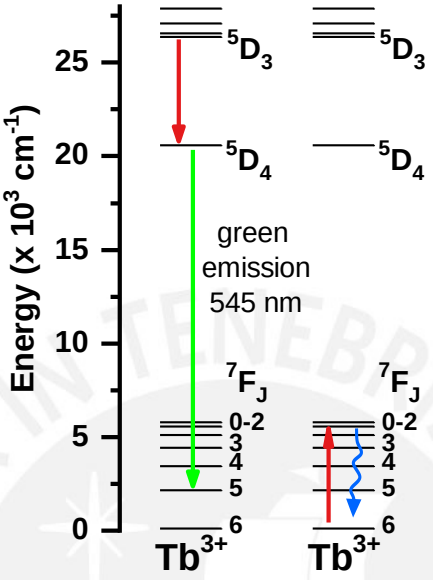

Figure 1.5. PL integrated intensity of Tb^{3+} ions of various Tb doped matrices versus the atomic Tb concentration, adapted from [44].

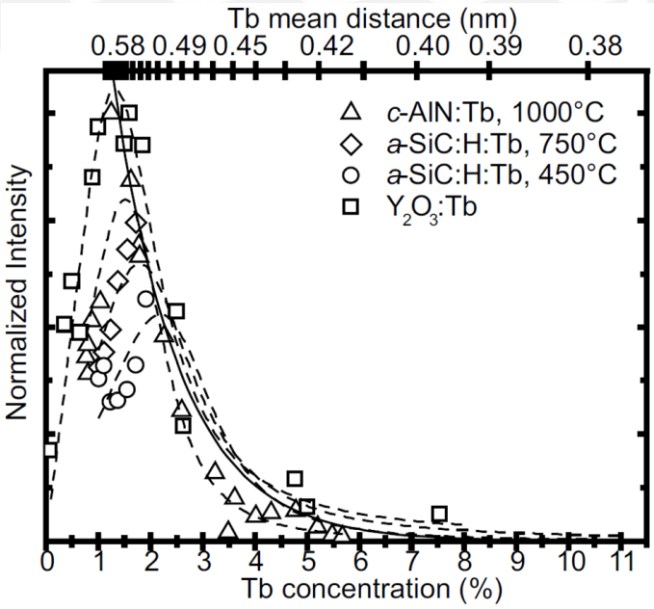

1.5 Quantum Cutting

Quantum cutting (QC) process can transform the energy of one absorbed photon into two emitted low-energy photons [45]. Thus, the internal photoluminescence quantum yield (*iPLQY*) of the QC process can theoretically achieve values greater than unity [53]. Also, it will be useful to define the external photoluminescence quantum yield (*ePLQY*).

$$iPLQY = \frac{number\ of\ photons\ emitted}{number\ of\ photons\ absorbed} \qquad (1.8)$$

$$ePLQY = \frac{number\ of\ photons\ emitted}{number\ of\ incident\ photons} \qquad (1.9)$$

1.5.1 Working principles of quantum cutting

In the 1950s, Dexter proposed the possibility to obtain quantum yields greater than unity through a "photon splitting" process [47]. The sensitized luminescence can take place between one donor and two acceptors. From the energy conservation principles, it is possible to obtain two visible photons emitted by the acceptors for each absorbed UV photon by the donor. In the 1970s, experimental QC results were shown using a single ion. The QC process yields two photons in a sequential two-step radiative process [48,49]. This process was also called the "photon cascade" emission. **Figure 1.6 (a)** represents the single ion-based QC on the ion with the number I by a sequential emission of two-visible photons. Examples of such effect include Pr^{3+}, Tm^{3+}, Er^{3+} among others. However, one major issue presented by the single ion-based QC is the unwanted emissions in the ultraviolet–visible spectral range and non-radiative recombination that compete with the desired emission [34].

Then, to prevent losses in the IR and UV regions, a second type of RE ions has been used [50]. At the end of the 1990s, an alternative concept called down-conversion (DC) in a system composed of two distinct RE ions was experimentally reported by Wegh et al. [50]. The quantum cutting via energy transfer DC is based on the energy transfer in a set of different lanthanide ions. The result obtained by Wegh et al. reported a theoretical visible quantum efficiency of 190%. Downconverter sets include Gd^{3+}-Eu^{3+} [50] and Er^{3+}-Gd^{3+}-Tb^{3+} [51], which were studied in the conversion of ultraviolet radiation (λ < 200 nm) into visible light in a vacuum for mercury-free fluorescent tubes. More recently, Ln^{3+}-Yb^{3+} (Ln=Tb, Tm, Pr, Er, Nd, Ho, and Dy) have been studied for quantum near infrared (NIR) cutting, because of its potential application in c-Si solar cells [34]. Additionally, the up-conversion process has also been studied for Si solar cell applications.

The DC mechanisms in a set of two types of ions are illustrated in **Figure 1.6 (b)-(e)** [34,50,51]. Type I is an ion that might show an emission at a high-energy level. Type II is an ion to which energy transfer takes place. The quantum-cutting process can be understood as a one-step, two-step, and simultaneous sensitizing process.

Figure 1.6. Summary of quantum cutting mechanisms.

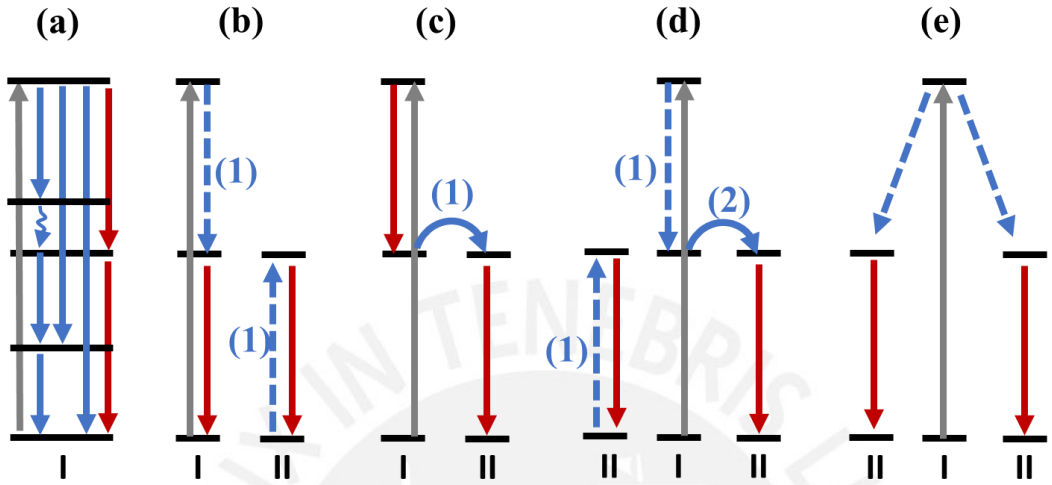

- One-step process, **Figure 1.6 (b)** and **(c)** represent two possibilities involve only one-step energy transfer from ion I to ion II (indicates by (1)). This is sufficient to obtain visible QC if one of the two visible photons can be emitted by the ion I.
- Two-step process, **Figure 1.6 (d)** represents the possibility of quantum cutting by a two-step energy transfer. In the first step, a part of the excitation energy is transferred from ion I to ion II by cross-relaxation (indicates by (1)). Ion II returns to the ground state by emitting one photon. Ion I is still in an excited state and can transfer the remaining energy to a second ion II (indicated by (2)).

The DC mechanisms discussed in **Figure 1.6 (b)-(d)** require resonance ET between the ion I and ion II in close proximity [34]. Here, the ET will be described as a first-order rate process, and according to **equation 1.4**, the energy transfer rate will be depending on the spectral overlap between the donor emission and the acceptor absorption spectrum. Splitting of the energy is reached by the population of an intermediate energy level of the donor [52].

- Simultaneous sensitizing process, **Figure 1.6 (e)**, when there is no spectral overlap, the second-order DC may dominate the relaxation process [52]. According to Jenkins and Andrews [53,54], the second-order mechanism may occur due to two mechanisms, cooperative and accretive. In both mechanisms, a virtual state is

involved. For the cooperative pathway, the virtual state is located on the donor, for example, Tb^{3+} ion, and this ion acts twice as a donor of energy. For the accretive pathway, the virtual state is located on one of the acceptors, for example, Yb^{3+} ion [52]. The cooperative mechanism comprises the simultaneous energy transfer from the donor to two acceptors. The accretive mechanism comprises the transfer from the donor to one of both acceptors where one of them accepts the energy. Afterward, part of such energy is transferred to the second acceptor ion. Verger et al. [52] reported evidence of the cooperative energy transfer in $Yb_xY_{1-x}PO_4:Tb^{3+}$ by comparing the experimental Tb^{3+} luminescence decay time for different Yb^{3+} concentration, whereas the accretive mechanism was ruled out of the second-order DC process.

1.5.2 Efficiency and limitations of the QC process

The energy transfer efficiency (η_{ET}) will be determined by [55]:

$$\eta_{ET} = 1 - \frac{F_{DA}}{F_D} = 1 - \frac{\int I_{DA}(t)dt}{\int I_D(t)dt} \qquad \textbf{(1.10)}$$

Where

F_{DA} and F_D are the steady state intensities of the donor luminescence in the presence and absence of the acceptor, respectively.

$I_{DA}(t)$ and $I_D(t)$ are the intensity decay of the donor in the presence and absence of the acceptor, respectively.

The energy transfer (ET) process from Tb^{3+} to Yb^{3+} was studied by Vergeer et al. [56]. The ET efficiency with a composition of x at.% of Yb concentration ($\eta_{ET,x\%Yb}$) will be defined by:

$$\eta_{ET,x\%Yb} = \frac{N_{Tb^{3+}to\ Yb^{3+}}}{N_{Tb^{3+}}} = 1 - \frac{\int I_{x\%Yb}(t)dt}{\int I_{0\%Yb}(t)dt} \qquad \textbf{(1.11)}$$

Where:

$N_{Tb^{3+}to\ Yb^{3+}}$: number of Tb^{3+} ions depopulated by the energy transfer to Yb^{3+}.

$N_{Tb^{3+}}$: total number of Tb^{3+} ions excited.

Following **equation 1.8** and assuming that all excited Yb^{3+} ions will decay radiatively, the theoretical DC efficiency was defined by Vergeer et al. [56]. Finally, an upper limit for the theoretical DC efficiency can be expressed by **equation 1.12**, which

follows a linear relationship between the energy transfer efficiency ($\eta_{ET,x\%Yb}$) and the theoretical DC efficiency ($\eta_{x\%Yb}$).

$$\eta_{x\%Yb} = \eta_{Tb}\left(1 - \eta_{ET,x\%Yb}\right) + 2\eta_{ET,x\%Yb} \quad \textbf{(1.12)}$$

Where

η_{Tb}: quantum efficiency for the Tb^{3+} ions, for theoretical estimations, it is set to 1.

$\eta_{x\%Yb}$: theoretical DC efficiency with a composition of x at.% of Yb concentration.

$\eta_{ET,x\%Yb}$: ET efficiency with a composition of x at.% of Yb concentration.

From the literature, the theoretical DC efficiency estimation is high. However, the experimental quantum efficiency reported in material with the DC process is low. As in the case of the Gd^{3+}-Eu^{3+} pair in $LiGdF_4$, despite the high theoretical DC efficiency value (~195%), its measured quantum efficiency is not higher than 32% [57]. Another example is the Tb^{3+}-Yb^{3+} couple in $Yb_xY_{1-x}PO_4$:Tb^{3+} with a maximum energy transfer efficiency of 88% leading to a theoretical DC efficiency value of an upper limit of 188% [52], but the emission spectrum showed a weak IR-signal so then a low experimental quantum efficiency would be expected.

The high acceptor concentration could explain the difference between the measured quantum efficiency and the theoretical DC efficiency. A high acceptor concentration is usually applied in doped materials for efficient energy transfer. However, the high acceptor concentration would lead to acceptor luminescence quenching. For example, concentration quenching of the Yb^{3+} ions in the Ce^{3+}-Yb^{3+} [58] and the Pr^{3+}-Yb^{3+} [59] pairs were reported. In the latter, the reported DC efficiency reaches about 200%. However, luminescence quenching was observed even at a relatively low Yb concentration (5 mol%).

1.5.3 Quantum cutting for photovoltaic applications

As was discussed earlier, luminescent materials are actively studied for applications in lighting, displays, telecommunication, Laser, Scintillation detectors for X-rays, among others. Also, considerable interest has been generated in developing luminescent materials to reduce losses in photovoltaic (PV) devices.

For any single-junction solar cell, the bandgap energy (E_g) of the semiconductor from which the PV device is fabricated sets a fundamental upper limit for its conversion efficiency. Shockley and Queisser [60] demonstrated that the one-Sun efficiency limit for a single material cell is around 30% for a silicon (Si) device. The two major loss mechanisms,

that need to be overcome to enhance the device efficiency, are (1) the lattice thermalization: a photon with higher energy produces an electron–hole (e-h) pair that relaxes to the band edges being lost to heat [61] and (2) the transparency to sub-bandgap photons: photons with lower energy cannot be absorbed by the solar cell [62]. Different approaches have been studied to overcome those loss mechanisms, for instance, multi-junction or tandem cells, which seek to rectify this problem. Here, a series of cells with varying bandgaps are combined together into a single structure [63]. Another option is based on modifying the Sun spectrum to suit the material. Thus, it modifies the spectrum instead modify the materials as in the tandem cell.

Spectral modification

The spectral modification can be achieved through the optical process called:

a) The Up-conversion (UC) of sub-bandgap light, which transforms two (or more) transmitted sub-bandgap photons into one usable above-bandgap photon, which is subsequently absorbed by the solar cell to generate electron–hole pairs [34].
b) The luminescent down-shifting (LDS), where a single photon process involves the transformation of one absorbed high-energy photon into one lower-energy photon. LDS is similar to quantum-cutting, but its conversion efficiency does not exceed 100% [34].
c) The QC already explained above. This process could minimize the energy loss caused by thermalization of hot charge carriers after the absorption of high-energy photons. After the QC process, photons are absorbed by solar cells. The photocurrent of the device can be theoretically doubled [62].

The AM1.5G intensity fraction that can be absorbed by a thick silicon device as well as the additional spectral regions available for up- and down-conversion or down-shifting are shown in **Figure 1.7**. It plots the AM1.5G spectrum (in blue) and the light fraction that can be absorbed by a bulk Si device (in green). Given that Si possesses an indirect bandgap of 1.12 eV (~1100 nm), this is the cut-off response. To achieve two-photon emission via QC, each high-energy incident photon must possess the energy of at least twice the Si bandgap, or a wavelength of shorter than 550 nm (red region in **Figure 1.7**). Likewise, for the UC, two sub-bandgap photons resulting in the emission of a single above-band gap photon. The former photons must exhibit an energy of at least half of the Si bandgap energy, or shorter wavelength than 2200 nm (purple region in **Figure 1.7**). The intensity available for

absorption in the QC process (~150 W/m^2) represents about 15% of the AM1.5G total intensity (1000 W/m^2). Likewise, for UC (~160 W/m^2) represents about 16%.

Figure 1.7. AM1.5G spectrum showing the fraction (highlighted in green) absorbed by a typical silicon-based PV cell and the spectral regions that can be utilized through quantum-cutting and up-conversion processes, adapted from [64].

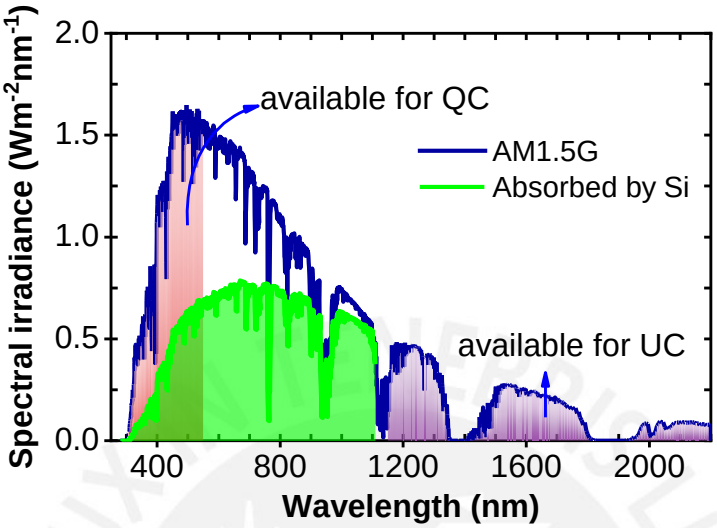

Improving solar cell efficiency by QC

As was discussed above, UC (nonlinear process) and QC could offer the spectral conversion of sunlight to enhanced solar cell performance [62]. Both UC and QC are passive components. So, the UC and QC-PV device provides the carrier collection still via a single PV junction.

Quantum-cutting limiting efficiency calculation was reported by Trupke et al. [65]. It presented a limiting efficiency calculation according to the detailed balance model (taking only radiative recombination into account) for a solar cell system. It was based on the generation of multiple e–h pairs per incident photon and uses the QC process upon the incident high-energy photons for the conversion into two or more photons of smaller energy. Significant improvements in solar cell efficiency were found for bandgap energies of about 1.1 eV. **Figure 1.8** shows a luminescence conversion film on the front surface of a PV cell, which has the advantage that it can be applied to any existing solar cell and can be optimized independently from the solar cell material itself. The efficiency which can be achieved with this geometry will have an upper limit for the efficiency of 38.6% for $E_g = 1.1$ eV. The 38.6% efficiency represents a significant improvement over 30.9%, which can be achieved with a conventional solar cell under the same assumption of only radiative recombination [65].

Figure 1.8. Schematic diagram of a QC system. The converter layer is located on the front surface of a solar cell.

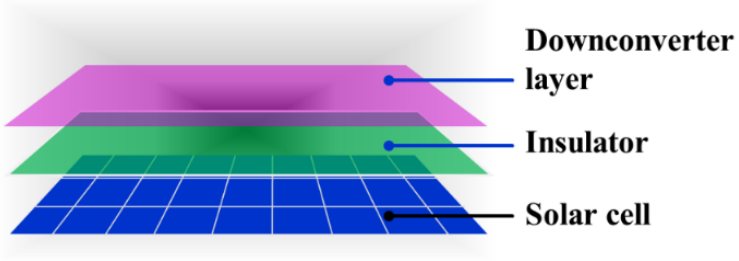

The wavelength-dependent response of a PV device can be described by its external quantum efficiency (EQE), which is defined by **equation 1.13** [63]. **Figure 1.9** shows representative EQEs of various PV cells. There is a reducing EQE at short wavelength. For mono-Si cell, the major loss mechanisms (in the UV-blue region) corresponds to the front surface recombination as well as an increased reflection and absorption from the anti-reflection coating [66]. The EQE includes the effect of the optical loss such as transmittance and reflectance [67]. The QC-PV device is expected to increase the EQE in the short-wavelength range (green region in **Figure 1.9**). There are many reports of materials for PV applications, mainly focussing on the improvement of the quality of new materials. Nevertheless, just few of them have been presented results from QC-PV devices.

$$EQE = \frac{number\ of\ e-h\ pairs\ generated}{number\ of\ incident\ photons} \qquad (1.13)$$

Figure 1.9. External quantum efficiency (EQE) for various PV cells.

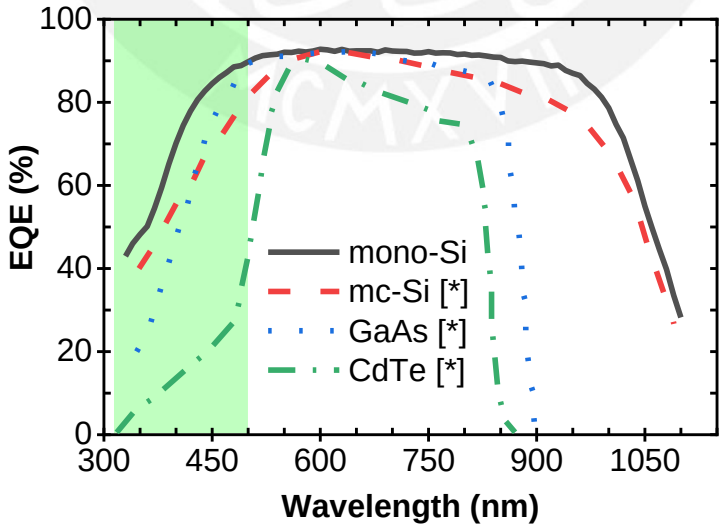

[*] Reference [68].

QC materials in PV systems

Many phosphors have been studied for QC; some of them require vacuum UV excitation (≤ 200 nm). However, this wavelength does not exist in the AM1.5G. So, a suitable QC system will be the one that can be excited by the UV-blue spectral range. A promising way to apply QC in PV devices consists of the use of co-doped systems RE^{3+}-Yb^{3+}. The advantage of the Yb^{3+} ion is first, the resulting NIR luminescence (λ = 980 nm), which corresponds to photon energy close to the bandgap of the Si solar cell. Second, there are no intermediate levels between the $^2F_{5/2}$ level and the $^2F_{7/2}$ (ground state). Thus, there is an increase in the probability of radiative emission from the Yb^{3+} $^2F_{7/2} \rightarrow {}^2F_{5/2}$ transition. A summary of QC co-doped materials can be found in **Table 1.4**. Also, a summary of QC-PV devices on various types of solar cells are shown in **Table 1.5**.

Table 1.4. NIR quantum-cutting materials co-doped with RE^{3+}-Yb^{3+} for PV applications, adapted from [34].

RE couple	Host lattice	$\lambda_{em.}$ (nm)	QC quantum efficiency (%)
Tb^{3+}-Yb^{3+}	YPO_4, $GdBO_3$, Zn_2SiO_4	~485	188, 182, 162
	SiN_xO_y [69], $SiO_210Al_{1.5}$ [70]	239, 484	197,159
Tm^{3+}-Yb^{3+}	$GdAl_3(BO_3)_4$, Glass ceramics containing LaF_3 nanocrystals, YPO_4	~470	164,162, 175
Er^{3+}-Yb^{3+}	$NaYF_4$, $Cs_3Y_2Br_9$	380, 490	128, 195 [34]
Pr^{3+}-Yb^{3+}	$GdAl_3(BO_3)_4$, $NaYF_4$, SrF_2	489, 441	165, 181, 140
Nd^{3+}-Yb^{3+}	YF_3	360	140
Ho^{3+}-Yb^{3+}	Glass ceramics containing YF3 nanocrystals, $NaYF_4$	488, 535, 359	155

Table 1.5. List of QC-PV devices from different type of solar cells [63].

Type of solar cell	Downconverter material	$\lambda_{exc.}$ (nm)	$\lambda_{em.}$ (nm)	Device response
Mono-Si	Eu^{3+} in silicon nitride matrix	325	980	N/A
	Eu^{3+} containing aromatic complex in PMMA	250-360	665	+5.8% EQE under 100 W Xe lamp
	Tb^{3+} -Yb^{3+} co-doped tellurite glass	355, 482	548, 980	+7% relative to the undoped glass
Dye-sensitized solar cell (DSSC)	Eu^{3+} -Dy^{3+} co-doped ZnO	338, 394	394, 458, 483, 575,593, 611	+6.06 mA/cm^2 and +3.18% power conversion efficiency (212% and 245% relative increases) under 0.1 W/cm
Perovskite solar cell	Eu^{3+} doped $ZnGa_2O_4$	380-500	450-720	+3.48 mA/cm^2 and +3.67% power conversion efficiency (17.2% and 34.4% relative increases) under AM1.5G

Optical properties to consider in a QC layer

The bare Si has a high reflectivity (more than 30%), and anti-reflection coating (ARC) should be applied to reduce the reflection losses. To maximize the efficiency in Si solar cells, the reflection losses have been minimized at λ = 600 nm (**Figure 1.10**). That means that the thickness (d) and refractive index (n) of the ARC should be controlled to reach a minimum reflectance. A schematic representation of components in an encapsulated Si solar cell is shown in **Figure 1.11 (a)**. After adding up the QC layer, the reflectance optimization has to be considered again. The new system with a down-conversion layer (DC-PV device) is outlined in **Figure 1.11 (b)** and must satisfy the condition of minimum reflectance at 600 nm. This wavelength is chosen since it is close to the peak power of the solar spectrum [71].

Figure 1.10.Comparison of surface reflection from a silicon solar cell, with and without a typical anti-reflection coating, adapted from [71].

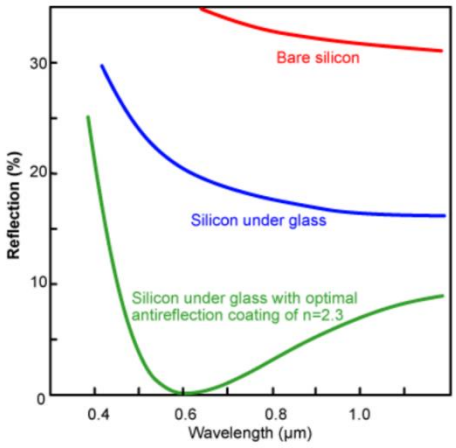

In a typical Si solar cell, the front surface is passivated with a hydrogenated amorphous silicon nitride layer, which acts simultaneously as ARC [72]. The hydrogenated amorphous silicon nitride (thickness ~75 nm and n_{SiN_x} ~2 in the visible region [72]) is often just called silicon nitride. The DC layer should be placed between the encapsulation glass (n_{glass} ~1.5) and the ARC (n_{SiN_x} ~2 - 2.3 [71]). Thus, the reflection is minimized when the DC refractive index ($n_{DC\ layer}$) and thickness ($d_{DC\ layer}$) satisfy the **equations 1.14** and **1.15** [71]. Resulting in optimized values $n_{DC\ layer}$ ~1.7 - 1.86 and $d_{DC\ layer}$ = 88.3 nm - 80.6 nm.

$$n_{DC\ layer} = \sqrt{n_{SiN_x} n_{glass}} \qquad \textbf{(1.14)}$$

and

$$d_{DC\ layer} = {}^{600\ nm}/_{4n_{DC\ layer}} \qquad \textbf{(1.15)}$$

Figure 1.11. **(a)** Schematic representation of components in an encapsulated Si solar cell. **(b)** Schematic representation with a DC layer on the front surface of the solar cell.

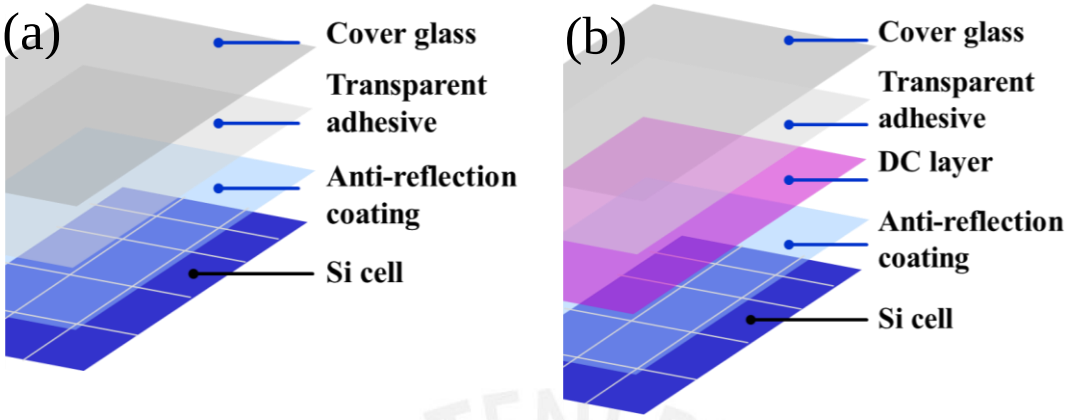

Another mechanism that leads to light loss, and therefore decreases the efficiency of the DC-PV device, is the light loss out of the front surface as a consequence of the geometrical arrangement in the DC system, because a fraction of the luminescence will escape back through the top front surface of the DC layer. The fraction of photons loss by the frontal surface can be estimated with the scape cone-losses out (**equation 1.16** [73,74]). Assuming $n_{DC\ layer}$ = 1.8, the fraction of photons loss (FPL) would be ~22%.

$$\mathrm{FPL} = \frac{1}{2}\left(1 - \sqrt{1 - \left(\frac{n_{glass}}{n_{DC\ layer}}\right)^2}\right) \qquad \textbf{(1.16)}$$

Additional important considerations are that the DC layer should be transparent over the range where the Si solar cell is efficient. And, to succeed in the implementation of DC in commercial systems, the DC film should show stability and robustness in ambient conditions [61].

CHAPTER 2. General Considerations in Silicon Oxycarbide

In the previous chapter, a detailed description of the electronic configuration of RE ions, their radiative and non-radiative recombination mechanisms, as well as energy transfer mechanisms between them, with special interest in the quantum cutting process, was introduced. In this chapter, a literature review of the general considerations of amorphous silicon oxycarbide (*a*-SiOC) in terms of atomic structure, optical constants, and luminescence is reviewed.

2.1 Overview of silicon oxycarbide structure

As far as the structure is concerned, silicon oxycarbide is reported to have an amorphous structure [75] and can be described as products resulting from the carbon incorporation into a silica network [76]. In general, perfect silicate structures are based on one silicon typically surrounded by four oxygen atoms leading to a stable tetrahedron [SiO_4] unit. The basic tetrahedron units are connected by sharing a corner oxygen ion, resulting in ≡Si−O−Si≡. The centered angle in the oxygen atom is called the bridge bond angle and the central angle in the silicon atom is called the tetrahedron angle (~110°) (**Figure 2.1**). In the *a*-SiOC network, the oxygen and carbon atoms share bonds with silicon O−Si–C [76–78]. The literature has a distinction between black glass and oxycarbide glasses. The former contains only a second phase carbon dispersion, and the latter usually includes both network carbon (joined to the silica network) and elemental carbon [78].

Figure 2.1. Schematic of two SiO_4 tetrahedrons sharing one corner oxygen. All bond angles around each silicon atom are ~110° (tetrahedron angle).

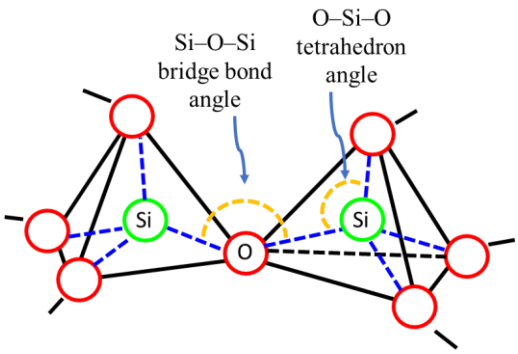

Concerning the SiOC bonding topology, the literature reports two characteristic distances between the nearest neighbor of the silicon ion. If carbon has been successfully inserted into the silica network, the Si–O bond length (~1.61 Å) will be shorter than that of

Si–C (~1.88 Å). In **Table 2.1**, the values of bond length, tetrahedron angle, and bridge bond angle are summarized and compared with *a*-SiO_2. According to the experimental results, the Si–O bond length and the tetrahedron angle are almost constant.

Table 2.1. Bond length, tetrahedron angle, and bridge bond angle for a-SiO_2 and a-SiOC.

Bond	***a*-SiO_2**	***a*-SiOC**
Si–O	1.58-1.61 Å	1.60-1.62 Å
Si–C	-	1.86-1.89 Å
O−Si−O (tetrahedron angle)	~110°	~109°
Si−O−Si (bridge bond angle)	120 - 180° (mainly reported at ~144°)	139-144° (decrease with the inserted C amount)
References	[79–81]	[82,83]

The SiOC structure can be represented by the three-dimensional covalent unit denoted by [SiO_xC_{4-x}], where $0 \leq x \leq 4$. The glass structure could exhibit five different tetrahedral units SiO_4, $SiCO_3$, SiC_2O_2, SiC_3O, and SiC_4 [82]. The possibility to replace the two-coordinated oxygen atoms with four-coordinated carbon atoms strengthens the amorphous network. As a consequence, the carbon incorporation would lead to improving thermal and mechanical properties [84]. When all C atoms are bonded to silicon (no excess free C), the SiOC stoichiometry can be stated on the SiC-SiO_2 line (in the Si, C, and O ternary diagram) with the chemical formula $SiO_{2(1-x)}C_x$ (stoichiometric glass silicon oxycarbide). However, SiOC systems can also contain an excessive amount of free carbon, so their composition will fall within the C-SiO_2-SiC triangle, represented in **Figure 2.2**. It will be expressed as the resulting chemical formula $SiO_{2(1-x)}C_x + yC_{free}$, where x+y is the total carbon in the system [82].

Figure 2.2. Si, C, and O ternary diagram.

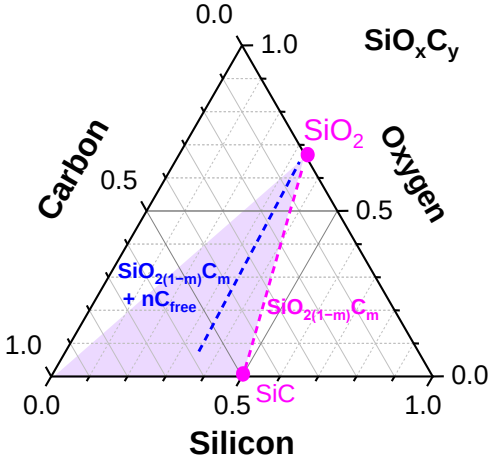

2.2 Effects on the SiOC atomic network by growth technique

The composition and structure of SiOC are known to be linked to the technique used for its synthesis. For this reason, it will be essential to make a brief analysis of the techniques used for it. The synthesis processes can be divided into two groups depending on the growth temperature, low and high temperatures.

- At high temperatures, most of them are based on polymer precursor techniques. The polymer-to-ceramic transformation consists of two steps: 1) The cross-linking of the polymers at low temperatures (100 - 400 °C) leading to infusible organic/inorganic networks. 2) The ceramization by processes involving a pyrolysis step at 1200 °C [85] or temperatures up to 1000 - 1400 °C [86]. Also, the high-temperature processing is reported by melting [83] and chemical vapor deposition at 800 °C [87].
- At low temperatures, synthesis with non-polymer precursor techniques is usually reported by radio frequency (RF) magnetron sputtering [88]. Even in deposited samples (without substrate annealing). The produced samples consist of Si–O and Si–C bonds [75] characteristic of the *a*-SiOC distribution. Therefore, RF sputtering could offer an advantageous approach for low-temperature synthesis.

The atomic arrangement of SiOC has been well established for temperatures above 800 °C. This is mainly because the processes usually used start from precursor polymers for its synthesis. Nuclear magnetic resonance spectroscopy studies mainly used in the elucidation of molecular structures show the presence of $\equiv Si - CH_3$. The latter represents a non-bridging site in the SiOC network. The presence of free carbon in the form of polyaromatics carbon species [nC_6H_x] bonded to or embedded into in the SiOC network was also reported [84]. **Figure 2.3** shows a schematic representation of the amorphous lattice structure between 800 and 1000 °C.

Phase separation at 1000 °C was reported [89], where the stoichiometric silicon oxycarbide $SiO_{2(1-x)}C_x$ shows a dense homogeneous amorphous matrix containing some refined regions, which seemed to be a local crystalline SiC arrangement. Another work reports the existence of C–H modes related to graphene rings in the pyrolyzed glasses and the appearance of a more efficiently packed Si–C–O network (due to the density increase) at 1000 °C [82]. Also, phase separation forms SiO_2- and SiC-based environments at ~1200 °C. Finally, nanometer-sized SiC particles precipitation embedded in vitreous SiO_2 at temperatures higher than 1300 °C was also reported [89].

Figure 2.3. Schematic representation of the *a*-silicon oxycarbide glass structure at 800 – 1000 °C growth temperature [78].

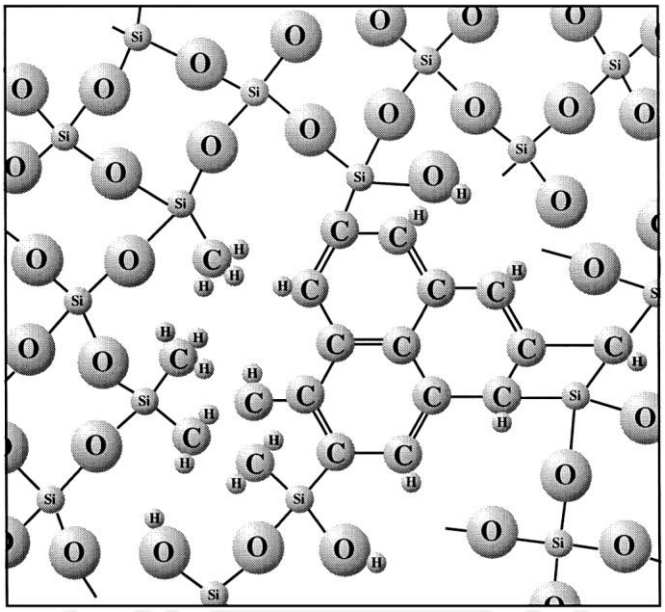

2.3 Bond redistribution under thermal process in SiOC

In this work, the RF-magnetron sputtering technique was used for the growth of SiOC films. The preparation temperature during the process was kept below 100 °C. Afterward, post-deposition annealing treatments were applied. During the annealing treatments, the bond redistribution mechanisms are expected to be similar to those reported during their synthesis by other techniques. Therefore, this section provides an overview of the bond redistribution mechanisms reported in the literature during the synthesis of SiOC samples. Thermal processes transform the precursors into ceramics in a controlled (typically inert) atmosphere [76]. The route of the conversion of preceramic polymers into the final inorganic product (SiOC glass or glass-ceramic) is summarized in the followed lines.

The general structure can be understood as silicon in tetrahedral molecular geometry, forming bonds with H, O, and C in the SiOC network. The Si–H, Si–C, and Si–O bonds are ascribed to 3.1 eV, 4.5 eV, and 8.3 eV dissociation energy [90], respectively. Therefore, the Si–H and Si–C bonds can be broken more easily than Si−O. Hence, the *a*-SiOC structure would mainly result in the favorable formation of Si–O bonds.

At lower temperatures (below 800 °C) studies report the cross-linking step of the polymer-to-ceramic transformation [91]. In polysiloxanes, at temperatures ranging from 300 to 600 °C, several redistribution reactions can occur between Si–O, Si–C, and Si–H bonds. The exchange of Si–O, Si–C, and Si–H is reported in Belot et al. (1992) [91]. A schematic

representation of some exchange bonds is shown in **Figure 2.4** [76,91]. In particular, Si–H and Si–O bond exchange occurs at temperatures below 300 °C and induces the escape of SiH_4 [92]. Above 450 °C, Si–H bonds cleavage lead to hydrogen loss. Subsequently, Si–C and Si–O bond exchange takes place at 500 °C [91]. After heating to 600 °C, all the Si–H groups are lost [91]. At temperatures above 600 °C, the degradation process involves the cleavage of Si–C and C–H bonds leading to an escape of hydrocarbons and hydrogen [91], which causes shrinkage and mass loss of the sample. **Figure 2.5** shows an overview of the bond evolution under annealing treatment.

Figure 2.4. Schematic representation of exchange bonds. Me: methyl ($–CH_3$).

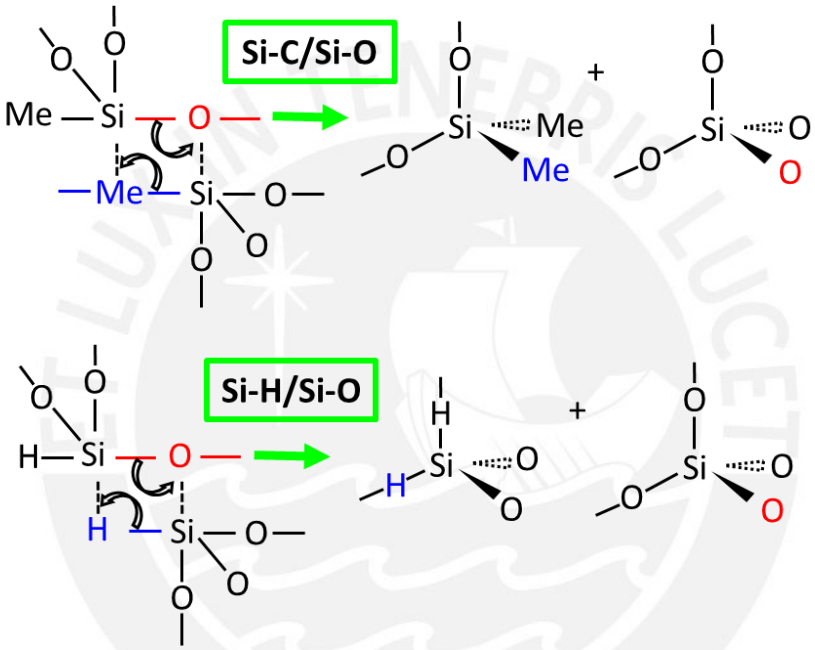

Figure 2.5. Overview of the bond evolution under annealing treatment.

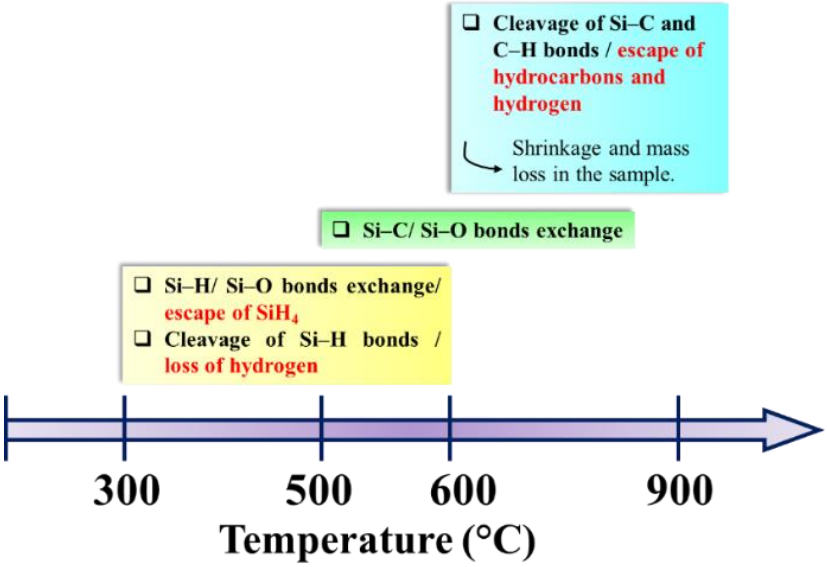

2.4 Optical properties of Silicon Oxycarbide Glasses

2.4.1 Refractive index and bandgap

In literature, SiOC thin films can be classified as SiC-like, Si−C−O, and SiO_2-like films. For these three cases, n increases with increasing carbon content [88,93]. As for the temperature change, n remains constant up to 700 °C. Whereas for higher temperatures, an increase is reported [93]. **Table 2.3** shows the n values for the three types of sorting (at two wavelengths). The C and O atomic composition were chosen as representative values and will be referred to in the discussion of results in **Chapter 4**.

Table 2.2. Refractive index values for three host classifications.

Matrix	C (at.%)	O (at.%)	O/C	$n_{\lambda=400\ nm}$ [93]	$n_{\lambda=1000\ nm}$ [88,93]
SiC-like	45.76	2.97	0.065	3.05	2.70 - 2.90
Si-C-O	17.12	41.09	2.4	1.83	1.75 - 1.80
SiO_2-like	6.37	54.14	8.5	1.52	1.49 - 1.60

Representative values for E_{gap}, E_{04}, and E_{Tauc}, both achieved from the absorption coefficient $\alpha(\lambda)$, are given in **Table 2.3**. With increasing oxygen composition, an increase in the bandgap, attributed to the energy difference between the bonding and antibonding orbitals, is reported to be higher for the Si−O than the Si−C case [93]. Furthermore, a linear dependence of the bandgap reduction has been reported with the increase of the [Si−C]/[Si−O] bond-density ratio [94].

Table 2.3. Representative values for E_{gap} and $\alpha(\lambda)$.

Matrix	$E_{04}^{T<700\ °C}$	$E_{Tauc}^{T<700\ °C}$	$\alpha_{(\lambda=400nm)}$
SiC-like	2.6 eV	2.4 eV	$3x10^4$ cm^{-1}
Si-C-O	3.6 eV	3.1 eV	$1x10^4$ cm^{-1}
SiO_2-like	4.9 eV	3.3 eV	$1x10^3$ cm^{-1}

2.4.2 Identification and origin of host emission

In this section, a review of the characteristics of the luminescence spectrum and its origin in the SiOC matrix is presented. SiOC emission is reported in the range of 400 to 800 nm [95]. In some cases, the emission spectrum is reported as a broad spectrum showing a redshift with increasing carbon [96]. In other cases, the spectrum is not symmetrical and appears to be composed of emission bands [97]. These can be identified as red, green, and blue emissions [96]. The origin of those bands is still under discussion [95]. In general, SiOC luminescence has been associated with a) defects similar to those reported in silicon oxides,

b) carbon-related defects, c) Si nanoclusters, and d) transitions between extended states in the valence and conduction bands and localized tail states.

a) Silica defects, a comparison between the luminescence bands observed in silicon oxides and those observed in SiOC might allow to attributing the same radiative defects for both. The best-known defect in silicon oxides is the E' center. It was detected in the mid-1990s by electron paramagnetic resonance (EPR) spectroscopy [98]. This non-radiative defect has an associated absorption at 5.85 eV and is denoted by ≡Si●. The three parallel lines represent the bonds with the three oxygen, and the dot represents the dangling bond (unpaired electron) [98]. Another defect is the non-bridging oxygen hole center NBOHC denoted by ≡Si−O●, which is associated with band emission centered at 1.85 - 1.95 eV [99] with a decay constant of about 20 μs [98]. The next luminescent defect is the oxygen-deficient center ODC. This diamagnetic defect consists of two Si atoms. In a stable interaction condition (relaxed oxygen vacancy), it is called ODC(I) or relaxed neutral oxygen vacancies NOV denoted by ≡Si−Si≡ [99]. The associated band emission is 2.7 eV with a decay constant of 10.4 ms [99].
b) Carbon-related defects, carbon-related defects have also been associated with the origin of luminescence in SiOC. In one of the first reports, the luminescence of two samples was compared; one after carbon implantation and the other after argon implantation in SiO_2 films [100]. The films were subjected to annealing treatments at 800 and 1000 °C. The emission spectra exhibited a strong broadband luminescence centered at ~490 nm for the carbon implantation case, while only a small luminescence was detected for the argon case. The observed luminescence was attributed to the formation of amorphous carbon clusters.
c) Si nanoclusters, luminescence of Si nanoclusters (Si-ncs) have also been reported in amorphous silicon oxide matrices. High temperature synthesis in SiO_x films can lead to the Si-ncs formation [101] due to Si diffusion and Si excess. The silicon particles diffuse to create silicon agglomerates around the nucleation sites. If the excess Si is high enough, the Si agglomerates crystallize to form Si-ncs. The broadening of the bandgap is induced by quantum confinement in Si-nc, which is why it can exhibit high energy luminescence peaks (blue-shifted PL peaks) [101].
d) Transitions from extended states (valence and conduction band) to tail states located in SiOC. According to Gallis et al. [102], XPS studies have confirmed the existence of Si−O−C and Si−C−O bonds.

e) Hence, the white light emission could be attributed to the carrier generation resulting from electronic transitions related to Si−C and C−Si−O bonds during optical absorption, followed by the recombination of these carriers between energy bands and their associated tail states [96]. The energy of which should vary with the bandgap energy. Another study associates the red emission with the radiative recombination from the extended Si states to the Si dangling bonds (localized states) [95]. The blue emission was attributed to triplet-to-singlet ($T_1 \rightarrow S_0$) electronic transitions in the neutral oxygen vacancies related to carbon ($_3O{\equiv}C{-}Si{\equiv}O_3$) [96].

In addition to the above, Karakuscu et al. (2009) [103] proposed the formation of SiC phases in the synthesis of SiOC thin films. SiOC films with C = 8.0 at.% showed an intense emission range of 450 to 900 nm and external quantum efficiency (EQE) of 11.5%. While SiCO films with C = 13.3 at.% showed a lower luminescence (EQE = 5%). The observed UV-blue emission was attributed to the formation of defects such as dangling bonds, the green emission to the SiC phase formation, and the yellow emission to the small amount of free C. **Table 2.4** and **Table 2.5** summarize the reported luminescence bands and their association with radiative defects.

It is worth mentioning that, according to the literature, an excess of carbon (C > ~13 at.%) should also be avoided due to re-absorption by carbon structures [103]. A previous study developed by Menapace et al.(2008) [104] for LED applications reported luminescence in commercial silicon-based polymers polysiloxane and polysilazane. The polysiloxane reveals maximum and white luminescence after annealing treatment at 500 and 600 °C, while the polysilazane (at 500 °C) reported emission in the red-green range. For both cases, polysiloxane and polysilazane (at 700 °C), the luminescence decreased as a result of re-absorption by the formation of free carbon. The free carbon results in dark and opaque material.

Table 2.4. Luminescence attributed to the presence of carbon in the samples.

Material	Annealing temperature	Observed luminescence	Attributed luminescence
commercial silicon-based polymers	up to 400 °C	UV region	carbon double bonds and carbon radicals [104]
	500 and 600 °C	red-green range	
carbon implantation in thermal SiO_2 films	800 and 1000 °C	broadband centered at 490 nm	amorphous carbon clusters [100]
SiCO thin films	800 and 1000 °C	UV-blue emission	dangling bonds [103]
	1200 and 1250 °C	green and yellow emission	SiC phase and a small amount of free C [103]

Table 2.5. Luminescence bands and their association with radiative defects

PL band (eV)	Specimen	Association	Reference
~1.85 - 1.95	a-SiO_2, SiO_x and α-SiO_2	≡Si−O● (NBOHC*)	[98,99]
	silicon rich a-SiOC	Si dangling bonds	[95]
~2.2 - 2.4	silicon rich oxide	Si-nanocluster	[101]
~2.2 - 3.0	a-SiOC	recombination of carriers between the energy bands and their tail states	[96]
blue emission	a-SiOC	$T_1 \rightarrow S_0$ of C-NOV*** ($_3O{\equiv}C{-}Si{\equiv}O_3$)	[96]
~2.7 - 2.8	silicon rich oxide	≡Si−Si≡ (NOV**)	[99]
	a-SiOC	$O_3{\equiv}C{-}Si{\equiv}O_3$ (C-NOV)	[96,102]

**NOV: Neutral oxygen vacancies
*NBOHC: Non-bridging oxygen hole center
$T_1 \rightarrow S_0$: triplet-to-singlet electronic transitions
***C-NOV: carbon-related neutral oxygen vacancies

CHAPTER 3. Experimental

3.1 Production of Thin Films

3.1.1 Sample preparation

Thin films were prepared by a radio frequency (RF) magnetron sputtering system. Three disks of 51 mm diameter were used as targets: high-purity SiC with nitrogen as the main impurity less than 10 ppm., Tb, and Yb with a purity of 3 N. A schematic representation of the target arrangement in the RF-magnetron sputtering system is shown in **Figure 3.1**. The target position in the vacuum chamber leads to a gradient concentration of C, O, Tb, and Yb elements. **Figure 3.2** shows the top view of the substrate holder (dotted square) and the position of the targets represented as circles (in green, red and blue). Sample thicknesses increase at substrate positions close to the SiC target. Tb and Yb concentrations also vary with position.

The targets were sputtered individual or in simultaneous, depending on the required sample. Substrates were cleaned in alcohol within an ultrasound system. Fused silica and single side polished crystalline (100) silicon wafers were used as substrates and cooled during the deposition process to keep them below 100 °C to ensure the amorphous state of the grown films. A pre-sputtering process of the targets for a time of 20 min was carried out. The deposition processes were conducted in a mixed atmosphere of hydrogen (5 N purity), argon (5 N purity), and oxygen. The residual oxygen inside the chamber was sufficient for use during the process. The base pressure, working pressure, and RF power are summaries in **Table 3.1**.

It is important to mention that hydrogen was included during the preparation based on two considerations. 1) Previously, an increase in bandgap due to hydrogen incorporation during the sputtering process was reported in *a*-SiC [105]. 2) Previously, a trend of C atom clustering in SiOC sensitive to the presence of hydrogen (H) was reported [106]. Without H, the C-C interaction is attractive, leading the C in SiOC to bind to each other and thus tend to segregate. With hydrogen, the C-C interaction is repulsive, and the carbon is evenly distributed throughout the lattice, leading to the enrichment of randomly distributed SiO_3C tetrahedral units.

Figure 3.1.Schematic representation of the RF-magnetron sputtering system

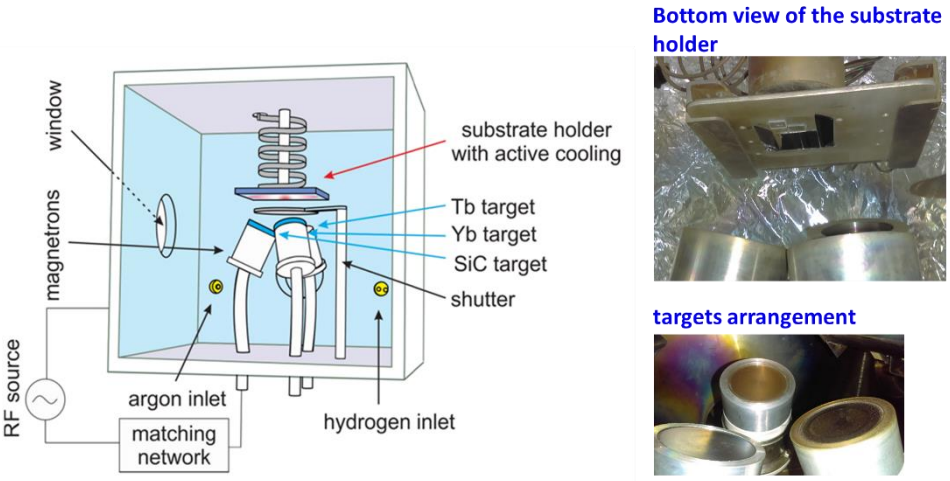

Figure 3.2. Schematic representation of Tb and Yb concentration as well as thickness gradient at the sample holder.

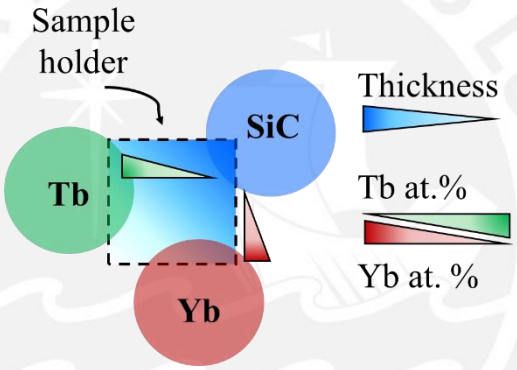

Table 3.1. Values of Ar and H_2 gas flow rate, base pressure, working pressure, and RF powers.

Material	Ar (sccm)	H_2 (sccm)	Basic pressure (mbar)	Working pressure (mbar)	RF power		
					SiC (W)	Tb (W)	Yb (W)
a-SiOC:H	50	5	2.9×10^{-6}	1.0×10^{-2}	120	-	-
	27	3	3.5×10^{-6}	1.0×10^{-2}	110	-	-
Tb-doped *a*-SiOC:H	50	5	3.9×10^{-6}	1.0×10^{-2}	140	10	-
Yb-doped *a*-SiOC:H	50	5	3.1×10^{-6}	1.0×10^{-2}	120	-	10
Tb-Yb doped *a*-SiOC:H	50	5	4.5×10^{-6}	1.0×10^{-2}	110	40	10
	27	3	2.4×10^{-6}	1.0×10^{-2}	130	30	7

3.1.2 Post-deposition annealing treatments

After thin films deposition, annealing treatments were carried out in a tube furnace whose schematic representation is presented in **Figure 3.3**. The furnace is set to the desired temperature. Subsequently the sample is introduced through a sliding quartz tube into the furnace. The temperature is recorded by a thermocouple placed directly in contact with the sample holder. The system allowed the desired temperature to be reached in ~2 minutes. The heating ramp rate from 500 to 900 °C annealing temperature are shown in **Figure 3.4**. The heating rate values are ~135, 146, 350, and 360 K/min for the achieved temperatures of 500, 600, 800 and 900 °C. After reaching the desired temperature, it is retained for 25 minutes to 4 hours as required. A constant flow of argon atmosphere with a purity of 5 N was used during the annealing treatments. In the cooling process, the sample is removed from the furnace, maintaining the argon flow until the system reaches room temperature.

Figure 3.3. Schematic representation of the tube furnace used for annealing treatments.

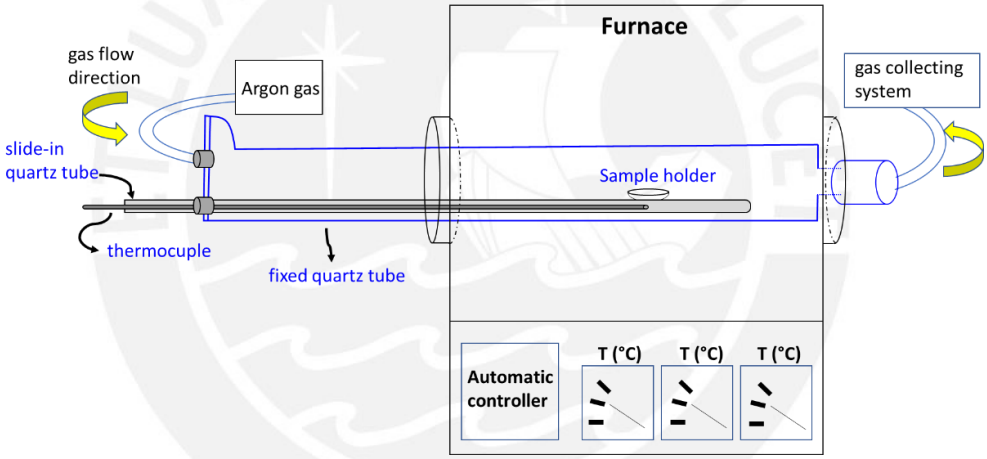

Figure 3.4. Heating ramp rate from 500 to 900 °C annealing temperature.

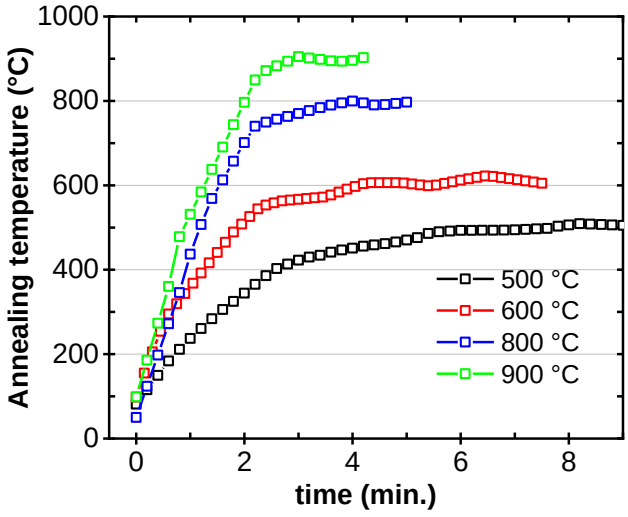

3.2 Characterization

Energy-dispersive X-ray spectroscopy

Samples elemental compositions were estimated using a scanning electron microscope (SEM) (JEOL JSM-7610F) implemented with a field emission gun worked at 5 kV accelerating voltage to attain a low enough electron penetration depth into the sample to suppress the contribution of the silicon substrate.

Fourier transform infrared spectroscopy

Bonding-related vibrational modes were determined by FT-IR spectroscopy in the range of 400 – 4000 cm^{-1} using a Bruker Tensor 27 FTIR spectrometer under normal incidence angle.

UV-Vis spectroscopy

The transmittance spectra of thin films were measured by a PerkinElmer Lambda 950 double-beam spectrometer with a photomultiplier and PbS detector in the wavelength range of 190 to 2000 nm.

Steady-state photoluminescence

Photoluminescence (PL) spectra were measured with a Renishaw inVia Reflex spectrometer system (1200 lines mm^{-1}) for Raman and PL spectroscopy with a silicon CCD. A He-Cd laser was used as an excitation source at 325 nm wavelength.

A second setup to obtain the PL emission spectra were used with a spectrometer (300 lines mm^{-1}) with an InGaAs detector and liquid-nitrogen cooled in the 800 – 1200 nm range. The same setup with a Si CCD-based detector was also used for the visible range emission. The samples were excited by an argon laser at 488 nm wavelength (power density 9.6 mW/cm^2) and laser diode 375 nm wavelength (power density 381.9 mW/cm^2). A calibrated Xenon light source L7810-02 (Hamamatsu Photonics K.K., Japan) was used to calibrate the spectra in the 400 – 700 nm range. An average of ten spectra was taken for each measure to improve the signal-to-noise ratio.

Photoluminescence excitation and time resolved Photoluminescence spectroscopy

Photoluminescence excitation (PLE) spectra were taken with a fluorescence lifetime spectrometer (FluoTime 300, PicoQuant GmbH) with a photomultiplier detector (PMA 192) in a single-photon-counting mode, using a Xe continuous wave lamp as excitation source with a spectral resolution of 8 nm.

PL decay curves were performed by the same spectrometer, using a Xe flash lamp as an excitation source at 375 nm excitation wavelength, as well as using a picosecond diode laser PDL 820 at 402.2 nm as excitation source.

A second setup with a double monochromator (detection spectrometer 600 lines mm^{-1}) was used for PLE spectra with a NIR photomultiplier detector (Hamamatsu).

3.3 Sample composition

EDX spectroscopy was used to estimate the compositions of the *a*-SiOC:H samples. A minimum accelerating voltage of 5 kV was used. This low accelerating voltage was used to avoid the strong contribution of the silicon substrate in the composition of the samples. The characteristic K_α X-ray (lowest energy) for the Si, O, and C atoms correspond to 1.739 keV, 0.525 keV, 0.277 keV, respectively. Therefore, the minimum accelerating voltage of 5 kV should be enough to detect the characteristic X-ray for each element. After the measurement, the atomic compositions of the samples grown on Si substrate were calibrated following the procedure in **section 3.3.2**.

3.3.1 Penetration depth simulation

The estimation of the electron beam penetration depth will be relevant for the analysis of the contribution of the silicon substrate to the atomic composition of the sample. For this reason, the simulation was performed for two arrangements. The first one considers only the substrate and the *a*-SiOC:H layer (100 nm thickness and 2.32 g/cm^3 density). **Figure 3.5 (a)** shows the simulation of the penetration depth. Accordingly, the excitation volume will also consider the Si coming from the substrate which will affect the composition values of samples. Therefore, the total composition will have an increase in Si concentration. The second system considers an aluminum layer (200 nm thick) between the *a*-SiOC:H sample and the Si substrate. According to **Figure 3.5 (b)**, the aluminum layer allows reliable measurements of the atomic compositions of Si, O and C because it does not consider the signal coming from the Si substrate. The simulations were performed by the CASINO program with 20000 number of electrons to simulate, 200 nm beam radius, and 5kV acceleration voltage. It is based on a Monte Carlo simulation of the electron trajectory of solid materials in a scanning electron microscope [107].

Figure 3.5 (a) Penetration depth simulation for a system of *a*-SiOC:H layer on Si substrate. **(b)** Penetration depth simulation for a system of *a*-SiOC:H layer and an aluminum layer (200 nm thickness) on Si substrate. The trajectories of the backscattered electrons are in red; those of the absorbed electrons are in blue.

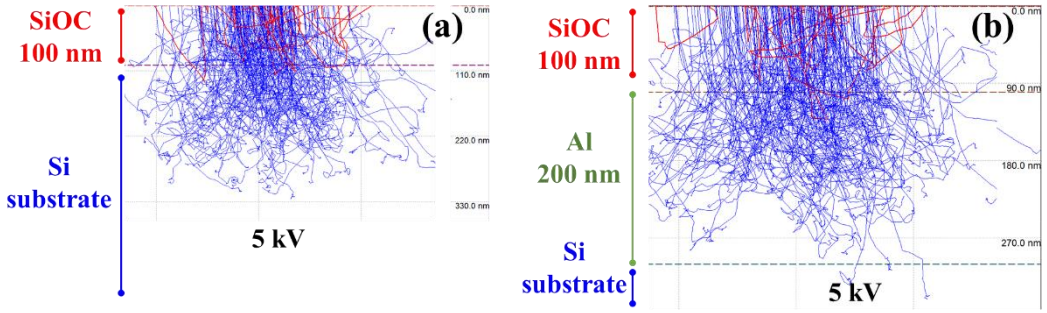

3.3.2 Calibration experiment

In this experiment, two types of substrates are used for sample deposition. The first one is Si substrates and the second one is Al substrates on Si. Both substrates were arranged as shown in **Figure 3.6** for the deposition of Tb-doped *a*-SiOC:H samples. The Si substrates (~1 cm^2) and the aluminum on top of the Si substrates are placed in the sample holder. The thickness of the sample will be changed with the position in the sample holder. Therefore, samples close to the SiC target will have a higher thickness compared to samples further away from the target. Ten points named from 1 to 10 were considered (**Figure 3.6**). EDX measurements were taken for films grown on Si substrates and on aluminum (200 nm thickness) on Si (Al/Si). Sample thickness were estimated by spectral reflectance measures from 200 to 1100 nm with the incident light normal (perpendicular) to the sample surface. The reflectance spectra were measured by a Filmetrics F20 film thickness measurement system. The thickness and normalized atomic composition (in at.%) without considering aluminum are shown in **Table 3.2**. The Si composition of samples grown on Si substrates is higher compared to samples grown on Al/Si, this is due to the contribution of Si from the substrate. For the cases of the C and O compositions, increasing the amount of Si will decrease the amount of C and O. This is because the total sum must reach 100%.

Table 3.2. Thickness and normalized atomic composition (in at.%) without considering aluminum.

Point number	Subst.	Thickness (nm)	Si (at.%)	C (at.%)	O (at.%)
1	Si	80	53.7	11.4	34.9
	Al/Si		29.8	15.3	54.9
2	Si	132	46.6	13.2	40.3
	Al/Si		28.8	15.5	55.7
3	Si	89	47.6	13.2	39.1
	Al/Si		28.3	17.5	54.1
4	Si	77	53.7	11.8	34.5
	Al/Si		30.4	16.9	52.7
5	Si	233	36.0	14.6	49.4
	Al/Si		28.1	16.4	55.4
6	Si	237	33.6	19.8	46.6
	Al/Si		28.5	20.6	50.9
7	Si	231	37.7	16.5	45.9
	Al/Si		28.8	17.0	54.1
8	Si	193	38.8	17.2	44.0
	Al/Si		28.6	18.6	52.8
9	Si	651	35.3	46.4	18.3
	Al/Si		34.2	48.0	17.8
10	Si	528	34.1	42.8	23.1
	Al/Si		33.4	41.3	25.2

Figure 3.6. Two types of substrates are used for sample deposition. The first one is Si substrates and the second one is Al substrates on Si.

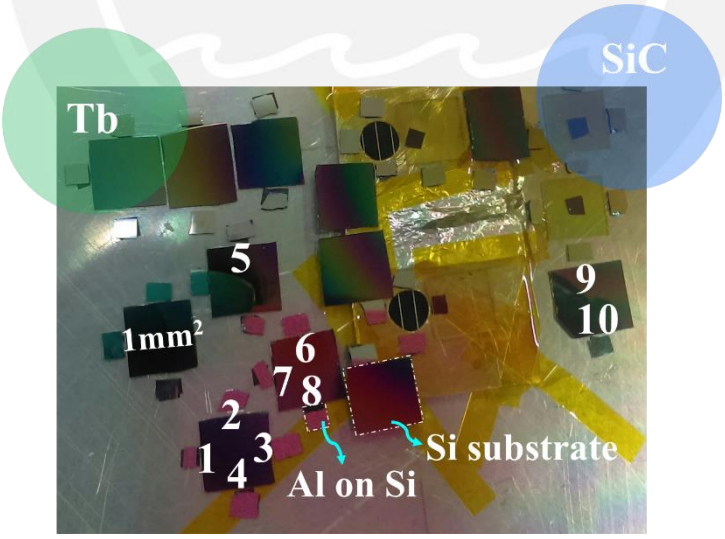

Experimental atomic composition calibration

The atomic composition correction fraction (Δ) due to the contribution of the Si substrate can be expressed as in **equation 3.1**. Where, the atomic compositions of Si, C, and O for samples grown on Si and Al/Si substrates are compared to each other.

$$\Delta_{Si} = \frac{Si_{on\ Al}(at.\%) - Si_{on\ Si}(at.\%)}{Si_{on\ Si}(at.\%)}$$
$$\Delta_{C} = \frac{C_{on\ Al}(at.\%) - C_{on\ Si}(at.\%)}{C_{on\ Si}(at.\%)} \quad \textbf{(3.1)}$$
$$\Delta_{O} = \frac{O_{on\ Al}(at.\%) - O_{on\ Si}(at.\%)}{O_{on\ Si}(at.\%)}$$

Where,

$Si_{on\ Si}$, $C_{on\ Si}$, and $O_{on\ Si}$ represent the measured atomic percentages (Si, C, and O) of samples on Si substrate. And $Si_{on\ Al}$, $C_{on\ Al}$, and $O_{on\ Al}$ represent the measured atomic percentages (Si, C, and O) of samples on Al/Si substrate.

The corrected or actual compositions of Si, C, and O in a sample can be expressed as in **equation 3.2**.

$$Si(at.\%) = Si_{on\ Si}(at.\%) + \Delta_{Si} * Si_{on\ Si}(at.\%)$$
$$C(at.\%) = C_{on\ Si}(at.\%) + \Delta_{C} * C_{on\ Si}(at.\%) \quad \textbf{(3.2)}$$
$$O(at.\%) = O_{on\ Si}(at.\%) + \Delta_{O} * O_{on\ Si}(at.\%)$$

On the other hand, the correction fractions for Si, C, and O as a function of thickness are shown in **Figure 3.7**. From the experimental data, a linear dependence is observed. Thus, we can introduce an empirical formula to describe Δ with respect to the thickness, as in **equation 3.3**. Following the linear fit in **Figure 3.7**, the m and b values are summarized in **Table 3.3**.

$$\Delta_{Si}(thickness) = m_1 * thickness + b_1$$
$$\Delta_{C}(thickness) = m_2 * thickness + b_2 \quad \textbf{(3.3)}$$
$$\Delta_{O}(thickness) = m_3 * thickness + b_3$$

Table 3.3. m and b values obtained from the linear fit in **Figure 3.7**.

Element	m ($x10^{-3}$)	Δm ($x10^{-4}$)	b	Δb
Si	1.5	1.4	-0.56	0.02
C	-2.0	2.9	0.51	0.05
O	-2.5	2.9	0.70	0.05

Figure 3.7.Correction fraction for Si, C, and O as a function of thickness.

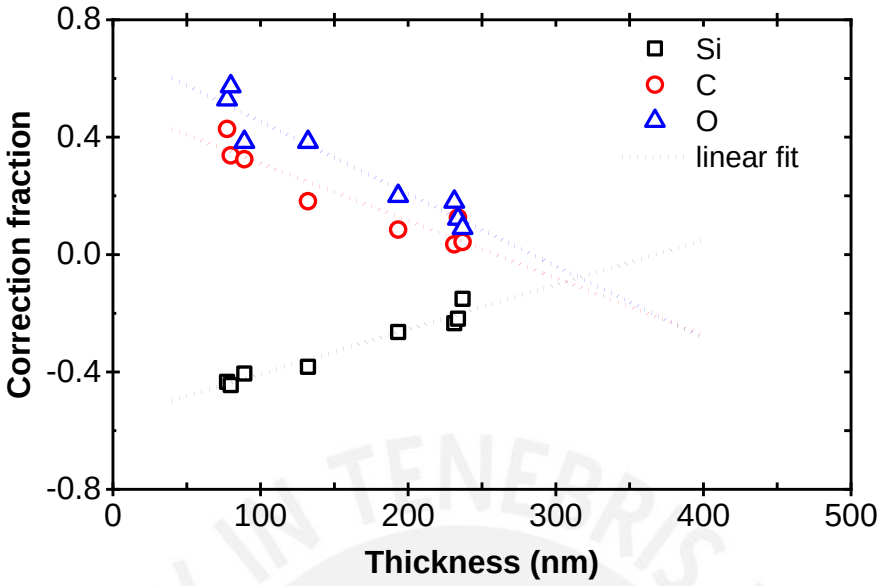

The corrected composition of Si, C, and O can be obtained by replacing **equation 3.3** in **equation 3.2**, resulting in **equation 3.4**.

$$\begin{aligned} \text{Si (at.\%)} &= \text{Si}_{\text{on Si}} + (m_1 * \text{thickness} + b_1) * \text{Si}_{\text{on Si}} \\ \text{C (at.\%)} &= \text{C}_{\text{on Si}} + (m_2 * \text{thickness} + b_2) * \text{C}_{\text{on Si}} \\ \text{O (at.\%)} &= \text{O}_{\text{on Si}} + (m_3 * \text{thickness} + b_3) * \text{O}_{\text{on Si}} \end{aligned} \qquad \textbf{(3.4)}$$

CHAPTER 4. Results and Discussion: Amorphous Hydrogenated Silicon Oxycarbide

This chapter studies the optical properties of amorphous hydrogenated silicon oxycarbide (*a*-SiOC:H) films grown by RF-magnetron sputtering. The chapter is divided into four sections. The first presents the results obtained from the composition and structure analysis. The second aims to discuss the results obtained from the bandgap and Urbach energy. The third aims to examine the annealing effect on the structural properties. The last one discusses the results obtained from host luminescence.

The composition and structure of *a*-SiOC:H samples was studied through the analysis of energy-dispersive X-ray (EDX), Fourier transform infrared (FT-IR), and Raman spectroscopy. The bandgap (E_{gap}) and the Urbach energy (E_{Urbach}) were obtained by the analysis of the Uv-Visible and NIR absorption Spectroscopy. The characteristic spectrum of the host luminescence was studied and compared with those found in the literature. The effect of thermal annealing and carbon composition on the host emission is also discussed.

4.1 Composition and Structure Analysis

The study of *a*-SiOC:H thin films starts with the analyzes of the sample composition through EDX measurements. The structure of the network can be understood based on the study of Si−O and Si−C bonds. The formation of structural defects was related to Si−H, C−H, C−C, C=C, and OH groups. For this purpose, FT-IR and Raman spectroscopy measurements were carried out.

4.1.1 Elemental composition

The elemental atomic concentrations for *a*-SiOC:H films were calculated following the sample composition calibration method featured in **Chapter 3**. The results are summarized in **Table 4.1**. An increase in oxygen is observed due to a decrease in carbon composition, suggesting the addition of carbon to the matrix structure. The O/C ratio falls within the range from 0.5 to 1.7, except by one with around nine. The low carbon concentration is due to the fact that this sample is the farthest from the SiC target and therefore its composition is closer to SiO_2 as can be seen in **Table 4.1**.

The O/C ratio is comparing with those found in the literature (three last rows in **Table 4.1**). Thus, sample compositions can be classified as the Si-C-O type because of the high O composition from 22.0 to 40.5 at.%. In the case of the sample with a carbon concentration of ~6 at.%, the classification can be assigned to the SiO_2-like. It is worth mentioning that even though the O/C ratio can be used for matrix classification, the carbon percentages are higher, and the oxygen percentages are lower than reported for the Si-C-O type in the literature. Therefore, the carbon excess in the sample would not necessarily be bound to the *a*-SiOC:H matrix. The sample on the silica substrate was used for transmittance measurements in the bandgap calculation.

Table 4.1. Elemental composition of *a*-SiOC:H samples (at as-grown).

Si at.%	**O at.%**	**C at.%**	**O/C**	**Stoichiometry SiO_xC_y**	**Substrate**	**Thickness nm**
34.3	22.0	43.7	0.50	$SiO_{0.64}C_{1.27}$	Si	542
34.5	22.1	43.4	0.51	$SiO_{0.64}C_{1.26}$	Si	575
33.3	24.1	42.6	0.57	$SiO_{0.72}C_{1.28}$	Si	432
33.2	26.1	40.7	0.64	$SiO_{0.79}C_{1.23}$	Si	426
32.8	27.7	39.5	0.70	$SiO_{0.84}C_{1.20}$	Si	371
32.6	27.9	39.5	0.71	$SiO_{0.86}C_{1.21}$	Si	383
32.4	29.4	38.2	0.77	$SiO_{0.91}C_{1.18}$	Si	339
32.2	31.2	36.6	0.85	$SiO_{0.97}C_{1.14}$	Si	302
28.5	35.6	35.9	0.99	$SiO_{1.25}C_{1.26}$	Si	283
30.3	40.1	29.6	1.35	$SiO_{1.32}C_{0.98}$	silica	440
38.4	38.2	23.4	1.63	$SiO_{0.99}C_{0.61}$	Si	94
35.1	40.5	24.4	1.66	$SiO_{1.15}C_{0.70}$	Si	94
34.6	59.1	6.3	9.38	$SiO_{1.71}C_{0.18}$	Si	100
42.37	2.97	45.76	0.0065	SiC-like	[108]	
34.25	41.09	17.12	2.4	Si-C-O		
31.85	54.14	6.37	8.5	SiO_2-like		

To elucidate the variation in stoichiometry, we will make the representation of the elements in a ternary diagram of compositions. **Figure 4.1** shows the ternary diagram. It visualizes the compositional variations of the samples. The stoichiometry of samples falls within the C-SiO_2-SiC triangle (green shaded area). The SiC-SiO_2 line with the chemical formula of $SiO_{2(1-m)}C_m$ is assigned to the stoichiometric glass silicon oxycarbide without free carbon (red line). Whereas the $SiO_{2(1-m)}C_m + nC_{free}$ is ascribed to an excess of carbon and would result in carbon segregation (blue line), m+n is the total amount of carbon in the system. According to results, the Si composition remains at ~33 at.%. Therefore, we can understand a structure in which a carbon atom replaces two oxygen atoms. In this way, the carbon would be incorporated into the matrix. Also, the samples contain an excess of carbon

and an approximately constant amount of silicon. The next step is to verify the chemical structure. According to the literature, the SiOC structure would be based on SiO_2 network. Therefore, FT-IR measurements will allow us to verify it.

Figure 4.1. Si-C-O ternary diagram. The red line shows the composition of stoichiometric silicon oxycarbide. The blue line shows silicon composition at 33 at.%.

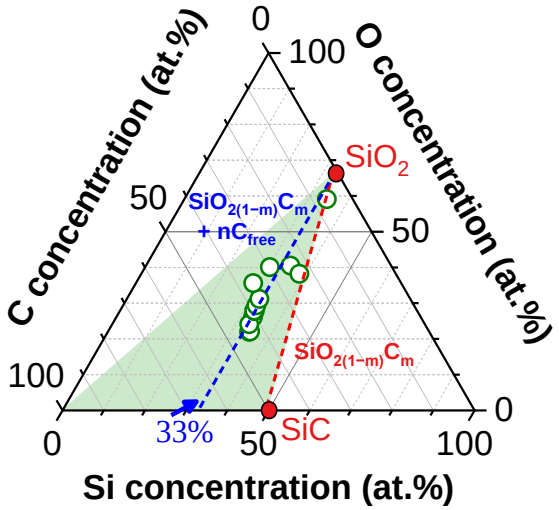

4.1.2 Bonding Formation

The *a*-SiOC:H network is studied based on similarities with sub-stoichiometric silicon oxide (SiO_x, $x < 2$) as well as amorphous silicon carbide (*a*-SiC) network. IR bands, which correspond to the vibration modes of Si−O and Si−C bonds, are compared with those of their amorphous counterparts. The dangling bonds will arise from the break of Si−H, C−H, and the hydroxyl group. The existence of C-related defects will also be studied, i.e., C−C and C=C will be an indication of carbon precipitates.

The IR absorption spectra of four *a*-SiOC:H samples with a carbon composition from ~6 to 40 at.% are shown in **Figure 4.2 (a)** and **(b)**. The following vibration modes were identified:

- The absorption band at 450 cm^{-1} is ascribed to the Si−O−Si rocking mode. The band at ~1000 cm^{-1} and the shoulder at ~1150 cm^{-1} are ascribed to the Si-O-Si stretching mode [109,110]. According to the literature, the last two bands are strongly depending on the sample composition in SiO_x samples. In our case, the shoulder at ~1150 cm^{-1} appears for larger x values ($x > 1.2$) and becomes more pronounced when oxygen contents increase as agrees with the behavior reported by N. Tomozeiu [109]. Another study also attributed the peak at ~1160 cm^{-1} to the Si–O–C related vibrational mode [111].

- The Si−C related vibrational mode is reported to be on broadband centered at ~780 cm^{-1} in *a*-SiC films [112–114]. Due to the band position of the Si−C and the Si−O related vibrational modes, both centered at ~800 cm^{-1}, it will be considered a second characteristic for the study. According to the literature, SiO_x samples show a ratio of intensities of the Si−O bands at 800 and 1080 cm^{-1} that corresponds to approximately 1/17 [109,115]. In *a*-SiOC:H samples, in the band at 800 cm^{-1}, in addition to those of Si−O, this band can also be ascribed to the contribution of the Si−C vibration modes because the ratio of intensities is higher than 1/17. The IR bands corresponding to the vibrational modes taken from the literature for SiO_x and *a*-SiC:H films are summarized in **Table 4.2**. It was used as a reference for our samples.

Table 4.2. IR band centers corresponding to the vibration modes of Si−C and Si−O bonds in SiO_x and *a*-SiC:H.

Vibration type	**SiO_x (cm^{-1})**	***a*-SiC:H (cm^{-1})**
Si-C stretching		~780
Si-O-Si rocking	~450-458	
Si-O-Si bending	~780-812	
Si-$(CH_2)_n$		~1000-1100
Si-O-Si stretching on phase	~1080	
Si-O-Si stretching out of phase	~1150-1177	
Si-H	~2000-2300	~2000-2140
C-H_n		~2860-3000
References	[109,110,116]	[112,113,117]

- The band at ~2140 cm^{-1} is associated with the Si–H vibrational mode, as reported in amorphous silicon carbide [112,117] and amorphous SiO_x:H ($x < 2$) [116]. The Si−H absorption band is not observed for the O/C ratio higher than one (**Figure 4.2 (b)**). The Si−H related band is depleted by oxygen incorporation in agreement with the reported by F. Stolze et al. [118]. Nevertheless, that effect could also be related to the low thickness of both samples ~100 nm (**Table 4.1**), where the Si−H bond signal is small to be detected by the IR detector.
- The band in the 3000 - 3700 cm^{-1} range is associated with the hydroxyl groups in the amorphous silica network. It is ascribed to covalent bonds as in the case of isolated silanol (iSiO−H, 3650 cm^{-1}), neighboring associated silanols (hydrogen-bonded) (nSiO−H, 3450 cm^{-1}), and HO−H (3250 cm^{-1}) in the case of trapped molecular water [119].

Figure 4.2. IR absorption spectra of *a*-SiOC:H thin films grown on c-Si(100), (a) from 400 to 1300 cm^{-1}, and (b) from 1900 to 4000 cm^{-1}.

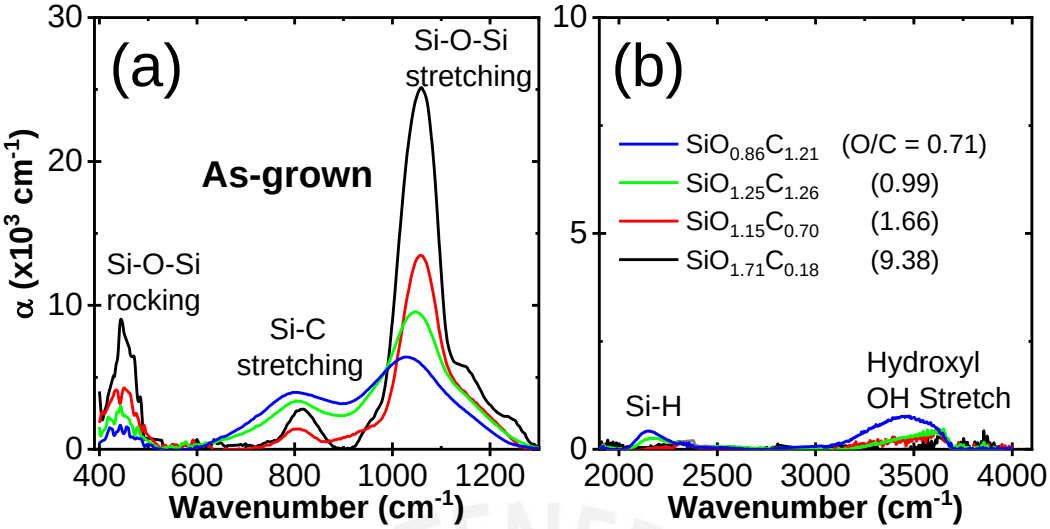

- No bands related to the $C(sp^2)=C(sp^2)$ and $C(sp^3)-C(sp^3)$ bonds were observed at 1608 cm^{-1} and 1100 cm^{-1}, respectively [120]. However, these bonds are weakly active in IR absorption. Therefore, Raman measurements were also attempted. According to **Figure 4.3,** no signal associated with carbon structures was observed for the as-grown samples. The broad background observed in the spectrum corresponds to the photoluminescence of the matrix due to the laser excitation wavelength.

Figure 4.3. Recorded Raman scattering spectra for as-grown samples, an excitation wavelength of 532 nm was used for excitation.

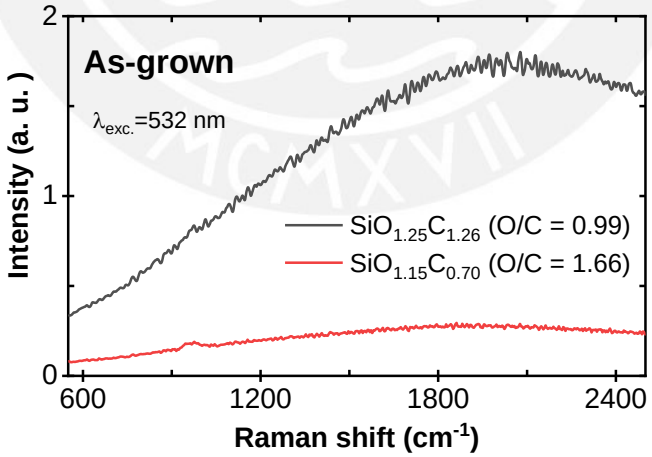

Effect of oxygen to carbon ratio in the host structure

The study of the atomic arrangement was studied by IR spectra. As was mention above, the band at ~1000 cm^{-1} and the shoulder at ~1150 cm^{-1} are identified with the Si−O−Si stretching mode. **Figure 4.4** shows the center bands associated with Si−O

vibration modes (the main peak and the shoulder, both in black), and the Si−C center peak (in red), both as a function of the O/(C+Si) ratio. As the O/(C+Si) ratio increases, the center band at ~800 cm^{-1} shifting from the Si−C related bond position in SiC to Si−O related band position in SiO_2 stoichiometric. Thus, the increase of the O/(C+Si) ratio leads to an *a*-SiOC:H network mainly dominated by a silica structure, which depends on the sample composition.

Figure 4.4. Center band associated with the Si−O and Si−C vibration modes in the IR spectrum for *a*-SiOC:H thin film grown on c-Si (100).

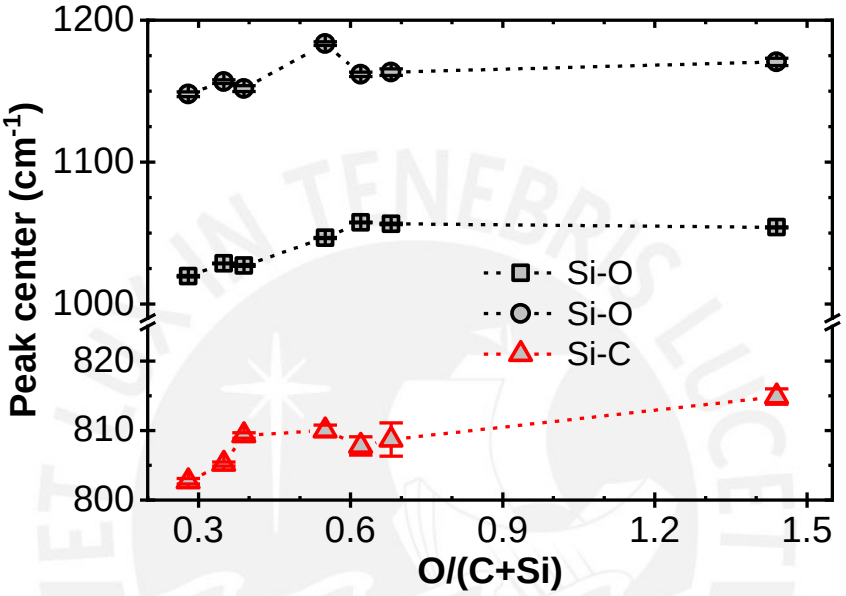

Summarizing the results, the elemental composition analysis revealed samples with a silicon composition of 33 at.%, which is close to the ideal in SiO_2. The carbon added to the lattice could replace the oxygen atoms. However, a slight excess of carbon would lead to carbon atoms not necessarily bound to the amorphous network. Carbon segregation is not observed in Raman spectra, so a small amount of these structures is inferred in the as-grown state. The formation of Si−O, Si−C, Si−H bonds, and OH groups were verified in the FT-IR spectra. No signal associated with carbon structures was observed for the as-grown samples in Raman measurements. Finally, the oxygen content in samples leads to an atomic organization mainly dominated by the silica structure.

4.2 Bandgap and Urbach Energy

It is known that amorphous materials show a lack of atomic periodicity in long-range order when compared with their crystalline counterpart. However, their structures coincide at short range. It is convenient for our study to mention the case of amorphous silica, with the same structure as alpha-crystalline quartz in a short-range order [121]. The lack of periodicity of the lattice gives rise to the existence of disorder due to deviations in the bond lengths and bond angles, broadening the edges of the conduction and valence bands, forming the band tails [122]. In the band tails, the electronic states have a localized character, i.e., the wave functions of neighboring quantum states do not extend far enough (or at all) to give significant overlap (or no overlap), and their nature changes from localized to delocalized at a critical boundary called the mobility edge [122]. Thus, in an amorphous semiconductor, the distributions of conduction and valence band electronic states do not end abruptly at the band edges [123]. Instead, the disorder results in the existence of band tails, which are formed by localized states penetrating the bandgap region. The density of electronic states in the tails decreases exponentially and continuously with the energy [124,125] and the width of band tails reflects the disorder in the material [126].

Also, the concept of defects is redefined in amorphous materials. The defects in amorphous semiconductors are considered to be all cases of departure from the regular nearest-neighbor coordination (or normal valence requirement) [123]. For example, dangling bonds such as in the case of amorphous silicon, where the non-bonding silicon orbitals (sp^3 hybrid orbitals) are not split by the bonding [125], leading to neutral dangling bonds, which introduce localized states near the middle of the bandgap region, acting as a deep trap for electrons and holes [112]. Neutral or charged dangling bonds, as well as voids, pores, cracks, and other macroscopic defects, are considered defects [123]. Thus, the noteworthy features of the electronic structure of an amorphous semiconductor are (1) the absence of sharp band edges and tails penetrating the bandgap and (2) the existence of broad bands corresponding to defect levels in the bandgap region in contrast to sharp discrete levels in crystals.

The optical transitions between the valence and conduction band are responsible for the main absorption and are the main measure of the bandgap energy (E_{gap}). However, the existence of tail states in amorphous solids leads to some considerations in the band-to-band optical absorption. The corresponding optical absorption coefficients due to electronic transitions for amorphous solids were considered in different energy ranges (**Figure 4.5**).

Near the absorption edge, it will be divided in [18]: 1) Transitions in which electrons are excited from the valence to conduction band extended states, referring to extended-extended transitions (region A in **Figure 4.5**). 2) Transitions involving the tail states, region B in **Figure 4.5**. The exponential tails, also referred as Urbach tails, follow an exponential increase with the incident photon energy [127]. 3) Finally, the transitions among the defect states, region C in **Figure 4.5**.

Figure 4.5. Schematic representations of the absorption coefficient for an amorphous semiconductor.

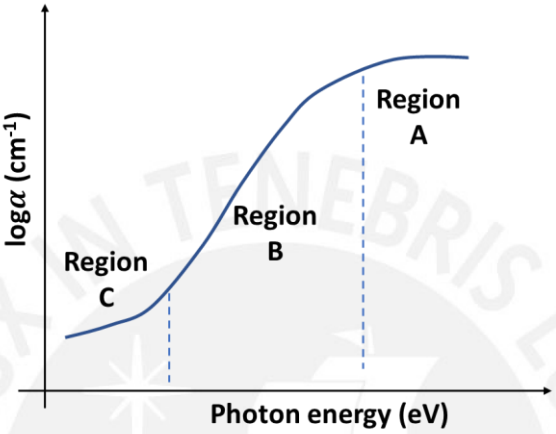

4.2.1 Determination of the absorption coefficient of *a*-SiOC:H samples

The study of the optical parameters was calculated by the transmittance spectrum. The amount of light that gets transmitted through an array, thin-film and substrate, depends on the amount of reflection and absorption that takes place along the light path. If the material is a thin film with a moderate absorption coefficient, there will be multiple reflections and interferences at the transmitted side of the sample [123]. In this case, some interference fringes can be observed in the transmittance spectra. **Figure 4.6** shows the transmittance spectra of an *a*-SiOC:H thin film. To retrieve the fundamental absorption and the optical bandgap energy, the analysis of the transmittance spectrum was done.

One of the methods to determine the optical parameters is the Swanepoel method [128]. This method allows obtaining the refractive index (n) and absorption coefficient (α) through the analysis of a single measurement of the transmittance spectrum for a thin film on a transparent substrate. However, an important condition for this method is a considerable number of interference fringes in the transmittance spectrum [129]. The method used in this work introduces improvements to the Swanepoel method and does not depend critically on the number of interference fringes. The method is based on the envelope

method and requires a simple dispersion model for the real part of the refractive index with few fitting parameters, while the absorption coefficient can be determined without the aid of a dispersion model, more details of the method can be found in A. Tejada et al. [130].

Figure 4.6. Transmittance spectra of an *a*-SiOC:H thin film grown on a silica substrate, from as-grown to 800 °C annealing, in argon atmosphere. The layer thickness is around 440 nm.

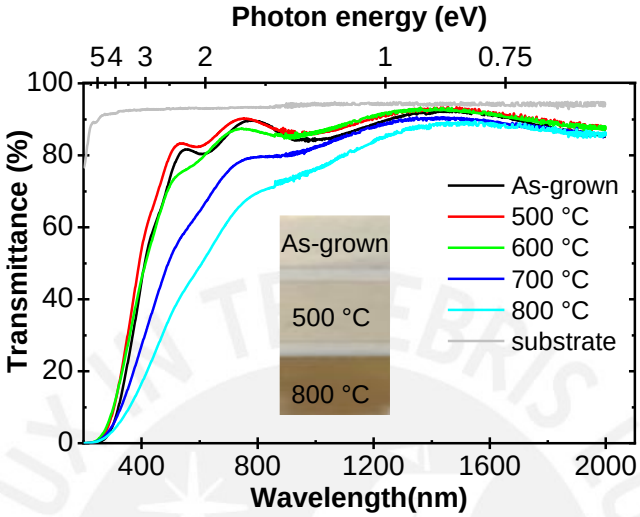

Figure 4.7 shows the refractive index of the *a*-SiOC:H film ($n_{a-SiOC:H}$), α-SiC film ($n_{\alpha-SiC}$), and *a*-SiO_2 film (n_{a-SiO_2}). It was calculated by the Cauchy dispersion model, $n(\lambda) = A_0 + {A_1}/{\lambda^2}$, A_0 and A_1 were taken from the envelope method described in [130]. Results show a refractive index closer to amorphous silica than to silicon carbide. Comparing with previous works n = ~1.8 (C = 17.12 at.%) and n= ~1.5 (C = 6.37 at.%) [108], the reported $n_{a-SiOC:H}$ are in the usual range.

Figure 4.7. Refractive index of *a*-SiOC:H thin film, from as-grown to 800 °C post-deposition annealing, in argon atmosphere. The refractive index of α-SiC* [131] and the refractive index of *a*-SiO2** [132] are also considered.

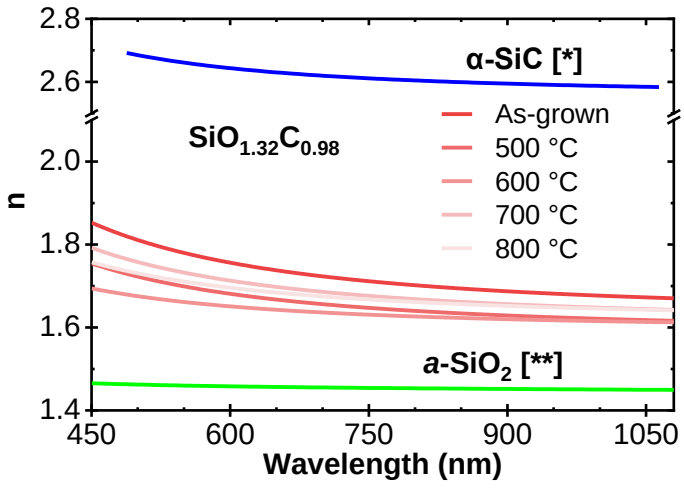

Figure 4.8 (a) shows the optical absorption coefficient (α) of an *a*-SiOC:H sample for different annealing temperatures. The fundamental absorption near the absorption edge was studied by two regions. The first region, corresponding to the strong absorption in the order of ~10^5 cm^{-1}, is studied for the optical bandgap energy (E_{gap}) calculation. The second region in the sub-bandgap region corresponds to the weak absorption (below ~10^4 cm^{-1}) and is studied to the Urbach parameter (E_{Urbach}) calculation, which is related to the structural and thermal disorder in the material [133].

Figure 4.8 (b) shows the optical absorption coefficient in a logarithmic scale of *a*-Si:H [134], *a*-SiO_x:H (O =52 at.%) [134], and *a*-SiOC:H (O = 40.1 at.%) samples (this work). Comparison with the *a*-Si:H case makes it possible to observe the three different absorption regions in amorphous semiconductors. Region (I) corresponds to the band-to-band absorption. Region (II) corresponds to absorption involving the tail states of the bands. Region (III) corresponds to the absorption of defects corresponding to dangling bonds in the middle of the bandgap. However, these three regions are difficult to identify with increasing oxygen concentration. **Figure 4.8 (b)** clearly shows how increasing oxygen concentration increases the bandgap that because of the gradual replacement of Si−Si by Si−O bonds. Furthermore, with increasing oxygen, the region (II) widens, i.e., oxygen increases the disorder in the matrix. Region (III) also becomes difficult to identify and shows a blue shift. Finally, a larger increase in absorption is observed in the band tails region and the defects region for samples containing carbon in their composition (*a*-SiOC:H).

Figure 4.8. **(a)** Absorption coefficient in a logarithmic scale of *a*-SiOC:H thin film grown on a silica substrate, from as-grown to 800 °C post-deposition annealing in argon atmosphere. **(b)** Absorption coefficient in a logarithmic scale of *a*-Si:H [134], *a*-SiO_x:H (O =52 at.%) [134], and *a*-SiOC:H (O = 40.1 at.%) samples. The spectral regions of ban-to-band (I), band-tail (II), and defect absorption (III) are indicated for the *a*-Si:H case.

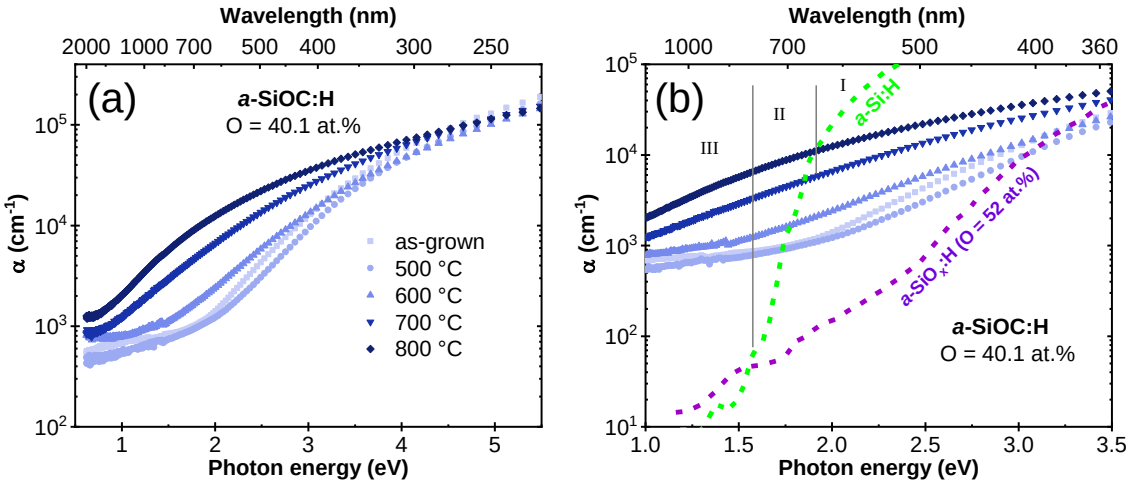

4.2.2 Determination of the bandgap and Urbach energy

In amorphous materials, the existence of tail states leads to ambiguities in the E_{gap} calculation. Therefore, different models for the fundamental absorption have been studied, all of them allowing to achieve representative E_{gap} values. Nevertheless, the obtained values by the different models are not expected to be exactly the same values; however, for the purposes of characterizing the materials, the E_{gap} behavior such as its increase or decrease upon the annealing temperature should be similar. For the strong absorption region, i.e., above the mobility edge, Tauc et al. (1966) [135] described the extended states related transitions. The dependence of the absorption coefficient on photon energy can be described as in **equation 4.1** [125] (in indirect semiconductors and amorphous materials).

$$\sqrt{\alpha\hbar\omega} = B'[\hbar\omega - E_{Tauc}] \qquad (4.1)$$

Where

$\alpha(\hbar\omega)$: absorption coefficient as a function of the photon energy, B: independent factor from the energy photon, $\hbar\omega$: photon energy, and E_{Tauc}: Tauc optical bandgap.

The plot of $\sqrt{\alpha\hbar\omega}$ as a function of $\hbar\omega$ is called the Tauc-plot and is usually used for the estimation of the optical bandgap energy in amorphous materials. **Figure 4.9** shows the Tauc-Plot, the extrapolation of the linear region leads to the E_{Tauc}. The E_{gap} value can be determined by linear extrapolation to zero. It would be sensitive to the range in which the extrapolation is taken [136]. Therefore, an alternative empirical value is sought out for the bandgap determination. That value will be the iso-absorption energy E_{04}, which is defined as the value of the energy at which the absorption coefficient is equal to 10^4 cm^{-1} (**Figure 4.8 (a)**).

Figure 4.9.Tauc-plot for bandgap calculation. The dashed lines represent the extrapolation linear region.

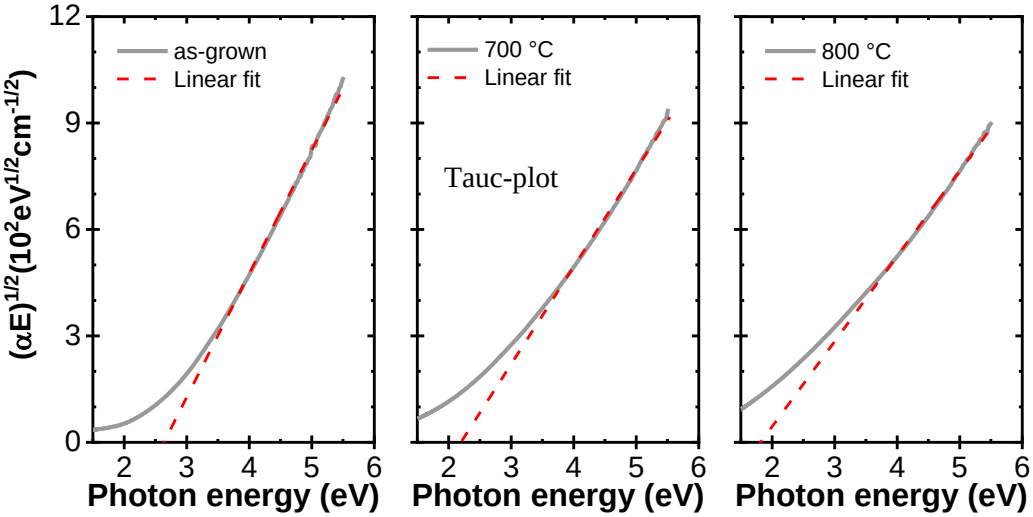

The sub-bandgap region, corresponding to the weak absorption, is typically found at $10^{-1} < \alpha < 10^{4}$ cm^{-1} [123]. It is studied to obtain the Urbach parameter E_{Urbach}, also called the Urbach width [123] or the Urbach energy [112]. E_{Urbach} is the width of the localized tail states and is generally attributed to disorder in the material [124]. The Urbach region is currently considered as caused by thermal effects as well as by static disorders (structural and compositional disorder) [126]. The Urbach tails as a function of the photon energy will follow **equation 4.2** [125].

$$\alpha(\hbar\omega) = \alpha_F \exp\left[\frac{\hbar\omega - E_F}{E_{Urbach}}\right] \qquad (4.2)$$

Where

α_F and E_F: material-dependent constants, $\hbar\omega$: photon energy, and E_{Urbach}: width of the exponential tail.

The plot of log (α) vs. $\hbar\omega$ is used for the estimation of Urbach energy. The E_{Urbach} is determined by a linear fit from the slope of the exponential absorption edge region as shown in **Figure 4.10**. It can be seen that the linear fit would be sensitive to the range in which the extrapolation is taken. Hence, the obtained E_{Urbach} value will be considered as an approximated value.

Figure 4.10. log (α) vs $\hbar\omega$ to obtain the Urbach energy. The dashed lines represent the linear fit region.

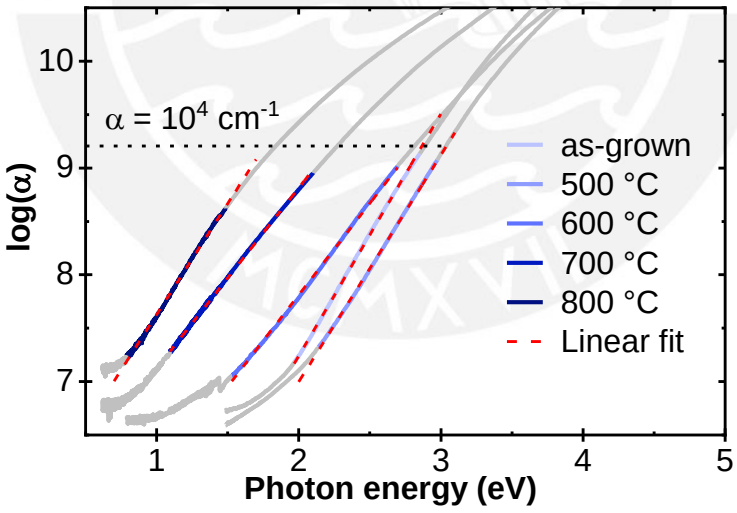

After the presentation of these two approaches (both in different photon energy ranges) to obtain the bandgap and the Urbach energy, the band fluctuation approach was also used. The band fluctuation model takes into consideration the whole absorption coefficient to retrieve the bandgap (E_{BF}), thus avoiding ambiguities related to the region chosen for the fitting, as is the case of the previous methods; more details can be founded in [105].

Figure 4.11 (a) shows the representative values for the *a*-SiOC:H bandgap, using the Tauc-plot model, band fluctuation (BF) model, and iso-absorption energy (E_{04}). The calculated optical bandgap (at as-grown) has a comparable bandgap value reported in *a*-SiC:H [105,122,137] as well as in SiOC [108]. The E_{gap} shows a relative constant value up to 500 °C. Afterward, a continuous decrease is observed with the increasing annealing temperature. **Figure 4.11 (b)** shows the representative values for E_{Urbach} and $1/\beta$. They were retrieved by the Urbach model and by the BF-model, respectively. The E_{Urbach} values are in the same order of magnitude reported for *a*-SiC:H [105,122,137] and in SiOC [138]. With increasing annealing temperature, an increase in E_{gap} would be expected. However, in the studied samples, the reduction of the E_{gap} and the increasing Urbach energy, after 500 °C, is observed. It is important to mention that the widening of the Urbach region above 500 °C overlaps with the bandgap region itself (mobility edges). So, reducing the E_{gap} is explained by the increase of disorder and not necessarily by a reduction per se (change in the mobility edge).

Figure 4.11. **(a)** Representative E_{gap} values, using the Tauc-plot model (E_{Tauc}), band fluctuation model (E_{BF}), and iso-absorption energy (E_{04}), from as-grown to 800 °C post-deposition annealing in argon atmosphere. **(b)** The Urbach energy values, using the Urbach model (E_{Urbach}) and the band fluctuation model ($1/\beta$).

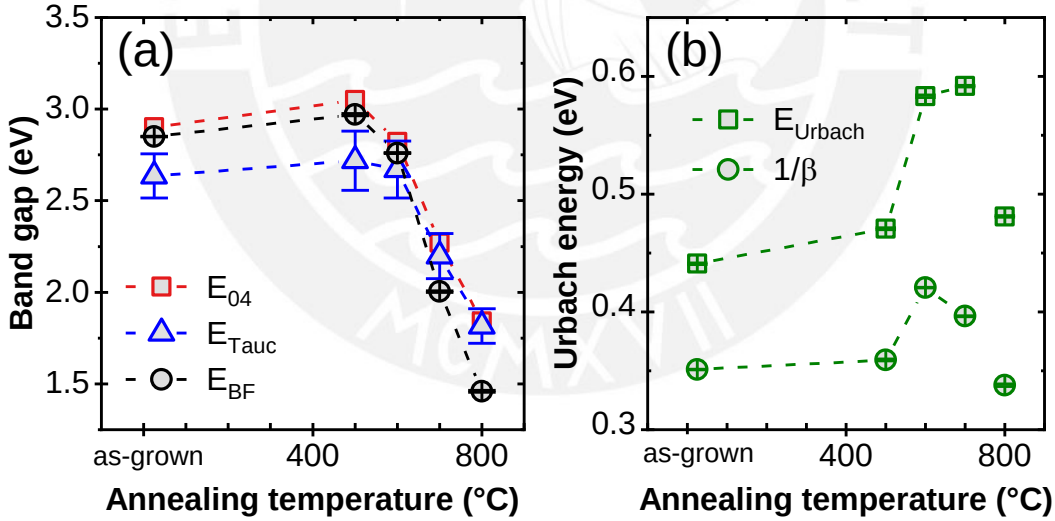

Summarizing the results, representative E_{gap} values were calculated using the Tauc-plot model (E_{Tauc}), band fluctuation model (E_{BF}), and iso-absorption energy (E_{04}), from as-grown to 800 °C post-deposition annealing in argon atmosphere. Also, the Urbach energy values were retrieved using the Urbach model (E_{Urbach}), and the band fluctuation model ($1/\beta$). The representative values remain relatively constant (~2.8 and 3.0 eV) up to 500 °C annealing temperature. Increasing the annealing temperature leads to the reduction of the

E_{gap} and the increasing Urbach energy. It is important to note that the absorption coefficient presented a significant increase in the range of 1 to 2 eV when the temperature increases from 600 to 800 °C. So, for temperatures above 600 °C, the increasing absorption allowed inferring an increase in the density of states in the bandgap. This increase in density of states corresponds to the creation of defects states in the gap or the widening of band tails.

4.3 Annealing effect on the structural properties

IR and Raman spectroscopy were conducted in samples with different carbon compositions and were analyzed in terms of their structural changes after thermal annealing. **Figure 4.12 (a)** and **(b)** show the IR absorption spectra of *a*-SiOC:H annealed samples. The samples have two different carbon compositions (C=35.9 and 43.7 at.%). The increasing annealing temperature increases the band intensity related to Si−O bonds in both cases. For the low carbon composition, the Si−C related band intensity remains approximately unchanged up to 500 °C, whereas an increase in the Si−C bonds (**Figure 4.12 (b)**) is observed for the high carbon composition. After 500 °C, the Si−H and C−H related bands are strongly depleted. Hence, the creation of silicon dangling bonds (SiDBs) can be inferred indirectly through the breaking of the Si−H bonds. The Si−H bonds depletion can be observed in **Figure 4.12 (a)** and **(b)**. Furthermore, according to Zhang et al. [137], in *a*-SiC:H, the hydrogen out-diffusion increases the structural disorder because the structural rearrangements increase the stress in the *a*-SiC:H sample. Thus, increasing the disorder could explain the increase in E_{Urbach} after 500 °C.

The Si and C dangling bonds, from the breaking Si−H and C−H bonds, could join to form new Si−C bonds in agreement with Choi et al. [117], so the increase in absorption intensity corresponding to Si-C bonds would be consistent. Nevertheless, it does not exclude that the carbon atoms could join to other carbons to form $C(sp^2)=C(sp^2)$ and $C(sp^3)-C(sp^3)$. The formation of new Si−O and $C(sp^2)=O$ bonds can also be observed in both IR spectra. To study carbon bonds evolution in detail, Raman spectroscopy was performed. **Figure 4.13** shows the Raman spectra recorded for an *a*-SiOC:H thin film from as-grown to 800 °C (post-deposition annealing) in an argon atmosphere. The D and G- bands were identified as fingerprints of a graphitic phase of carbon [139,140]. Therefore, carbon structures formed ~700 °C annealing temperature would contribute to the formation of defect states.

It is important to remember that the region called the Urbach region is usually understanding as the region involving states in the band tails (defects and disorder). Nevertheless, due to the calculation method used and the chosen region, it is not clear

whether the calculated E_{Urbach} value presented above contains information on transitions involving defect states such as deep defects. In our case, SiDBs are highly probable in *a*-SiOC, and it reports their deep localized states near the middle of the bandgap [95]. So, similar to the case of *a*-Si:H, SiDBs can act as centers of high recombination probability [141,142]. Moreover, the increase in temperature (especially for temperatures above 500°C) left an increase in Si−O bonds which would entail a reduction of SiDBs. This is not observed in the increasing E_{Urbach} value. Therefore, the deep defects such as SiDBs located near the middle of the *a*-SiOC:H bandgap might not be represented in the E_{Urbach} value.

Figure 4.12. The IR absorption spectra of *a*-SiOC:H thin films grown on c-Si(100), (a) from 400 to 1300 cm^{-1}, and (b) from 1900 to 4000 cm^{-1}. The carbon compositions correspond to samples in as-grown conditions.

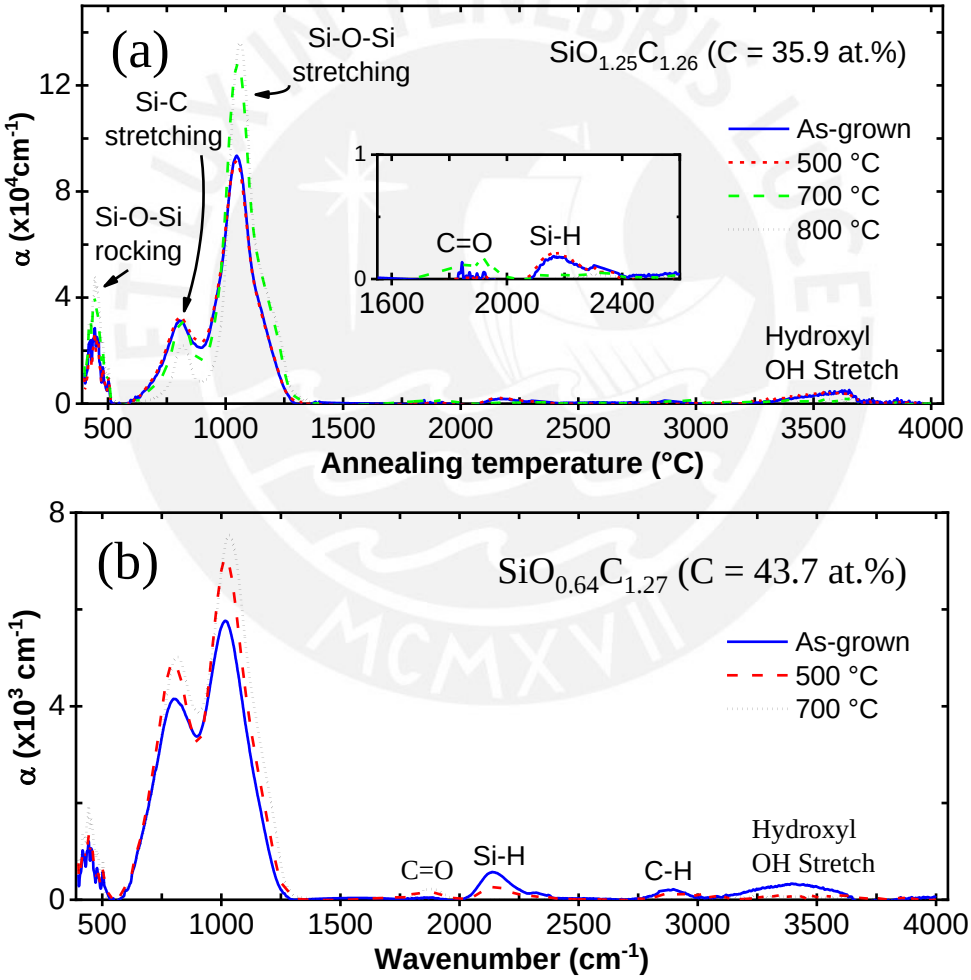

Figure 4.13. Raman scattering spectra recorded from *a*-SiOC:H thin film, from as-grown to 800 °C post-deposition annealing in argon atmosphere, an excitation wavelength of 532 nm.

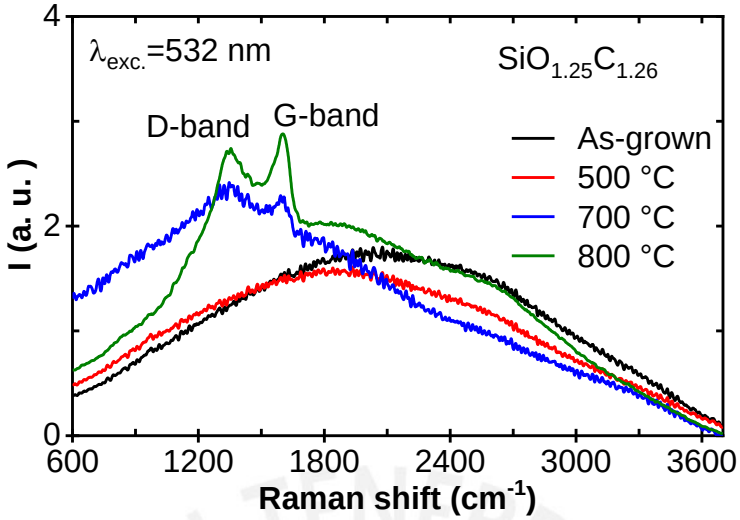

Contrasting the FT-IR and Raman results with the E_{gap} and E_{Urbach} (**Figure 4.11**). The increase in E_{Urbach} correlates well with the creation of carbon-related defects (carbon conglomerations and C-dangling bonds) observed in the results. This result might seem contradictory because increasing temperature, an improvement in lattice order is expected. Moreover, the formation of ordered carbon clusters in the graphite structure form can be interpreted as a sort of crystalline order. Therefore, the increase in the E_{Urbach} value would be contradictory. However, it is important to mention that when structural rearrangements increase, the stress in the sample can increase, leaving an increase in disorder. Therefore, one would have an increase in disorder due to the formation of carbon-related defects.

Summarizing the results, according to FT-IR spectra, increasing the annealing temperature allows the formation of new Si−C and Si−O bonds. After 500 °C, depletion of Si−H and C−H bonds was observed, suggesting the formation of intrinsic defects attributed to dangling bonds. However, above 600 °C, the formation of Si-O bonds over Si-C bonds could decrease the density of defects related to SiDBs. On the other hand, the formation of structural defects ascribed to the carbon structures was verified in the Raman spectra and observed for temperatures close to 700 °C. Therefore, the formation of dangling bonds from the depletion of C−H bonds and the formation of carbon-related structural defects are in good agreement with the increase of E_{Urbach}, the broadening of Urbach tails, and the reduction the E_{gap}.

4.4 Host Luminescence

Figure 4.14 (a) shows the PL spectra of a *a*-SiOC:H thin film (C = 29.6 at.%) from as-grown to 800 °C (post-deposition annealing). The maximum luminescence intensity was achieved at 500 °C. Afterward, the quenching of the luminescence is observed. The low luminescence not always results above 500 °C. For instance, Karakuscu et al. [103] reported UV-blue emission at 800 °C and 1000 °C. In our case, after 500 °C, the weak luminescence could be ascribed to the re-absorption of the luminescence by carbon structures (discussed in the previous section).

The laser excitation energy (375 nm) was above-bandgap but close to the Urbach tails. So, the luminescence is expected to be broad and without a particular shape. That because it comes from the transitions between conduction and valence band as well as band tails. The inhomogeneous spectra observed in luminescence can, in principle, be explained by interference patterns due to internal reflection from the surfaces [143]. However, studies on nanowires [144] and powders [120] also report inhomogeneous spectra. This has led many reports on carbon-doped SiO_x [120,145] and SiOC [95] to ascribe the luminescence to intrinsic point defects in the network. Moreover, given that the optical properties of SiO_x-based materials are mainly defect-driven defect engineering studies have been carried out to tune the light emission by changing the concentration of the radiative centers [144,146].

Figure 4.14. (a) PL emission of *a*-SiOC:H thin film grown on c-Si (100), from as-grown to 800 °C post-deposition annealing in an argon atmosphere. (b) The Gaussian deconvolution shows the different components in the red (~1.9 eV), green (~2.4 eV), and blue (~2.8 eV) range. All measurements were taken at room temperature.

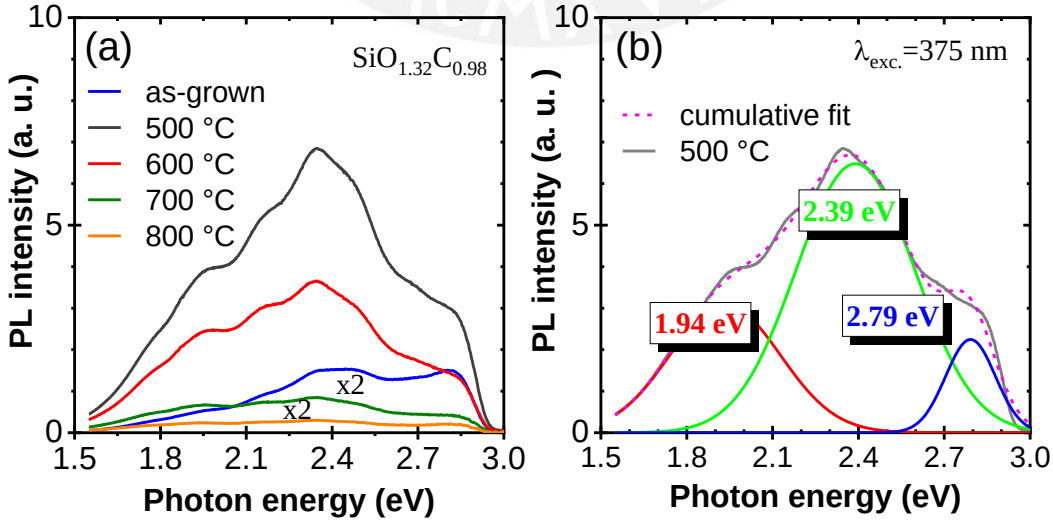

Three bands can be defined in **Figure 4.14 (b)**. The bands are centered at ~2.8 eV, ~2.4 eV, and ~1.9 eV, i.e., blue, green, and red emission, respectively. Those bands can ascribe to 1) The non-bridging oxygen hole center (NBOHC) ≡Si-O• wide accepted to be responsible for the red component (1.85-1.95 eV) in amorphous silicon oxides [99]. 2) For the green component (~2.4 eV), different attributions have been suggested. For example, the green emission has been attributed to electronic transitions in the ≡Si−H groups founded in silica nanoparticles [147], as well as to the radiative recombination in the Si−O−C and Si−C bond states [96]. 3) The blue component (~2.8 eV) was ascribed to the oxygen-deficiency centers, more specifically, the silicon-neutral oxygen vacancy (Si-NOV) ≡Si-Si≡ [99].

Atmosphere effect on the host luminescence

A further study was done to focus on improving the luminescence of the *a*-SiOC:H thin films. Two different atmospheres were used during the post-deposition annealing.

The first one is the argon atmosphere, which can be understood as a self-system reorganization. In this case, self-system reorganization means a rearrangement of the atoms in the matrix, i.e., the angles or lengths of the bonds are slightly changed, approaching the crystalline structure and forming new bonds between the atoms in the amorphous network. It is important to mention that in this case a loss of hydrogen is expected due to its diffusion out of the sample, resulting in the formation of new defects.

The second one is the hydrogen atmosphere (forming gas H_2+N_2). As mentioned in **Chapter 3**, the use of H during the preparation process was due to two considerations: 1) According to the literature, the incorporation of H (during the sputtering process) leaves an increase in the bandgap. 2) The clustering tendency of C atoms in SiOC is sensitive to the H presence, i.e., H in the sample can reduce the formation of carbon structures. Hydrogen was also used during the annealing treatments for two reasons. 1) The use of H decreases its diffusion out of the sample due to the reduction of the H concentration gradient between the environment and the sample. 2) On the other hand, although to a lesser degree, it could allow the addition of H_2 into the voids of the atomic network, which could drive the mobility of hydrogen in the sample, thus passivating the dangling silicon bonds.

Considering the two atmospheres mentioned above, **Figures 4.15 (a)** and **(b)** show the maximum emission at 500 °C for both cases (H_2 and argon atmosphere). A better emission is observed for the forming gas case. The higher intensity luminescence obtained for the hydrogenated atmosphere is attributed to the effect passivation and the low hydrogen

out-diffusion. **Figure 4.15 (c)** shows the ratio of the PL intensities for the centered bands at ~2.4 eV and ~1.9 eV in relation to the central band at ~2.8 eV (taken as a reference). In both cases, the trend evolution with the temperature seems to be similar, which means that the two luminesce bands are in the same way promoted with the increasing temperature.

Figure 4.15. (a) and (b) PL emission of *a*-SiOC:H thin film grown on c-Si (100), from as-grown to 700 °C post-deposition annealing, in forming gas and argon atmosphere. (c) Ratio of the PL intensities for the centered bands at ~2.4 eV and ~1.9 eV.

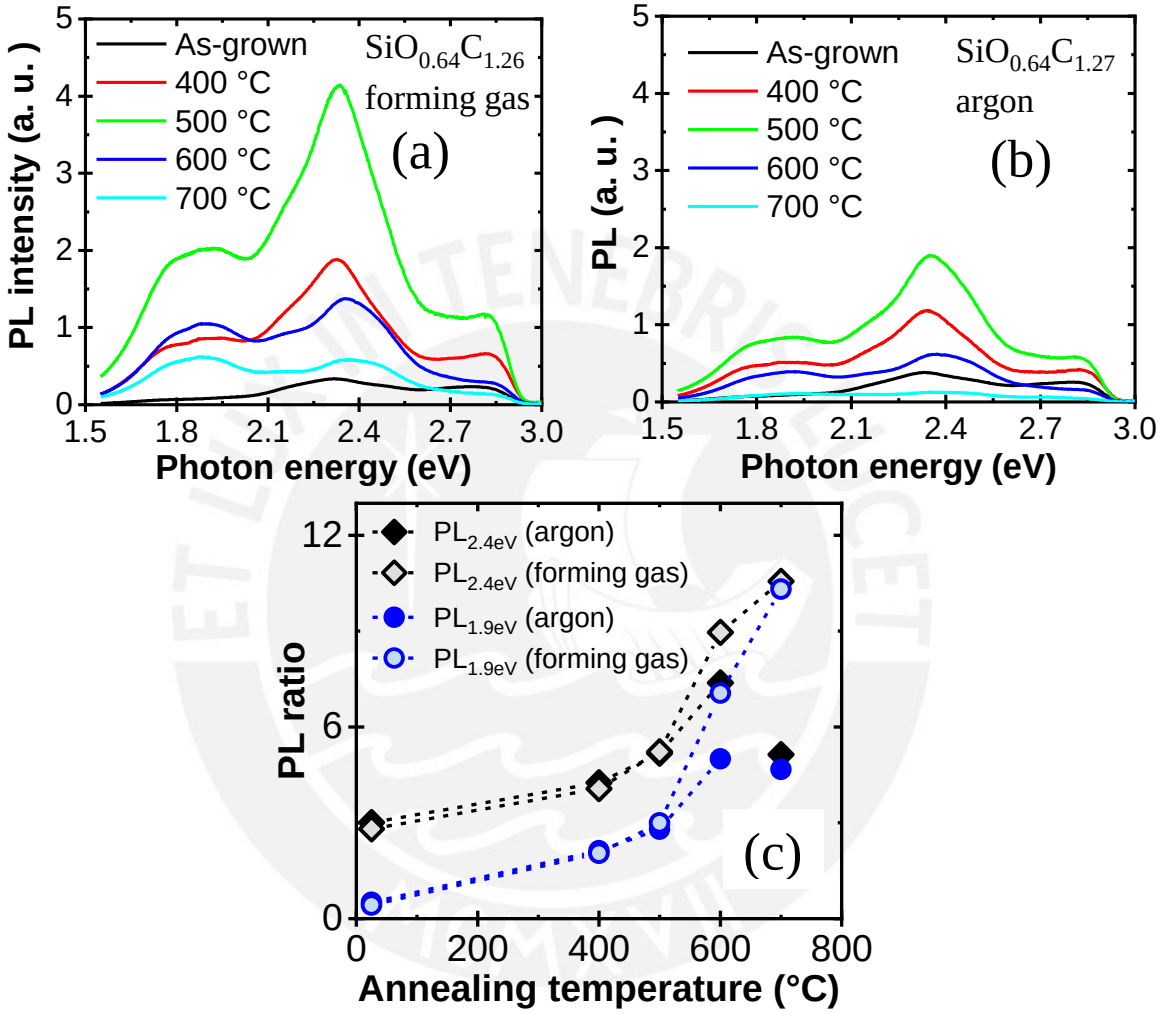

Carbon composition and the annealing time effect on the host luminescence

The luminescence spectra of different carbon compositions and the annealing time were analyzed in this study. **Figure 4.16 (a)** shows an increasing luminescence with the carbon composition. The band at ~2.4 eV is especially affected by the carbon effect. It would be related to forming new bonds such as Si−O−C and Si−C bonds as suggested by [96]. Also, the band at ~1.9 eV seems to be sensitive to the carbon increase. This band is mainly associated with non-bridging oxygen hole center (NBOHC) ≡S−O•. Carbon atoms could join to oxygen dangling bonds to form C=O bonds, which is consistent with the IR spectra

(**Figure 4.12 (a)** and **(b)**). The band at ~2.8 eV was ascribed to silicon-neutral oxygen vacancy (≡Si−Si≡). It is observed to be less sensitive to increasing carbon composition.

Figure 4.16. PL emission of *a*-SiOC:H thin film at 500 °C post-deposition annealing, (a) for different compositions and (b)for different annealing times. (c) The ratio of the absorption bands intensities corresponding to the Si−O and Si−C bonds as a function of the annealing temperature.

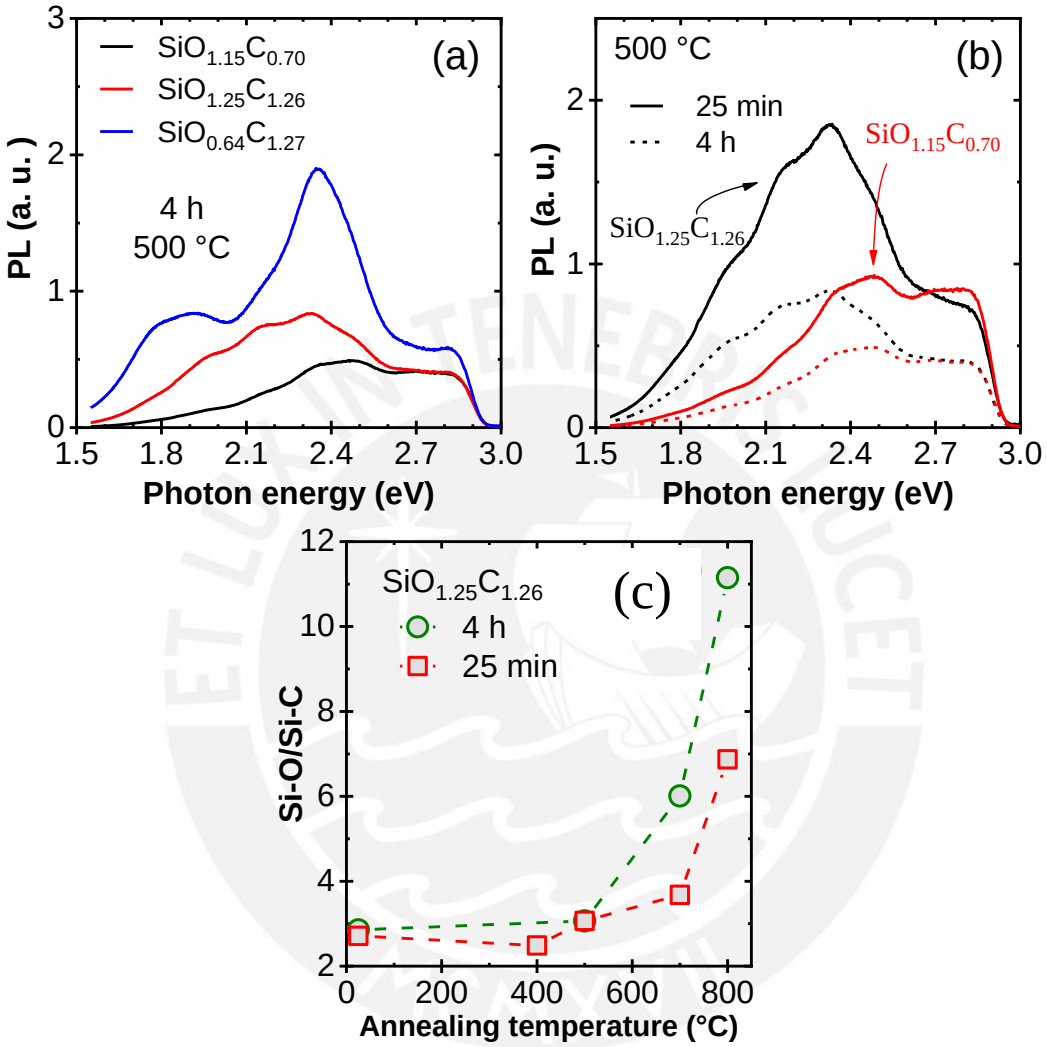

For future discussion on samples doped with rare earth, it is important to study the behavior of the host luminescence with increasing annealing time. Therefore, studies at 25 min and 4 hours annealing time were carried out.

Figure 4.16 (b) shows the effect on the matrix luminescence by the annealing time. An increase in the annealing time reduces the luminesce. Such reduction was observed in two representative samples, low and high carbon composition. The change in the Si−O and Si−C bond density is analyzed by FT-IR spectra. **Figure 4.16 (c)** shows the ratio of the absorption bands intensities corresponding to the Si−O and Si−C bonds. Up to 500 °C, the ratio of Si−O over Si−C bonds seems to play a minor role in the host luminescence as no

major changes are observed for the 4 h and 25 min annealing time. Thus, the reason for the reduction of the matrix luminescence with increasing annealing time would not be directly related to the Si−O and Si−C bonds formation. The reason for the quenching of host luminescence with increasing time is unclear. However, based on the fact that host luminescence is related to transitions between band tails, one would expect that annealing time modifies the density of states in the tails.

4.5 Conclusion

In this chapter, the atomic composition and structure, the bandgap and Urbach energy, the effect of annealing on the structural properties, and the luminescence of the matrix were studied in hydrogenated amorphous silicon oxycarbide (*a*-SiOC:H) films grown by RF-magnetron sputtering.

The elemental composition analysis revealed samples with a silicon composition of 33 at.%, which is close to the ideal in SiO_2. The carbon added to the samples would replace the oxygen atoms in the lattice. However, a slight excess of carbon would lead to carbon atoms not necessarily bound to the amorphous network. The formation of Si−O, Si−C, Si−H bonds and OH groups were verified in the FT-IR spectra. No signal associated with carbon structures was observed for the as-grown samples in Raman spectra. Finally, the oxygen content in samples results in a structure mainly dominated by the silica structure.

Representative E_{gap} values were calculated from as-grown to 800 °C post-deposition annealing. The used models were the Tauc-plot model (E_{Tauc}), band fluctuation model (E_{BF}), and iso-absorption energy (E_{04}). Also, the Urbach energy values were retrieved using the Urbach model (E_{Urbach}), and the band fluctuation model ($1/\beta$). The representative E_{gap} values remain relatively constant (~2.8 and 3.0 eV) up to 500 °C annealing temperature. After this, a continuous decrease is observed with the increasing annealing temperature. The widening of the Urbach region above 500 °C overlaps with the bandgap region itself (mobility edges). So, reducing the bandgap is explained by the increase of disorder and not necessarily associated with any shifting of the mobility edges.

After 500 °C, depletion of Si−H and C−H bonds was observed, suggesting the formation of intrinsic defects attributed to dangling bonds. However, above 600 °C, the formation of Si−O bonds over Si−C bonds could decrease the density of defect related to silicon dangling bonds. On the other hand, the formation of structural defects ascribed to the carbon structures was verified in the Raman spectra and observed for temperatures close to

700 °C. The formation of new Si−O bonds and ordered carbon groups in the form of graphite structure can be interpreted as a sort of crystalline order. Therefore, the increase of the Urbach energy value would be contradictory. However, it is important to mention that when the structural rearrangements increase, the stress on the sample may increase, leaving an increase in disorder. So, disorder would increase due to atomic rearrangement. On the other hand, the increase in annealing temperature also led to the formation of defects associated with carbon structures. Therefore, the reduction of the E_{gap} and the increasing Urbach energy, after 500 °C, can be understood as a consequence of the formation of dangling bonds from the depletion of C-H bonds and the formation of carbon-related structural defects, i.e., broadening the Urbach tails, and hence the reducing the E_{gap}.

The luminescence of the *a*-SiOC:H matrix is mainly attributed to electronic recombination in the Urbach region. It may also receive contributions from luminescent sources ascribed to multiple intrinsic defects, for example, the NBOHC (≡Si-O•), the ≡Si−H groups, and Si-NOV (≡Si-Si≡), among others. The luminescence spectrum can be divided into three bands centered at ~2.8, 2.4, and 1.9 eV, i.e., blue, green, and red emission. The effect of passivation resulting from the annealing treatments was studied in argon and hydrogen atmospheres. The annealing treatments in the hydrogen atmosphere led to an enhancement of luminescence. An increase in carbon composition increases the luminescence centered at ~2.4 and 1.9 eV. The band at ~2.8 eV seems to be less sensitive to this change. The annealing times also show their effect on the luminescence of the matrix, i.e., increasing the time leads to a quenching of the luminescence.

CHAPTER 5. Results and Discussion: Tb and Yb-doped amorphous SiOC:H thin films

This chapter studies the Tb^{3+} and Yb^{3+} ion luminescence in Tb and Yb-doped hydrogenated amorphous silicon oxycarbide (*a*-SiOC:H) films grown by RF-magnetron sputtering. The chapter will be divided into three subsections. The first aims to discuss the results obtained from the atomic composition. The second aims to study the effect of post-deposition annealing on the luminescence of Tb and Yb ions. The third aims to discuss the effect of the matrix composition on the luminescence of the above mentioned ions. The goal in this section is to maximize the luminescence of the RE ions by means of the annealing treatments, the composition of the host matrix, and the RE ion doping concentration.

The composition and structure of the *a*-SiOC:H samples were studied by the analysis of energy-dispersive X-ray (EDX) and Fourier transform infrared (FT-IR). The excitation and emission spectrum were investigated by photoluminescence excitation (PLE) and steady-state photoluminescence (PL) measurements. Transient PL measurements were also performed to study the Tb and Yb luminescence excited state lifetime. Details of measurement conditions were previous presented in **Chapter 3**.

5.1 Introduction

Rare-earth (RE)-doped solids have been considered for several applications such as lighting, telecommunication, laser, biological imaging, among others. The interest in these materials arises from their characteristic emissions from the intra-4f-shell transitions. The characteristic RE emission is due to the fact that the filled $5s^2$ and $5p^6$ subshells screening of the 4f electrons from the influence of the local crystal field. Consequently, the RE energy levels of the $4f^n$ configuration are only slightly different from the free ion case. Thus, the wavelengths of these emissions are almost matrix-independent, so by referring to specific rare earth, we will know what to expect in terms of the emission wavelength.

As it stated, the photon energy emission is particular to each RE^{3+} ions. However, a major challenge is to overcome the low efficiency of direct intra-4f-shell excitation of RE ions, so the search for suitable RE indirect excitation mechanisms has been very active in recent years. Therefore, the host matrix and its related defects will play an essential role in the excitation mechanisms. **Figure 5.1** shows a simplified illustration for RE^{3+} ion optical

excitation. The resonance excitation energy coincides with the RE^{3+} ion energy levels. Non-resonant processes can also take place in which the host matrix is excited first. These indirect mechanisms can involve excitation paths such as electron-hole pairs, change of RE ion charge, and donor-acceptor pairs [148,149]. The sunlight range we want to use in the present work is in the range from 300 to 500 nm (4.1 to 2.5 eV). Hence, the Tb^{3+} ion can be resonantly excited. In contrast, the Yb^{3+} ion excitation will entirely depend on the host sensitization. The *a*-SiOC:H bandgap of ~2.5 eV (calculated bandgap in **chapter 4**) would make a broad absorption in the wavelength working range, thus offering a wide range of energy available for the absorption.

Previous studies on Eu-doped SiOC for silicon photonics applications [150–154] and Er for optical waveguide applications [87,155,156] showed that SiOC reduces the RE clustering phenomenon compared to the silicon oxide matrix [150,151], thus increasing the RE ion concentration without precipitation, and consequently reducing the quenching of the luminescence. In addition, an increase of the Er excitation efficiency was also reported by an increase of the effective cross-section magnitude compared to the direct optical excitation of Er, indicating an indirect Er excitation process in the SiOC matrix [155]. Moreover, the using carbon in matrices, such as *a*-Si:H [157] and Si-rich silicon oxide [156] lead to the improvement of the 1540 nm Er photoluminescence at room temperature, and to an order of magnitude increase in Tb photoluminescence [158]. The SiOC matrix also has additional properties such as flexibility in its refractive index which can be tuned in a range from 1.35 to 2.85 [114], chemical durability in highly basic or acidic solutions [159], remarkable stability under hydrothermal corrosion conditions [160], thermal stability concerning to decomposition [161] and passive oxidizing [85], among others.

Figure 5.1. Schematic illustration for an RE^{3+} ion optical excitation.

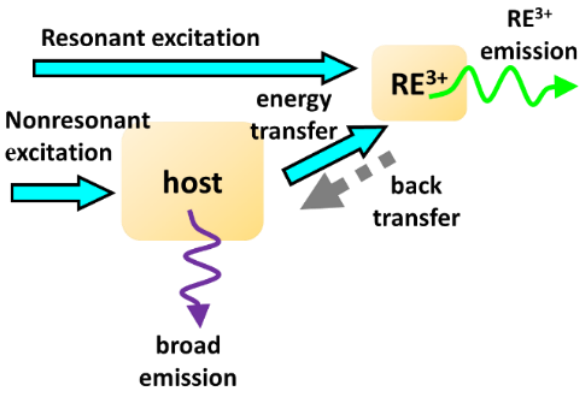

5.2 Sample composition

The chemical composition in the *a*-SiOC:H matrix was first analyzed. The samples compositions are present in **Table 5.1**. The silicon compositions were slightly lower compared with the undoped sample (~33 at.%, **chapter 4**). This silicon deficient could be attributed by considering the RE concentration in the total atomic count of the samples. The slight increase in oxygen composition in the doped samples compared with the not doped case (**chapter 4**) could be explained by the oxygen affinity to the RE ions. It is worth mentioning that the variations of oxygen and carbon among doped sample compositions are not related to the increase or decrease of the total percentage of RE elements but rather to the position of the substrate with respect to the SiC target.

The carbon effect on the Tb and Yb luminescence is studied in two sample groups. For the Tb-doped samples, the carbon composition was in the range of 3.1-12.0 at.%. The carbon atoms were considered in the SiO_x matrix by replacing oxygen atoms joining the silicon leading to the formation of the amorphous *a*-SiOC:H network. The carbon concentration lower than ~12 at.% was selected to avoid the light reabsorption in the visible range (main Tb emission peak at 545 nm) by carbon structures (**Chapter 4**). For the Yb-doped samples, the carbon compositions were in the range of 6.1- 40.1 at.%. Additionally, as the emission of Yb ions is in the infrared region, the reabsorption in the visible will not represent an issue. Therefore, the carbon composition was increased up to ~40 at.%.

Table 5.1. Elemental composition of *a*-SiOC:H samples (as-grown).

Si at.%	O at.%	C at.%	Tb at.%	Yb at.%	O/C	O+C/Si	RE wt.%	RE mean distance Å
27.7	59.2	12.0	1.1	-	4.93	2.57	8.6	6.2
30.1	63.5	5.4	1.0	-	11.76	2.29	7.6	6.5
30.8	64.7	3.1	1.4	-	20.87	2.20	10.3	6.0
30.2	26.8	40.1	-	2.9	0.67	2.22	22.2	4.5
28.8	32.7	36.1	-	2.4	0.91	2.32	19.0	4.7
24.3	48.5	21.8		5.4	2.22	2.39	35.2	3.9
27.9	52.8	15.5	-	3.8	3.41	2.89	26.6	4.3
24.7	61.2	11.5	-	2.6	5.32	2.45	19.9	4.8
27.7	61.6	8.6	-	2.1	7.16	2.53	16.3	5.2
26.9	63.0	6.1	-	4.0	10.33	2.57	27.4	4.4
32.2	31.2	36.6			0.85	2.11	Chapter 4	
34.6	59.1	6.3	-	-	9.38	1.89	Chapter 4	
31.85	54.14	6.37	-	-	8.5	1.89	SiO_2-like [108]	
34.25	41.09	17.12	-	-	2.4	1.70	Si-C-O [108]	

In the literature, the films composition is usually given in atomic percent (at.%) or weight percent (wt.%). Hence, for easy comparison, the weight percent is also reported in **Table 5.1**, detail of calculation can be consulted in **Appendix 1**. It is known that the space distribution of doping atoms like RE leads to different type of interaction, such as the exchange or Coulomb interaction. Therefore, an estimation of the RE mean distance is calculated for a better comprehension of the possible mechanisms that could take place in our samples. The Calculated RE mean distances are consigned in **Table 5.1**. Mean distance calculations were done in **Appendix 3** taking into account a variable density from ~2.01 to 2.48 g/cm^3 (**Appendix 2**) due to the changing Si, C, and O compositions in the studied samples. The RE mean distance exhibits a range of ~0.4 – 0.7 nm and are presented in **Table 5.1**. Thus, the exchange interaction could be excluded and ascribed to the electric dipole-dipole interaction. Finally, comparing these distances with the crystalline silicon oxide lattice parameter (~5 Å [162]), one would expect an interaction between RE across several cells.

5.3 Post-deposition annealing effect on the RE^{3+} luminescence

In this subsection, the aim is to optimize the RE ions emission by means of post-deposition annealing. It is known that post-deposition annealing can enhance the luminescence of the RE ion by reducing defects acting as energy loss sites. Also, the annealing might active the ionic centers by improve their local environment, for instance, leading to a non-centrosymmetric crystalline field appropriated for partially allow the 4f transitions initially forbidden by the Laporte rule.

On the other hand, RE emission lines in amorphous materials are broad compared to emission in crystalline materials. This is due to intrinsic disorder as a consequence of random variations in structure (bond lengths and angles) as well as stoichiometry. However, it is important to note that amorphous materials have a short-range order. Thus, the RE ion local environment can be compared to that found in crystalline materials.

5.3.1 Tb^{3+} luminescence in *a*-SiOC:H

In this section, the behavior of the Tb^{3+} ion luminescence as a function of the annealing temperature is studied in Tb-doped samples. Annealing treatments were carried out up to 1000 °C. Emission and excitation spectra are shown in **Figures 5.2 (a)-(c)** and **Figures 5.2 (d)-(f)**, respectively. Tb emission spectra in *a*-SiOC:H is reported in **Figure 5.2 (a)** for an increasing annealing temperature up to 800 °C, and all cases with 20 min annealing time. Results show a strong background assigned to the host matrix

emission as well as the Tb^{3+} main transition at 545 nm ($^5D_4 \rightarrow {}^7F_5$). Their respective Tb excitation spectra are presented in **Figure 5.2 (d)**. It shows a strong excitation for higher energies than 4.13 eV (300 nm), whereas a weak signal is observed for lower energies (up to 3.1 eV).

Figure 5.2.(a)-(c) PL emission spectra of Tb-doped samples at 375 nm excitation wavelength. (d)-(f) PLE excitation spectra of Tb-doped samples (1.1 at.%) at 545 nm detection wavelength. The annealing temperature was ranged up to 1000 °C.

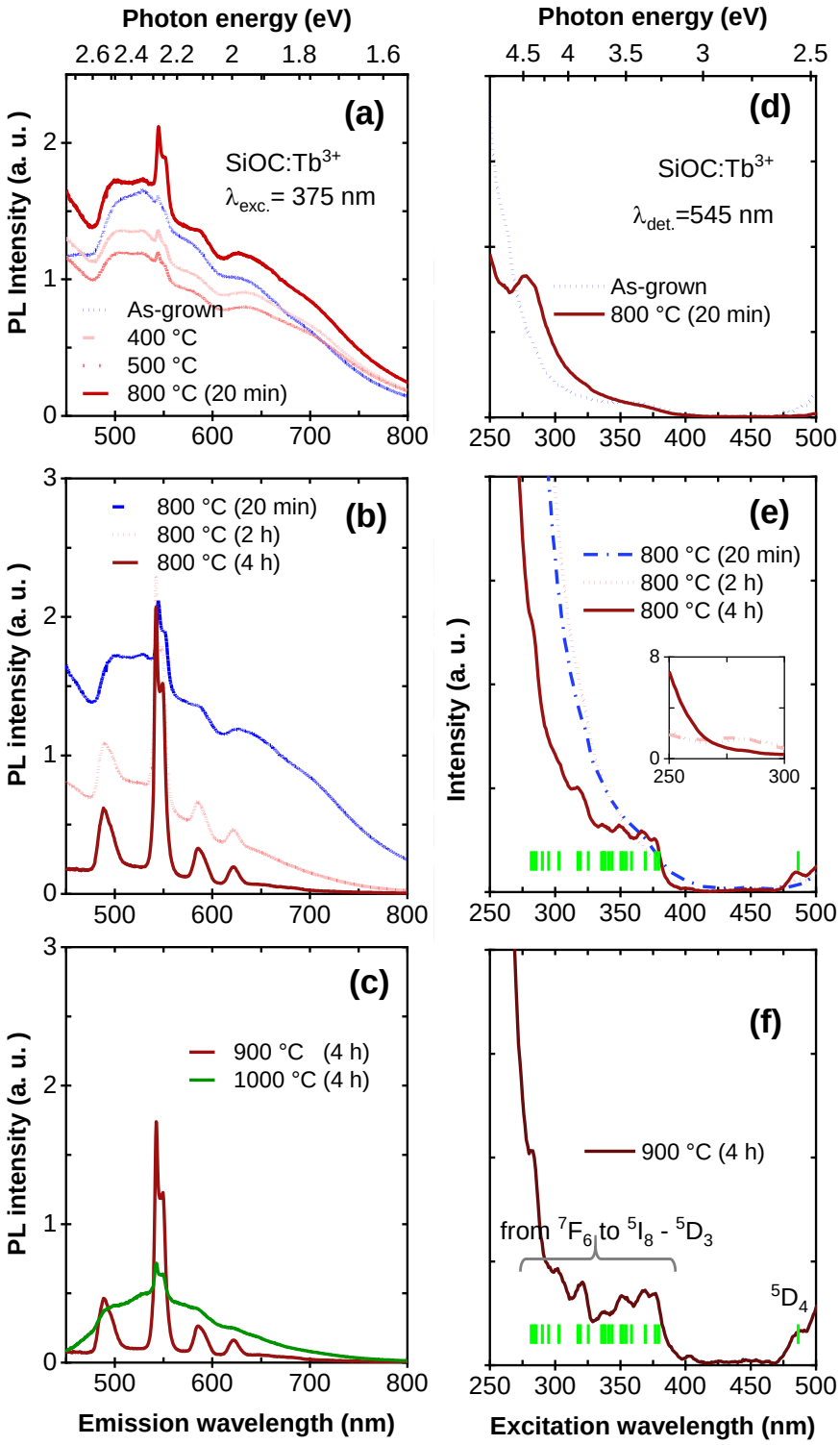

At 800 °C with 20 min annealing time, the excitation band at ~265 nm could contribute to the excitation of both the matrix and the Tb ion, as the 545 nm detection wavelength has a strong host PL contribution (**Figure 5.2 (a)**). To determine this, an analysis of PLE detected at matrix emission (517 nm) was performed. The results show a similar band at 265 nm (**Figures 5.3 (a)** and **(b)**). Therefore, the band at ~265 nm was mainly associated to the matrix excitation and would have a weak contribution to Tb excitation.

Figure 5.3.(a) PL emission of Tb-doped samples at 375 nm excitation wavelength. (b) PLE excitation spectra of Tb-doped samples at 517 nm detection wavelength.

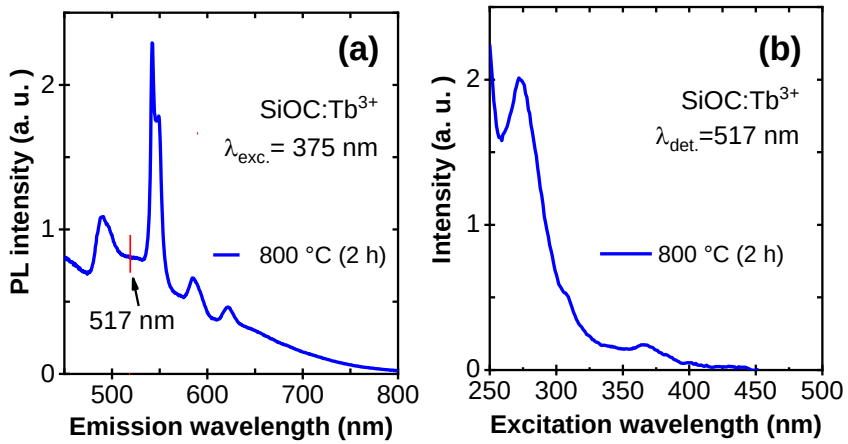

Figure 5.2 (b) shows the PL emission spectra for an increasing annealing time up to four hours at 800 °C. In all cases, it is clearly observed an increasing Tb PL intensity ascribed to the $^5D_4 \rightarrow {}^7F_J$ (J=3, 4, 5 and 6) Tb^{3+} transitions accompanied by a decreasing matrix luminescence. Their respective PLE spectra are shown in **Figure 5.2 (e)**. The PLE spectra start to be dominated by Tb transitions (green lines) and are intensified at the four hours annealing time. The low energy band corresponding to the Tb $^7F_6 \rightarrow {}^5D_4$ transition (488 nm) is also observed. The cut-off at ~389 nm near the $^7F_6 \rightarrow {}^5D_3$ transition (~375 nm) suggests that the optical Tb excitation is dominated mainly by transitions coming from the $^5D_3$ and higher Tb levels. That is, the observation of the transition from $^7F_6$ to $^5D_3$ in the PLE spectra is clearly correlated with the enhancement of the Tb luminescence intensity in **Figure 5.2 (b)**.

Figure 5.2 (c) shows the PL spectrum at 900 and 1000 °C, a low Tb intensity and an increase in host luminescence is observed for the 1000 °C case. The PLE spectrum at 900 °C is shown in **Figure 5.2 (f)**. The Tb transition lines as $^7F_6$ to $^5D_3$ (~376 nm) as well as transitions from $^7F_6$ to the next higher levels are clearly observed. Thus, the increase of the annealing temperature leads to an excitation mainly dominated by the Tb resonant excitation. However, even when the resonant excitation is clearly observed in the PLE (at 800 and

900 °C for 4 hours annealing time), the absorption coefficient (red dotted lines in **Figure 5.4**) did not show any absorption bands corresponding to Tb. Therefore, the Tb direct excitation is scarce in the studied samples. Consequently, the excitation will happen first in the host matrix, and then transfer to the active Tb ions. A more detailed discussion will be presented later.

The optical bandgap (E_{gap}) values were assigned to be in the ~2.8-3.6 eV range (**Chapters 3** and **4**). In the luminescence spectra, the wavelength used for excitation was 375 nm (~3.31 eV). So, the excitation could be considered slightly above the bandgap. Due to the large Urbach region in amorphous materials, the disorder and defects-induced localized states in the *a*-SiOC:H band tails will play an important role in the sensitization of Tb ions. Thus, after excitation, the energy will transfer from the matrix (in the disorder-induced localized states) to the $^5D_3$ level, followed by a strong contribution from $^5D_3$ to the $^5D_4$ level to increase the $^5D_4 \rightarrow {}^7F_J$ (J = 3, 4, 5 and 6) transitions (main emission at 545 nm) as it shows in the PL emission spectra (**Figures 5.2 (e)-(f)**).

Figure 5.4. PLE excitation spectra of Tb-doped (1.1 at.%) samples at 545 nm detection wavelength for as-grown and 900 °C. Absorption coefficient spectra in blue (as-grown) and red (900 °C) dotted lines.

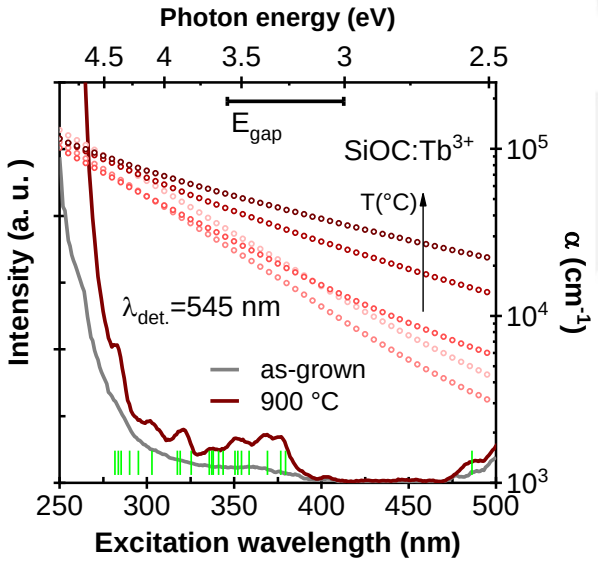

Figures 5.5 (a)-(f) show the room temperature PL decay curves for the Tb^{3+} main emission line (~545 nm, $^5D_4 \rightarrow {}^7F_5$) excited at 375 nm. From as-grown to 800 °C (two hours annealing time), the decay curves exhibit a nonexponential dependence as shown in **Figures 5.5 (a)-(c)**, indicating energy migration offsite of the Tb^{3+} ion. After the increase of annealing temperature up to 900 °C (**Figures 5.5 (d)** and **(e)**) a nearly single exponential curve is observed indicating recombination paths only at the Tb^{3+} ion. At 1000 °C,

Figure 5.5 (f) again shows the non-exponential curve indicating the energy migration offsite of the Tb^{3+} ion.

The average luminescence lifetime ($\bar{\tau}$), which results from a two-exponential fit of the decay curves are consigned in **Table 5.2**. For the calculation of the luminescence decay time, a multi-exponential fit was used. It is important to remember that the multi-exponential model (**equation 5.1**) can be used for almost any intensity decay [55]. However, the interpretation of the multiple exponents will depend on the system being studied. Therefore, we will consider the results obtained from the average lifetime ($\bar{\tau}$). The calculation of $\bar{\tau}$ is given by the **equation 5.2**.

$$I(t) = \sum_{i=1}^{n} \alpha_i \exp\left(-t/\tau_i\right) \qquad \textbf{(5.1)}$$

Where, τ_i are the decay times, α_i represent the amplitudes of the components at t=0, and *n* is the number of decay times.

$$\bar{\tau} = \frac{\sum_i^n \alpha_i \tau_i^2}{\alpha_i \tau_i} \qquad \textbf{(5.2)}$$

Figure 5.5. Normalized decay curves for Tb-doped (1.1 at.%) samples. (a) At as-grown, (b) - (d) at 800 °C and 25 min., 2 hours, and 4 hours, respectively. (e) At 900 °C and 4 hours. (f) At 1000 °C and 4 hours. All measurements were taken at room temperature.

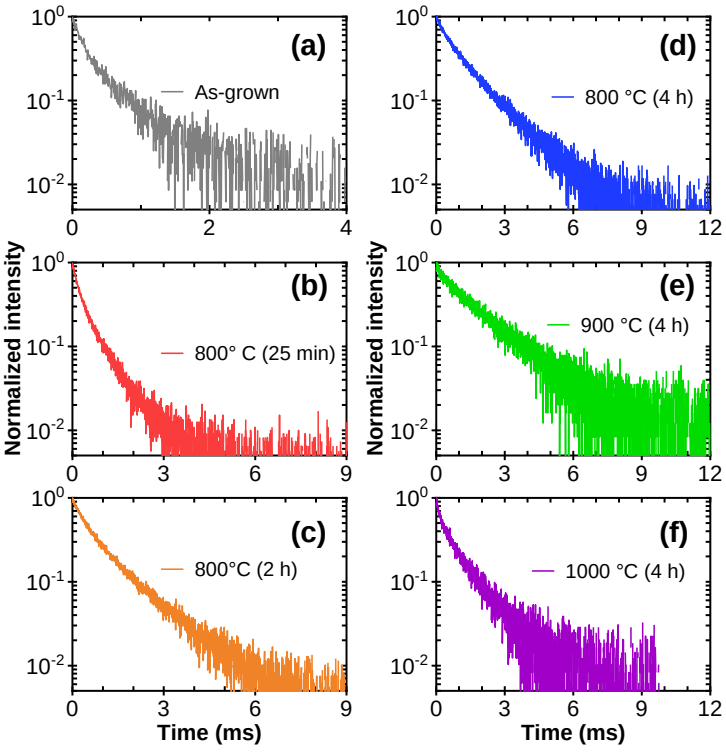

Table 5.2. Tb excited state luminescence lifetime for a Tb doped sample.

	$\bar{\tau}$ (ms)
as-grown	0.54 ± 0.03
800 °C (25 min)	0.67 ± 0.02
800 °C (2 h)	1.18 ± 0.02
800 °C (4 h)	1.41 ± 0.01
900 °C (4 h)	1.93 ± 0.02
1000 °C (4h)	1.10 ± 0.02

Discussion

An increasing RE luminescence requires: (1) RE ions in the 3+ charge state, (2) an increasing number of active RE ions, (3) reducing sources of energy loss, and (4) an increasing excitation. In principle the optically active 3+ state is favoured in a matrix with oxygen as it in our case. It is important to mention that in *a*-SiOC, the RE will not replace any of the ions in the matrix as in the case of RE doped crystalline materials. In the case of amorphous materials containing oxygen, the RE will be located at a site locally surrounded by oxygen atoms. It is therefore necessary to discuss the possible atomic configurations of the RE-O as well as the role of oxygen in RE activation.

The coordination of rare earths with oxygen is well established for the case of crystalline materials, however, the literature reports varying results in the amorphous case. For instance, studies on crystalline silicon established that the most stable coordination number for the Er^{3+} ion is six oxygens [163] as in Er_2O_3. However, in amorphous materials as in *a*-Si:H, there are some differences. Some authors suggest that RE^{3+} ions are in [RE-O] clusters [164] where, for instance, Er is forming ErO_6 complexes [165]. Another work establishes that in co-sputtered samples the first neighbouring coordination consists of oxygen atoms with an average coordination between 2 and 3.6. Therefore, coordination with six oxygen atoms is not always satisfied in amorphous materials. Furthermore, it is also likely that REO_x cluster formation occurs during deposition, as reported for the case of Er atoms which tends to bond to residual O available during deposition, and is incorporated into the *a*-Si:H lattice in the form of ErO_x clusters with ErO_3 clusters being the most energetically favoured configuration [166]. Moreover, in as-deposited *a*-SiO_x:H samples, EXAFS results [167] have shown that, the average Er coordination increases with O concentration up to approximately three and saturates at this value, regardless of how much oxygen is available to be bonded to Er ions.

In this work, the annealing treatments of the Tb doped *a*-SiOC:H samples led to a slight increase in oxygen content (~5 at.%). It is important to mention that the annealing

process were performed in a continuous argon flux, however, residual oxygen could oxidise the surface of the sample, that would explain the increasing oxygen. Previous work in *a*-SiO_x:H samples informed that increasing the annealing temperature causes an increase in the coordination number from 3 to 6 oxygens at 850 °C annealing temperature [167]. However, it has been reported that additional oxygen does not primarily influence the optically active RE concentration, but does reduce the temperature quenching as the temperature is raised from 10 K to room temperature [168]. Besides, it was found that annealing does not always modify the RE chemical vicinity (O-coordination number). For instance, the oxygen coordination by the effect of annealing treatments was reported in Tb doped *a*-SiN_x:H. Results shown that the fourfold oxygen coordination for the Tb ion in the as-grown samples is approximately the same as in annealed samples [169]. This contrasts with the results of Er doped *a*-SiO_x:H samples, in which the Er ion coordinates to three oxygen atoms and evolves to six only when annealed at 850°C [167]. Thus, the increasing Tb luminescence in the *a*-SiOC:H host matrix (**Figures 5.6 (a)** and **(b)**) cannot be only attributed to changes in the oxygen coordination resulting from the annealing treatments.

Figure 5.6. **(a)** PL emission spectra of Tb-doped (1.1 at.%) samples at 375 nm excitation wavelength. **(b)** Integrated Tb and host related PL. The annealing temperature was ranged up to1000 °C.

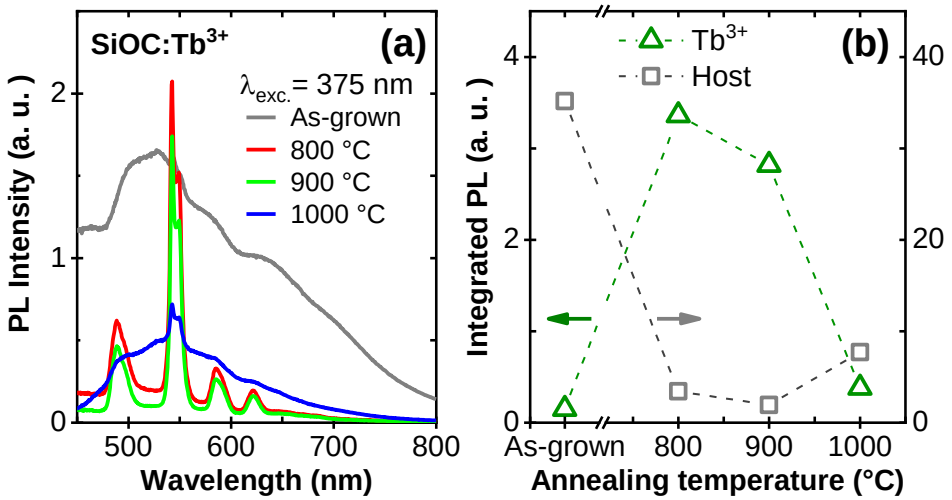

On the other hand, RE luminescence is also strong related to the role played by defects in the host matrix. Indeed, an optically active ionic centre can be surrounded by intrinsic or extrinsic defects where the defects might play the role of sensitizer, which leads to an increase in RE luminescence; or they might play a role as quenching sites where energy is consumed non-radiatively. Therefore, the study of defects in the vicinity of the RE ions will be a relevant discussion.

According to literature, the post-deposition annealing can decrease the density of deep and (or) tail defects leading to a substantial suppression of the nonradiative processes [170,171]. In our case the increased annealing temperature can passivate deep defects such as silicon dangling bonds as observed in the FT-IR spectra. More in detail, FT-IR results show a significant increase of the ratio Si-O/Si-C bond ratio for annealing temperatures higher than 700 °C (**Chapter 4**). Therefore, passivation of deep defects would be expected due to the formation of new bonds. This is in good agreement with the observed PL decay results (**Figures 5.5 (a)-(f)**) where the change from non-exponential to exponential behaviour is observed with increasing annealing temperature. Thus, the increasing Tb luminescence in *a*-SiOC:H would be explained by deep defects passivation.

It is important to mention that the increase in Tb luminescence has a correlation with the reduction in host luminescence, as can be seen in **Figure 5.2 (b)**. However, above 800 °C a decrease in the luminescence of both is observed (**Figure 5.6 (e)**). Therefore, two options for the Tb excitation mechanism can be considered. 1) The Tb excitation mechanism might be associated with an energy transfer from radiative recombination channels of the host. 2) The Tb excitation mechanism can be a parallel recombination process, which can compete with the radiative recombination of the host. The excitation mechanism will be discussed in more detail in **section 5.4**, where the carbon composition in the matrix was varied.

5.3.2 RE^{3+} luminescence based on a two-level model

The previous section found that the passivation of deep defects leaves an increase in Tb luminescence. We now discuss whether the annealing treatment increases the number of optically active ions. A careful analysis of RE PL properties may offer details of the effects of thermal annealing on the RE activation in the *a*-SiOC:H matrix. Based on a two-level model [155,172], the dynamics of RE ions relaxation will be studied under an increasing photon flux of the excitation light. The rate equation for RE^{3+} ions in the first excited state is expressed in **equation 5.3**. The model rest on the pumping regime where most RE ions are in the ground state and the de-excitation processes are negligible.

$$\frac{dN^*}{dt} = \sigma_{\text{eff}}\phi(N_0 - N^*) - \frac{N^*}{\tau_{RE}} \qquad \textbf{(5.3)}$$

where

N^* is the number of RE ions in the excited state.

N_0 is the total number of optically active RE ions

ϕ is the excitation light photon flux.

σ_{eff} is the effective cross section for the excitation of RE.

τ_{RE} is the luminescence lifetime of the RE excited state.

The first term on the right side of the **equation 5.3** represents the RE ions excitation rate, and the second term represents the de-excitation rate of the excited RE ion.

Therefore, in the steady-state conditions, the population of excited RE ions is given by

$$N^* = \frac{N_0}{1 + \frac{1}{\sigma_{\text{eff}}\phi\tau_{RE}}} \qquad \textbf{(5.4)}$$

It is known that the RE PL intensity (I_{RE}) is proportional to N^* and can be expressed by

$$I_{RE} \propto {N^*}/{\tau_{RE}^{rad}} \qquad \textbf{(5.5)}$$

where τ_{RE}^{rad} is the radiative lifetime of the RE excited state.

Thus, replacing **equation 5.4** in **5.5**, the RE PL intensity can be written as **equation 5.6**, which is the typical sigmoidal curve that defines the population of a simplified two-level system.

$$I_{RE} \propto \frac{N_0}{\left(1 + \frac{1}{\sigma_{\text{eff}}\phi\tau_{RE}}\right)\tau_{RE}^{rad}} = \frac{I_{max}}{1 + \frac{1}{\sigma_{\text{eff}}\phi\tau_{RE}}} \qquad \textbf{(5.6)}$$

In the case of $\sigma_{\text{eff}}\phi\tau_{RE} \gg 1$, the I_{RE} yields its maximum at RE PL saturation (I_{max}).

$$I_{RE} = I_{max} \propto {N_0}\Big/{\tau_{RE}^{rad}} \qquad \textbf{(5.7)}$$

where N_0 is the total number of optically active RE ions

In the case of very small value of $\sigma_{\text{eff}}\phi\tau_{RE} \ll 1$, the **equation 5.6** shows a linear dependence on laser photon flux:

$$I_{RE} \approx I_{max}\sigma_{\text{eff}}\tau_{RE}\phi \qquad \textbf{(5.8)}$$

The excitation power model was applied for the Tb-doped samples. The photoluminescence intensity was measured for a sample at different post-deposition annealing from as-grown to 750 °C. **Figure 5.7 (a)** shows the typical Tb emission and also a weak host luminescence. **Figure 5.7 (b)** shows the Tb^{3+} luminescence intensity as a function of a normalized excitation power. The typical sigmoidal curve starts at the low excitation power, where a linear relation between I_{RE} and ϕ can be observed (**equation 5.8**). **Figure 5.7 (b)** also shows the region of high excitation, where a sub-linear dependency

indicates the starting of the PL intensity saturation (**equation 5.7**). Thus, the typical sigmoidal curve can be understood in agreement with **equation 5.6**.

The PL intensity for the highest excitation power can be expected to reach a plateau, which is in agreement with the fact that there is a maximum of optically active Tb ions that can be excited. On the other hand, according to **equation 5.7**, the difference in the saturation levels reached by the annealing steps can be interpreted as that the increasing annealing temperature increase the total number of active RE ions (N_0). Thus, the increase of annealing temperature led to an increase in the total number of optically active Tb ions.

Figure 5.7. (a) PL emission spectra of Tb-doped (1.4 at.%) *a*-SiOC:H samples at 325 nm excitation wavelength. (b) Excitation power dependence of Tb-doped samples from as-grown up to 750 °C annealing temperature. The dashed line is a guide for the eye.

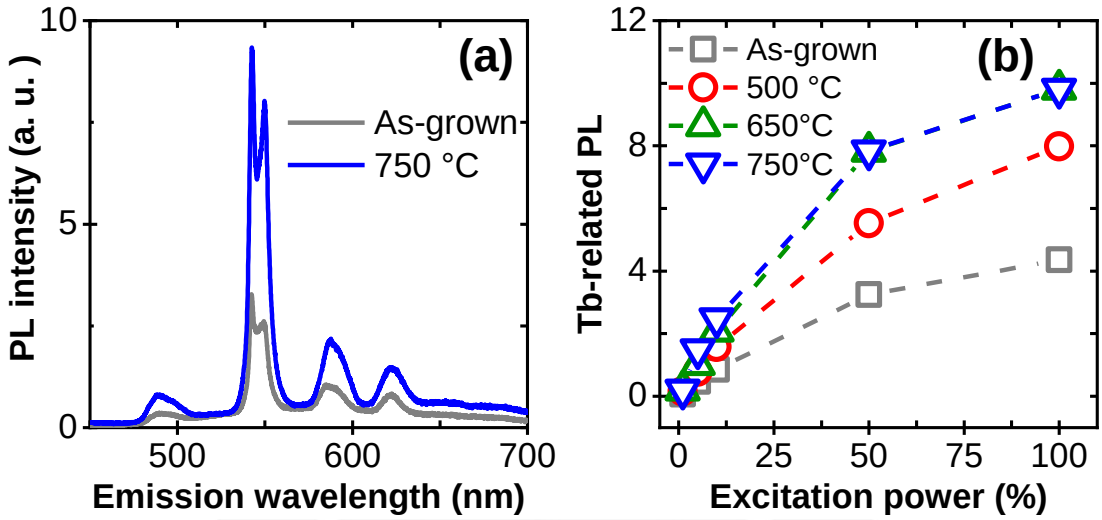

Figures 5.8 (a) and **(b)** show a comparison of the Tb^{3+} and the host luminescence intensity at as-grown and 750 °C, respectively. The PL curve of Tb^{3+} and host exhibit the same sigmoidal trend with power excitation, this trend is generally ascribed to the process of sensitization of Tb by the host, i.e., not by direct excitation to the RE ion. The sigmoidal curves are not always observed in RE^{3+} emission, for instance the Er^{3+} luminescence has a linear dependency in SiO_2 [155]. However, carbon doping seems to favor indirect rare-earth excitation. This was reported in C-doped Si oxides [156], and C doped *a*-Si:H [157,173], the sublinear dependence being attributed in both cases to an indirect excitation of the RE^{3+} by their host matrices. Therefore, indirect Tb excitation is also observed in the *a*-SiOC:H host matrix.

Figure 5.8. (a) excitation power dependence of Tb doped *a*-SiOC:H samples at as-grown, and (b) excitation power dependence at 750 °C annealing temperature. The dashed line is a guide for the eye.

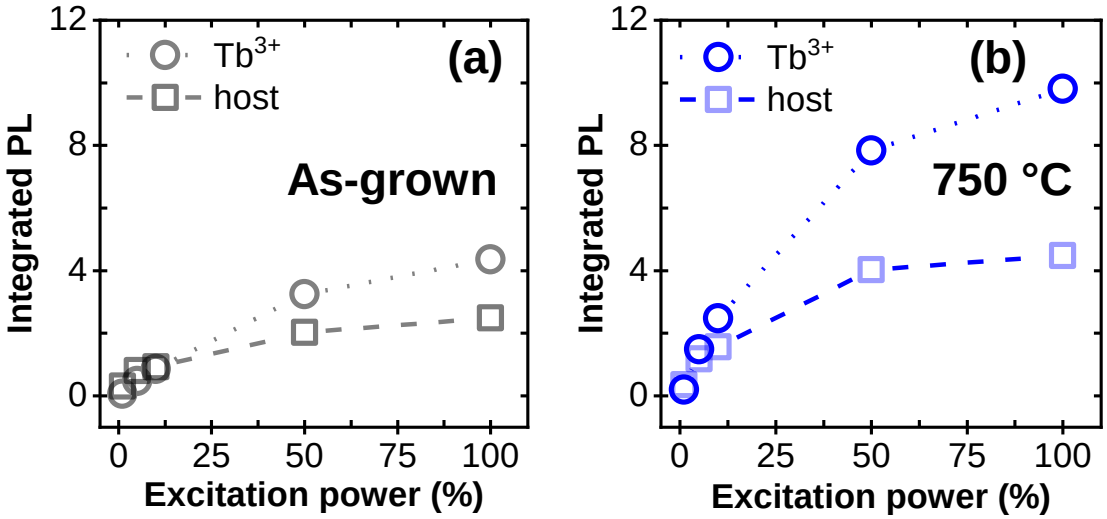

The same plateau at 650 and 750 °C (**Figure 5.7 (b)**) could be explained by: (1) the quenching of the luminescence by the increase of host related defect acting as a quenching center for the excited ion. (2) A second option could be a limit number of host-provided sensitizers to the Tb active ions. Analyzing the first option, the monoexponential behaviors observed in the luminescence decay curves ruled out the energy migration off-site of the Tb^{3+} ion. Therefore, host related defects acting as quenching sites for the Tb ion in the excited state will play a minor role at those annealing temperatures. On the other hand, the second option could explain the same plateau at 650 and 750 °C for Tb luminescence. In other words, a limited number of host-provided sensitizers could lead to low Tb luminescence, similar to a previous work, where a limited number of host-provided sensitizers lead to a limited Er luminescence [172]. Section 5.4 will discuss excitation sources that act as sensitizers for Tb^{3+} and Yb^{3+} ions.

5.3.3 Yb^{3+} luminescence in *a*-SiOC:H

In this section, the behavior of the Yb^{3+} ion luminescence as a function of the annealing temperature is studied in Yb-doped samples. Annealing treatments were carried out up to 600 °C. Emission spectra are shown in **Figures 5.9 (a)** and **(b)**. Excitation spectrum detected at ~ 980 nm (Yb emission) is shown in **Figure 5.9 (c)**. Integrated PL intensity as a function of the annealing temperature is shown in **Figure 5.9 (d)**.

Figure 5.9.(a) Matrix PL emission at 375 nm excitation wavelength, (b) PL emission spectra of Yb^{3+} ion, (c) PLE excitation spectrum of Yb-doped (2.9 at.%) sample, and (d) Integrated PL intensity as a function of the annealing temperature. The annealing temperature was ranged up to 600 °C.

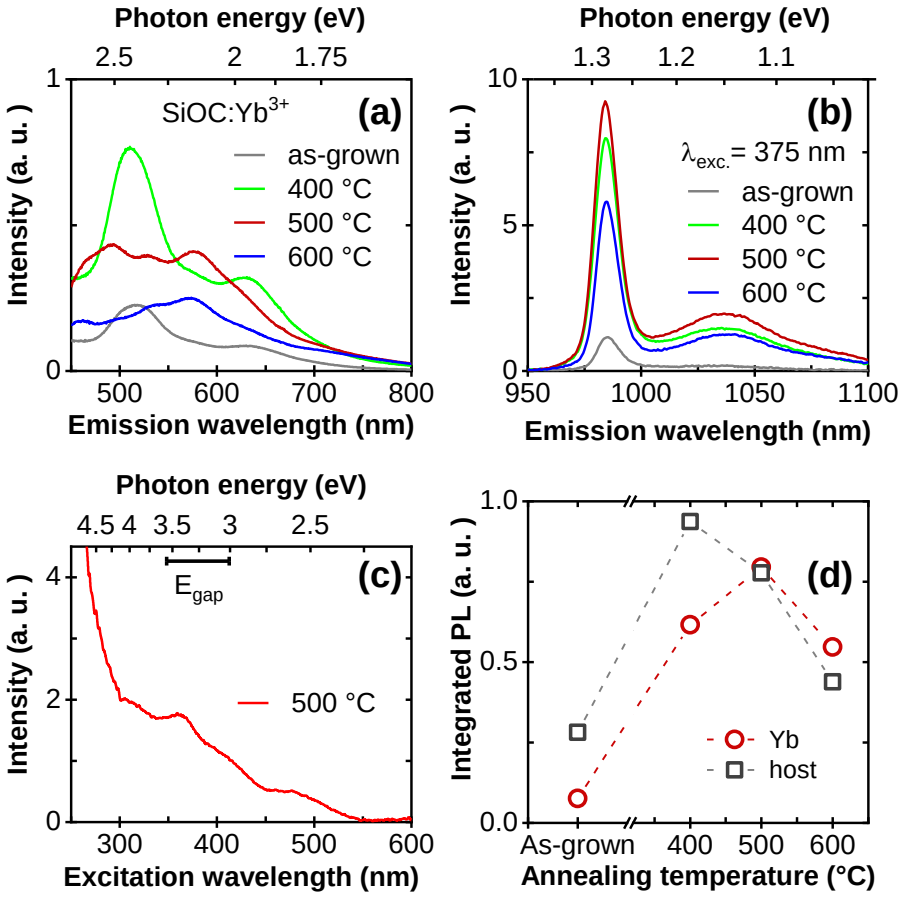

Figure 5.9 (a) shows the host luminescence up to 600 °C annealing temperature in the visible region. At as-grown and 400 °C, the host spectrum coincides in shape but differ in their intensities while a different case is observed at 500 and 600 °C, where there is a change in shape and intensity of the spectra. The aforementioned change with increasing annealing temperature was also observed for the undoped samples (**Chapter 4**), indicating that Yb doping does not modify the radiative recombination sources in the host. The luminescence of the matrix has been attributed to radiative recombination between the band

states and their respective tail states (emission at ~2.4 eV), as well as to unpassivated bonds (~1.9 eV) and neutral vacancies left by oxygen (~2.8 eV). **Figure 5.9 (b)** shows the near IR emission spectrum for the Yb^{3+} ion in the *a*-SiOC:H matrix. The main peak at ~980 nm and the sub-peak at ~1020 nm result from the 4f transitions between the Stark levels of the excited $^2F_{5/2}$ and the ground $^2F_{7/2}$ sate.

The PLE spectrum at 500 °C is shown in **Figure 5.9 (c)**. Given that the position of the ligand-to-metal charge transfer (CT) bands is host dependent [29], the band at ~365 nm might be associated with the Yb^{3+}-O^{2-} CT. However, usually, the CT position bands in silica are reported at shorter wavelengths (~256 nm) [174]. It is therefore more appropriate to associate it with the excitation of defect states (intrinsic or extrinsic) located near the band edges or in the bandgap. It is important to mention that the band at ~365 nm was also observed in the host PLE spectrum (**Figure 5.3 (b)**). Therefore, the defect states responsible for the host excitation are also available for the Yb ion, as the same band was observed for the case without (and with) doping. Hence, the participation of Yb-related defect states can be ruled out.

Figures 5.10 (a) - (d) show the PL decay curves (up to 600 °C annealing temperature) for the Yb^{3+} main emission line (~980 nm, $^2F_{5/2}\rightarrow{}^2F_{7/2}$). The average luminescence lifetimes ($\bar{\tau}$), which result from two-exponential fit of the decay curve (**equation 5.1**) are consigned in **Table 5.3**. By analyzing **equation 5.9**, the lifetime provides information on the increase or decrease of the non-radiative recombination processes, since increasing or decreasing the k_{NR} decreases or increases the value of τ_{RE}.

$$\tau_{RE} = \frac{1}{k_R + k_{NR}} \qquad \textbf{(5.9)}$$

Where k_R is the rate constant of a radiative process and k_{NR} is the cumulative rate constant of the nonradiative processes.

The increase in the PL decay values indicates the reduction of multiple non-radiative channels acting as energy loss centers for the excited Yb ion. In general, energy loss by non-radiative process can be attributed to multi-phonon relaxation, interaction with OH groups, structural defects, non-radiative energy transfer among Yb^{3+} ions, among others. For the case of *a*-SiOC:H, the multi-phonon assisted process would be ruled out due to the high number of simultaneous phonons needed to satisfy it. On the contrary, the low lifetime values can be attributed to the interaction with OH groups or by energy transfer to structural defects acting

as sources of quenching like reported in glass matrices [175–177], which would partially explain the low values for the lifetime in **Table 5.3**.

Table 5.3. Yb excited state luminescence lifetime for an Yb-doped sample.

	$\bar{\tau}$ (μs)
as-grown	0.94 ± 0.13
400 °C	1.85 ± 0.05
500 °C	1.56 ± 0.05
600 °C	1.00 ± 0.04

Figure 5.10.Normalized decay curves for Yb-doped (2.9 at.%) samples at 402 nm excitation wavelength, (a) at as-grown, (b) at 400 °C, (c) at 500 °C, and (d) at 600 °C annealing temperature. All measurements were taken at room temperature.

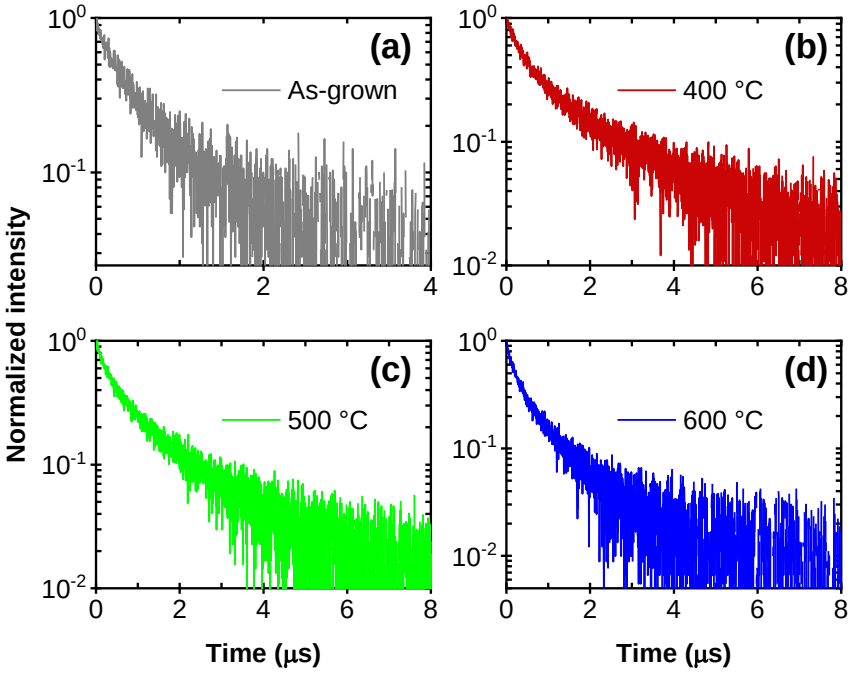

Discussion

As previously discussed, annealing can lead to a rearrangement of the oxygen atoms coordinating the RE ion, which could enhance the RE ion luminescence. More in detail, the local structure of Yb ions was recently reported in Yb-doped silica glass samples. It was found that the number of oxygens coordinating Yb ion increases from 3 to 4.5 with increasing Yb concentration [178]. Furthermore, in samples with high Yb content, the reported local structure partially matches the observed in Yb_2O_3 and $Yb_2Si_2O_7$ crystals. Therefore, a favorable formation of Yb−O−Yb and Yb−O−Si bonds could be suggested for hight Yb doping in *a*-SiOC:H samples. Also, the formation of Si−O bonds in the *a*-SiOC:H matrix could play an important role in the enhancement of Yb luminescence. According to **Figure 5.9 (d)** the maximum Yb emission is observed at 500 °C, however,

FT-IR spectra studied in **Chapter 4** shown that the Si−O/Si−C bond ratio has a modest growth in the temperature range up to 500 °C compared to higher temperatures (700 °C or 800 °C). Therefore, the formation of new Si−O bonds in the *a*-SiOC:H matrix would not be directly related to the increase of the Yb luminescence as it did in the case of Tb.

On the other hand, in the temperature range of the Yb luminescence activation (up to 500 °C), a significant change was reported in the Si−H bond density. Previous reports for RE doped *a*-Si:H films showed that the maximum PL intensity achieved in both RE-doped and undoped *a*-Si:H takes place at ∼400 °C annealing temperature and is associated with some diffusion of hydrogen atoms and structural reordering [179] while at temperatures higher than ∼400 °C, the RE-related light emission is reduced due to the out-diffusion of hydrogen atoms [179].

The hydrogen evolution processes in *a*-Si:H is understand as (1) starting at temperature ~350 °C, hydrogen atoms are released from internal surfaces, diffuse through the network of voids, and recombine to form H_2 [112,180]. (2) Between 350 and 500 °C, a continuous hydrogen effusion signal can be observed. This signal is attributed to material reconstruction by hydrogen diffusion and amorphous network relaxation [181]. Furthermore, starting hydrogen effusion at 350 °C were reported in Er-doped *a*-SiO_x:H samples [134]. (3) At higher temperatures (~550 °C), the released atomic hydrogen in the material was limited by the diffusion process [181]. Therefore, the hydrogen effusion process at a high temperature will depend on material properties.

Considering the above-mentioned behavior, the hydrogen evolution in the *a*-SiOC:H matrix would exhibit essentially the same features. This is supported by the FT-IR results, where the Si−H bonds evolution with the annealing temperature is in good agreement with the reported in *a*-Si:H (**Chapter 4**). Moreover, the central process in hydrogen diffusion is the breaking of a Si−H bond, in which hydrogen is promoted from a stable configuration (in which it is strongly bonded to a Si atom) to a higher-energy interstitial position (in which it can easily move through the lattice). This basic framework was established by Street et al. (1987) [182], the reaction was described as the breaking of a Si—H bond and insertion of H into a Si—Si bond, leaving a silicon dangling bond (SiDB) behind. This reaction has been invoked in the context of defect creation. The bond breaking and the weak-bond to dangling-bond conversion are commonly accepted now [183]. Therefore, an increasing SiDB states would be expected in the *a*-SiOC:H matrix with the increasing annealing temperature.

The increasing Yb luminescence (up to 500 °C) observed in **Figure 5.9 (d)** could be then related to the creation of defects such as SiDBs located near the middle of the bandgap. Furthermore, an increase in the density of such intrinsic defects can be expected due to extrinsic doping with Yb. It is worth mentioning that as in *a*-Si:H, SiDBs could act as centers of high non-radiative recombination probability in the *a*-SiOC:H matrix, thus limiting the host emission, which is consistent with the decreasing host PL intensities (**Figure 5.9 (d)**). The temperature of maximum host luminescence at 400 °C is lower than the usually observed for undoped samples (500 °C, **Chapter 4**). So, this early quenching of the *a*-SiOC:H luminescence would be related to the enhancement of the Yb luminescence. Similar results were reported in a previous work, where the presence of Er ions completely inhibits the PL signal of the amorphous host and the Er emission is improved [179]. This is in agreement with the fact that RE^{+3} ions are recombination centers that effectively compete with other (non-) radiative processes operating in the amorphous host. The Yb excitation mechanism will be discussed in more detail in **section 5.4**.

5.4 Matrix composition effect on the RE^{3+} luminescence

As previously stated, indirect excitation is important for the efficient excitation of RE ions. To this end, many Si-based host matrices have been investigated for their potential applications. Recently, a new Si-based material has been proposed, SiOC matrix has been reported to increase the Er luminescence and reduce the Eu clustering phenomenon. However, most of the work on C-doped Si oxides and SiOC matrices have focused on the intrinsic luminescence properties in the visible range, whereas reports of such material as host for RE ions are still scarce. For this reason. This section aims to study the role of carbon in the luminescence of Tb and Yb ions.

Figure 5.11. Schematic representation of (a) resonant energy transfer, (b) Si nanoclusters mediated excitation, (c) defect-related Auger excitation (DRAE) mechanism, and (d) nonradiative resonant energy transfer by dipole coupling (Förster mechanism). Adapted from [184–186].

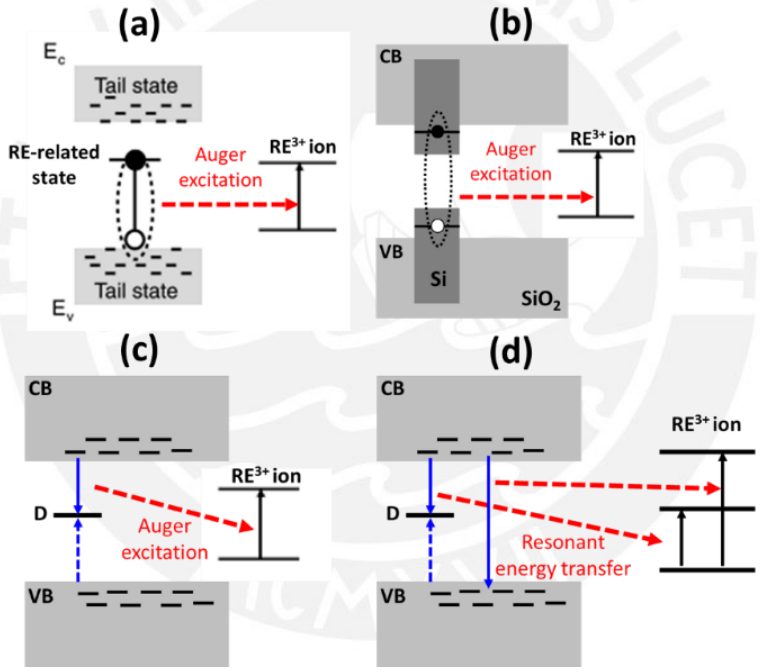

In Si-based materials, several mechanisms have been proposed for RE excitation via defects. **Figure 5.11 (a)** shows the nonradiative energy transfer by Auger excitation [186–189], where RE excitation is mediated by the RE-related state. **Figure 5.11 (b)** shows the nonradiative energy transfer by Auger excitation, where RE excitation is mediated by Si nanoclusters studied in Si-rich silicon oxide [185,190,191]. **Figure 5.11 (c)** shows the defect-related Auger excitation mechanism (DRAE) [192,193], where the RE excitation is mediated by defect states (left by dangling bonds) near the middle of the bandgap. The Auger-type excitation is the result of the Coulombic interaction between carriers and

strongly localized f-electrons [194]. During the Auger-type excitation, the possibility of multiphonon transitions is taken into account for energy compensation [195]. **Figure 5.11 (d)** shows the resonant nonradiative energy transfer by dipole coupling (Förster interaction) mechanism [184], transitions involve defect and deep localized tail states.

5.4.1 Tb^{3+} luminescence in *a*-SiOC:H

In this section, the behavior of the Tb^{3+} ion luminescence as a function of the carbon composition is studied in Tb-doped samples. **Figures 5.12 (a) - (f)** show the room-temperature PL and PLE spectra for the Tb-doped samples with two carbon compositions, C = 5.4 and 12 at.%. To be able to compare both PLE, the spectra were normalized, i.e., $\int F(\lambda)\, d\lambda = 1$, where $F(\lambda)$ represents the PLE spectra, which are normalized.

The as-grown PL spectra (**Figure 5.12 (a)**) show the Tb characteristic emission lines for the low carbon composition, whereas mainly host emission is observed for high carbon composition. At 800 and 900 °C (**Figures 5.12 (b)** and **(c)**), the spectra show the $^5D_4 \rightarrow {}^7F_J$ (J=3, 4, 5 and 6) Tb transitions being intense for both samples. The main difference is the weak host emission band for the low carbon composition sample. The collected spectra were used to determine the experimental branching ratios ($\beta_{j \rightarrow i}$) for the four above-mentioned Tb transitions by calculating the integrated intensity of each band. The luminescence spectra were corrected using a calibrated Xenon light source to calibrate the signal first (**Chapter 3**). An average of ten spectra was taking for each measure to improve the signal-to-noise ratio, then collected spectra were used to find the branching ratios for samples. Results are listed in **Table 5.4**. At 800 °C, $\beta_{j \rightarrow i}$ experimental values are similar for both carbon compositions. However, at 900 °C, a small increase in the branching ratio for the 545 nm lines is observed for the high carbon composition sample. This result agrees with what has been reported in the literature, where carbon can not only affect luminescence intensity but also change the RE intensity ratios [196]. That effect was ascribed to the local environment around the RE ion, which changes the transition probability of the excited ionic centers.

The comparison for the as-grown PLE spectra for two samples (low and high carbon composition) is shown in **Figure 5.12 (d)**. The main difference is the band center at ~265 nm, which contributes to the host emission. By increasing the annealing temperature to 800 °C (**Figure 5.12 (e)**), the spectra are dominated by the Tb resonant excitation (green lines), being more intense for the sample with high carbon composition. The low energy band corresponds to the Tb excitation from $^7F_6$ to $^5D_4$ (~ 2.54 eV) is also observed in the spectrum for the sample with high carbon content. Finally, at 900 °C (**Figure 5.12 (f)**), the

lines from $^7F_6$ to $^5I_8$-$^5D_3$ are clearly observed to be more intense for the high carbon composition. Even when resonant excitations are clearly observed in the PLE, the Tb direct excitation is ruled out (**section 5.3.1**). Thus, the excitation will happen first in the host matrix and then transfer to the active Tb ions. In addition, the $^5D_3$ and higher levels seem to strongly contribute to the $^5D_4$ population, thus increasing the $^5D_4 \rightarrow {}^7F_J$ (J=3,4,5, and 6) emission lines.

Table 5.4. Experimental branching ratios ($\beta_{j\rightarrow i}$) for the four $^5D_4 \rightarrow {}^7F_J$ (J=3, 4, 5 and 6) Tb transitions of Tb doped *a*-SiOC:H samples.

Sample	$\beta_{^5D_4 \rightarrow {}^7F_6}$	$\beta_{^5D_4 \rightarrow {}^7F_5}$	$\beta_{^5D_4 \rightarrow {}^7F_4}$	$\beta_{^5D_4 \rightarrow {}^7F_3}$
	488 nm	545 nm	586 nm	621 nm
As-grown (C = 5.4 at.%)	0.21	0.64	0.10	0.05
As-grown (C = 12.0 at.%)	-	-	-	-
800 °C (C = 5.4 at.%)	0.23	0.61	0.11	0.06
800 °C (C = 12.0 at.%)	0.23	0.62	0.10	0.05
900 °C (C = 5.4 at.%)	0.23	0.59	0.11	0.06
900 °C (C = 12.0 at.%)	0.23	0.62	0.10	0.05

Figures 5.13 (a) – **(c)** show the room temperature time-resolved photoluminescence for the Tb^{3+} main emission line (~545 nm, $^5D_4 \rightarrow {}^7F_5$) excited at 375 nm. At as-grown, **Figure 5.13 (a)** exhibits a nonexponential dependence. At 800 and 900 °C, **Figures 5.13 (b)** and **(c)** exhibit almost monoexponential curves. Thus, indicating a reduction in the rate of non-radiative pathways, i.e., an enhancement of the local environment of the excited Tb ion by the reduction of defects acting as energy loss centers. Annealing treatment could also reduce back-transfer by changing the density of states in the host. The average luminescence lifetimes ($\bar{\tau}$), which result from a two-exponential fit of the decay curves, are consigned in **Table 5.5**. From these, we can say that in both cases (low and high carbon content), increasing the annealing temperature reduces the non-radiative recombination rate, thus leading to an increase in $\bar{\tau}$. Carbon seems to enhance the excitation coming from the $^5D_3$ and higher Tb levels (**Figures 5.12 (d)-(f)**), and at the same time slightly decreases the luminescence lifetime value. Thus, the increase of carbon up to ~12 at.% does not have a strong degradation effect in the Tb luminescence, which explains the exponential behavior of the PL decay curves at high temperatures.

Figure 5.12. PL spectra of Tb-doped samples at 375 nm excitation wavelength, (a) at as-grown, (b) at 800 °C, and (c) at 900 °C annealing temperature. PLE spectra of Tb-doped samples at 545 nm detection wavelength, (d) as-grown, (e) at 800 °C, and (f) at 900 °C annealing temperature.

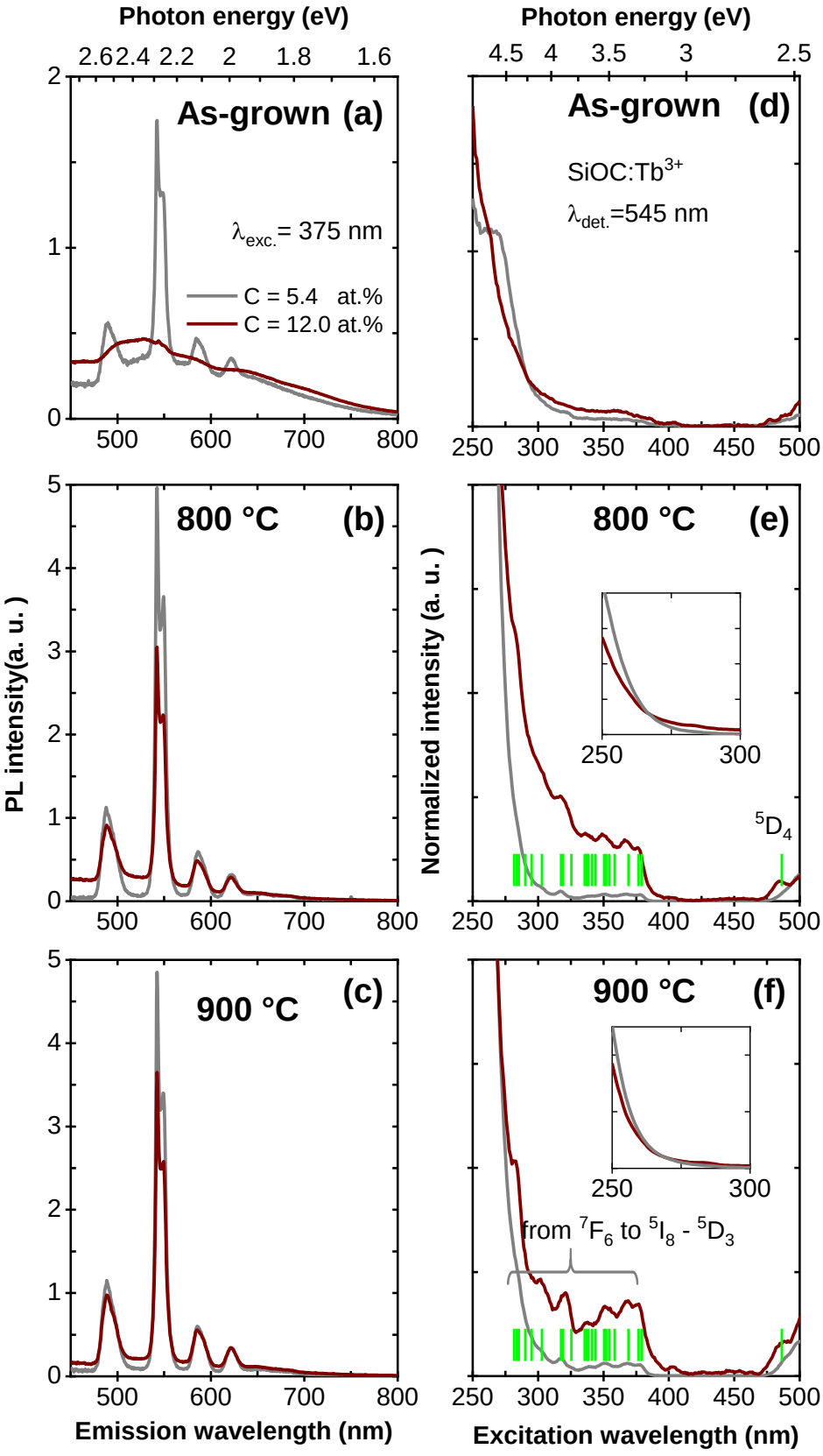

Figure 5.13. Normalized decay curves for Tb doped samples at 375 nm excitation wavelength, (a) as-grown, (b) at 800 °C, and (c) at 900 °C annealing temperature. All measurements were taken at room temperature.

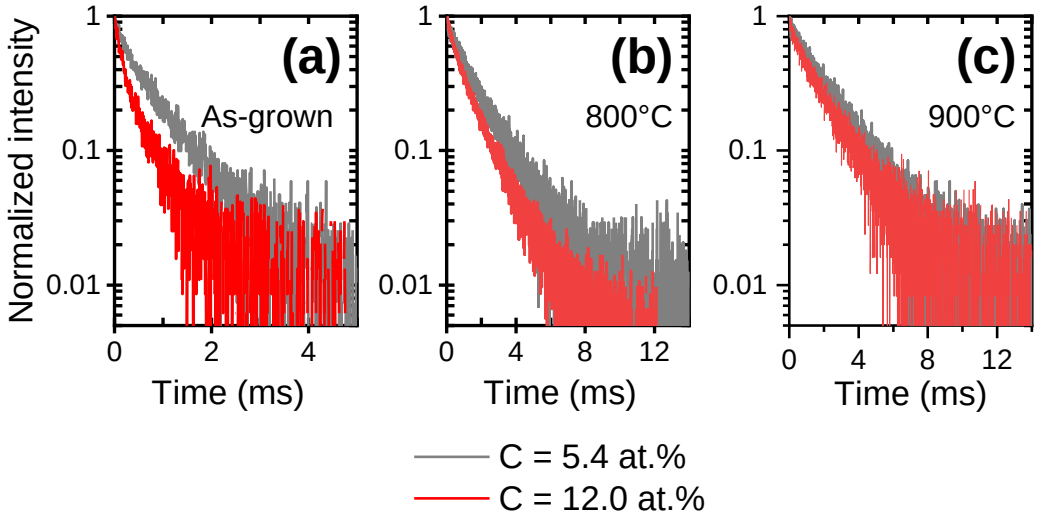

Table 5.5. Tb average luminescence lifetime for Tb doped samples with different carbon concentrations.

Sample	$\bar{\tau}$ (ms)	
	C = 5.4 at%.	C = 12.0 at%.
as-grown	0.85 ± 0.01	0.54 ± 0.03
800 °C (4 h)	1.80 ± 0.03	1.41 ± 0.01
900 °C (4 h)	2.19 ± 0.01	1.93 ± 0.02

Discussion

In **section 5.3.1** was established that for Tb excitation, energy absorption must first occur in the host (via a near band-to-band transition), following by thermalization processes that will take place towards the band edges. Afterward, energy transfer from the host to the Tb ions will leave ions in the excited state, subsequently undergoing radiative transitions. Therefore, the photoluminescence process can be divided into (1) absorption of a photon by the host matrix, generating an electron-hole pair, (2) transfer of the excitation to an RE ion, and (3) emission of the RE ion. During any of the steps (1), (2), and (3), non-radiative loss of the energy might occur. In the following, we will discuss the Tb excitation mechanism in *a*-SiOC based on the mechanisms proposed in **Figure 5.11**.

In the first excitation mechanism in **Figure 5.11 (a)**, the non-radiative energy transfer associated with RE excitation mediated by a RE-related level requires two successive steps [197], (1) trapping of an electron–hole pair (exciton) at a RE-related level in the semiconductor bandgap, i.e., RE excitation involves carriers localized at a certain RE-related level, following by (2) 4f electrons are excited by the Auger process. For instance, The Er

ion in crystalline Si samples co-implanted with oxygen was reported to fulfill the mentioned excitation mechanism where the RE-related levels were associated with Er−O complexes [198]. However, if exciton dissociation occurs before the energy transfer takes place, the effective excitation rate will be severely reduced. Therefore, carrier thermalization will become increasingly important as the temperature increases [198]. Thus, at room temperature, we rule out this type of excitation for Tb in *a*-SiOC:H.

In the second excitation mechanism, the nonradiative energy transfer mediated by Si nanoclusters in **Figure 5.11 (b)** requires the strong coupling between the RE ion and the Si nanoclusters [190]. The introduction of Si nanoclusters can improve the RE luminescence in Si-rich oxides host [191]. Defects such as Si nanocrystals [191,199] or Si nanoclusters [200,201], formed due to phase separation, could be efficient sensitizers for RE^{3+} ions. Given that the studied samples in this work contain silicon in their composition, the formation of nanostructures might be expected after the annealing treatments. Standard silicon compatible processes, e.g., ion implantation of Si in SiO_2 or deposition of Si-rich silicon oxide layers (SiO_x), require high-temperature annealing (usually higher than 900 °C) to induce Si nanocrystal formation. Nevertheless, in this work, the Si content in samples and the post-annealing deposition until 900 °C rule out the presence of Si nanoclusters as far as the Si composition in *a*-SiOC (**Table 5.1**) was lower than the reported in those cases (higher than 40 at.% [202]).

The excitation mechanisms, third and fourth in **Figures 5.11 (c)** and **(d)**), showed the defect-related Auger excitation (DRAE) mechanism [192,193] and the nonradiative resonant energy transfer by dipole coupling (Förster interaction) mechanism [184], respectively. In both cases, Tb excitation mediated by defect states (left by Si dangling bonds) located near the middle of the bandgap was disregarded. This is because the SiDBs state reported in SiOC is located at 1.85 eV from the valence band [95], making it energetically lower than the required excitation energy for Tb excitation (~3.26 or 2.54 eV), see **Figure 5.14**. On the other hand, when the excitation mechanism involves transitions between Urbach tail states, the DRAE mechanism can satisfy the Tb excitation. It is known that in the Auger-type excitation, the multiphonon transitions is taking into account for energy compensation [195]. In our case, the energy transfer between the host and the Tb transition (from the ground state to the $^5D_3$ excited state) could be satisfied by the multiphonon contribution, being possible due to the small energy mismatch between the transitions in the host and the Tb ion. In the case of the Förster mechanism, a spectral overlap is needed between the Tb absorption energy (above $^7F_6 \rightarrow {}^5D_3$, ~3.26 eV) and the matrix emission (~2.2 - 3.1 eV). So, for high

energies, the Förster mechanism is not satisfied. However, for low energies, at ~2.54 eV ($^7F_6 \rightarrow {}^5D_4$), the dipole coupling mechanism can well satisfy the Tb excitation.

According to the above lines, the DRAE and Förster mechanism can both play an important role in the Tb excitation. The proposed excitation mechanism is shown in **Figure 5.14**. The schematic diagram shows the possible transitions leading to the excitation of Tb in the *a*-SiOC:H matrix. Process (I) shows an excitation caused by a band-to-band transition. Process (II) shows the thermalization process towards the tail states. Process (III) shows the non-radiative recombination at the SiDB-related deep defects. Process (IV) shows the matrix recombination, which corresponds to the transitions between the states located in the tails of the valence and conduction bands. Finally, process (V) shows the energy transfer from the host to the Tb ion. Note that the increase of the energy transfer rate (process (V)) limits the recombination rate of the matrix, which would result in the quenching of host luminescence coming from the process (IV). Moreover, if process IV (transitions between the states located in the tails) is the Tb excitation source, we should observe a quenching of the matrix luminescence, and at the same time an increase in the Tb luminescence. This requirement is clearly satisfied from As-grown to 900 °C (**Figure 5.12 (a)-(c)**) for low and high carbon-doped samples. It is also important to mention that the process (V) might be limited by the energy transfer from the Tb ion to the host (back-transfer [203–205]), which would limit its luminescence.

Figure 5.14. Schematic representation of the mechanism for Tb ion excitation in Tb-doped *a*-SiOC:H. Energy levels are not scaled, adapted from [134].

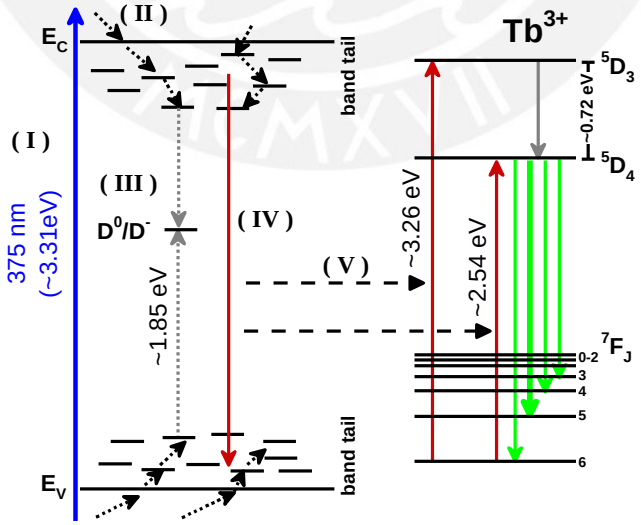

5.4.2 Yb^{3+} luminescence in *a*-SiOC:H

In this section, the behavior of the Yb^{3+} ion luminescence as a function of the carbon composition is studied in Yb-doped samples. **Figures 5.15 (a)** and **(b)** show the host luminescence spectra in Yb-doped *a*-SiOC:H matrix for two representative samples with 8.6 and 40.1 at.% carbon concentration, corresponding to low and high carbon compositions, respectively. The Yb concentration was 2.1 at.% and 2.9 at.% for C=8.6 at.% and 40.1 at.%, respectively. The difference in the shape of the host emission spectra can be explained by the different carbon compositions in samples (**Chapter 4**). **Figure 5.15 (c)** shows the Yb emission spectra in the *a*-SiOC:H matrix at 500 °C. The main peak at ~980 nm and a sub-peak at ~1020 nm result from the 4f transitions between the Stark levels of the $^2F_{5/2}$ excited and $^2F_{7/2}$ ground state. **Figure 5.15 (d)** shows the PLE spectra for both mentioned samples detected at 980 nm. The spectra show no major difference. So, the increase of carbon does not seem to alter the excitation process. Moreover, as discussed in **section 5.3.3**, the defect states responsible for the host excitation are also available for the Yb^{3+} ion.

Figure 5.15. Host PL spectra of Yb-doped samples at 375 nm excitation wavelength, (a) carbon 8.6 at.% and Yb 2.1 at.%. (b) carbon 40.1 at.% and Yb 2.9 at.%. (c) Yb PL spectra of Yb-doped samples at 375 nm excitation wavelength. (d) Yb PLE spectra at ~980 nm detection wavelength at 500 °C annealing temperature.

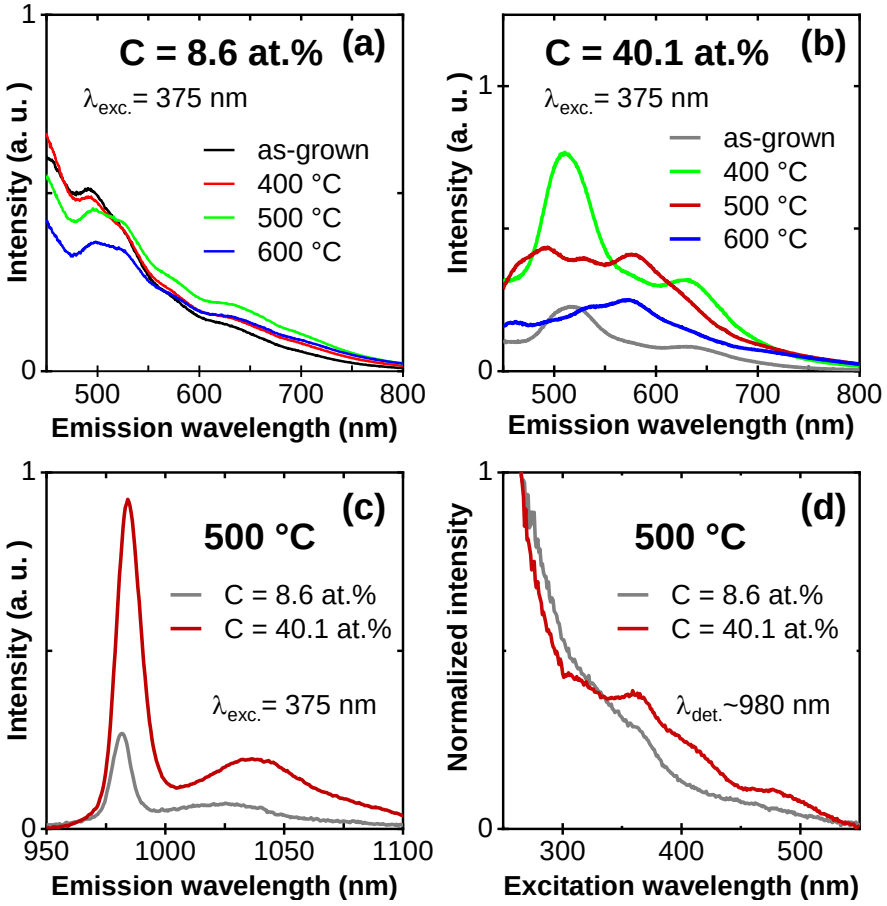

Figures 5.16 (a) - (c) show photoluminescence decay curves for the Yb^{3+} main emission line (~980 nm) up to 600 °C annealing temperature. The non-monoexponential dependence of the Yb PL decay curves indicates the presence of energy migration offsite of the ion, e.g., the non-radiative energy transfer from Yb^{3+} ion to structural defects or others ions. The average luminescence lifetimes ($\bar{\tau}$) were calculated by multi-exponential fits (**equation 5.1**). The resulting lifetime values from a two-exponential fit are presented in **Table 5.6**. According to results, non-radiative processes are reduced with increasing temperature as the $\bar{\tau}$ values increase up to 500 °C. However, the non-exponential behavior is maintained.

Figure 5.16. Normalized decay curves for Yb-doped samples at 402 nm excitation wavelength, (a) at as-grown, (b) at 500 °C, and (c) at 600 °C annealing temperature. All measurements were taken at room temperature.

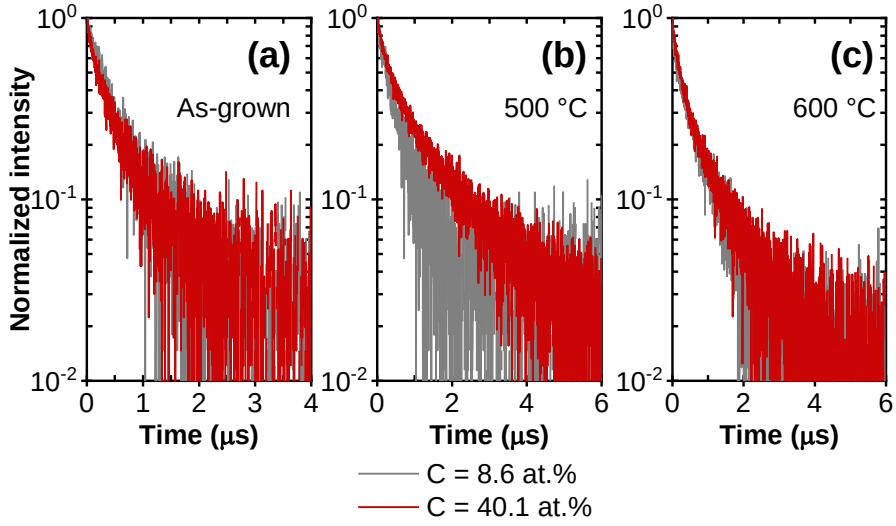

In addition to the analysis of the luminescence intensity, it is also important to study the luminescence quantum yield. The luminescence lifetime (τ_{RE}) and the intrinsic quantum yield (Φ_{int}) are related by **equation 5.10** [206]. Therefore, the quantum yield can be evaluated by observing changes (shorter or longer) in lifetime values. According to **Table 5.6**, the sample with high carbon content shows long luminescence lifetimes at all stages of annealing, suggesting an improvement in the Yb luminescence quantum yield as the lifetimes value increases by almost two times due to the presence of carbon in the matrix.

$$\Phi_{int} = \frac{\#photons_{em}^{RE}}{\#photons_{abs}^{RE}} = \frac{k_R}{k_R + k_{NR}} = \frac{\tau_{RE}}{\tau_{RE}^{rad}} \qquad (5.10)$$

Where,

$\#photons^{RE}$ is the number of absorbed (abs) or emitted (em) photons per unit time by the RE^{3+} ion.

k_R is the rate constant of a radiative process.

k_{NR} is the cumulative rate constant of the nonradiative processes.

τ_{RE}^{rad} is the radiative lifetime of the RE excited state.

Table 5.6. Average luminescence lifetime for Yb-doped samples with different carbon concentration.

Sample	$\bar{\tau}$ (μs)	
	C = 8.6 at%.	**C = 40.1 at%.**
As-grown	0.63 ± 0.07	0.94 ± 0.13
400 °C	0.86 ± 0.07	1.85 ± 0.05
500 °C	0.88 ± 0.05	1.56 ± 0.05
600 °C	0.79 ± 0.02	1.00 ± 0.04

The Yb photoluminescence was studied from 8.6 to 40.1 at.% carbon concentrations for samples with Yb doping from 2.1-2.9 at.%. The excitation wavelength was 375 nm. In order to compare the Yb and matrix luminescence intensity of different samples, Yb photoluminescence spectra were integrated and normalized to the maximum value for each sample. It was label by Yb PL. This procedure was repeated for matrix luminescence. The Yb PL and host PL in the carbon concentration range from 8.6 to 40.1 at.% are shown in **Figures 5.17 (a)** and **(b)**, respectively. The maximum host emission is reported at 400 °C annealing temperature for carbon concentrations below 30 at.%. The Yb^{3+} ion emission for the low-carbon samples is reached at 600 °C, while with increasing carbon, the maximum luminescence is obtained at a lower temperature (~500 °C). Therefore, increasing carbon concentration allows achieving an early Yb luminescence activation upon the annealing process.

Figure 5.17. (a) Normalized Yb PL of Yb-doped *a*-SiOC:H samples. (b) Normalized matrix PL of Yb-doped *a*-SiOC:H samples. The carbon composition was set up between ~9 and 40 at.%, annealing treatments were performed up to 600 °C.

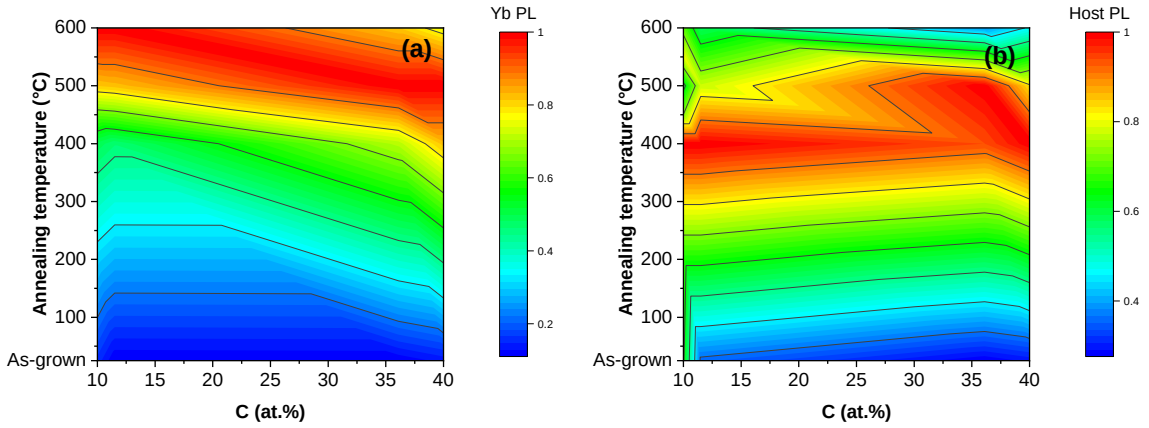

Discussion

It is known that extrinsic dopants play an important role in activating the luminescence of the RE ion. In the case of carbon, it has been reported to reduce the Er clustering phenomenon in SiOC compared to the silicon oxide matrix [150,151], consequently increasing the luminescence of the RE ion. This is because it promotes higher diffusion of Er ions during annealing treatments [196]. In addition, carbon has been reported to improve the Er [156,157] and Tb [158] luminescence. In the following, we will discuss the Yb excitation process in the *a*-SiOC:H matrix based on the mechanisms previously shown in **Figure 5.11**.

In the first excitation mechanism, the nonradiative energy transfer mediated by a RE-related state (**Figure 5.11 (a)**) requires an exciton bound to a RE-related level. However, if exciton dissociation occurs before energy transfer takes place, the effective excitation rate through this mechanism will be drastically reduced. Therefore, at room temperature, similar to the discussion for Tb excitation, we can rule out this type of excitation for the Yb^{3+} ions in the *a*-SiOC:H matrix. In the second excitation mechanism, the RE excitation mediated by Si nanoclusters (**Figure 5.11 (b)**) requires the formation of Si structures. However, high temperatures (generally above 900 °C [207]) are required, and it is outside the temperature range studied for the Yb-doped samples. Furthermore, the Si content in the samples rules out the presence of such Si nanoclusters as an excess of this atom is needed (above 40 at.% [202]) for the formation of such nanoclusters. Moreover, their luminescence, typically at 800 nm [208], was not observed in the spectra obtained in the IR range. Therefore, this mechanism was excluded in the case of Yb-doped *a*-SiOC:H.

The defect-related Auger excitation (DRAE) mechanism and the nonradiative resonant energy transfer by dipole coupling (Förster interaction) mechanism, these could satisfy the Yb^{3+} ion excitation because both can mediate the excitation by defect states (left by dangling bonds) located near the middle of the bandgap. In this case, the defects located near the middle of the bangap are the SiDBs reported in SiOC, which are 1.85 eV above the valence band [95]. Moreover, as the excitation energy required for the excitation of the Yb ion is ~1.27 eV, this transfer would be energetically possible. In addition, the energy difference is compensated by the multiphonon contribution.

The proposed Yb excitation mechanism is depicted in **Figure 5.18**. In the schematic diagram, Process (I) shows an excitation caused by a band-to-band transition. Process (II) shows the thermalization process towards the tail states. Process (III) shows the matrix recombination, which corresponds to the transitions between the states located in the tails of the valence and conduction bands. Process (IV) shows the non-radiative recombination at the SiDB-related deep defects. Process (V) shows the energy transfer from deep defects to the Yb^{3+} ion. Note that the density of SiDB-related defects would limit the energy transfer rate (process (V)). In addition, processes (III) and (IV) are also competitive. Thus, a decrease in the host radiative recombination rate would indirectly benefit the excitation of Yb ions in the Yb-doped *a*-SiOC:H samples.

Figure 5.18. Schematic representation of the mechanism for Yb^{3+} ion excitation in Yb-doped *a*-SiOC:H. Energy levels are not scaled.

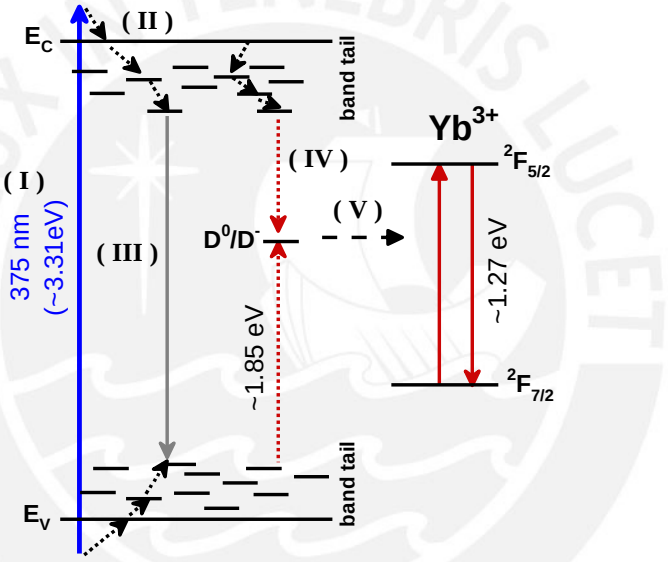

The increase in the SiDBs density has been reported by Street et al. (1985) in *a*-Si:H [209]. The density of intrinsic defects would increase by the introduction of extrinsic dopants (in our case by the Yb doping) and the increase of carbon composition. Two notable aspects were reported after doping in the *a*-Si:H matrix: 1) the density of dangling bonds is an order of magnitude higher than in the equivalent undoped material. 2) the dangling bond density increases as the square root of the doping concentration. Therefore, an effective Yb ion excitation by SiDBs can be expected in *a*-SiOC:H. Summarizing the results, the increasing annealing temperature and the increasing carbon composition can enhance the Yb luminescence through energy transfer mediated by defect states located near the middle of the bandgap. However, an excessive increase of carbon composition would lead to a higher non-radiative recombination rate at carbon-related defects, which would lead to a total quenching of the Yb luminescence.

5.5 Conclusions

In this section, the Tb^{3+} and Yb^{3+} ion luminescence was studied in the *a*-SiOC:H matrix. The role of the matrix (different carbon compositions) and the effect of the annealing treatments on the luminescence were discussed. The photoluminescence intensity was measured for a sample at different annealing temperatures from as-grown to 1000 °C (for the Tb-doped samples) and 700 °C (for the Yb-doped samples). PLE and transient PL measurements were also carried out.

The dynamics of Tb^{3+} ions relaxation under an increasing excitation power of the excitation light were studied by a two-level model. The typical sigmoidal curve starts at the low excitation power with a linear relationship between the PL intensity and the excitation power. Conversely, increasing the excitation power left a sub-linear dependency indicating the starting of the PL intensity saturation. Results point out that the sublinear dependence refers to an indirect excitation of the Tb^{3+} ion by the *a*-SiOC:H matrix. Furthermore, excitation spectra (PLE) and absorption coefficient verify that the excitation occurs from the host towards the Tb^{3+} ion. The increasing PL intensity with annealing temperature suggests an increasing total number of optically active Tb^{3+} ions. In addition, the Tb PL intensity saturation is understood as a limited number of host-provided sensitizers which lead to a limited Tb luminescence.

In Tb-doped samples, the passivation of deep defects, such as silicon dangling bonds above 700 °C, can explain the significant enhancement of Tb luminescence as well as the increasing Tb lifetime in the *a*-SiOC:H matrix. The increase of carbon composition enhances the excitation coming from the 300 – 400 nm range. Also, the $^5D_3$ and higher levels strong contribute to $^5D_4$ population, increasing the $^5D_4 \rightarrow {}^7F_J$ (J = 3,4,5, and 6) emission lines. Carbon doping also affected the Tb intensity ratios. The last effect could be ascribed to a change in the Tb^{3+} ion local environment, which changes the transition probability of the excited ionic centers. In addition, the increase of carbon up to ~12 at.% does not leave a strong shortening in the Tb luminescence lifetime. This indicates that carbon does not add sources of non-radiative recombination for the Tb^{3+} ion. However, high carbon doping should be limited due to the formation of carbon structures that can re-absorb the Tb emission. Finally, the defect-related Auger excitation (DRAE) and the nonradiative resonant energy transfer by dipole coupling (Förster interaction) can both satisfy the Tb excitation when the mechanism requires transitions between matrix localized tail states.

In Yb-doped samples, the main peak at ~980 nm and a sub-peak at ~1020 nm result from the 4f transitions between the Stark levels of the $^2F_{5/2}$ excited and $^2F_{7/2}$ ground state. The Yb doping does not modify the radiative recombination sources in the host (tail states, unpassivated bonds, neutral vacancies left by oxygen). Also, the defect states responsible for the host excitation are also available for the Yb^{3+} ion, because the same band in the PLE spectra was observed for the case without (and with) doping. Furthermore, the increase of carbon composition does not seem to alter the Yb excitation mechanism.

Carbon concentration and annealing temperature optimization led to a maximum Yb luminescence activation at 500 °C for carbon compositions higher than ~25 at.%, and at 600 °C for low carbon compositions. The Yb lifetime was increased from 0.88 to 1.85 μs with increasing carbon concentration. Therefore, samples with high carbon content showed longer luminescence lifetimes, suggesting an increase in the Yb luminescence quantum yield by the carbon incorporation into the matrix.

The enhancement of Yb luminescence with increasing annealing temperature was related to the creation of intrinsic defects (such as the SiDBs) located near the middle of the bandgap. The hydrogen evolution in the *a*-SiOC:H matrix would leave a silicon dangling bond (SiDB) behind for annealing temperature below 600°C. Moreover, an increase in the density of such intrinsic defects can be expected due to the extrinsic Yb doping and the increasing carbon composition. Therefore, an early quenching of the host luminescence in Yb-doped *a*-SiOC:H can be expected. The defect-related Auger excitation mechanism (DRAE) and the nonradiative resonant energy transfer by dipole coupling (Förster) mechanism, both satisfy the Yb ion excitation when the mechanism involves energy transfer from deep localized states such as SiDBs in the middle of the bandgap to the Yb^{3+} ion.

CHAPTER 6. Results and Discussion: Yb-Tb doped *a*-SiOC:H thin films

One of the applications studied for RE ions is their use in silicon solar cells' spectral up- and down-converter systems. One of the main limiting factors in solar energy conversion efficiency into electricity is the spectral mismatch. Low-energy photons are not absorbed by the solar cell, while high-energy photons are not used efficiently due to thermalization [34,210]. In the case of up-conversion (UC), two low-energy photons are absorbed by the RE ions emitting one high-energy photon, which can be subsequently absorbed by the solar cell [211,212]. In the case of down-conversion (DC) or quantum cutting (QC), one high-energy photon is absorbed by the RE ions to emit two low-energy photons, which can be efficiently absorbed by the solar cell [62,64].

Among different RE^{3+} ions systems for near-infrared QC applications, those including Yb ions seem to be the most appropriate because the Yb ion has a transition at about 980 nm (~1.22 eV) from the $^2F_{5/2}$ to the $^2F_{7/2}$ energy level just above the crystalline silicon bandgap of 1.1 eV. As a consequence, the losses by thermalization would diminish in the silicon solar cells. The Yb ion has been used, for example, together with the Pr [59,213], Nd [214], or Tb [52,215] ions. In the latter case, the Tb ion has a transition from the excited state $^5D_4$ to the ground state $^7F_6$ at about 488 nm (~2.54 eV), which has around twice the photon energy of the Yb ion transition. Therefore, one high-energy photon absorbed by the Tb ion might transfer energy to two neighboring Yb ions.

In this section, the effect of annealing treatments and co-doping with Tb ions on the Yb luminescence in *a*-SiOC:H double doped samples was studied. Photoluminescence quantum yield measurements of the spectral converter layers were performed. Finally, the layers were prepared on the front surface of mc-silicon cells and their effect on the external quantum efficiency was studied. Experimental details were reported in **Chapter 3**.

Some of the results of this chapter were published by the author ([216,217]*) in cooperation with K. Y. Tucto, J. A. Guerra, J. A. Töfflinger, E. S. Serquen, and R. Grieseler from Science department, Pontificia Universidad Católica del Perú, and A. Osvet, M. Batentschuk, A. Winnacker, and R. Weingärtner from i-MEET, Department of Materials Science and Engineering, University of Erlangen Nürnberg.*

6.1 Sample composition

Sample compositions are presented in **Table 6.1**. The effect of Tb doping on Yb luminescence was studied in two groups of samples. The first group has a Tb concentration of 0.8 at.% with a variation of the Yb concentration from 1.8 to 6.0 at.%. In order to increase the number of Tb ions available in the vicinity of the Yb ions, the second group has a Tb concentration higher than 1.5 at.%. It is important to mention that the increase of doping would increase the defect density in the matrix [209]. Thus, an increase in the density of such defects might decrease the RE ion luminescence, as they could act as non-radiative relaxation channels.

The Tb percentage was chosen below those reported in energy migration between Tb ions, i.e., to reduce cross-relaxation and luminescence quenching by concentration [218]. The co-doped samples showed an increase in oxygen concentration compared to the undoped samples (last three rows in the **Table 6.1**). This increase in oxygen can be attributed to the affinity of the rare earth elements for oxygen. However, the variations of oxygen up to ~9 at.% and carbon up to ~9 at.% among co-doped sample compositions are not related to the increase or decrease of the total percentage of RE elements but rather to the position of the substrate with respect to the SiC target.

Table 6.1. Elemental composition of *a*-SiOC:H samples (as-grown).

Si at.%	O at.%	C at.%	Tb at.%	Yb at.%	O/C	O+C/Si
28.4	62.9	6.1	0.8	1.8	10.31	2.43
26.3	65.0	4.2	0.8	3.7	15.48	2.63
25.0	56.0	13.1	0.8	5.1	4.27	2.76
22.9	60.7	9.6	0.8	6.0	6.32	3.07
29.3	61.2	5.8	2.6	1.1	10.6	2.29
27.8	57.4	10.9	1.5	2.4	5.27	2.46
27.4	56.7	10.5	1.9	3.5	5.40	2.45
26.9	57.3	10.0	2.6	3.2	5.73	2.50
27.7	56.6	9.9	1.8	4.0	5.72	2.40
26.3	58.1	8.8	1.7	5.1	6.60	2.54
34.6	59.1	6.3	-	-	9.38	Chapter 4
31.85	54.14	6.37			8.5	SiO_2-like [108]
34.25	41.09	17.12			2.4	Si-C-O [108]

6.2 Post-deposition annealing effect on the Tb^{3+} and Yb^{3+} luminescence

In this section, the behavior of the Yb ion luminescence as a function of the post-deposition annealing is studied in co-doped samples. The PL emission spectra of the undoped and the Yb (6.0 at.%) -Tb (0.8 at.%) co-doped samples are shown in **Figure 6.1 (a)**. The host-related broad emission and the typical Tb and Yb emission are clearly observed. At a wavelength higher than 900 nm, the Yb PL signal overlaps with the second-order of the host emission in the infrared region. However, the good coincidence of the host-related emission in the undoped and co-doped samples allows the extraction of the Tb and Yb luminescence after background correction (host emission). The sample emission is clearly assigned to the Tb transitions, occurring at ~545 nm ($^5D_4 \rightarrow {}^7F_5$), 588 nm ($^5D_4 \rightarrow {}^7F_4$), and 621 nm ($^5D_4 \rightarrow {}^7F_3$). The ~980 nm line was identified as the $^2F_{5/2} \rightarrow {}^2F_{7/2}$ Yb transition. The emission of the Tb^{3+} and Yb^{3+} ions after subtraction of the matrix emission is shown in **Figure 6.1 (b)**. To observe the effect of the pos-deposition annealing on the Tb and Yb luminescence, the integrated luminescence signals for different annealing temperatures are shown in **Figure 6.1 (c)**. A significant increase in the Yb luminescence is reached at 500 °C, while for Tb ion, modest growth is reached at 650 °C.

The Tb PLE spectrum detected at 545 nm was also studied for the co-doped sample (**Figure 6.1 (d)**). The spectrum is dominated by matrix excitation, and no major change is observed when compared with the PLE spectrum of the Tb-doped sample at 500 °C. The Yb PLE spectrum is shown in **Figure 6.1 (e)**. It is known that UV radiation is efficiently absorbed by the charge-transfer (CT) states. Therefore, the strong absorption at ~280 nm center band can be associated with the Yb^{3+}-O^{2-} CT band. When comparing it with the one reported in the SiO_2 matrix (~256 nm [174]), a shift to the longer wavelengths is observed. According to the literature, the shift position to the longer wavelength of the CT absorption bands could be related to the increasing covalency of the host lattice [29]. Thus, results suggest a higher covalence of the Yb^{3+}-ligand in the *a*-SiOC:H matrix compared to SiO_2. Additionally, the shift of the CT band to longer wavelengths has also been associated with the increase in the O-coordination of the RE ion in oxides [219].

Figures 6.2 (a) and **(b)** show the time-resolved photoluminescence for the Yb emission line (~980 nm) and the Tb main emission line (~545 nm) excited at 375 nm in Yb (6.0 at.%) -Tb (0.8 at.%)-doped *a*-SiOC:H. The average luminescence lifetimes ($\bar{\tau}$), which result from a two-exponential fit of the decay curves are presented in **Table 6.2**. The non-exponential dependence of the Yb and Tb PL decay curves indicates the presence of

energy migration offsite of the RE ions. Furthermore, a high rate of non-radiative recombination can be inferred due to the short Tb lifetime. Energy loss by processes like excited-stated absorption (ESA) or cooperative up-conversion (CUC) can be ruled out due to the low Tb concentration. On the other hand, a major role seems to be played by migration processes related to the energy transfer to defects in the matrix, as well as the energy migration to Yb ions. The increasing temperature (up to 500 °C) leads to a clear increase in the Yb lifetime, explained by the decrease of the non-radiative processes for the Yb ion case (**Table 6.2**). Meanwhile, the small reduction in the Tb lifetime values would refer to a slight increase in its energy migration rate.

Table 6.2. Tb and Yb average luminescence lifetime for a Yb-Tb co-doped sample.

Annealing temperature (°C)	Tb = 0.8 at.% $\bar{\tau}$ (ms)	Yb = 6.0 at.% $\bar{\tau}$ (μs)
as-grown	0.55 ± 0.03	0.69 ± 0.12
400	0.53 ± 0.02	1.09 ± 0.37
500	0.48 ± 0.03	2.19 ± 0.11
600	0.54 ± 0.02	1.65 ± 0.17
700	0.46 ± 0.02	0.58 ± 0.08

Discussion

One of the most studied mechanisms in the Tb-Yb pair is the cooperative transfer mechanism between Tb and Yb used to explain the quantum cutting (QC) process. The QC process has been reported in host glasses, such as phosphate glasses [220], oxyfluoride glass [221], tellurite glass [222], silica-hafnia glass [223], aluminum oxynitride [224], silicon oxycarbide [216], and silicon oxynitride thin films [225] among others. And, It has also been reported in a number of crystalline hosts, examples include yttrium oxide [226], yttrium phosphate [52] among others. Despite numerous papers claiming the existence of QC supported by the cooperative transfer mechanism, few actually demonstrate it. This is due to the challenge of proving which energy transfer mechanism is actually operative in a particular pair of RE ions [227].

On the other hand, other mechanisms have also been reported in the Yb, Tb pair; the one-photon process, in which the energy transfer from one Tb to one neighboring Yb ion happens through cross-relaxation (CR) mediated with a virtual level in the Tb ion, and with a subsequent multiphonon decay process in the Tb ion [228]. In addition, CR is well reported to assist the QC process, in the Nd-Yb [214] and Pr-Yb pairs [59,213]. Likewise, the up conversion process, where the energy of two Yb ions is transferred to one Tb ion, has been reported [229,230].

Figure 6.1. (a) PL emission spectra of Yb-Tb co-doped *a*-SiOC:H sample (blue line). The red dashed line shows the matrix emission. The three arrows indicate the ~545 nm ($^5D_4 \rightarrow {}^7F_5$), 588 nm ($^5D_4 \rightarrow {}^7F_4$), and 621 nm ($^5D_4 \rightarrow {}^7F_3$) emission. (b) Yb and Tb PL spectra after background (host emission) correction. (c) Yb and Tb integrated luminescence signal for different annealing temperatures. (d) Tb PLE spectra at 545 nm detection wavelength at 500 °C annealing temperature. (e) Yb PLE spectra at 980 nm detection wavelength at 500 °C annealing temperature. The Yb and Tb concentration were 6.0 and 0.8 at.%, respectively.

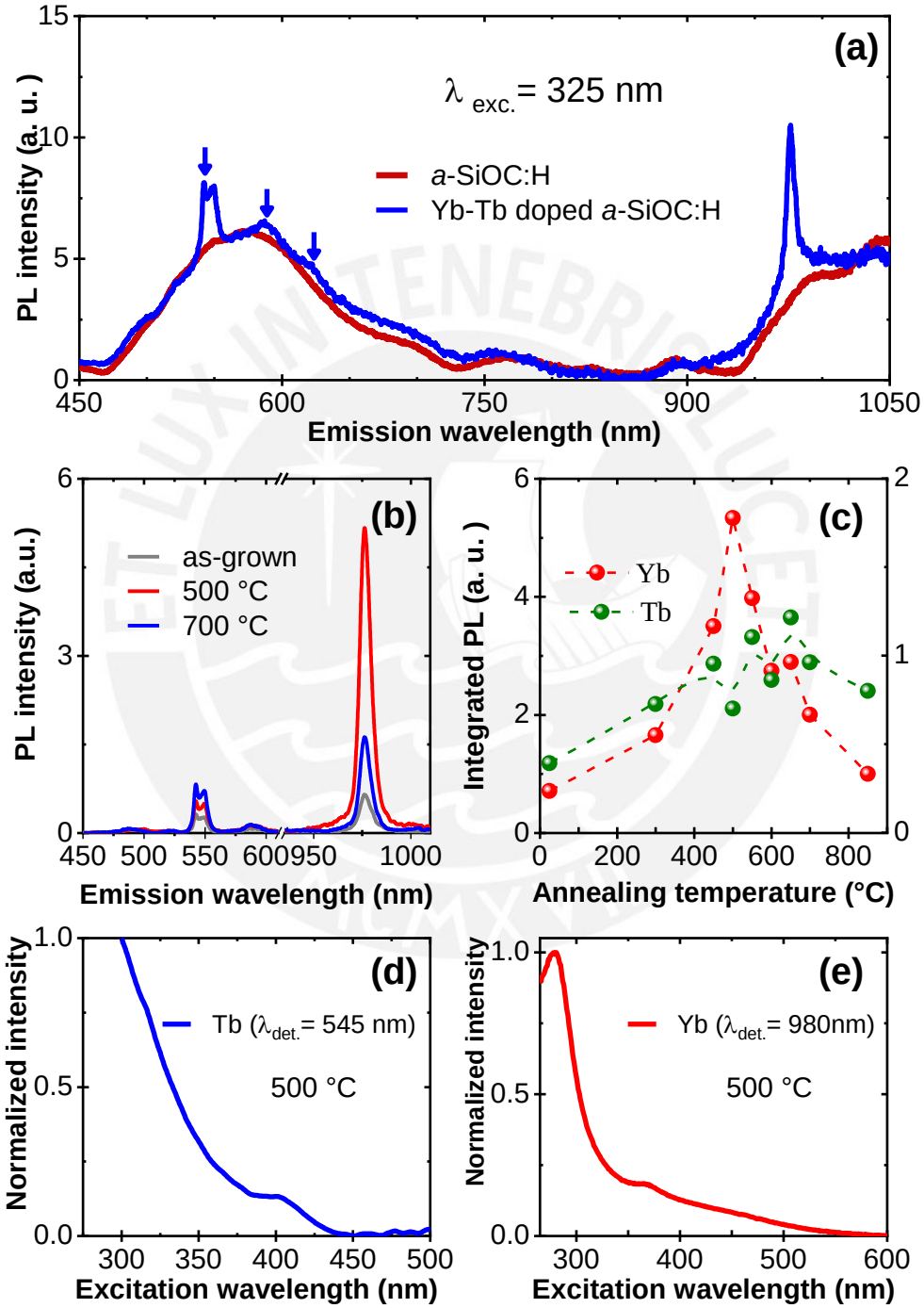

Figure 6.2. Normalized decay curves for Yb-Tb co-doped *a*-SiOC:H samples at 375 nm excitation wavelength, (a) Yb decay curves, detection at 980 nm, (b) Tb decay curves, detection at 545 nm.

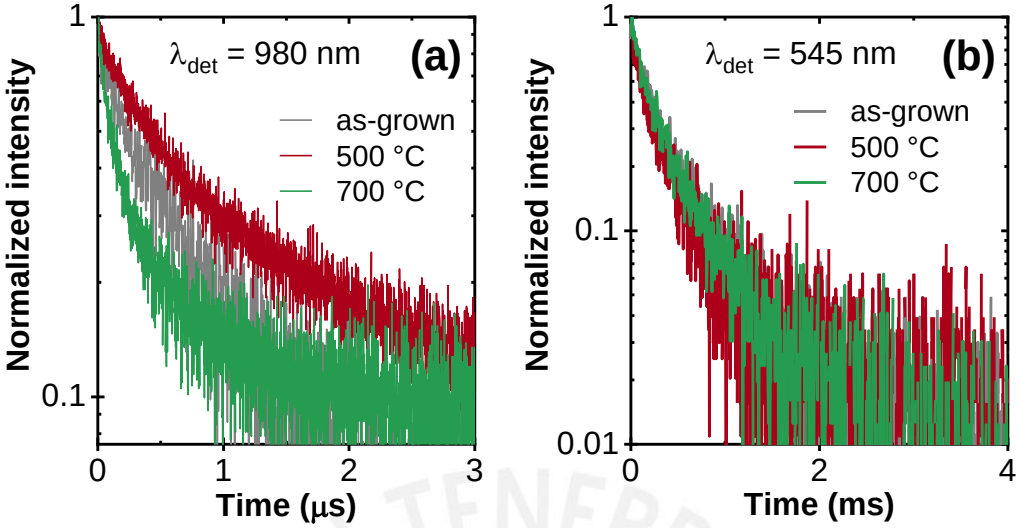

Experimentally, the energy transfer from Tb to Yb ions would be evidenced by observing the transition at 488 nm (corresponding to the Tb ion transition) in the Yb PLE spectrum. According to **Figure 6.1 (e)**, at 488 nm, no signal participating in the Yb excitation is observed. Therefore, there would be no energy transfer, or it would have a low rate of occurrence, e.g., because a proper local spatial distribution of the Tb and Yb ions is required. So, the detector will register a weak signal.

Summarizing results, a low Tb emission intensity is observed in co-doped samples (**Figures 6.1 (b)** and **(c)**) when compared to the luminescence in Tb-doped samples. Furthermore, annealing treatments decrease the Tb lifetime value (**Table 6.2**), in contrast with the results obtained in Tb-doped samples where Tb excited state lifetime increases with the increase of the annealing temperature. At the same time, the annealing treatments increase the Yb lifetime. Therefore, it is clear that the Tb ion changes its luminescence behavior in the presence of Yb ions as well as increases the Yb luminescence. To study the effect of Tb doping in the Yb luminescence, series of samples with different Tb and Yb atomic concentrations were prepared, results will be discussed in **Section 6.4**.

6.3 Yb concentration in Yb-doped *a*-SiOC:H

Improving the phosphor luminescence intensity could be achieved by increasing its concentration. However, it is found that the luminescence decreases if the concentration exceeds a value known as the critical concentration. The increasing doping or co-doping concentrations cause the ionic centers to be close enough to interact. The strong interaction between two active ions can transfer excitation energy from one to the other. The excitation energy can pass from one ion to another and eventually be lost in some defect. This is called concentration quenching or self-quenching (SQ) [231]. Therefore, the luminescence intensity decreases despite increasing RE ion concentration.

Two additional effects, radiation trapping (RT) and cooperative luminescence, are commonly reported when Yb doping is increased. RT arises from the immediate reabsorption of the spontaneous emission of a metastable level by neighboring ions in the ground state [232,233]. Cooperative luminescence is an up-conversion process based on the interaction of two excited ions that decay simultaneously to their ground state, and thus emit a photon of twice the energy in a single transition [234–236]. For this reason, the study of the effect of Yb concentration on Yb luminescence in *a*-SiOC:H samples is addressed in this section.

Table 6.3. Average lifetime of Yb-doped samples with 2.1 and 4.0 at.% Yb doping.

Annealing temperature (°C)	average luminescence lifetime for Yb doped samples	
	Yb = 2.1 at.% (μs)	Yb = 4.0 at.% (μs)
As-grown	0.63 ± 0.07	0.90 ± 0.02
400	0.86 ± 0.07	1.09 ± 0.02
500	0.88 ± 0.05	0.93 ± 0.02
600	0.79 ± 0.02	0.89 ± 0.01

Figure 6.3 shows the trend of the Yb luminescence intensity in Yb-doped *a*-SiOC:H samples (concentration data in **Table 5.1**, **Chapter 5**). The maximum luminescence is achieved at 400°C with 4 at.% doping. Increasing Yb doping leads to emission maxima at low annealing temperatures. For 5.4 at.% Yb concentrations, a strong quenching of luminescence is observed regardless of the annealing temperature. Yb lifetime of two representative samples (for 2.1 and 4.0 at.% doping) are given in **Table 6.3**, the carbon composition of those samples was lower than ~9 at.%. Comparing the Yb luminescence lifetime, the close values suggest that Yb luminescence efficiency is not particular affect by

the Yb concentration, which can be interpreted as that there is no energy migration between the Yb^{3+} ions at 4 at.% Yb doping.

Figure 6.3. Integrated PL intensity in Yb-doped *a*-SiOC:H samples

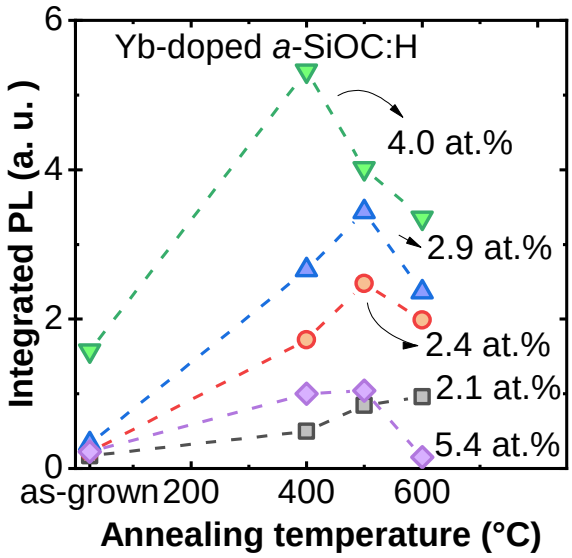

As mentioned, RT and cooperative luminescence processes can also be present with the increasing Yb doping. As there is no increase in luminescence in the 480 - 500 nm range, the cooperative luminescence process can be ruled out for these concentrations. For the RT process, an increasing PL intensity at the lower energy band (~1020 nm) relative to the higher energy band (~980 nm) [237] has been reported. Therefore, the comparison of those bands intensities would indicate the existence of such a mechanism. **Figures 6.4 (a)** and **(b)** compare of two normalized PL spectra for two representative Yb doping concentrations. For Yb doping at 4.0 at.%, the coincidence of the spectra allows us to infer that the ratio of intensities between the two bands remains constant after the annealing process. On the other hand, for Yb at 5.4 at.%, the high increase in the PL intensity at the lower energy band would suggest the contribution of the RT process. Thus, it can be considered as resulting in a strong extinction of the luminescence, as noted in **Figure 6.3**.

Summarizing the results, the maximum Yb luminescence activation was reached after annealing treatments at 400 and 500 °C. The mechanisms of radiation trapping and cooperative luminescence were ruled out for Yb doping up to ~4 at.%, while a strong quenching of the luminescence was observed for higher doping. It is important to note that luminescence lifetime values can be improved by increasing carbon (**Chapter 5**). However, these values are still low when compared to values obtained from other glasses. Therefore, in the next section, we will study the improvement of the Yb emission efficiency by co-doping with Tb.

Figure 6.4. Normalized PL spectra of two representative Yb doping concentrations in Yb-doped *a*-SiOC:H samples **(a)** 4.0at% and **(b)** 5.4 at.%.

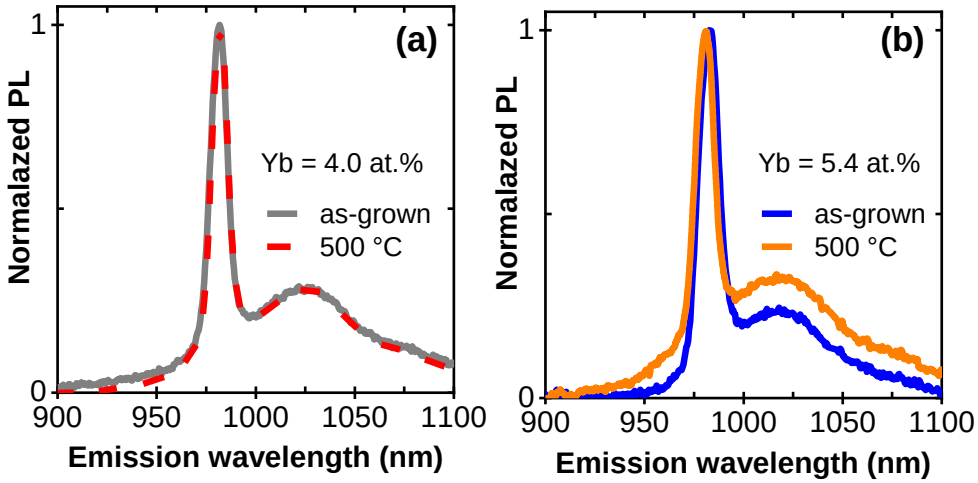

6.4 Tb concentration effect on the Yb^{3+} luminescence

The previous study gives information about: (1) the behavior of Yb luminescence with thermal annealing, (2) The Yb lifetimes in samples only doped with Yb, (3) The Yb doping concentration at which the quenching of Yb luminescence would be observed. Next, we seek to improve the luminescence of Yb through co-doping with Tb. Therefore, in this section, the effect of Tb doping on Yb luminescence was studied. It is important to note that introducing a new dopant would increase the defects density in the matrix, so it is necessary to keep the total percentage of rare-earth doping as low as possible to minimize this effect.

PL spectra of two representative samples with Yb (1.8 at.%)-Tb (0.8 at.%) doping and Yb(6.0 at.%)-Tb (0.8 at.%) were studied. The PL spectra in the visible and IR region are shown in **Figures 6.5 (a)-(d)**. In the visible region, the broad luminescence of the matrix is observed as well as the main Tb emission at ~545 nm. The Yb emission corresponding to the Stark splitting levels is observed at ~980 nm and ~1020 nm. A similar carbon concentration was maintained in all cases, which is verified with the same shape of the matrix emission as shown in **Figures 6.5 (a)** and **(c)**.

By increasing the Yb doping and keeping the Tb doping constant, the maximum Yb emission was reached at a lower annealing temperature. To verify this trend, samples with Yb concentrations of 3.7 and 5.1 at.% were also studied. Next, to compare the Yb luminescence intensity of the different samples, Yb photoluminescence spectra were integrated and normalized to the maximum value for each sample. It was label by Yb PL. **Figure 6.6** shows the Yb PL in the concentration range from 1.8 to 6.0 at.%. With increasing Yb doping, it is verified the intensity maxima are reached at a lower annealing temperature.

This behavior can be explained by considering that a higher dopant percentage leaves a more significant number of active ions. Therefore, quenching of luminescence is expected to appear early at the annealing temperature.

Figure 6.5. PL spectra in the visible and IR region for two representative Tb (0.8 at.%) and Yb (1.8 and 6.0 at.%) doping concentrations. (a) and (c) PL spectra in the visible range. (b) and (d) PL spectra in the IR region at 375 nm excitation wavelength.

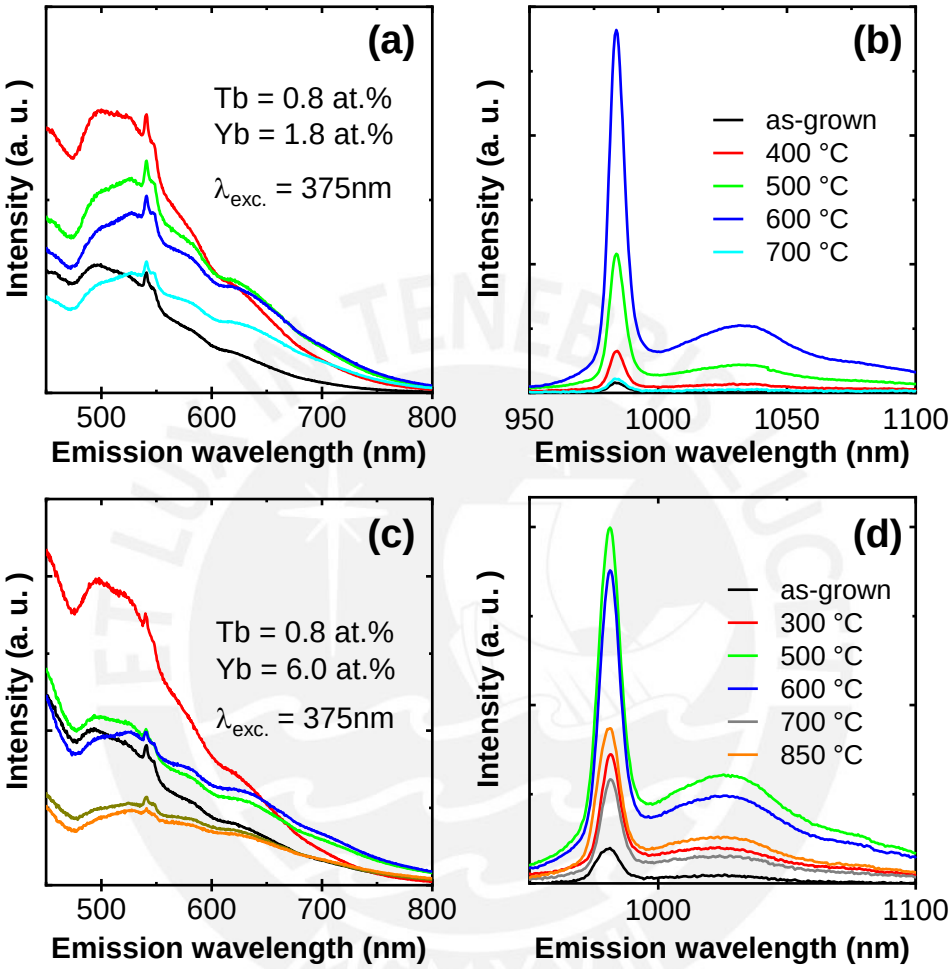

It is also important to discuss the weak Tb emission signal obtained in the co-doped samples (**Figures 6.5 (a)** and **(c)**). The low Tb luminescence suggests modifications during the Tb excitation (and emission) process, which may be due to 1) the Tb in the ground state finds fewer available channels for its excitation, which disfavors its luminescence. 2) the excited Tb state could transfer its energy towards the Yb ion(s). 3) The excited Tb ion undergoes a quenching of its luminescence due to increased defect density left by the increasing Tb and Yb doping. Thus, to study the effect of Yb co-doping in more detail, transient photoluminescence measurements were taken. The decay curves are observed in **Figure 6.7**, where the Tb decay curves are compared in samples with different Yb concentrations from 0 to 6.0 at.%.

Figure 6.6. Relative Yb PL of Yb-Tb co-doped a-SiOC:H samples. The Tb doping was set up at 0.8 at.%, annealing temperature up to 700 °C.

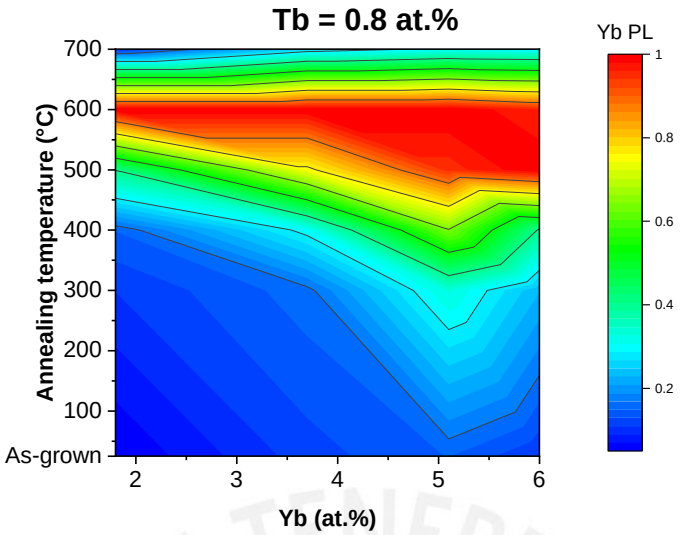

Figure 6.7. Normalized Tb decay curves for Yb-Tb co-doped samples at 375 nm excitation wavelength, detection at 545 nm for samples at 500 °C annealing temperature.

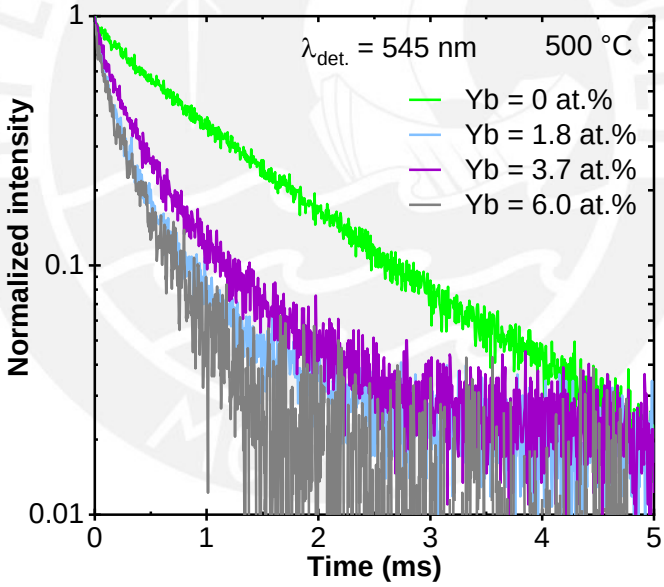

Table 6.4. Tb and Yb average lifetime for Yb-doped, Tb-doped, and Yb-Tb co-doped samples at 500 °C annealing temperature.

	Tb (ms)	**Yb (*μs*)**
Tb = 0 at.% Yb = 2.1 at.%	-	0.88 ± 0.05
Tb = 0 at.% Yb = 4.0 at.%	-	1.09 ± 0.02
Tb = 1.0 at.% Yb = 0 at.% (as-grown)	0.85 ± 0.01	-
Tb = 0.8 at.% Yb =1.8 at.%	0.50 ± 0.02	16.77 ± 0.87
Tb = 0.8 at.% Yb =3.7 at.%	0.72 ± 0.02	1.98 ± 0.12
Tb = 0.8 at.% Yb =6.0 at.%	0.48 ± 0.03	2.19 ± 0.11

The change of exponential behavior (**Figure 6.7**) and the decrease in Tb lifetime values (**Table 6.4**) with increasing Yb doping verify the energy migration offsite the ion, which would imply the transfer of energy, for example, to defects in the matrix, and to the Yb^{3+} ion(s), while energy migration between Tb ions can be ruled out due to the low concentration of the Tb doping. On the other hand, the Yb lifetime values (**Table 6.4**) in the co-doped samples have a significant increase compared to the Yb-doped samples only. Therefore, co-doping with Tb significantly improves the Yb luminescence efficiency while decreasing the Tb luminescence. As mention before, one explanation could be the energy transfer from the excited Tb state to the Yb ion(s). To verify this, samples with Tb centration of up to 2.6 at.% were studied. The chosen Tb concentration is slightly lower than the reported in the literature for Tb luminescence extinction [238]. The results are discussed below.

Figure 6.8. PL spectra in the visible and IR region for two representative Tb (2.6 at.%)-Yb (1.1 at.%) and Tb (1.9 at.%)-Yb (3.5 at.%) doping concentrations. (a) and (c) PL spectra in the visible range. (b) and (d) PL spectra in the IR region at 375 nm excitation wavelength.

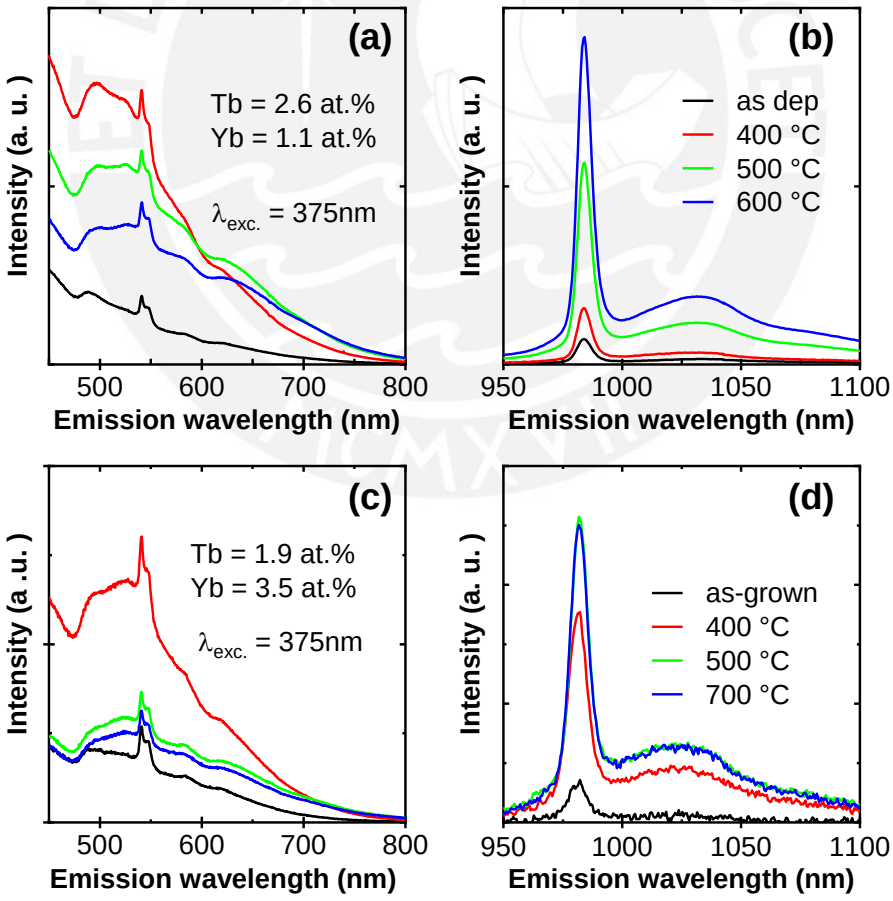

The PL spectra in the visible region and IR region with Tb doping up to 2.6 at.% are shown in **Figures 6.8 (a) - (d)** for two samples. In the visible region, the broad luminescence of the matrix is observed as well as the main Tb emission at ~545 nm, while in the IR region, the Yb emission corresponding to the Stark splitting levels at ~980 nm and ~1020 nm is observed. In all cases, a similar carbon concentration was maintained, which is verified with the same shape of the matrix emission as shown in **Figures 6.8 (a)** and **(c)**. Besides that, comparing the Tb emission signal, an improvement in its luminescence is observed at 1.9 at.%, while a lower Tb emission is reported with increasing Tb doping at ~2.6 at.%. The low luminescence of Tb in the latter case is ascribed to concentration quenching of luminescence.

In order to compare the Yb luminescence intensity of different samples, Yb photoluminescence spectra were integrated and normalized to the maximum value for each sample. **Figure 6.9** shows the Yb PL in the Tb concentration range from 0.8 to 2.6 at.% (atomic composition in **Table 6.1**). Increasing the Tb concentration favors the activation of Yb luminescence at lower annealing temperatures. To study the co-doping effect on the Yb luminescence quantum yield, transient photoluminescence measurements were done.

Figure 6.9. Relative Yb PL of Yb-Tb co-doped *a*-SiOC:H samples. The Tb doping was set up from 0.8 to 2.6 at.%, annealing temperature up to 700 °C.

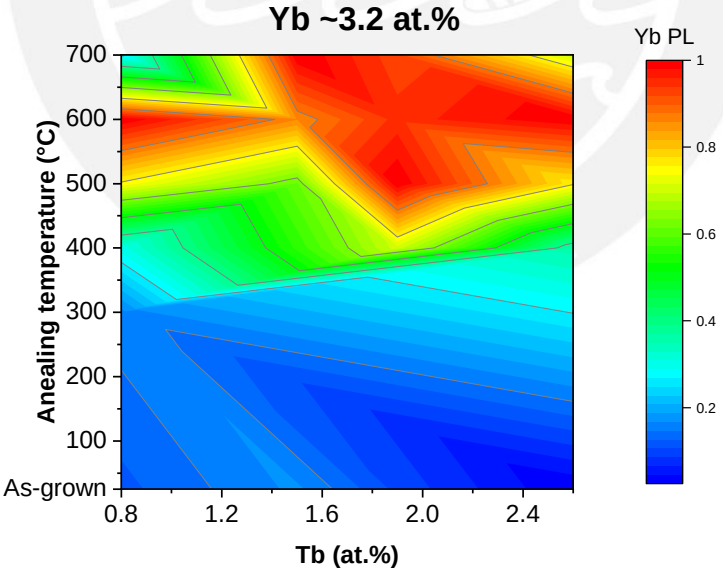

Figure 6.10 shows the lifetime values for Tb main emission (~ 545 nm) and Yb emission (~ 980 nm) for Yb-Tb co-doped and Yb-doped *a*-SiOC:H as a function of RE total concentration. A significant difference is observed in the values achieved for the Yb lifetime. The results can be divided into two groups:

1) Longer Yb lifetimes are achieved for concentrations below ~2 at.% Yb doping. The Yb lifetimes are much longer than those obtained for the Yb single doped samples (**Figure 6.10**). Furthermore, the values remain close even at 2.6 at.% Tb doping.

2) Shorter Yb lifetimes are achieved for Yb concentrations above ~3.5 at.%. However, These Yb lifetimes show relatively higher values when compared with their values in Yb-doped samples.

From the results, long Yb luminescence lifetimes are achieved by co-doping with Tb. Meanwhile, short Tb luminescence lifetimes were recorded (**Table 6.4**). Thus, co-doping with Tb modifies the Tb and Yb emission, making the Yb emission more efficient in Yb-Tb doped samples compared to the Yb-doped case.

Figure 6.10. Average lifetime values for Tb (main emission at ~545 nm) and Yb (~ 980 nm) for Yb-Tb co-doped and Yb-doped *a*-SiOC:H as a function of RE total concentration.

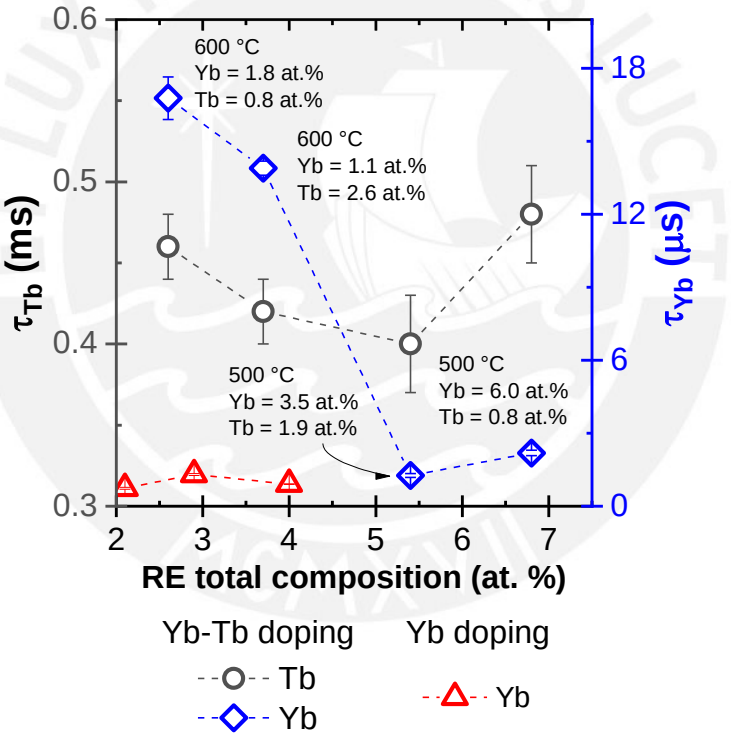

Discussion

The low Tb emission efficiency and the enhanced Yb emission efficiency in co-doped samples could be explained by two possibilities: 1) a Tb^{3+} ion is excited and transfers its energy to a neighboring Yb ion(s), causing a low Tb emission. 2) The Tb excitation may reduce by the reduction of its excitation channels due to doping with Yb.

In the first statement, the energy transfer from Tb to Yb is usually ascribed to a simultaneous sensitizing process (two Yb^{3+} ions). More in detail, there is no spectral overlap

between the Tb emission and Yb absorption spectrum. The energy transfer is then a second-order QC, and it dominates the energy transfer process. Furthermore, According to Jenkins and Andrews [53,54], the second-order mechanism may occur due to two mechanisms, cooperative and accretive. In both mechanisms, a virtual state is involved.

The virtual state is located on the donor for the cooperative pathway, i.e., Tb^{3+} ion, and this ion acts twice as a donor of energy. In contrast, the virtual state is located on one of the acceptors for the accretive pathway, i.e., Yb^{3+} ion. Thus, the cooperative mechanism comprises the simultaneous energy transfer from the donor to two acceptors (**Figure 6.11**). On the other hand, the accretive mechanism is satisfied when the energy is transfer from the donor to one of both acceptors. Afterward, part of such energy is transferred to the second acceptor ion. Despite the proposal of these two mechanisms, only the cooperative energy transfer has been identified in the literature. The study was reported in $Yb_xY_{1-x}PO_4$:Tb by comparing the experimental Tb luminescence decay time for different Yb concentrations [52].

Figure 6.11. Schematic representation of QC by cooperative process in Yb-Tb co-doped *a*-SiOC:H. Energy levels are not scaled.

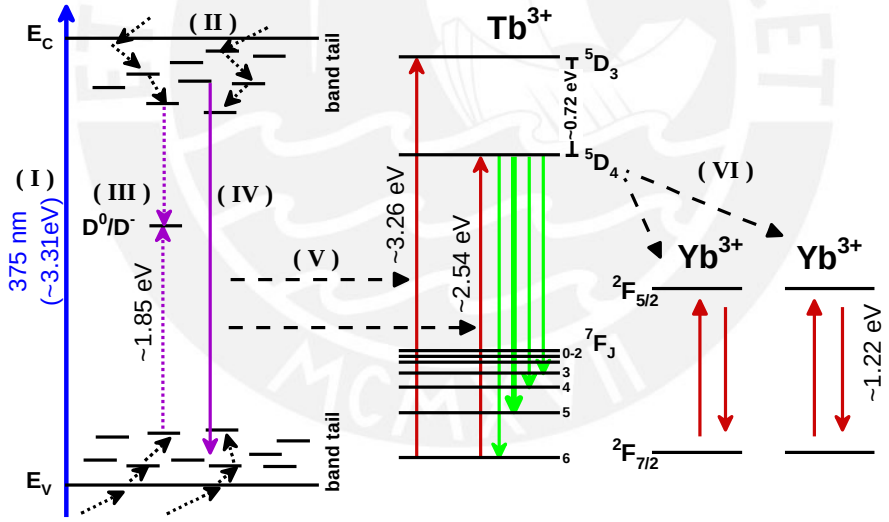

The reduction of the donor (Tb^{3+} ion) lifetime in the presence of the acceptor (Yb^{3+} ion) is usually reported as proof [52] that the energy transfer mechanism takes place. In this work, **Figure 6.7** shows this characteristic. However, the cooperative mechanism, process (VI) in **Figure 6.11**, requires an essential condition between the Tb and Yb lifetimes, i.e., it needs the Tb lifetime to be shorter than the Yb lifetime so that the energy can be transferred. Although results show an improvement of the Yb luminescence and a reduction for the Tb luminescence in the co-doped samples, the Tb luminescence lifetime in milliseconds and the Yb lifetime in microseconds scale would exclude the possibility of

energy transfer from the Tb^{3+} ion to Yb^{3+} ion. Because of this, an additional experiment was directed towards the search for Tb lifetimes in the microsecond range. Experimental details were reported in **Chapter 3**.

Figure 6.12. Average lifetime as a function of annealing temperature. (a) Tb excited state lifetime in milliseconds range detection. (b) Yb excited state lifetime in microseconds range detection. (c) Tb excited state lifetime in microseconds range detection, in Tb-doped and Yb-Tb co-doped samples. (d) matrix excited state lifetime in microseconds range detection.

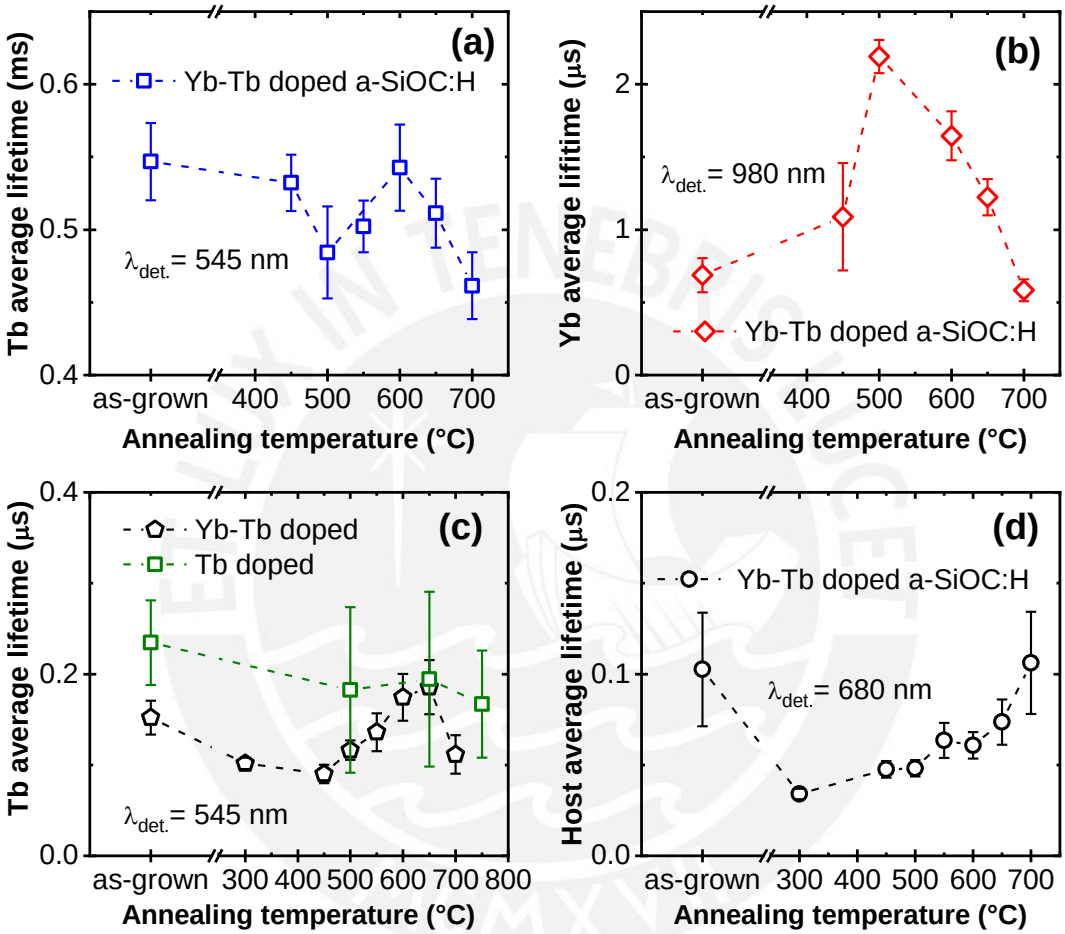

The Tb lifetimes in milliseconds and microseconds scale are shown in **Figures 6.12 (a)** and **(c)**, respectively. The Yb lifetimes are shown in **Figure 6.12 (b)**, and the matrix lifetimes are reported in **Figure 6.12 (d)**. The short host lifetimes are consistent with energy transfer from the host to Tb and Yb ions. The Tb lifetime in microseconds in co-doped samples is slightly shorter than that found in Tb-doped samples, suggesting an additional non-radiative pathway for the Tb excited in the co-doped samples. In addition, the short Tb lifetime would allow the energy transfer from the Tb^{3+} ion to Yb^{3+} ion. Thus, the QC process could be considered as a non-radiative relaxation channel for the Tb excited state. Finally, although the QC process could be considered in the co-doped samples. This is

not entirely correlated with the Tb lifetime reduction on the microsecond scale (**Figure 6.12 (c)**), so there is no conclusive evidence of energy transfer between the Tb^{3+} and Yb^{3+} ions.

On the other hand, at the beginning of the discussion, it was mentioned that the Tb excitation may reduce by a decrease of his excitation channels due to co-doping with Yb. Therefore, the following mechanism is proposed to explain the reducing Tb luminescence. The schematic representation is shown in **Figure 6.13**. For this purpose, the excitation mechanisms proposed in **Chapter 5** for Tb^{3+} and Yb^{3+} ions are used. Process (V) shows the energy transfer from deep defects to the Yb^{3+} ion. Process (VI) shows the energy transfer from Urbach tails to the Tb^{3+} ion. It is important to note that processes (V) and (VI) are indirectly competitive because their excitation channels are competitive in the matrix [217]. This would explain the decrease in Tb luminescence and the increase in the Yb luminescence. Moreover, the increase of SiDBs that favors the excitation of the Yb^{3+} ions reduce the Tb lifetime by acting as energy loss centers. On the other hand, co-doping increases the creation of deep defects such as SiDBs. Perhaps a small difference in the local oxygen distribution around Tb and Yb may favor the creation of such defects.

Figure 6.13. Schematic representation of the mechanism for Yb and Tb ion excitation in Yb-Tb co-doped *a*-SiOC:H. Energy levels are not scaled.

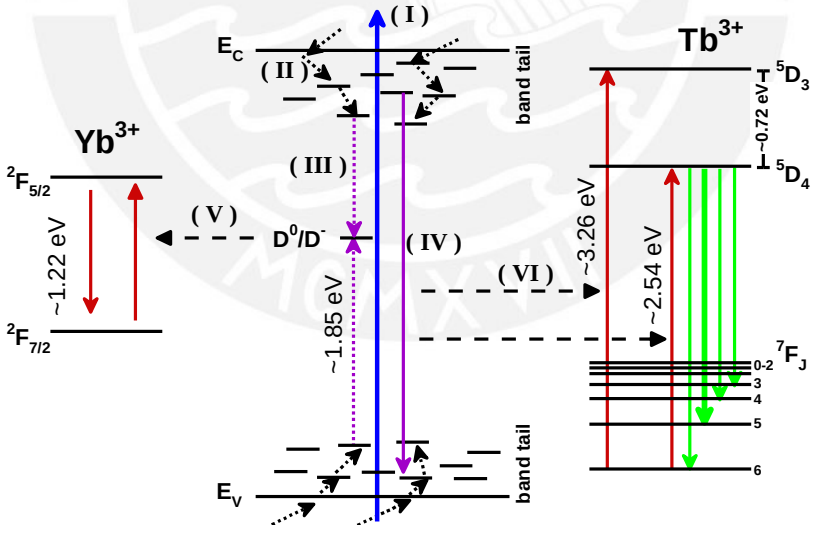

6.5 Photoluminescence quantum yield of Yb-Tb doped *a*-SiOC:H thin films

According to the luminescence spectra obtained in the previous sections, the luminescence of the co-doped films shows visible emission (400 to 800 nm) assigned to the host and the weak Tb luminescence, and the Yb luminescence in the NIR region. Two methods were used to obtain the photoluminescence quantum yield (Φ) in the visible region of the co-doped samples. The absolute method was first performed using an integrating sphere. However, due to the weak signal obtained, the estimation of the photoluminescence quantum yield was performed by the comparative method, i.e., using a reference sample of known Φ.

Absolute method

In the absolute method, an integrating sphere is used to collect all the light emitted and scattered by the luminescent sample. The spectral region is divided into two components: "L" is the wavelength region of the incident irradiance, and "P" is the emission wavelength region of the sample. After taking the spectra, the calculation of

1) L_1: integrated scatter of light (integrated scatter of light at $\lambda_{exc.}$) when the sample holder is empty (in our case with a fused silica substrate) and illuminated at the excitation wavelength (Rayleigh scattering).

2) L_2: integrated intensity at the same excitation wavelength when the sample is introduced into the sphere.

3) P_2 : integrated intensity of the emission spectrum. The three quantities are replaced in **equation 6.1** [239] for the calculation of the quantum yield of the sample (Φ_{sample}).

$$\Phi_{sample} = \frac{\#photons_{em}}{\#photons_{abs}} = \frac{P_2}{L_1 - L_2} \qquad \textbf{(6.1)}$$

Where, the subscripts "abs" and "em" are the number of photons absorbed or emitted per unit time by the sample.

Figure 6.14 shows the scatter of light at $\lambda_{exc.}$=370 nm (with and without sample), while in the region from 400 to 700 nm, no signal collected by the device is observed. The co-doped sample Yb (3.5 at.%)-Tb (1.9 at.%) has a thickness of ~700 nm. The measurements were performed at room temperature.

Figure 6.14. Light emitted and scattered by a luminescent sample of Yb -Tb co-doped *a*-SiOC:H, collected by an integrating sphere. Excitation wavelength 370 nm.

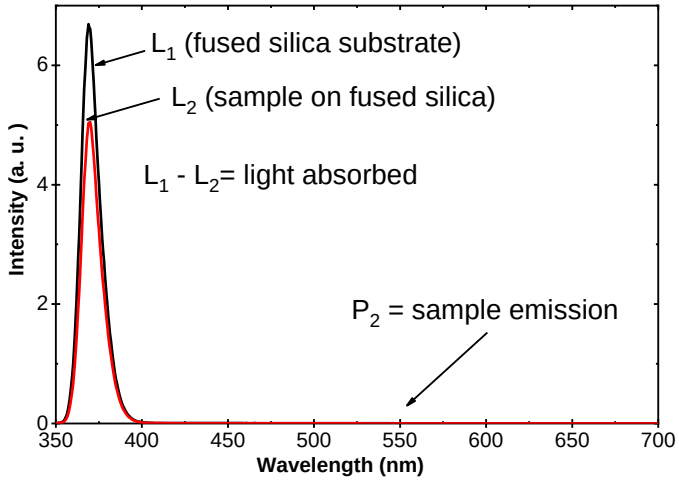

Relative method

In the comparative method, the sample under examination is compared to a standard with known quantum yield (**Figure 6.15**).

The quantum yield of the unknown sample (subscript S) is given relative to the quantum yield of the reference (subscript R) by [240,241]:

$$\Phi_{sample} = \Phi_{\text{reference}} \times \frac{E_R}{E_S} \times \frac{1-10^{A_R}}{1-10^{A_S}} \times \frac{I_S}{I_R} \times \frac{n_S^2}{n_R^2} \qquad (6.2)$$

where

E: intensity (irradiance) of the excitation source at the excitation wavelength.
A : absorbance at the excitation wavelength.
I : integrated emission spectrum (corrected for instrumental function).
n: refractive index

Since the irradiance of the excitation source was the same, the term $\frac{E_R}{E_S} = 1$. In addition, the term $\frac{n_S^2}{n_R^2} \approx 1$. The values of A and I are calculated from **Figure 6.16**. From **equation 6.2**, $\Phi_{sample} = 5 \times 10^{-3}$ or 0.5%

Table 6.5. Quantum yield values for silica-based matrices

Material	$\lambda_{exc.}(nm)$	$\lambda_{exc.}(nm)$	Φ_{sample} (%)	References
a-SiO_xC_y ~1200°C annealing	365	430-900	5.0-11.5 (calculated)	[103]
a-SiN_xO_y as-grown	375	400-650	1.57-4.84 (measured)	[242]
Yb-Tb co-doped *a*-SiOC:H as-grown	370	500-800	0.5 (calculated)	This work

Figure 6.15. Light emitted and scattered by a reference sample, collected by an integrating sphere. Excitation wavelength 370 nm.

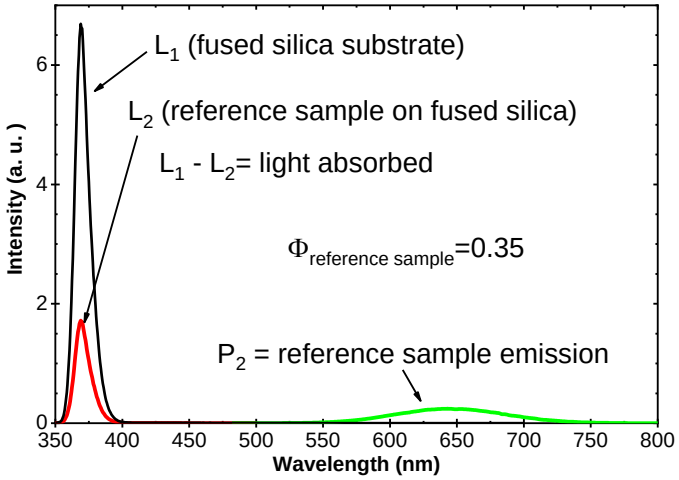

Figure 6.16. **(a)** Transmittance spectra for fused silica substrate, reference sample on fused silica substrate, and Yb (3.5 at.%)-Tb (1.9 at.%) co-doped *a*-SiOC:H as-grown. (b) PL spectra at 375 nm excitation wavelength.

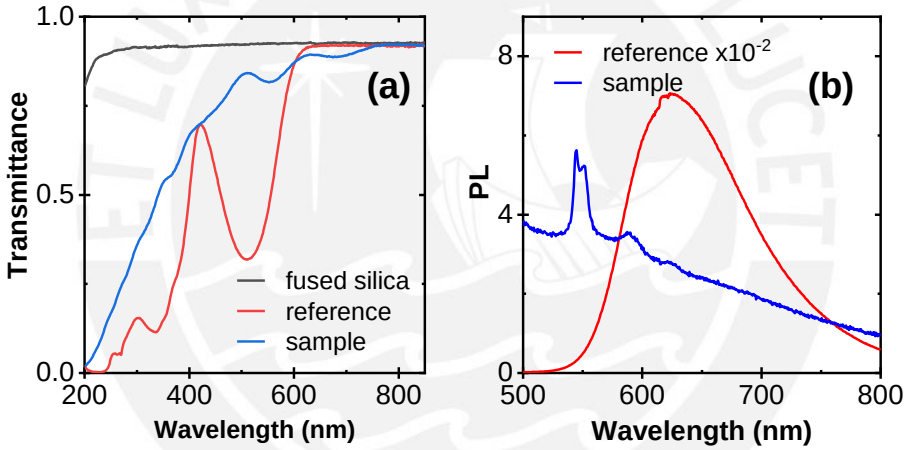

The quantum yield values reported in the literature (**Table 6.5**) for SiO_x-based hosts are in a wide range ~1.5 to 11.5. However, at $\lambda_{exc.}$~370 nm, the quantum yield obtained in our sample is low in the visible range. It is expected due to the weak Tb and matrix emission when the sample is co-doped (previous sections). Furthermore, the low matrix quantum yield can be partly explained by the energy transfer from the matrix to the RE ion. Hence, a reduction in matrix quantum yield is consistent when doped with RE ions.

Considering Φ_{a-SiOC} = 5% from **Table 6.5**, in the case of the undoped host, we can understand that out of a total of 100 absorbed photons, only 5 are emitted. On the other hand, in the case of the rare-earth-doped host, only 0.5 photons are emitted out of 100 ($\Phi_{co-doped\ a-SiOC:H}$ = 0.5%). In the best case, the fraction of non-emitted energy (4.5 photons /5 photons) will be transferred to the RE ions. Therefore, there is a limit to the amount of

energy transferred from the matrix to the RE ion. It is an energy fraction of 0.9. Then the matrix sensitization efficiency in the doped case would have a maximum of 0.9 ($\eta_{sens\ (host \rightarrow RE^{3+})}$= 0.9). In addition, we can also estimate the Yb quantum yield in the sample ($\Phi_{overall}^{Yb^{3+}}$,) when excitation is first performed on the host and then transfers to the Yb^{3+} ion.

The overall quantum yield ($\Phi_{overall}^{RE^{3+}}$) compares the number of photons emitted by the RE^{3+} ion with respect to the number of photons absorbed by the host, as in **equation 6.3** [240].

$$\Phi_{overall}^{RE^{3+}} = \frac{\#emitted\ photons\ by\ the\ RE^{3+}}{\#absorbed\ photons\ by\ the\ host} = \eta_{sens(host \rightarrow RE^{3+})} \times \Phi_{intrinsic}^{RE^{3+}} \quad \textbf{(6.3)}$$

Where

η_{sens} : sensitization efficiency, this is the overall energy transfer efficiency from the matrix to the luminescent activator state (RE^{3+} ion).

$\Phi_{intrinsic}^{RE^{3+}}$: intrinsic quantum yield

It is important to mention that the intrinsic quantum yield ($\Phi_{intrinsic}^{RE^{3+}}$) does not consider the energy loss due to the host sensitization pathway. Still, it does consider all deactivations of the lanthanide, including those due to the presence of the ligand, such as a back-transfer (transfer from the lanthanide to the ligand) or some quenching phenomenon.

From **equation 6.3**, $\Phi_{overall}^{Yb^{3+}} = \eta_{sens(host \rightarrow Yb^{3+})} \times \Phi_{intrinsic}^{Yb^{3+}}$. Thus, we can have a maximum of $\Phi_{overall}^{Yb^{3+}} = 0.9 \times \Phi_{intrinsic}^{Yb^{3+}}$. Also, $\Phi_{intrinsic}$ is calculated by $\Phi_{intrinsic} = \frac{\tau_{RE}}{\tau_{RE}^{rad}}$, so the maximum quantum yield at Yb emission is written as:

$$\Phi_{overall}^{Yb^{3+}} = 0.9 \times \frac{\tau_{Yb}}{\tau_{Yb}^{rad}} \quad \textbf{(6.4)}$$

where τ_{RE}^{rad} is the radiative lifetime of the RE excited state, and τ_{Yb} is the measured decay lifetime.

Assuming τ_{Yb}^{rad}=1.31 ms [241], and the maximum τ_{Yb} =16.8 μs obtained in **Table 6.4** (previous section). Thus, the maximum $\Phi_{overall}^{Yb^{3+}} \approx$ 11.5 x 10^{-3} or 1.2% for $\lambda_{exc.}$=370 nm.

Summarizing the results, a reduction of the matrix luminescence quantum yield in the co-doped sample compared to the undoped matrix was found. This behavior was expected because the matrix transfers part of its energy to the RE^{3+} ions. The maximum

energy transfer efficiency from the matrix to the RE ion was estimated to be 0.9. The previous calculations do not consider the energy transfer from Tb to Yb since, in the last section, it concluded that the cooperative transfer process between these two ions would be scarce. The maximum $\Phi_{overall}^{Yb^{3+}}$ was estimated in 1.2% for $\lambda_{exc.}$=370 nm in the Yb-Tb co-doped *a*-SiOC:H matrix. It is important to note that the τ_{Yb} value is a determining factor in the $\Phi_{overall}^{Yb^{3+}}$. Thus, it should be improved before practical applications. Furthermore, the previous section explained that the lifetimes of τ_{Yb} are affected by the OH groups. Therefore, the control of these groups must be strongly considered during the preparation.

6.6 Performance of Yb-Tb co-doped *a*-SiOC:H layers on Si solar cells

In the previous section, the QC process was ruled out, while the down-shifting process is the one that is best associated with the samples. Therefore, we will refer to the luminescent layer as a down-shifting layer (DSL). In this section, we study two important aspects for the practical application of Yb-Tb co-doped *a*-SiOC:H films. The first aspect is the modification of the incident solar spectrum in the silicon cell, and the second is the light loss due to the reflectance of the layer arrangement (Si cell, SiN_x, and DSL).

6.6.1 Modification of the incident solar spectrum by a Down-shifting layer

As mentioned, the first aspect to discuss is the modification of the incident solar spectrum. The layering arrangement is shown in **Figure 6.17 (a)**. The modification of the AM1.5G incident solar spectrum can be understood in two sequential steps.

The first step considers the DSL absorption. The AM1.5G incident spectrum, $P_{sun}(\lambda)$, is modified due to the absorption of photons by the DSL. The number of absorbed photons in the DSL is denoted by $P_{abs}(\lambda)$ and depends on the thickness of the DSL (Lambert-Beer). The $P_{abs}(\lambda)$ is then subtracted from the incident spectrum. Thus, the photons available for absorption in the solar cell are $P_{sun}(\lambda)$ - $P_{abs}(\lambda)$.

The second step takes into account the emission of the DSL. The down-shifting layer, after absorbing part of the solar spectrum, will show luminescence. The number of emitted photons is represented as $P_{em}(\lambda)$. Then, the total number of photons in the final modified spectrum is expressed as in **equation 6.5** [243,244].

$$P_{resul}(\lambda) = P_{sun}(\lambda) - P_{abs}(\lambda) + P_{em}(\lambda) \qquad (6.5)$$

Figure 6.17 (b) shows the luminescence spectrum (red line), the absorption coefficient (blue line), the incident spectrum AM1.5G, and the region of the spectrum absorbed by the silicon (green). From the absorption coefficient, we observe that the high absorption occurs at wavelengths shorter than 600 nm. On the other hand, the most efficient region of the Si solar cell is in the region close to its bandgap, so the Yb emission ($P_{em}(\lambda)$) contributes to an efficient absorption in the Si-cell.

Figure 6.17. **(a)** Layering arrangement on mc-Si cell. **(b)** Luminescence spectrum (red line), absorption coefficient (blue line), incident spectrum AM1.5G, and the region of the spectrum absorbed by the silicon (green). **(c)** Film absorption in function of thickness and wavelength.

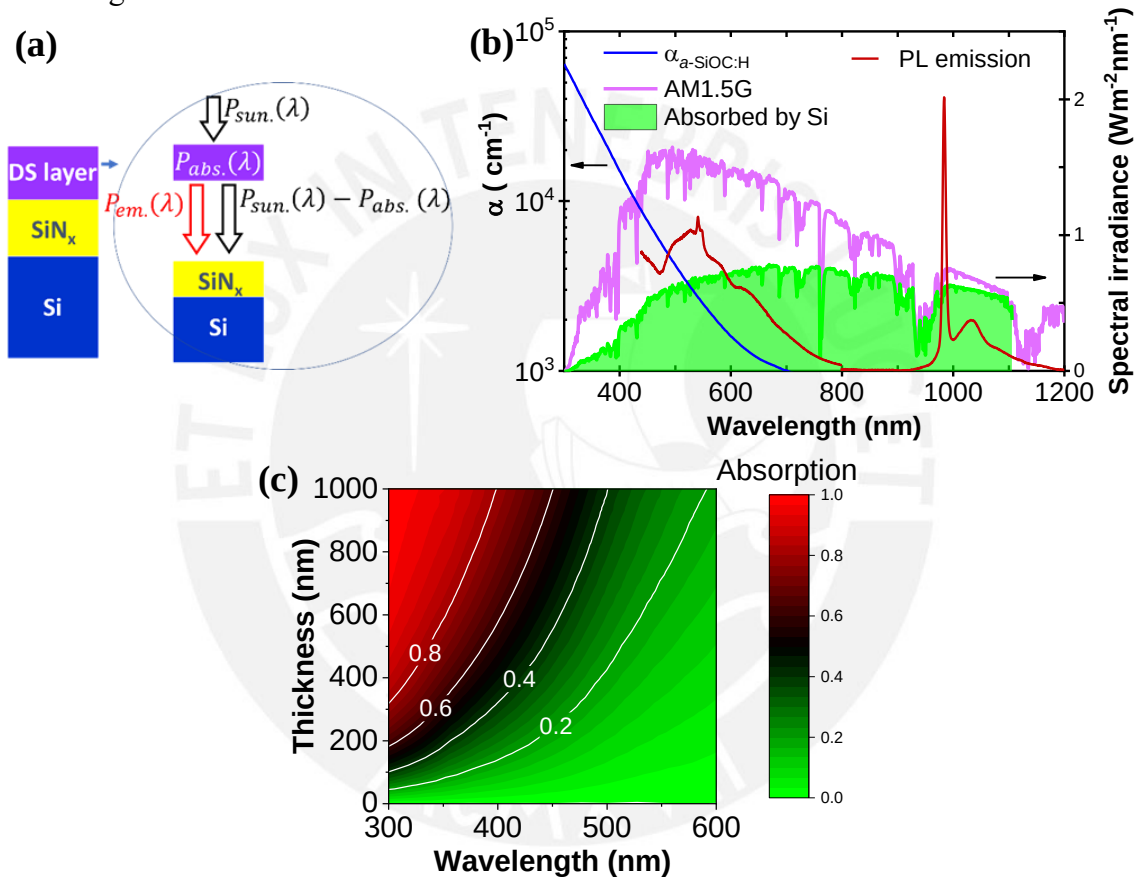

The previous section reported a maximum energy transfer efficiency from the matrix to Yb^{3+} ion was 0.9 (**section 6.5**). However, the estimated PLQY for the Yb emission ($\lambda_{exc.}$=370 nm) was a maximum of ~ 1.2%. On the other hand, if we compare the PLQY with the DSL absorption, for instance, at λ<450 nm, the film's absorption (**Figure 6.17 (c)**) is essentially higher than 40 %. Thus, the $P_{em}(\lambda)$ has a weak contribution compared to the $P_{abs}(\lambda)$. Therefore, the final incident spectrum in the mc-Si cell has a reduction in the number of high-energy photons and a weak gain in the NIR region (emission of the Yb^{3+} ion).

6.6.2 Modeling of the reflectance

The second aspect being discussed is the loss of light from the incident spectrum due to reflections at the interfaces of the films belonging to the array. The considered layer system was shown in **Figure 6.17 (a)**. The thickness of the SiN_x layer is kept at 75 nm, which corresponds to the thickness of the anti-reflection layer in a commercial Si cell [72]. **Figure 6.18 (a)** shows a simulation of the reflectance with increasing DSL layer thickness "d" nm.

Figure 6.18. **(a)** Simulation of the reflectance with increasing DSL layer thickness "d" nm. **(b)** and **(d)** Total number of photons lost in the range of the solar spectrum (300-1100 nm) as a function of thickness and its variation (%) with respect to the bare cell. **(c)** Film reflectance in function of thickness and wavelength.

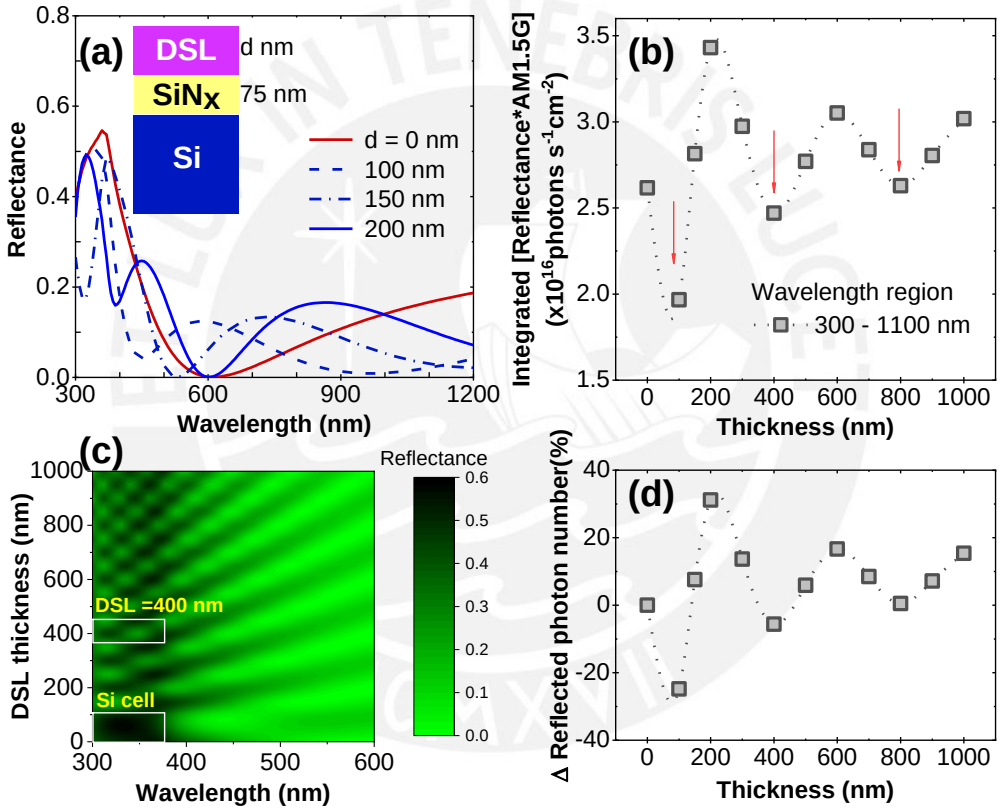

As expected, the reflectance will vary with the wavelength and film thickness. **Figure 6.18 (c)** shows this effect from 0 to 1000 nm thickness. The system without DSL has a reflectance of ~0.5 (in the range of λ= 300-375 nm). As the thickness of the DSL layer increases, e.g., 400 nm, the reflectance decreases. So, the DSL will absorb more photons.

To study photon loss, the total photon loss due to reflection was calculated based on the AM1.5G spectrum (photon flux) and the reflectance spectrum. The total number of photons lost in the range of the solar spectrum (300-1100 nm) as a function of thickness is shown in **Figure 6.18 (b)**. The minimum points on the graph (red arrows) indicate the

thicknesses where few photons are lost due to reflection. Furthermore, the total number of reflected photons with respect to the bare cell can vary from ~5 to 30 % (**Figure 6.18 (d)**). Therefore, it will modify the total number of absorbed photons compared to the bare cell (Si and SiN_x). It is important to mention that for a more precise calculation of the number of photons lost, the isotropic emission of the DSL [245] must also be taken into account, i.e., only a part of the emitted photons will be used by the solar cell and another part is emitted into the air.

6.6.3 External quantum efficiency of *a*-SiOC:H on Si cells

EQE measurements were performed on mc-Si cells (13 mm x 41 mm) on which *a*-SiOC:H layers doped with RE elements were grown. For further control of the studied area, a mask with 6.30 mm diameter holes was used (**Figure 6.19 (a)**). This allows control of the area of the illuminated region and homogeneity in the thickness of the studied films.

Figure 6.19. **(a)** Yb-Tb co-doped *a*-SiOC:H layer on the front surface of an mc-Si cell. **(b)** EQE spectra for bare mc-Si cells. **(c)** EQE spectra for mc-Si cells with Tb-doped *a*-SiOC:H layers.

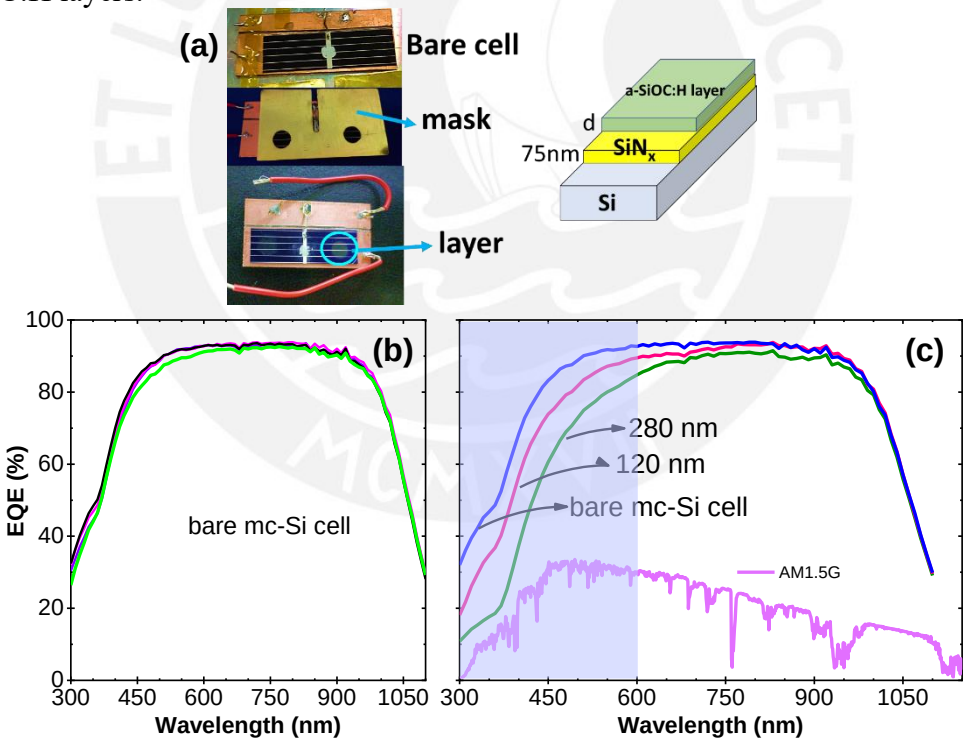

The EQE spectra for bare mc-Si cells are shown in **Figure 6.19 (b)**. A very similar initial performance is observed between the studied cells. **Figure 6.19 (c)** shows the EQE behavior with increasing thickness in Tb-doped *a*-SiOC:H samples. As expected, due to the modification of the AM1.5G solar spectrum, i.e., a low number of photons in the $\lambda<600$ nm range, a reduction in EQE values was obtained in this range. The region of the most considerable EQE change, from 300 to 600 nm, is compared with the absorption coefficient

of the DSL. The reduction in EQE coincides with the strong absorption of DSL in the order of ~10^5 to 10^3 cm^{-1}. On the other hand, the total photon loss due to reflectance (**Figure 6.18 (b)** and **(d)**) also decrease the silicon cell EQE.

Before presenting the EQE spectra for cells with co-doped films, it is important to remember that a DSL must fulfill certain conditions to increase the cell conversion efficiency [246]: 1) Close to unity photoluminescence quantum yield (PLQY), which represents the fraction of absorbed photons that are reemitted at longer wavelengths. 2) Absorption and emission well separated to prevent self-absorption. 3) Strong absorptivity in the high-energy range. 4) Transparency at longer wavelengths. 5) Luminescence around the maximum of the EQE, where the solar cell is more efficient. From the above, the Yb-Tb co-doped *a*-SiOC:H samples satisfy conditions 2 to 5. However, condition 1 is the one that should be improved.

The characteristics mentioned above can be studied according to **equation 6.6** [247]. The first summand takes into account the absorbed photons, the quantum yield of the DSL ($PLQY_{DSL}$), the "optical efficiency" of the layers, and the coincidence of the down-shifting wavelength (the DSL emits at a λ') with the high-efficiency region of the cell. The term with the integrals is called "the spectral matching" [246]. The "optical efficiency" considers the refractive indices and thicknesses of the layers, expected side losses, and losses of the emitted light owing to the isotropic emission of the DSL in all directions [248].

The second summand represents the EQE of the fraction of transmitted photons arriving at the solar cell's surface with its original wavelength λ. Therefore, in our case, the first summand is strongly affected by the small $PLQY_{DSL}$. On the other hand, the f_{trans} is also decreased by the DSL absorption.

$$EQE_{Mod}(\lambda) = f_{abs}(\lambda) \times PLQY_{DSL} \times optical\ efficiency \times \frac{\int PL(\lambda')EQE_{\mathrm{ref}}(\lambda')d\lambda'}{\int PL(\lambda')d\lambda'} + f_{trans}(\lambda) \times EQE_{\mathrm{trans}}(\lambda) \quad \textbf{(6.6)}$$

Where

$f_{abs}(\lambda)$ is the fraction of photons absorbed and down-shifted by the DSL

$f_{trans}(\lambda)$ is the fraction of photons transmitted through the DSL

$PLQY_{DSL}$ is the quantum yield of the DSL

$PL(\lambda')$ is the photoluminescence spectrum

EQE is the external quantum efficiency.

Figure 6.20. **(a)** and **(c)** EQE spectra of mc-Si cells with *a*-SiOC:H and Tb doped *a*-SiO:H films. **(b)** and **(d)** EQE spectra for mc-Si cells with Tb-doped and Yb-Tb doped *a*-SiOC:H layers.

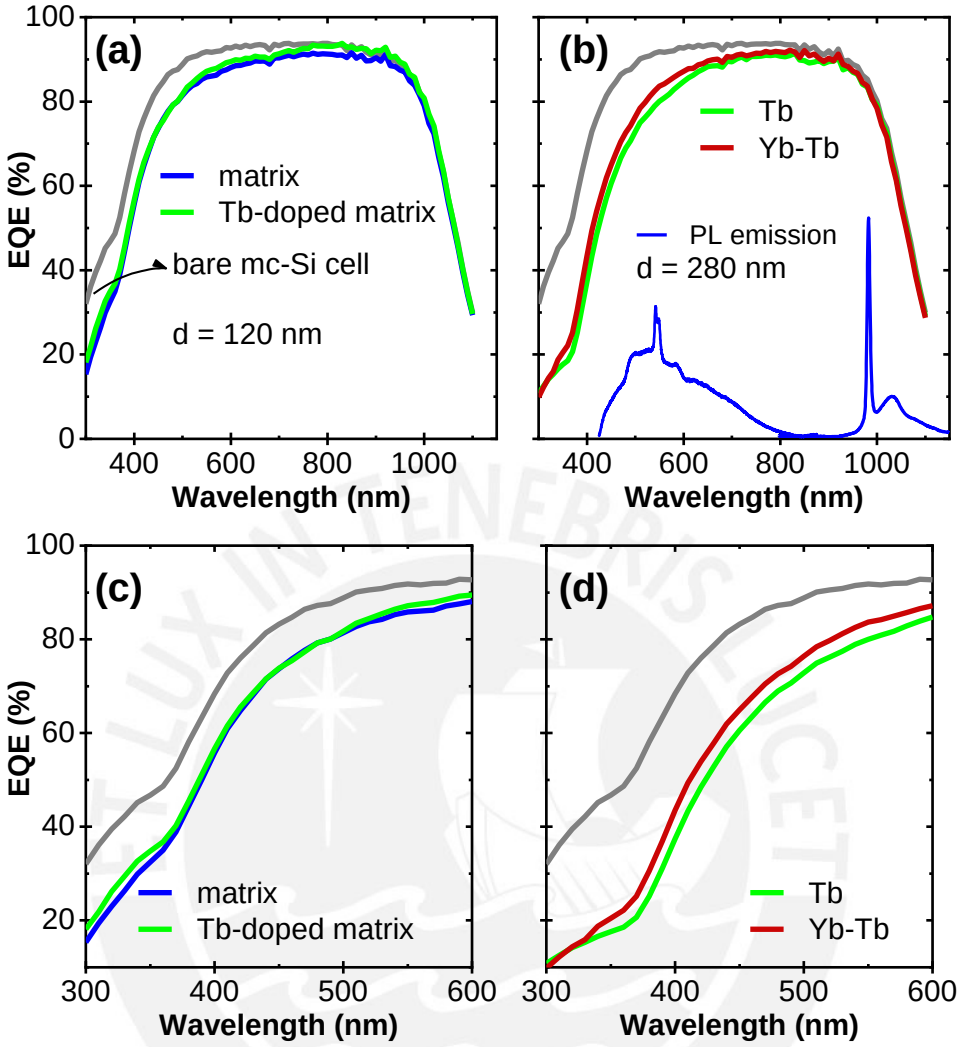

Films of the same thickness are compared to avoid the change in reflectance modifying the absorption in the film. However, because the samples were produced in different processes (matrix, single doped, and co-doped samples), the surface roughness could also produce some difference in light scattering. This factor is not considered in the following analysis.

Figure 6.20 (a) compares the EQE spectra of mc-Si cells with *a*-SiOC:H and Tb-doped *a*-SiO:H films. In this case, the EQEs are significantly the same (Figure 6.20 (c)). On the other hand, the EQE spectra for cells with Tb-doped *a*-SiO:H and Yb-Tb co-doped *a*-SiO:H films are compared in **Figure 20 (b)**. An improvement of the EQE is observed for the co-doped case with respect to the single doped one. This result is interesting because, despite the low efficiency and narrow luminescence of the Yb^{3+} ion in the matrix, an increase in their EQE spectra can be quantified. Therefore, if the photoluminescence quantum yield

of the layer increase, for example, by better control of OH- groups, and also the thickness of the SiN_x layer is modified to obtain lower reflectivity in the Si, SiN_x, and *a*-SiOC:H system, then the Yb^{3+} ions could be used to improve the silicon solar cell efficiency.

6.7 Conclusions

In this chapter, the optimization of the Tb and Yb doping concentration and the post-deposition annealing was studied to maximize the Yb luminescence in Yb-Tb co-doped *a*-SiOC:H samples. Since increased RE doping would increase the defect density in the matrix, the total atomic percentage of RE elements was kept as low as possible during the study. Furthermore, the Tb doping was chosen below those reported for Tb energy migration, thus reducing cross-relaxation and Tb concentration quenching.

In Yb-doped samples, the maximum Yb luminescence activation is reached after annealing treatments at 400 and 500 °C. The Yb lifetime for Yb doping reaches values of ~1 μs for samples with a carbon composition below ~9 at.%. The short luminescence lifetime is mainly attributed to the interaction with OH groups recorded in the FT-IR spectra. Radiation trapping and cooperative luminescence mechanisms were ruled out, while for Yb doping higher than ~4 at.%, strong Yb luminescence quenching is reported.

In Yb-Tb co-doped samples, the Yb and Tb doping variations allow to enhances the Yb luminescence lifetime. More in detail, the Tb doping leads to an important improvement in the Yb lifetime (~16.8 μs) in co-doped samples compared with the Yb-doped sample case (~1 μs). Furthermore, Yb lifetime values can be divided into two groups: 1) The longer Yb lifetime values achieved for Yb concentrations below ~2 at.%. 2) The shorter Yb lifetimes for Yb concentrations above ~3.5 at.%. This indicates that a determining factor in the Yb lifetime is the Yb doping concentration. Meanwhile, Tb doping concentration has a range to be used from 0.8 to 2.6 at.% at which the Yb lifetime is not strongly affected.

The quantum cutting process was analyzed as the energy transfer mechanism from Tb^{3+} to Yb^{3+} ions. The energy transfer is enabled by the shorter Tb luminescence lifetime (microsecond range) compared to the Yb lifetime. However, the excitation channels of Tb and Yb would be competitive in the *a*-SiOC:H matrix and the quantum cutting process is ruled out. On the other hand, co-doping would increase the creation of deep defects such as SiDBs that enhance the Yb luminescence in the co-doped samples.

The energy transfer efficiency from the matrix to Yb was estimated. The calculation did not include the energy transfer from the Tb^{3+} ions to the Yb^{3+} ion. In addition, the maximum photoluminescence quantum yield of ~1.2 % was estimated for the Yb luminescence at $\lambda_{exc.}$=370 nm. The modified solar spectrum AM1.5G, which reaches the mc-Si cell after passing through the down-shifting layer, has fewer high-energy photons (compared with the AM1.5G) and a weak gain in the NIR region (emission of the Yb^{3+} ion).

The spectral down-shifting layer (DSL) based on the *a*-SiOC:H matrix reduces the EQE of the mc-Si cell. The EQE reduction coincides with the matrix strong absorption of the wavelengths lower than 600 nm. It is also affected by the total photon loss due to reflectance. However, despite the low efficiency and narrow luminescence of the Yb^{3+} ion in the matrix, an improvement of the EQE is observed for the co-doped case with respect to the single doped one. This result presents the Yb^{3+} ion as capable of improving the efficiency of silicon solar cells. Nevertheless, an improvement in their luminescence quantum yield is indispensable before practical applications.

CHAPTER 7. General Conclusions and Outlook

This chapter presents a brief summary of the goals and conclusions developed in this work as well as the outlook.

7.1 Goals

The central study of this work was to maximize the luminescence of Tb^{3+} and Yb^{3+} ions in the relatively new *a*-SiOC:H matrix for luminescent applications as spectral downconverter layers. The method used for luminescence optimization was based on annealing treatments, matrix composition and co-doping with Tb and Yb elements.

The first goal of this work focused on the preparation of *a*-SiOC:H layers that can be grown on the surface of a test solar cell (Si cell + antireflective layer). The preparation process is intended to meet two characteristics. 1) low preparation temperature. 2) low quantity of by-products left by the precursors. The aforementioned characteristics make it possible to avoid deterioration of the layers that comprise the solar cell. Therefore, growth techniques at relatively low temperatures were sought. The literature reports a variety of previous work on SiOC. However, most of them are mainly based on preparation at temperatures close to 1000 °C. Among the reported techniques, the RF-sputtering technique offers relatively low temperature film growth, and in this work, the system used has a substrate cooling system that keeps it below 30°C. In addition, this technique would allow the simultaneous preparation of different composition samples (Si, C and O) under the same preparation conditions. The modification of compositions is achieved by the arrangement of the substrate in relation to the SiC target in the vacuum chamber. Furthermore, the process reduces costs and time during sample preparation. In parallel, the optimization of rare-earth (RE) ion luminescence requires knowledge of the matrix atomic network structure as well as its optical properties. Therefore, **Chapter 4** focused on the study of (1) composition and structure analysis, (2) the bandgap and Urbach energy calculation, (3) the effect of the annealing treatment on the atomic network structure, and (4) the processes driving the matrix luminescence.

The second goal of this work was to maximize the Tb^{3+} and Yb^{3+} ions luminescence in single doped *a*-SiOC:H samples. In this part, the aim is to use the sunlight range of 300 to 500 nm (4.1 to 2.5 eV). Therefore, the Tb^{3+} ion can be excited resonantly. In contrast, excitation of the Yb^{3+} ion will depend entirely on host sensitization. Among the many

ongoing investigations on the SiOC matrix, the literature has reported few studies of SiOC doped with rare earth elements (Eu and Er). SiOC has recently attracted attention due to its high reduction of Eu ion clustering even at high temperatures (~1000 °C). Therefore, this work provides findings on the luminescence behavior of Tb^{3+} and Yb^{3+} ions in this matrix. Moreover, there is limited discussion of the mechanisms of non-radiative energy transfer from defect states to RE dopants in Si-based materials. Hence, this work discusses the excitation mechanisms for Tb^{3+} and Yb^{3+} ions. Those mechanisms can be applied not only in the *a*-SiOC:H matrix but also can be extended to Si and SiO_x-based materials. Finally, the role of carbon in enhancing the luminescence of RE^{3+} ions is also discussed. Early studies of the effect of carbon showed an enhancement of the luminescence of RE^{3+} ions. However, the literature has not systematically studied the composition and structures formed in Si-based matrices. Therefore, this work seeks to answer the advantages or disadvantages of carbon doping in activating the RE luminescence. The results were presented in **Chapter 5**.

The third goal of this work was the optimization of the Yb luminescence in co-doped *a*-SiOC:H samples. One of the applications studied in RE elements is the development of spectral up- and downconverter systems. In the case of down-conversion (DC) or quantum cutting (QC), one high-energy photon is absorbed by the RE^{3+} ions to emit two low-energy photons, which could be efficiently absorbed by the solar cell. Among different RE^{3+} ion systems for near-infrared QC applications, those including Yb ions seem to be the most appropriate because the Yb ion has a transition at about 980 nm (~1.22 eV) just above the crystalline silicon bandgap of 1.1 eV. Thus, near-infrared downconverters have found a possible application in silicon solar cells. The spectral converter layer will be grown on the front surface of the Si solar cell. The incorporation of the DC layer on the top of the solar cell leads to the advantage of a layer that can be optimized independently of the cell. To this end, silicon-based materials were study to be doped with RE elements. This work studies the *a*-SiOC:H matrix doped with the Yb-Tb couple widely used in downconverter applications. In addition, this work seeks to study the cooperative transfer mechanism between Tb and Yb used to explain the quantum cutting process (QC). This mechanism has been attributed to QC processes in many crystalline and amorphous matrices. However, despite numerous documents that ascribe their results to the cooperative transfer mechanism, few actually prove it. Therefore, the cooperative energy transfer mechanism is discussed in this work. Photoluminescence quantum yield measurements of the spectral converter layer were performed. Finally, the layers were prepared on the front surface of mc-silicon cells and their

effect on the external quantum efficiency was studied. The results were presented in **Chapter 6**.

7.2 Conclusions

The sample characterization was based on energy dispersive X-ray (EDX), Fourier transform infrared (FT-IR) and Raman spectroscopy measurements to study the sample composition and atomic structure. Photoluminescence excitation (PLE) and steady-state photoluminescence (PL) measurements to study the Tb, Yb and, host excitation and emission. Transient PL measurements were also performed to study recombination mechanism and rates of the Tb and Yb luminescence excited states. Experimental details were presented in **Chapter 3**.

The general findings are presented below:

Structural analysis and optical properties of *a*-SiOC:H

The samples obtained in this work showed a silicon elemental composition of 33 at.%, which is close to the ideal in SiO_2. Also, the stoichiometric analysis in the composition ternary diagram clearly shows that the carbon added to the network could replace the oxygen atoms. In addition, a slight excess of carbon would give rise to carbon atoms not necessarily bound to the amorphous atomic network. The formation of Si−O, Si−C, Si−H bonds, and OH groups was verified in the FT-IR spectra. The high oxygen content compared to carbon leaves a structure mainly dominated by the silica structure. Increasing the annealing temperature allows the formation of new Si−C and Si−O bonds. After 500 °C annealing, complete depletion of Si−H and C−H bonds was observed, suggesting the formation of dangling bonds during the annealing treatments.

Using the Tauc-plot model (E_{Tauc}), band fluctuation model (E_{BF}), and iso-absorption energy (E_{04}), the representative E_{gap} values were calculated from as-grown to 800 °C post-deposition annealing. The representative values remain relatively constant (~2.8 and 3.0 eV) up to 500 °C annealing temperature. Above 500 °C, a continuous E_{gap} decrease is observed with increasing annealing temperature. In addition, the increasing value of the Urbach energy above 500 °C (widening of the Urbach region) overlaps with the bandgap region itself (mobility edges). So, reducing the bandgap is explained by the increase of disorder and not necessarily associated with any shifting of the mobility edges. On the other hand, the formation of new Si−O bonds and ordered carbon groups in the form of graphite structure can be interpreted as a sort of crystalline order. Thus, the increase of the Urbach energy value

would be contradictory. However, it is important to mention that disorder would increase due to atomic rearrangement (**Chapter 4**). Therefore, the reduction of the E_{gap} and the increasing Urbach energy, after 500 °C, can be understood as a consequence of the formation of dangling bonds from the depletion of C-H bonds and the formation of carbon-related structural defects, i.e., broadening the Urbach tails, and hence the reducing the E_{gap}.

The luminescence of the *a*-SiOC:H matrix is mainly attributed to electronic recombination in the states belonging to the Urbach region. It might also receive contributions from luminescent sources attributed to multiple intrinsic defects similar to those found in silicon oxides. The luminescence spectrum can be divided into three bands centered at ~2.8, 2.4 and 1.9 eV (**Figure 4.14**), i.e., blue, green, and red emission. The effect of passivation resulting from the annealing treatments was studied in two atmospheres, argon and hydrogen. The annealing treatments in the hydrogen atmosphere verify the hypothesis that better passivation of non-radiative defects leads to an enhancement of luminescence. In addition, an increase in carbon composition increases the luminescence centered at ~2.4 eV, which would be related to the formation of new bonds such as Si−O−C and Si−C. The band at ~2.8 eV seems to be less sensitive to this change. The annealing times also affects the matrix luminescence, i.e., increasing the time leaves a quenching of the luminescence.

Tb ion luminescence in Tb-doped *a*-SiOC:H

The Tb^{3+} ion luminescence was studied in Tb-doped *a*-SiOC:H samples. The role of the matrix for two different carbon compositions as well as the annealing treatments up to 1000 °C were studied. In addition, the dynamics of Tb^{3+} ions relaxation under an increasing excitation power of the excitation light were studied by a two-level model. Results were presented in **Chapter 5**

An increasing annealing temperature led to an increasing total number of optically active Tb ions, which was verified by the sigmoidal curve. Furthermore, the sigmoidal curve in the saturation region also indicates a limited number of sensitizers available for the Tb ion excitation, which would limit the Tb luminescence. On the other hand, the $^5D_3$ and higher levels contribute significantly to the $^5D_4$ population, thus increasing the $^5D_4 \rightarrow {}^7F_J$ (J=3,4,5, and 6) emission lines intensities. Deep defects such as silicon dangling bonds (SiDB) were passivated by the annealing treatment, explaining the enhancement of the Tb luminescence and the increasing luminescence lifetime in the *a*-SiOC:H matrix. In addition, the increase of carbon up to ~12 at.% does sightly decrease the Tb luminescence lifetime. However, high carbon doping should be limited due to the formation of carbon structures that can re-absorb

the Tb emission. The defect-related Auger excitation (DRAE) and the non-radiative resonant energy transfer by dipole coupling (Förster interaction) mechanism can both satisfy the Tb excitation by transitions between localized tail states.

Yb ion luminescence in Yb-doped *a*-SiOC:H

The Yb^{3+} ion luminescence was studied in Yb-doped *a*-SiOC:H samples. The role of the matrix by different carbon compositions as well as the annealing treatments up to 700 °C were studied. Results were presented in **Chapter 5**.

In Yb-doped samples, the main peak at ~980 nm and a sub-peak at ~1020 nm result from the 4f transitions between the Stark levels of the $^2F_{5/2}$ excited and $^2F_{7/2}$ ground state. Luminescence optimization by carbon concentration and annealing temperature achieves maximum Yb luminescence activation at 500 °C for carbon compositions higher than ~25 at.%, and at 600 °C for lower carbon compositions. The enhancement of Yb luminescence with increasing annealing temperature was associated with the creation of intrinsic defects (such as the SiDBs) located near the middle of the bandgap. The hydrogen evolution in the *a*-SiOC:H matrix would leave a SiDB behind as in the *a*-Si:H case. Moreover, an increase in the density of such intrinsic defects can be expected due to the extrinsic Yb doping and the increasing carbon composition. Therefore, an early quenching of the host luminescence in Yb-doped *a*-SiOC:H can be expected. The defect-related Auger excitation mechanism (DRAE) and the nonradiative resonant energy transfer by dipole coupling mechanism are proposed for the excitation of the Yb^{3+} ion. Both mechanisms involve energy transfer from deep localized states such as SiDBs in the middle of the bandgap to the Yb^{3+} ion.

The Yb lifetime was increased from 0.88 to 1.85 μs with increasing carbon concentration. Therefore, samples with higher carbon content showed longer luminescence lifetimes, suggesting the Yb luminescence quantum yield increased by the carbon incorporation into the matrix. The short luminescence lifetimes are mainly attributed to the interaction with OH groups recorded in the FT-IR spectra. Radiation trapping and cooperative luminescence mechanisms were ruled out, while for Yb doping higher than ~4 at.%, strong Yb luminescence quenching is reported (**Chapter 6**).

Yb luminescence in Yb-Tb doped *a*-SiOC:H

Yb^{3+} ion luminescence was studied in Yb-Tb co-doped *a*-SiOC:H samples. The role of Tb and Yb doping concentration and the post-deposition annealing in the luminescence were discussed. Since increased RE doping would increase the defect density in the matrix, the total atomic percentage of RE elements was kept as low as possible during the study. Furthermore, the percentage of Tb was chosen below those reported for Tb energy migration, thus reducing cross-relaxation and concentration quenching.

In Yb-Tb co-doped samples, the Yb and Tb doping variations allow the enhancement of the Yb luminescence lifetime. More in detail, the Tb doping leads to an important improvement in the Yb lifetime (~16.8 μs) in co-doped samples compared with the Yb-doped sample case (~0.9 μs). Furthermore, Yb lifetimes were studied in samples with Yb doping from 1.8 to 6.0 at.% and it was observed that at ~3.5 at.% a clear reduction of the Yb lifetime is reported. Thus, it is understood that for high Yb doping (> ~3.5 at.%) the energy migration processes offsite of the ion would increase significantly. Meanwhile, the doping values of Tb have a larger range to be used from 0.8 to 2.6 at.%.

Co-doping enhances the Yb luminescence. Therefore, the quantum cutting process was analyzed as the energy transfer mechanism from Tb^{3+} to Yb^{3+} ions. Usually, the literature has taken the cooperative mechanism of energy transfer for granted. However, it is crucial to verify whether the Tb lifetimes satisfy the condition for energy transfer. This is why this work focused on measuring the Tb lifetimes (donor ion) on the time scale of the Yb lifetimes (acceptor). The enhancement of Yb luminescence by Tb doping is feasible in the *a*-SiOC:H matrix. However, the explanation would not be based on an energy transfer mechanism but instead on the creation of defects by Tb doping. The reason why this is favored requires further studies where the density of deep states can be analyzed in the material. On the other hand, the excitation channels of Tb^{3+} and Yb^{3+} ion would be competitive in the *a*-SiOC:H matrix. This would explain the decreasing Tb luminescence.

The energy transfer efficiency from the matrix to the Yb ion was estimated. The calculation did not include the energy transfer from the Tb^{3+} ions to the Yb^{3+} ion. In addition, a photoluminescence quantum yield of ~1.2 % was estimated for the Yb luminescence at $\lambda_{exc.}$=370 nm. The modified solar spectrum AM1.5G, which reaches the mc-Si cell, after passing through the down-shifting layer, has fewer high-energy photons (compared with the AM1.5G) and a weak gain in the NIR region (emission of the Yb^{3+} ion).

The spectral down-shifting layer (DSL) based on the *a*-SiOC:H matrix reduces the EQE of the mc-Si cell. The EQE reduction coincides with the strong DSL absorption of the wavelengths lower than 600 nm. It is also affected by the total photon loss due to reflectance. However, despite the low efficiency and narrow luminescence of the Yb^{3+} ion in the matrix, an improvement of the EQE is observed for the co-doped case with respect to the single doped one. This result presents the Yb^{3+} ion as capable of improving the efficiency of silicon solar cells. Nevertheless, an improvement in their luminescence quantum yield is indispensable before practical applications.

7.3 Outlook

The use of renewable energy sources such as solar photovoltaic, wind energy, and biomass are presented as solutions to address the continuous increase in energy consumption worldwide, as well as to reduce carbon emissions that have had a major impact on ozone depletion and global warming. Nowadays, solar panel technology is increasingly used worldwide, but it is of special interest in developing countries where the lack of infrastructure in the conventional electricity system leaves room for a rapid transition to new energy sources. Therefore, reducing the price of solar energy is the goal. To achieve this, it is necessary to increase the efficiency of solar cells. One approach is to modify the solar spectrum. This aims to reduce thermalization losses in the higher energy region of the spectrum and non-absorption losses at longer wavelengths.

Research in the area of spectral down-converting layers is fertile in the optimization or development of new materials (semiconductor quantum dots, fluorescent organic dyes, hybrid molecular complexes, and phosphors). While the literature reports several materials with promising luminescence quantum yields (theoretically and experimentally), in the case of solar cell applications, the material needs to be stable over time and resistant to degradation by solar radiation. Therefore, spectral converter layers based on lanthanide-based phosphors are actively studied.

The up- and down-conversion mechanisms are sought since additional photons generate electron-hole pairs, which are distinct from the down-shifting case where no additional photons are generated. In 2002, Trupke calculated a 1.1 eV bandgap solar cell's maximum theoretical efficiency could increase from 30.9% to 38.6%, following the addition of an optimal QC layer. Since then, remarkable progress has been made in studying rare-earth pairs in QC systems. In these systems, one of the ions acts as the donor ion (absorbs the spectrum in the higher energy region), and the other acts as the acceptor (emits in the

lower energy region). In addition, advances have been made in understanding the mechanisms of energy transfer between these ions.

Nevertheless, the current state of QC remains challenging to implement. While the energy transfer efficiency (between donor and acceptor ions) can be high, the quantum yield of the acceptor ion depends not only on the energy transfer received from the donor but also on the non-radiative channels available to its relaxation. Moreover, because high RE doping is needed to guarantee quantum cutting, usually, the acceptor ion suffers energy losses due to its concentration. Therefore, one of the main challenges is to achieve high energy transfer efficiency without sacrificing the loss of luminescence due to the high RE ion concentration.

For that reason, efforts should be made to present the experimental value of acceptor quantum yield as it is important information and is usually not discussed in the literature but is of fundamental importance for estimations in practical applications. Furthermore, the QC process is often taken for granted. However, not in all cases is it actually possible to observe it. A feasible way is to compare the luminescence lifetimes of the ions and the PLE spectra. Therefore, future work should present evidence of the QC mechanism. Moreover, when the existence of energy transfer between ions is evident, do the energy transfer efficiency calculation, and measure the quantum yield of the acceptor ion.

As for the efficiency results of Si solar cells, theoretical estimations are done assuming QC efficiencies close to 200 %, so the proposals are promising. However, as mentioned, it is essential to have experimental data on the acceptor quantum yield and make estimations with these data. On the other hand, the literature does not always quantify the variation in EQE due to the increase or decrease in reflectance. That is, although the change in EQE may be due to spectral conversion, the variation in EQE could also be a direct consequence of reflectance and not necessarily due to a change in the solar spectrum itself. Therefore, further studies are needed where spectral conversion layers are grown directly on solar cells, and the above aspects are discussed.

APPENDIX

Appendix 1: Conversion of atomic percentage (at.%) to total number density and weight percent (wt. %)

The composition of doped films in the literature is usually given in atomic percentage (at.%) or weight percentage (wt. %). Furthermore, for calculation of doping atoms distribution, it is necessary to know the atomic number density ($\tilde{n}_i$), as in the case of rare-earth doping in thin films. It is therefore important to have the equations to convert between these units. Therefore, the aim of this appendix is to provide the corresponding conversion formulae that are of importance in this work.

Assumptions: The mass density (ρ) of thin film is composed of atoms A, B, C… with atomic percentages (at.%) n_A , n_B, n_C,… and (atomic) weight percentages (wt. %) w_A , w_B, w_C,…

Additionally, it is assumed:

- Homogeneous concentration distribution throughout the film.
- The mass density (ρ) is homogeneous and known.
- The composition of the film is completely known and given by a normalized set of either atomic concentrations (at.%) or weight concentrations (wt. %).

Definition of atomic concentration percentages (at.%)

The total numbers of each type of atom (N_i) adds up to the total number of atoms N in the film:

$$N_\mathrm{A} + N_\mathrm{B} + N_\mathrm{C} + \cdots = N$$

Dividing by N to achieve the atomic percentage of individual atoms (n_i) that add up to one:

$$\frac{N_\mathrm{A}}{N} + \frac{N_\mathrm{B}}{N} + \frac{N_\mathrm{C}}{N} + \cdots = n_\mathrm{A} + n_\mathrm{B} + n_\mathrm{C} + \cdots = 1$$

Definition of atomic weight percentages (wt. %)

The total mass M of the film consists of the sum of the total mass of each atom type M_i:

$$M = M_\mathrm{A} + M_\mathrm{B} + M_\mathrm{C} + \cdots$$

Dividing through M to achieve weight percentage of the individual atoms w_i that add up to one:

$$\frac{M_A}{M} + \frac{M_B}{M} + \frac{M_C}{M} + \cdots = w_A + w_B + w_C + \cdots = 1$$

Total number density determination

The total mass M_A of type A atoms is N_A times the atomic mass m_A: $M_A = N_A\, m_A$

$$M = N_A m_A + N_B m_B + N_C m_C + \cdots$$

Inserting this expression into the density of the film we find:

$$\rho = \frac{M}{V} = \frac{N_A m_A + N_B m_B + N_C m_C + \cdots}{V} = \frac{N_A m_A + N_B m_B + N_C m_C + \cdots}{N}\frac{N}{V}$$

$$= (n_A m_A + n_B m_B + n_C m_C + \cdots)\frac{N}{V}$$

And therefore, the total number density (N_V) in terms of the atomic concentration

$$N_V = \frac{N}{V} = \frac{\rho}{n_A m_A + n_B m_B + n_C m_C + \cdots} \qquad \textbf{(A.1)}$$

Where, the atomic compositions (in at.%) of an individual atom (n_i) and the atomic mass (m_i) are known from measurements and literature, respectively.

Determination of partial number densities

The atomic number density ($\widetilde{N}_i$) for an atomic type *i* (*i* = A, B, C, …):

$$\widetilde{N}_i = \frac{N_i}{V} = \frac{N_i}{N}\frac{N}{V} = n_i N_V \qquad \textbf{(A.2)}$$

Conversion of atomic percent (at.%) into weight percent (wt. %)

Dividing by the total mass M in $M_i = N_i\, m_i$

$$\frac{M_i}{M} = \frac{N_i}{N} N \frac{m_i}{M} \;\Rightarrow\; w_i = n_i N \frac{m_i}{M} = n_i m_i \frac{N}{\rho V}$$

Substituting the total number density N/V:

$$w_i = \frac{n_i m_i}{\rho}\frac{\rho}{n_A m_A + n_B m_B + n_C m_C + \cdots}$$

$$w_i = \frac{n_i m_i}{n_A m_A + n_B m_B + n_C m_C + \cdots} \qquad \textbf{(A.3)}$$

Where, the atomic compositions (in at.%) of an individual atom (n_i) and the atomic mass (m_i) are known from measurements and literature, respectively.

Appendix 2: Derivation of the mass density of a-silicon oxycarbide

Estimating the distribution of rare earth ions requires knowledge of the mass density of the material. In this work, the oxygen and carbon compositions are varied, which will lead to a variation in density. It is therefore necessary to find a tool to calculate the density based on the compositions. In the following an empirical approach is developed based on data taken from the literature.

Figure A. Mass density of silicon oxycarbide as a function of the logarithmic oxygen-to-carbon ratio. Data from the literature are shown in Ref. (a) [88] and Ref. (b) [108]. The red line indicates a linear fit to the data reported in the references. Density value ranges of crystalline and amorphous, SiC [249] and SiO_2 [250], are presented in cyan and green bar, respectively.

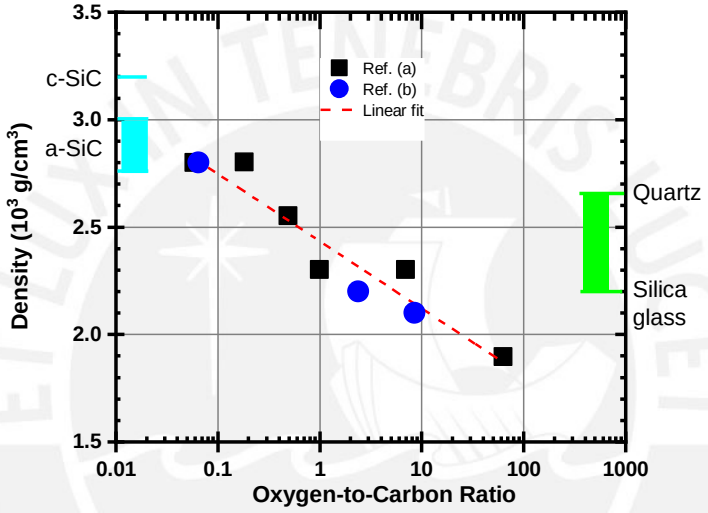

The semi-logarithmic presentation in Figure A shows a linear behavior of the mass density (ρ) with the oxygen-to-carbon ratio (k), indicating a logarithmic behavior. Therefore, the following empirical formula is presented to describe the mass density with respect to the oxygen-carbon ratio:

$$\mathrm{k} = \mathrm{k}_0 e^{-\frac{\rho}{\rho_0}} \quad \Leftrightarrow \quad \rho = -\rho_0 \ln\left(\frac{\mathrm{k}}{\mathrm{k}_0}\right)$$

The parameters k_0 (dimensionless) and ρ_0 (units of density) are material parameters which describe the silicon oxycarbide system as a whole, i. e., they do not depend on the composition. They can be determined by standard fitting procedures. To find the linear fit parameter relationship, the equation x is rewritten as:

$$\rho = -\rho_0 \ln(\mathrm{k}) + \rho_0 \ln \mathrm{k}_0 = -\rho_0 \ln(\mathrm{k}) + \mathrm{c}_0 \qquad \textbf{(A.4)}$$

The fitting parameters for Figure A were:

$\rho_0 = 0.14 \pm 0.01$ (x10^3g/cm^3) and $\mathrm{c}_0 = 2.43 \pm 0.03$ (x10^3g/cm^3)

Appendix 3: Nearest-neighbor distances in a random distribution of particles

The average center-to-center distance, $\langle R \rangle$, between a particle and its nearest neighbor will allow in the case of rare-earth doping to estimate the type of mechanism present between the ions, i.e., multipole interaction is governed at distances of up to several tens of Å, while exchange interaction at distances of up to a few Å.

In a three-dimensional random array of "point" particles (i.e., particles with extremely small radius), the distribution of nearest neighbor distances, $f(r)$, can be calculated exactly, as shown first by Hertz [251] and then by Chandrasekhar [252]. The distribution function, $f(r)$, proposed by Chandrasekhar is defined such that $f(r)$.dr is the probability of finding at least one near neighbor between a region with radius r and r+dr from a given center.

$$f(r) = 4\pi r^2 \widetilde{N}_i \, e^{-\frac{4}{3}\pi r^3 \widetilde{N}_i} \qquad \textbf{(A.5)}$$

Where, $\widetilde{N}_i$ is the number of particles per unit volume.

Note that the distribution function is asymmetric. Therefore, the average center-to-center distance does not coincidence with the most probable distance.

Average center-to-center distance $\langle R \rangle$:

$$\langle R \rangle = \frac{\int_0^\infty r f(r) dr}{\int_0^\infty f(r) dr} \qquad \textbf{(A.6)}$$

By replacing **equation A.5** in **A.6**

$$\langle R \rangle = \frac{\int_0^\infty 4\pi r^3 \widetilde{N}_i \, e^{-\frac{4}{3}\pi \widetilde{N}_i r^3} dr}{1} = \frac{\Gamma\left(\frac{4}{3}\right)}{\left(\frac{4\pi}{3}\right)^{1/3}} \widetilde{N}_i^{-1/3} \approx 0.554 \widetilde{N}_i^{-1/3}$$

$$\langle R \rangle \approx 0.554 \widetilde{N}_i^{-1/3} \qquad \textbf{(A.7)}$$

Most probable distance:

This corresponds to the maxima of the distribution $f(r)$:

$$\frac{d}{dr} f(r) = 0 \Rightarrow \; R_{max} = \frac{1}{(2\pi)^{1/3}} \widetilde{N}_i^{-1/3} \approx 0.54 \widetilde{N}_i^{-1/3}$$

If instead of considering point particles, we assume particles with finite radius r_0, then the volume fraction V_F can be defined as:

$$V_F = \frac{4\pi r_0^3}{3} \widetilde{N}_i$$

Thus, **equation A.7** would be written in the form

$$\langle R \rangle \approx 0.554 \left(\frac{4\pi}{3V_F}\right)^{1/3} r_0 \qquad \textbf{(A.8)}$$

Bansal and Ardell [253] analyzed **equation A.8** and found inconsistencies in the point model for V_F >8.84x10^{-2}, however for lower values of V_F the model was found to be consistent. In this work, for the case of rare-earth doping, particle density is studied in the range 5x10^{20} - 2x10^{21}cm^{-3}, which give values of V_F in the range 2x10^{-3}-5x10^{-3}, therefore, the point approximation can be applied.

Table A. RE mean distance in RE doped-*a*-SiOC:H samples (as-grown).

density g/cm^3	Si at.%	O at.%	C at.%	Tb at.%	Yb at.%	RE wt.%	number density ions/cm^3	RE mean distance Å
2.21	27.7	59.2	12.0	1.1	-	8.6	7.17E+20	6.2
2.09	30.1	63.5	5.4	1.0	-	7.6	6.07E+20	6.5
2.02	30.8	64.7	3.1	1.4	-	10.3	7.87E+20	6.0
2.48	30.2	26.8	40.1	-	2.9	22.2	1.92E+21	4.5
2.44	28.8	32.7	36.1	-	2.4	19.0	1.62E+21	4.7
2.32	24.3	48.5	21.8		5.4	35.2	2.84E+21	3.9
2.26	27.9	52.8	15.5	-	3.8	26.6	2.10E+21	4.3
2.20	24.7	61.2	11.5	-	2.6	19.9	1.53E+21	4.8
2.16	27.7	61.6	8.6	-	2.1	16.3	1.23E+21	5.2
2.11	26.9	63.0	6.1	-	4.0	27.4	2.01E+21	4.4

REFERENCES

[1] G. Blasse and B. C. Grabmaier, *Luminescent Materials* (Springer Berlin Heidelberg, Berlin, Heidelberg, 1994).

[2] J. Lucas, P. Lucas, T. Le Mercier, A. Rollat, and W. Davenport, in *Rare Earths* (Elsevier, 2015), pp. 281–318.

[3] J.-C. G. Bünzli, in *Handb. Phys. Chem. Rare Earths* (2016), pp. 141–176.

[4] J. Lucas, P. Lucas, T. Le Mercier, A. Rollat, and W. Davenport, in *Rare Earths* (Elsevier, 2015), pp. 319–332.

[5] T. Kano, in *Phosphor Handbook, Second Ed.*, edited by S. Shionoya, W. M. Yen, and H. Yamamoto, 2nd ed. (CRC Press, Boca Raton, 2006), pp. 215–238.

[6] J. Lucas, P. Lucas, T. Le Mercier, A. Rollat, and W. Davenport, in *Rare Earths* (2015), pp. 123–139.

[7] H. Felinto Brito, O. Manoel Loureiro Malta, M. Claudia França Cunha Felinto, and E. Epaminondas de Sousa Teotonio, in *PATAI'S Chem. Funct. Groups* (John Wiley & Sons, Ltd, Chichester, UK, 2010), pp. 2–47.

[8] E. Sarantopoulou and A.-C. Cefalas, in *Ultrav. Spectrosc. Uv Lasers* (CRC Press, 2002), pp. 281–337.

[9] F. S. Richardson, Chem. Rev. **82**, 541 (1982).

[10] B. Di Bartolo and J. Collins, in *Handb. Appl. Solid State Spectrosc.* (Springer US, Boston, MA, 2007), pp. 509–575.

[11] O. L. Malta and L. D. Carlos, Quim. Nova **26**, 889 (2003).

[12] P. C. De Sousa Filho, J. F. Lima, and O. A. Serra, J. Braz. Chem. Soc. **26**, 2471 (2015).

[13] J. Lucas, P. Lucas, T. Le Mercier, A. Rollat, and W. Davenport, in *Rare Earths* (2015), pp. 251–280.

[14] G. H. Dieke, *Spectra and Energy Levels of Rare Earth Ions in Crystals* (Interscience, New York, 1968).

[15] K. N. Shinde, S. J. Dhoble, H. C. Swart, and K. Park, in *Phosphate Phosphors*

Solid-State Light. (2012), pp. 41–59.

[16] W. M. Yen and P. M. Selzer, *Laser Spectroscopy of Solids* (Springer Berlin Heidelberg, Berlin, Heidelberg, 1981).

[17] E. Nakazawa, in *Phosphor Handbook, Second Ed.*, edited by S. Shionoya, W. M. Yen, and H. Yamamoto, 2nd ed. (CRC Press, Boca Raton, 2006), pp. 11–19.

[18] B. R. Judd, Phys. Rev. **127**, 750 (1962).

[19] G. S. Ofelt, J. Chem. Phys. **37**, 511 (1962).

[20] B. M. Walsh, in *Adv. Spectrosc. Lasers Sens.* (Springer Netherlands, Dordrecht, 2006), pp. 403–433.

[21] P. A. Tanner, in *Springer Ser. Fluoresc.* (2010), pp. 183–233.

[22] G. Blasse, in *Solid State Lumin.* (Springer Netherlands, Dordrecht, 1993), pp. 21–51.

[23] M. Sato, S. W. Kim, Y. Shimomura, T. Hasegawa, K. Toda, and G. Adachi, in *Handb. Phys. Chem. Rare Earths*, 1st ed. (Elsevier B.V., 2016), pp. 1–128.

[24] H. Yamamoto, in *Phosphor Handbook, Second Ed.*, edited by S. Shionoya, W. M. Yen, and H. Yamamoto, 2nd ed. (CRC Press, Boca Raton, 2006), pp. 35–47.

[25] J. M. F. Van Dijk and M. F. H. Schuurmans, J. Chem. Phys. **78**, 5317 (1983).

[26] M. F. H. Schuurmans and J. M. F. van Dijk, Phys. B+C **123**, 131 (1984).

[27] B. Z. Malkin, in *Spectrosc. Prop. Rare Earths Opt. Mater.* (Springer-Verlag, Berlin/Heidelberg, 1987), pp. 130–190.

[28] J. F. Suyver, A. Aebischer, D. Biner, P. Gerner, J. Grimm, S. Heer, K. W. Krämer, C. Reinhard, and H. U. Güdel, Opt. Mater. (Amst). **27**, 1111 (2005).

[29] L. van Pieterson, M. Heeroma, E. de Heer, and A. Meijerink, J. Lumin. **91**, 177 (2000).

[30] E. Nakazawa, in *Phosphor Handbook, Second Ed.*, edited by S. Shionoya, W. M. Yen, and H. Yamamoto, 2nd ed. (CRC Press, Boca Raton, 2006), pp. 83–97.

[31] M. Clara Gonçalves, L. F. Santos, and R. M. Almeida, Comptes Rendus Chim. **5**, 845 (2002).

[32] M. A. Omary and H. H. Patterson, *Luminescence, Theory*, 3rd ed. (Elsevier Ltd.,

2017).

[33] D. L. Dexter, J. Chem. Phys. **21**, 836 (1953).

[34] X. Huang, S. Han, W. Huang, and X. Liu, Chem. Soc. Rev. **42**, 173 (2013).

[35] E. Nakazawa, in *Phosphor Handbook, Second Ed.*, edited by S. Shionoya, W. M. Yen, and H. Yamamoto, 2nd ed. (CRC Press, Boca Raton, 2006), pp. 99–110.

[36] M. Inokuti and F. Hirayama, J. Chem. Phys. **43**, 1978 (1965).

[37] C. R. Ronda, in *Luminescence* (Wiley-VCH Verlag GmbH & Co. KGaA, Weinheim, Germany, 2007), pp. 1–34.

[38] N. Yamada, S. Shionoya, and T. Kushida, J. Phys. Soc. Japan **32**, 1577 (1972).

[39] B. Di Bartolo, in *Adv. Energy Transf. Process.*, edited by B. Di Bartolo and X. Chen (World Scientific, Singapore, 2001), pp. 1–71.

[40] F. Auzel, Chem. Rev. **104**, 139 (2004).

[41] M. Yokota and O. Tanimoto, J. Phys. Soc. Japan **22**, 779 (1967).

[42] T. Miyakawa and D. L. Dexter, Phys. Rev. B **1**, 2961 (1970).

[43] C. Ronda, Ref. Modul. Mater. Sci. Mater. Eng. (2017).

[44] J. A. Guerra, F. Benz, A. R. Zanatta, H. P. Strunk, A. Winnacker, and R. Weingärtner, Phys. Status Solidi Curr. Top. Solid State Phys. **10**, 68 (2013).

[45] R. S. Meltzer, in *Phosphor Handbook, Second Ed.*, edited by S. Shionoya, W. M. Yen, and H. Yamamoto, 2nd ed. (CRC Press, Boca Raton, 2006), pp. 507–529.

[46] A. Boccolini, J. Marques-Hueso, D. Chen, Y. Wang, and B. S. Richards, Sol. Energy Mater. Sol. Cells **122**, 8 (2014).

[47] D. L. Dexter, Phys. Rev. **108**, 630 (1957).

[48] W. W. Piper, J. A. DeLuca, and F. S. Ham, J. Lumin. **8**, 344 (1974).

[49] J. L. Sommerdijk, A. Bril, and A. W. de Jager, J. Lumin. **9**, 288 (1974).

[50] R. T. Wegh, H. Donker, K. D. Oskam, and A. Meijerink, Science (80-.). **283**, 663 (1999).

[51] R. . Wegh, H. Donker, E. V. . van Loef, K. . Oskam, and A. Meijerink, J. Lumin. **87**–**89**, 1017 (2000).

[52] P. Vergeer, T. J. H. Vlugt, M. H. F. Kox, M. I. Den Hertog, J. P. J. M. Van Der Herden, and A. Meijerink, Phys. Rev. B -Condensed Matter Mater. Phys. **71**, 1 (2005).

[53] D. L. Andrews and R. D. Jenkins, J. Chem. Phys. **114**, 1089 (2001).

[54] R. D. Jenkins and D. L. Andrews, J. Phys. Chem. A **102**, 10834 (1998).

[55] J. R. Lakowicz, in *Princ. Fluoresc. Spectrosc.* (1999), pp. 95–140.

[56] H. Rinnert, M. Vergnat, G. Marchal, and A. Burneau, Appl. Phys. Lett. **72**, 3157 (1998).

[57] C. Feldmann, T. Jüstel, C. R. Ronda, and D. U. Wiechert, J. Lumin. **92**, 245 (2001).

[58] J. Zhou, Y. Teng, G. Lin, and J. Qiu, J. Non. Cryst. Solids **357**, 2336 (2011).

[59] B. M. Van Der Ende, L. Aarts, and A. Meijerink, Adv. Mater. **21**, 3073 (2009).

[60] W. Shockley and H. J. Queisser, J. Appl. Phys. **32**, 510 (1961).

[61] M. B. De la Mora, O. Amelines-Sarria, B. M. Monroy, C. D. Hernández-Pérez, and J. E. Lugo, Sol. Energy Mater. Sol. Cells **165**, 59 (2017).

[62] B. S. Richards, Sol. Energy Mater. Sol. Cells **90**, 2329 (2006).

[63] J. Day, S. Senthilarasu, and T. K. Mallick, Renew. Energy **132**, 186 (2019).

[64] B. S. Richards, Sol. Energy Mater. Sol. Cells **90**, 1189 (2006).

[65] T. Trupke, M. A. Green, and P. Würfel, J. Appl. Phys. **92**, 1668 (2002).

[66] E. Klampaftis, D. Ross, K. R. McIntosh, and B. S. Richards, Sol. Energy Mater. Sol. Cells **93**, 1182 (2009).

[67] Quantum Efficiency, PVEducation (n.d.).

[68] B. S. Richards, A. Ivaturi, S. K. W. MacDougall, and J. Marques-Hueso, in *Photonics Sol. Energy Syst. IV*, edited by R. Wehrspohn and A. Gombert (2012), p. 843802.

[69] Y. An, C. Labbé, J. Cardin, and M. Morales, 855 (2013).

[70] R. E. Rojas-Hernandez, L. F. Santos, and R. M. Almeida, J. Lumin. **197**, 180 (2018).

[71] Anti-Reflection Coatings, PVEducation, Date Accessed 2020-02-19 (n.d.).

[72] C. Battaglia, A. Cuevas, and S. De Wolf, Energy Environ. Sci. **9**, 1552 (2016).

[73] B. S. Richard and A. Shalav, Synth. Met. **154**, 61 (2005).

[74] S. McDowall, T. Butler, E. Bain, K. Scharnhorst, and D. Patrick, Appl. Opt. **52**, 1230 (2013).

[75] H. Miyazaki, Jpn. J. Appl. Phys. **47**, 8287 (2008).

[76] C. Stabler, E. Ionescu, M. Graczyk-Zajac, I. Gonzalo-Juan, and R. Riedel, J. Am. Ceram. Soc. **101**, 4817 (2018).

[77] K. Lu and D. Erb, Int. Mater. Rev. **63**, 139 (2018).

[78] C. G. Pantano, A. K. Singh, and H. Zhang, J. Sol-Gel Sci. Technol. **14**, 7 (1999).

[79] M. O' Keeffe and B. G. Hyde, Acta Crystallogr. **B34**, 27 (1978).

[80] H. Ohsaki, K. Miura, A. Imai, M. Tada, and M. A. Aegerter, J. Sol-Gel Sci. Technol. **2**, 245 (1994).

[81] P. G. Coombs, J. F. De Natale, P. J. Hood, D. K. Mcelfresh, R. S. Wortman, F. Shackelford, J. F. De Natale, P. J. Hood, D. K. Mcelfresh, R. S. Wortman, and P. M. A. G. Letters, Philos. Mag. B **51**, L39 (1985).

[82] H. Bréquel, J. Parmentier, S. Walter, R. Badheka, G. Trimmel, S. Masse, J. Latournerie, P. Dempsey, C. Turquat, L. Le Neindre-prum, U. A. Jayasooriya, D. Hourlier, H. Kleebe, G. D. Soraru, S. Enzo, and F. Babonneau, 2585 (2004).

[83] J. Homeny and G. G. Nelson, J. Am. Ceram. Soc. **71**, 386 (2005).

[84] C. G. Pantano, A. K. Singh, and H. Zhang, **25**, 7 (1999).

[85] S. Modena, G. D. Sorarù, Y. Blum, and R. Raj, J. Am. Ceram. Soc. **88**, 339 (2005).

[86] E. Ionescu, H. J. Kleebe, and R. Riedel, Chem. Soc. Rev. **41**, 5032 (2012).

[87] S. Gallis, M. Huang, H. Efstathiadis, E. Eisenbraun, A. E. Kaloyeros, E. E. Nyein, and U. Hommerich, Appl. Phys. Lett. **87**, 7 (2005).

[88] J. V Ryan, C. G. Pantano, J. V Ryan, and C. G. Pantano, J. Vac. Sci. Technol. **A 25**, (2007).

[89] H. J. Kleebe, C. Turquat, and G. D. Sorarù, J. Am. Ceram. Soc. **84**, 1073 (2001).

[90] J. A. Dean, *Langre's Handbook of Chemistry* (1992).

[91] V. Belot, R. J. P. Corriu, D. Leclercq, P. H. Mutin, and A. Vloux, J. Polym Sci A.

30, 613 (1992).

[92] V. Belot, R. Corriu, D. Leclercq, P. H. Mutin, and A. Vioux, Chem. Mater. **3**, 127 (1991).

[93] S. Gallis, V. Nikas, M. Huang, E. Eisenbraun, and A. E. Kaloyeros, J. Appl. Phys. **102**, 024302 (2007).

[94] V. Nikas, N. Tabassum, B. Ford, L. Smith, A. E. Kaloyeros, and S. Gallis, J. Mater. Res. **30**, 3692 (2015).

[95] Z. Lin, H. Li, R. Huang, Y. Zhang, J. Song, H. Li, Y. Guo, C. Song, and J. Robertson, ACS Appl. Mater. Interfaces **9**, 22725 (2017).

[96] V. Nikas, S. Gallis, M. Huang, A. E. Kaloyeros, A. P. D. Nguyen, A. Stesmans, and V. V. Afanas'ev, Appl. Phys. Lett. **104**, 061906 (2014).

[97] Z. Lin, Y. Guo, C. Song, J. Song, X. Wang, Y. Zhang, R. Huang, and X. Huang, J. Alloys Compd. **633**, 153 (2015).

[98] R. Salh, in *Cryst. Silicon - Prop. Uses*, edited by S. Basu (IntechOpen, 2011).

[99] L. Skuja, J. Non. Cryst. Solids **239**, 16 (1998).

[100] Y. H. Yu, S. P. Wong, and I. H. Wilson, **168**, 531 (1998).

[101] J. A. L. López, J. C. López, D. E. V. Valerdi, G. G. Salgado, T. Díaz-Becerril, A. P. Pedraza, and F. J. F. Gracia, Nanoscale Res. Lett. **7**, 604 (2012).

[102] S. Gallis, V. Nikas, H. Suhag, M. Huang, and A. E. Kaloyeros, Appl. Phys. Lett. **97**, 081905 (2010).

[103] A. Karakuscu, R. Guider, L. Pavesi, and G. D. Sorarù, J. Am. Ceram. Soc. **92**, 2969 (2009).

[104] I. Menapace, G. Mera, R. Riedel, E. Erdem, R. A. Eichel, A. Pauletti, and G. A. Appleby, J. Mater. Sci. **43**, 5790 (2008).

[105] J. A. Guerra, J. R. Angulo, S. Gomez, J. Llamoza, L. M. Montañez, A. Tejada, J. A. Töfflinger, A. Winnacker, and R. Weingärtner, J. Phys. D. Appl. Phys. **49**, 195102 (2016).

[106] H. Ding and M. J. Demkowicz, Sci. Rep. **5**, 1 (2015).

[107] R. Gauvin, D. Drouin, A. R. Couture, P. Hovongton, D. Drouin, P. Horny, and H.

Demers, (n.d.).

[108] S. Gallis, V. Nikas, M. Huang, E. Eisenbraun, and A. E. Kaloyeros, J. Appl. Phys. **102**, (2007).

[109] N. Tomozeiu, in *Optoelectron. - Mater. Tech.* (InTech, 2011).

[110] P. G. Pai, S. S. Chao, Y. Takagi, and G. Lucovsky, J. Vac. Sci. Technol. A Vacuum, Surfaces, Film. **4**, 689 (1986).

[111] D. M. Wolfe, B. J. Hinds, F. Wang, G. Lucovsky, B. L. Ward, M. Xu, R. J. Nemanich, and D. M. Maher, J. Vac. Sci. Technol. A Vacuum, Surfaces, Film. **17**, 2170 (1999).

[112] J. Bullot and M. P. Schmidt, Phys. Status Solidi **143**, 345 (1987).

[113] V. P. Tolstoy, I. V. Chernyshova, and V. A. Skryshevsky, *Handbook of Infrared Spectroscopy of Ultrathin Films* (John Wiley & Sons, Inc., Hoboken, NJ, USA, 2003).

[114] J. V. Ryan and C. G. Pantano, J. Vac. Sci. Technol. A Vacuum, Surfaces, Film. **25**, 153 (2007).

[115] E. San Andrés, A. del Prado, F. L. Martínez, I. Mártil, D. Bravo, and F. J. López, J. Appl. Phys. **87**, 1187 (2000).

[116] D. V. Tsu, G. Lucovsky, and B. N. Davidson, Phys. Rev. B **40**, 1795 (1989).

[117] W. K. Choi, T. Y. Ong, L. S. Tan, F. C. Loh, and K. L. Tan, J. Appl. Phys. **83**, 4968 (1998).

[118] F. Stolze, M. Zacharias, S. Schippel, and B. Garke, Solid State Commun. **87**, 805 (1993).

[119] F. M. Elam, B. C. A. M. Van Der Velden-Schuermans, S. A. Starostin, M. C. M. Van De Sanden, and H. W. De Vries, RSC Adv. **7**, 52274 (2017).

[120] A. V. Vasin, M. Adlung, V. A. Tertykh, D. Kysil, S. Gallis, A. N. Nazarov, and V. S. Lysenko, J. Lumin. **190**, 141 (2017).

[121] M. Cannas, GNSR 2001 State Art Futur. Dev. Raman Spectrosc. Relat. Tech. 91 (2002).

[122] K. Morigaki and C. Ogihara, in *Springer Handb. Electron. Photonic Mater.* (Springer International Publishing, Cham, 2017), pp. 1–1.

[123] J. Singh, *Optical Properties of Condensed Matter and Applications* (John Wiley & Sons, Ltd, Chichester, UK, 2006).

[124] S. Adachi, *Optical Properties of Crystalline and Amorphous Semicondutors* (Springer Science+Business Media, New York, 1999).

[125] R. A. Street, *Hydrogenated Amorphous Silicon* (Cambridge University Press, New York, 1991).

[126] J. Singh and K. Shimakawa, *Advances in Amorphous Semiconductors* (Taylor & Francis, 2003).

[127] F. Urbach, Phys. Rev. **92**, 1324 (1953).

[128] R. Swanepoel, J. Phys. E. **16**, 1214 (1983).

[129] D. Poelman and P. F. Smet, J. Phys. D. Appl. Phys. **36**, 1850 (2003).

[130] A. Tejada, L. Montañez, C. Torres, P. Llontop, L. Flores, F. De Zela, A. Winnacker, and J. A. Guerra, Appl. Opt. **58**, 9585 (2019).

[131] S. Singh, J. R. Potopowicz, L. G. Van Uitert, and S. H. Wemple, Appl. Phys. Lett. **19**, 53 (1971).

[132] I. H. Malitson, J. Opt. Soc. Am. **55**, 1205 (2008).

[133] G. D. Cody, T. Tiedje, B. Abeles, B. Brooks, and Y. Goldstein, Phys. Rev. Lett. **47**, 1480 (1981).

[134] A. Janotta, M. Schmidt, R. Janssen, M. Stutzmann, and C. Buchal, Phys. Rev. B - Condensed Matter Mater. Phys. **68**, 1 (2003).

[135] J. Tauc, R. Grigorovici, and A. Vancu, Phys. Stat. Sol. **15**, 627 (1966).

[136] D. E. Sweenor, S. K. O'Leary, and B. E. Foutz, Solid State Commun. **110**, 281 (1999).

[137] F. Zhang, H. Xue, Z. Song, Y. Guo, and G. Chen, Phys. Rev. B **46**, 4590 (1992).

[138] B. Ford, N. Tabassum, V. Nikas, and S. Gallis, Materials (Basel). **10**, (2017).

[139] G. Das, G. Mariotto, and A. Quaranta, J. Electrochem. Soc. **153**, F46 (2006).

[140] A. V. Vasin, S. Muto, Y. Ishikawa, A. V. Rusavsky, T. Kimura, V. S. Lysenko, and A. N. Nazarov, Thin Solid Films **519**, 2218 (2011).

[141] R. A. Street, D. K. Biegelsen, and R. L. Weisfield, Phys. Rev. B **30**, 5861 (1984).

[142] R. A. Street, Appl. Phys. Lett. **41**, 1060 (1982).

[143] A. V. Vasin, Y. Ishikawa, S. P. Kolesnik, A. A. Konchits, V. S. Lysenko, A. N. Nazarov, and G. Y. Rudko, Solid State Sci. **11**, 1833 (2009).

[144] F. Fabbri, F. Rossi, M. Negri, R. Tatti, L. Aversa, S. Chander Dhanabalan, R. Verucchi, G. Attolini, and G. Salviati, Nanotechnology **25**, (2014).

[145] S. Y. Seo, K. S. Cho, and J. H. Shin, Appl. Phys. Lett. **84**, 717 (2004).

[146] Y. Ishikawa, A. V. Vasin, J. Salonen, S. Muto, V. S. Lysenko, A. N. Nazarov, N. Shibata, and V. P. Lehto, J. Appl. Phys. **104**, 1 (2008).

[147] Y. D. Glinka, S.-H. Lin, and Y.-T. Chen, Appl. Phys. Lett. **75**, 778 (1999).

[148] A. Braud, Top. Appl. Phys. **124**, 269 (2010).

[149] M. Godlewski, A. J. Zakrzewski, and V. Y. Ivanov, J. Alloys Compd. **300**, 23 (2000).

[150] S. Boninelli, G. Bellocchi, G. Franzò, M. Miritello, and F. Iacona, J. Appl. Phys. **113**, (2013).

[151] G. Bellocchi, G. Franzò, S. Boninelli, M. Miritello, T. Cesca, F. Iacona, and F. Priolo, IOP Conf. Ser. Mater. Sci. Eng. **56**, 012009 (2014).

[152] G. Bellocchi, F. Fabbri, M. Miritello, F. Iacona, and G. Franzò, ACS Appl. Mater. Interfaces **7**, 18201 (2015).

[153] S. Boninelli, A. Shakoor, K. Welma, T. F. Krauss, L. O'Faolain, R. Lo Savio, S. Portalupi, D. Gerace, M. Galli, P. Cardile, G. Bellocchi, G. Franzò, M. Miritello, F. Iacona, and F. Priolo, J. Phys. Conf. Ser. **471**, (2013).

[154] G. Bellocchi, F. Iacona, M. Miritello, T. Cesca, and G. Franzò, Opt. Express **21**, 20280 (2013).

[155] S. Gallis, M. Huang, and A. E. Kaloyeros, Appl. Phys. Lett. **90**, 19 (2007).

[156] V. Nikas, S. Gallis, M. Huang, and A. E. Kaloyeros, J. Appl. Phys. **109**, (2011).

[157] G. K. Mebratu, M. J. Kim, and J. H. Shin, Japanese J. Appl. Physics, Part 1 Regul. Pap. Short Notes Rev. Pap. **43**, 444 (2004).

[158] S. Y. Seo and J. H. Shin, Appl. Phys. Lett. **84**, 4379 (2004).

[159] G. D. Sorarù, S. Modena, E. Guadagnino, P. Colombo, J. Egan, and C. Pantano, J.

Am. Ceram. Soc. **85**, (2002).

[160] C. Linck, E. Ionescu, B. Papendorf, D. Galuskova, D. Galusek, P. Šajgalík, and R. Riedel, Int. J. Mat. Res. **103**, 31 (2012).

[161] T. Varga, A. Navrotsky, J. L. Moats, R. M. Morcos, F. Poli, K. Müller, A. Saha, and R. Raj, J. Am. Ceram. Soc. **90**, 3213 (2007).

[162] Crystal-gmbh, *Silicon Dioxide (Quartz Crystal)* (n.d.).

[163] J. Wan, Y. Ling, Q. Sun, and X. Wang, Phys. Rev. B - Condens. Matter Mater. Phys. **58**, 10415 (1998).

[164] V. F. Masterov, F. S. Nasredinov, P. P. Seregin, V. K. Kudoyarova, A. N. Kuznetsov, and E. I. Terukov, Appl. Phys. Lett. **72**, 728 (1998).

[165] S. B. Aldabergenova, M. Albrecht, H. P. Strunk, J. Viner, P. C. Taylor, and A. A. Andreev, Mater. Sci. Eng. B Solid-State Mater. Adv. Technol. **81**, 29 (2001).

[166] C. Piamonteze, L. R. Tessler, M. C. Martins Alves, and H. Tolentino, Brazilian J. Phys. **29**, 756 (1999).

[167] C. Piamonteze, A. C. Iñiguez, L. R. Tessler, M. C. Martins Alves, and H. Tolentino, Phys. Rev. Lett. **81**, 4652 (1998).

[168] J. H. Shin, R. Serna, G. N. Van Den Hoven, A. Polman, W. G. J. H. M. Van Sark, and A. M. Vredenberg, Appl. Phys. Lett. **997**, 997 (1995).

[169] L. R. Tessler and G. F. Bosco, ECS Trans. **72**, 27 (2016).

[170] A. R. Zanatta, A. Khan, and M. E. Kordesch, J. Phys. Condens. Matter **19**, (2007).

[171] A. R. Zanatta, J. Phys. D. Appl. Phys. **42**, (2009).

[172] B. Garrido, C. García, S. Y. Seo, P. Pellegrino, D. Navarro-Urrios, N. Daldosso, L. Pavesi, F. Gourbilleau, and R. Rizk, Phys. Rev. B - Condens. Matter Mater. Phys. **76**, 1 (2007).

[173] G. K. Mebratu, M. J. Kim, and J. H. Shin, J. Non. Cryst. Solids **347**, 279 (2004).

[174] Z. Yang, J. Yang, J. Qiu, and Z. Song, Phys. Chem. Chem. Phys. **19**, 31997 (2017).

[175] C. Jacinto, S. L. Oliveira, L. A. O. Nunes, T. Catunda, and M. J. V. Bell, Appl. Phys. Lett. **86**, 1 (2005).

[176] S. Kuhn, M. Tiegel, A. Herrmann, J. Körner, R. Seifert, F. Yue, D. Klöpfel, J.

Hein, M. C. Kaluza, and C. Rüssel, Opt. Mater. Express **5**, 430 (2015).

[177] W. G. Quirino, M. J. V Bell, S. L. Oliveira, and L. A. O. Nunes, J. Non. Cryst. Solids **351**, 2042 (2005).

[178] T. Okazaki, E. H. Sekiya, and K. Saito, Jpn. J. Appl. Phys. **58**, 3 (2019).

[179] V. I. De Oliveira, F. L. Freire, and A. R. Zanatta, J. Phys. Condens. Matter **18**, 7709 (2006).

[180] W. Beyer, W. Hilgers, P. Prunici, and D. Lennartz, J. Non. Cryst. Solids **358**, 2023 (2012).

[181] S. Choi, O. Kwon, K. H. Min, M. S. Jeong, K. T. Jeong, M. G. Kang, S. Park, K. K. Hong, H. E. Song, and K. H. Kim, Sci. Rep. **10**, 9672 (2020).

[182] R. A. Street, MRS Proc. **95**, 13 (1987).

[183] C. G. V. de Walle, *Chapter 6: Hydrogen Interactions with Polycrystalline and Amorphous Silicon - Theory* (ACADEMIC PRESS, 1999).

[184] H. Kühne, G. Weiser, E. I. Terukov, A. N. Kusnetsov, and V. K. Kudoyarova, J. Appl. Phys. **86**, 896 (1999).

[185] G. Franzò, V. Vinciguerra, and F. Priolo, Appl. Phys. A Mater. Sci. Process. **69**, 3 (1999).

[186] A. Taguchi, K. Takahei, M. Matsuoka, and S. Tohno, J. Appl. Phys. **84**, 4471 (1998).

[187] N. Hamelin, P. G. Kik, J. F. Suyver, K. Kikoin, A. Polman, A. Schönecker, and F. W. Saris, J. Appl. Phys. **88**, 5381 (2000).

[188] I. Tsimperidis, T. Gregorkiewicz, H. H. P. T. Bekman, and C. J. G. M. Langerak, Phys. Rev. Lett. **81**, 4748 (1998).

[189] A. Taguchi and K. Takahei, J. Appl. Phys. **79**, 4330 (1996).

[190] P. G. Kik and A. Polman, J. Appl. Phys. **88**, 1992 (2000).

[191] M. Fujii, M. Yoshida, Y. Kanzawa, S. Hayashi, and K. Yamamoto, Appl. Phys. Lett. **71**, 1198 (1997).

[192] W. Fuhs, I. Ulber, and G. Weiser, Phys. Rev. B - Condens. Matter Mater. Phys. **56**, 9545 (1997).

[193] I. Yassievich, M. Bresler, and O. Gusev, J. Non. Cryst. Solids **226**, 192 (1998).

[194] I. N. Yassievich and L. C. Kimerling, Semicond. Sci. Technol. **8**, 718 (1993).

[195] A. Taguchi, K. Takahei, and Y. Horikoshi, J. Appl. Phys. **76**, 7288 (1994).

[196] F. Priolo, S. Coffa, G. Franzò, C. Spinella, A. Carnera, and V. Bellani, J. Appl. Phys. **74**, 4936 (1993).

[197] A. R. Zanatta, Appl. Phys. Lett. **82**, 1395 (2003).

[198] F. Priolo, G. Franzò, S. Coffa, A. Polman, S. Libertino, R. Barklie, and D. Carey, J. Appl. Phys. **78**, 3874 (1995).

[199] I. Izeddin, A. S. Moskalenko, I. N. Yassievich, M. Fujii, and T. Gregorkiewicz, Phys. Rev. Lett. **97**, 2 (2006).

[200] Ś. Cueff, C. Labb́, B. Dierre, F. Fabbri, T. Sekiguchi, X. Portier, and R. Rizk, J. Appl. Phys. **108**, (2010).

[201] D. Navarro-Urrios, A. Pitanti, N. Daldosso, F. Gourbilleau, R. Rizk, B. Garrido, and L. Pavesi, Phys. Rev. B - Condens. Matter Mater. Phys. **79**, 2 (2009).

[202] O. Savchyn, P. G. Kik, R. M. Todi, and K. R. Coffey, Phys. Rev. B - Condens. Matter Mater. Phys. **77**, 1 (2008).

[203] A. S. Souza, L. A. Nunes, M. C. F. C. Felinto, H. F. Brito, and O. L. Malta, J. Lumin. **167**, 167 (2015).

[204] A. Aebischer, F. Gumy, and J. C. G. Bünzli, Phys. Chem. Chem. Phys. **11**, 1346 (2009).

[205] S. Omagari, T. Nakanishi, Y. Kitagawa, T. Seki, K. Fushimi, H. Ito, A. Meijerink, and Y. Hasegawa, Sci. Rep. **6**, 1 (2016).

[206] A. Jain, C. Blum, and V. Subramaniam, *Fluorescence Lifetime Spectroscopy and Imaging of Visible Fluorescent Proteins*, First Edit (Elsevier, 2009).

[207] G. W. Adeola, H. Rinnert, P. Miska, and M. Vergnat, J. Appl. Phys. **102**, (2007).

[208] M. Fujii, M. Yoshida, S. Hayashi, and K. Yamamoto, J. Appl. Phys. **84**, 4525 (1998).

[209] R. A. Street, J. Non. Cryst. Solids **77**–**78**, 1 (1985).

[210] B. M. Van der Ende, L. Aarts, and A. Meijerink, Phys. Chem. Chem. Phys. **11**,

11081 (2009).

[211] H. Dong, L.-D. Sun, and C.-H. Yan, Chem Soc Rev **44**, 1608 (2015).

[212] H.-Q. Wang, M. Batentschuk, A. Osvet, L. Pinna, and C. J. Brabec, Adv. Mater. **23**, 2675 (2011).

[213] J. T. Van Wijngaarden, S. Scheidelaar, T. J. H. Vlugt, M. F. Reid, and A. Meijerink, Phys. Rev. B - Condens. Matter Mater. Phys. **81**, 1 (2010).

[214] J. M. Meijer, L. Aarts, B. M. Van Der Ende, T. J. H. Vlugt, and A. Meijerink, Phys. Rev. B - Condens. Matter Mater. Phys. **81**, 1 (2010).

[215] X. Liu, S. Ye, Y. Qiao, G. Dong, B. Zhu, D. Chen, G. Lakshminarayana, and J. Qiu, Appl. Phys. B Lasers Opt. **96**, 51 (2009).

[216] L. F. Flores, K. Y. Tucto, J. A. Guerra, R. Grieseler, J. A. Töfflinger, A. Osvet, M. Batentschuk, and R. Weingärtner, Adv. Mater. Proc. **3**, 372 (2018).

[217] L. F. Flores, K. Y. Tucto, J. A. Guerra, J. A. Töfflinger, E. S. Serquen, A. Osvet, M. Batentschuk, A. Winnacker, R. Grieseler, and R. Weingärtner, Opt. Mater. (Amst). **92**, 16 (2019).

[218] N. Duhamel-Henry, J. L. Adam, B. Jacquier, and C. Linarès, Opt. Mater. (Amst). **5**, 197 (1996).

[219] H. E. Hoefdraad, J. Solid State Chem. **15**, 175 (1975).

[220] G. Li, C. Zhang, P. Song, P. Zhu, K. Zhu, and J. He, J. Alloys Compd. **662**, 89 (2016).

[221] Q. Duan, F. Qin, D. Wang, W. Xu, J. Cheng, Z. Zhang, and W. Cao, J. Appl. Phys. **110**, 1 (2011).

[222] X. Zhou, Y. Wang, G. Wang, L. Li, K. Zhou, and Q. Li, J. Alloys Compd. **579**, 27 (2013).

[223] F. Enrichi, C. Armellini, S. Belmokhtar, A. Bouajaj, A. Chiappini, M. Ferrari, A. Quandt, G. C. Righini, A. Vomiero, and L. Zur, J. Lumin. **193**, 44 (2018).

[224] K. Tucto, L. Flores, J. Guerra, J. Töfflinger, J. Dulanto, R. Grieseler, A. Osvet, M. Batentschuk, and R. Weingärtner, MRS Adv. **2**, 2989 (2017).

[225] Y.-T. An, C. Labbé, J. Cardin, M. Morales, and F. Gourbilleau, Adv. Opt. Mater. **1**, 855 (2013).

[226] J.-L. Yuan, X.-Y. Zeng, J.-T. Zhao, Z.-J. Zhang, H.-H. Chen, and X.-X. Yang, J. Phys. D. Appl. Phys. **41**, 105406 (2008).

[227] F. T. Rabouw and A. Meijerink, J. Phys. Chem. C **119**, 2364 (2015).

[228] I. A. A. Terra, L.J.Borrero-González, T. R. Figueredo, J. M. P. Almeida, A. C. Hernandes, L. A. O. Nunes, and O.L.Malta, J. Lumin. **132**, 1678 (2012).

[229] W. Stręk, A. Bednarkiewicz, and P. J. Dereń, J. Lumin. **92**, 229 (2001).

[230] T. Yamashita and Y. Ohishi, J. Non. Cryst. Solids **354**, 1883 (2008).

[231] K. Petermann, D. Fagundes-Peters, J. Johannsen, M. Mond, V. Peters, J. J. Romero, S. Kutovoi, J. Speiser, and A. Giesen, J. Cryst. Growth **275**, 135 (2005).

[232] A. Brenier, J. Opt. Soc. Am. B **23**, 2209 (2006).

[233] M. O. Ramírez, D. Jaque, and L. E. Bausá, Appl. Phys. Lett. **89**, 87 (2006).

[234] D. Deng, S. Xu, R. Bao, S. Zhao, B. Wang, H. Wang, and H. Ju, J. Phys. D. Appl. Phys. **42**, (2009).

[235] P. V. Dos Santos, M. V.D. Vermelho, E. A. Gouveia, M. T. De Araújo, A. S. Gouveia-Neto, F. C. Cassanjes, S. J. L. Ribeiro, and Y. Messaddeq, J. Chem. Phys. **116**, 6772 (2002).

[236] R. Zhou, X. Wei, C. Duan, Y. Chen, and M. Yin, ECS J. Solid State Sci. Technol. **1**, R147 (2012).

[237] W. Q. Santos, A. S. S. de Camargo, D. Wu, W. F. Silva, L. Zhang, and C. Jacinto, Sci. Adv. Mater. **5**, 1948 (2013).

[238] J. A. Guerra, F. De Zela, K. Tucto, L. Montañez, J. A. Töfflinger, A. Winnacker, and R. Weingärtner, J. Phys. D. Appl. Phys. **49**, 375104 (2016).

[239] S. Leyre, E. Coutino-Gonzalez, J. J. Joos, J. Ryckaert, Y. Meuret, D. Poelman, P. F. Smet, G. Durinck, J. Hofkens, G. Deconinck, and P. Hanselaer, Rev. Sci. Instrum. **85**, (2014).

[240] K. L. Wong, J. C. G. Bünzli, and P. A. Tanner, J. Lumin. **224**, 117256 (2020).

[241] J.-C. G. Bünzli and S. V. Eliseeva, in *Springer Ser. Fluoresc.* (2010), pp. 1–45.

[242] P. Zhang, L. Zhang, Y. Wu, S. Wang, and X. Ge, Opt. Express **26**, 31617 (2018).

[243] W. G. J. H. M. Van Sark, A. Meijerink, R. E. I. Schropp, J. A. M. Van Roosmalen,

and E. H. Lysen, Sol. Energy Mater. Sol. Cells **87**, 395 (2005).

[244] W. G. J. H. M. van Sark, Thin Solid Films **516**, 6808 (2008).

[245] Y. Jestin, in *Compr. Renew. Energy* (Elsevier, 2012), pp. 563–585.

[246] D. Alonso-Álvarez, D. Ross, and B. S. Richards, Conf. Rec. IEEE Photovolt. Spec. Conf. 9 (2012).

[247] R. Rothemund, Sol. Energy Mater. Sol. Cells **120**, 616 (2014).

[248] A. Solodovnyk, C. Kick, A. Osvet, H. J. Egelhaaf, E. Stern, M. Batentschuk, K. Forberich, and C. J. Brabec, Energy Technol. **4**, 385 (2016).

[249] M. Li and Y. Yue, RSC Adv. **4**, 23010 (2014).

[250] B. Skinner and D. Appleman, Am. Mineral. **48**, 854 (1963).

[251] P. Hertz, Math. Ann. **67**, 387 (1909).

[252] S. Chandrasekhar, Rev. Mod. Phys. **15**, 1 (1943).

[253] P. P. Bansal and A. J. Ardell, Metallography **5**, 97 (1972).

Papers and conferences

The following papers and attended conferences are related to my research activity during my Ph.D.

Papers

First author

- Luminescence properties of Yb3+-Tb3+ co-doped amorphous silicon oxycarbide thin films, Opt. Mater. (Amst). 92 (2019) 16–21.
- Fabrication and Luminescence Properties in Yb–Tb Co-Doped a-SiCO Thin Films," Adv. Mater. Proc. 3.6 (2018): 372–76.

Co-author

- Determination of the fundamental absorption and optical bandgap of dielectric thin films from single optical transmittance measurements, Appl. Opt. 58 (2019) 9585.
- Effect of Post-Annealing Treatment on the Structure and Luminescence Properties of ALN:Tb3+ Thin Films Prepared by Radio Frequency Magnetron Sputtering, Mater. Sci. Forum. 890 (2017) 299–302.
- Production and Characterization of Tb3+/Yb3+ Co-Activated AlON Thin Films for Down Conversion Applications in Photovoltaic Cells, MRS Adv. (2017).

Conferences

- B-MRS 2021 (XIX Brazil Materials Research Society Meeting), virtual conference, Brazil: L. Flores, et al., "Carbon role on the luminescence of Yb3+-doped silica-based glasses", poster.
- ICL 2020 (19th International Conference on Luminescence), online/in-person conference, Changchun, China: L. Flores, et al., "Improving the near-infrared Yb3+ emission in carbon-silica systems", talk.
- JOPES 2018 (Jornadas Peruanas de Energía Solar), Lima, Perú: L. Flores, K. Tucto, A. Töfflinger, J. A. Guerra and R. Grieseler, "Investigation of Tb3+/Yb3+co-doped oxide glasses thin films for down-conversion", poster.

- EURODIM 2018 (Europhysical Conference on Defects in Insulating Materials), Bydgoszcz, Poland: L. Flores, et al., "Study of Near Infrared Photoluminescence in Yb3+, Er3+ and Yb3+, Tb3+ co-doped Silicon Oxycarbide Thin Films", talk.
- E-MRS 2017 (European Materials Research Society - Spring Meeting), Strasbourg, France: L. Flores, et al., “Fabrication and Luminescence Properties in Rare Earth Doped a-SiCxOy Thin Films”, talk.
- B-MRS 2017 (XVI Brazil Materials Research Society Meeting), Gramado, Brazil: L. Flores, et al., "Effect of thermal annealing on the luminescence properties of rare earth (Yb-Tb) co-doped silicon oxycarbide thin films”, talk.
- PRE’17 (International Workshops on Photoluminescence of Rare-Earth: Photonic Materials and Applications), Rome, Italy: L. Flores, et al., “Luminescence properties of rare earth (Yb–Tb) co-doped a-SiCxOy thin films”, talk.